Evaluating hydraulic and mechanical properties of weathered intrusive and chemical sedimentary bedrock in South Africa

UNIVERSITEIT VAN PRETORIA
UNIVERSITY OF PRETORIA
YUNIBESITHI YA PRETORIA
Denkleiers • Leading Minds • Dikgopolo tša Dihlalefi

By:

Duan Swart
1431 2868

Supervisor:

Prof. Matthys A. Dippenaar

Submitted in the fulfilment of the requirements for the degree

PhD Engineering Geology

In the

Department of Geology
School of Physical Sciences
Faculty of Natural and Agricultural Sciences
University of Pretoria

November 2024

DECLARATION ON PLAGIARISM

The **Department of Geology (University of Pretoria)** places great emphasis upon integrity and ethical conduct in the preparation of all written work submitted for academic evaluation. While academic staff teaches you about referencing techniques and how to avoid plagiarism, you too have a responsibility in this regard. If you are at any stage uncertain as to what is required, you should speak to your lecturer before any written work is submitted.

You are guilty of plagiarism if you copy something from another author's work (e.g. a book, an article or a website) without acknowledging the source and pass it off as your own. In effect you are stealing something that belongs to someone else. This is not only the case when you copy work word-for-word (verbatim), but also when you submit someone else's work in a slightly altered form (paraphrase) or use a line of argument without acknowledging it. You are not allowed to use work previously produced by another student. You are also not allowed to let anybody copy your work with the intention of passing if off as his/her work.

Students who commit plagiarism will not be given any credit for plagiarised work. The matter may also be referred to the Disciplinary Committee (Students) for a ruling. Plagiarism is regarded as a serious contravention of the University's rules and can lead to expulsion from the University.

The declaration, which follows, must accompany all written work submitted while you are a student of the **Department of Geology (University of Pretoria)**. No written work will be accepted unless the declaration has been completed and attached.

I, the undersigned, declare that:

1. I declare that this thesis, which I hereby submit for the degree of PhD Engineering Geology, at the University of Pretoria, is my own original work and has not previously been submitted by me for a degree at this or any other tertiary institution.
2. Where other people's work has been used (either from a printed source, Internet or any other source), this has been properly acknowledged and referenced in accordance with Departmental requirements.
3. I have not allowed and will not allow anyone to copy my work with the intention of passing it off as his or her own work.
4. I understand the Department of Geology's policy on plagiarism and the criteria set for using Turnitin by the Department.
5. I acknowledge that I am allowed to use Turnitin to evaluate my own work prior to submission.

Full names:	Duan Swart
Student number:	14312868
Date submitted:	30/11/2024
Topic of work:	Engineering Geology
Supervisor:	Prof. Matthys Dippenaar

Table of Contents

List of Figures

List of Tables

I dedicate this thesis to my wife, Elizabeth, for her compassion, support and love.

Abstract

Weathered rock profiles are frequently encountered during geological, engineering, hydrological, ecological and forestry projects in South Africa. The *soil-end* exists in the most decomposed portion of a weathering rock profile. This zone comprises residual soil and completely weathered rock, both of which can be excavated as a soil.

In this study, completely weathered rock retains the parent rock fabric and macro-structure with secondary minerals forming in place of the primary rock-forming minerals. Residual soil forms through further intensive chemical weathering to the point where most parent rock structure and grain relations have been lost either through decomposition or volumetric strain or a combination of both.

The study was conducted with the use of traditional geotechnical laboratory methods of which the results were compared and analysed with advanced visual techniques. The laboratory testing included particle size analysis and Atterberg limits testing, chemical testing methods, compression testing in oedometers, and saturated permeabilities in a triaxial cell. The advanced visual testing comprised X-Ray Computed Tomography (XRCT) scan that allowed for the modelling of 2D and 3D porosity and density models. These models provide invaluable insight on the structural properties that govern the compression behaviour the completely weathered rock and residual soils.

The soil texture of the completely weathered rock and residual soil can be determined from simple field tests that only require water and common stationery. These tests make use of use well-understood behaviour characteristic of fine-sand, silt, and clay at varying moistures to determine the plasticity of the material, and subsequently the soil texture.

The process through which completely weathered rock and residual soil forms is governed by the physical and chemical changes caused by chemical weathering. The degree of the weathering decreases with an increase in depth into the ground profile. The state of weathering can be quantified with the use of chemical weathering indices. The close relationship between the chemical and physical states of completely weathered rock, allows for the determination of structural *prominence* which characterises the degree to which the relict rock structure influences compression behaviour. The structural *prominence* decreases as weathering increase and, consequently, this increases the compressibility of the material, regardless of the material's void ratio or dry density. The novel concept of structural *prominence* can be used to assist engineering geologists and geotechnical engineers to better understand the behaviour of completely weathered rock and residual soil and has been shown in this study to be a better predictor of soil compressibility than the dry density or void ratio.

1 Introduction

1.1 Rationale

Weathering rock profiles are frequently encountered during geological, engineering, hydrological, ecological and forestry projects in South Africa. The *soil-rock* interface typically exists in the most decomposed portion of a weathering rock profile. This interface comprises residual soil and completely weathered rock, both of which can be excavated as a soil. The term saprolite is often used to collectively define this portion of a weathering profile (National Research 2001; Dos Santos et al. 2018; Dos Santos et al. 2022; Silva et al. 2022; Bonnet et al. 2022). However, to keep with the terminology used in geotechnics and geology in general, the terms completely weathered rock and residual soil will be used in this research (origin description in Dippenaar et al. 2024). For this study, completely weathered rock retains the parent rock fabric and macro-structure with secondary minerals forming in place of the primary rock-forming minerals. Residual soil forms through further intensive chemical weathering to the point where most parent rock structure and grain relations have been lost either through decomposition or volumetric strain or a combination of both. The weathering profile that will be studied must be near to the surface for practicable sampling and must be free draining.

The ability of completely weathered rock to store water influences groundwater recharge and return flow, impacting both the quantity and quality of surface and subsurface water (National Research 2001; van Tol 2020; Dippenaar et al. 2022). In this material, the porosity is a combination of primary voids between mineral grains and secondary fractures inherited from the original rock structure. These secondary pores often serve as preferential flow paths for moisture until the relict rock structure is completely lost through further decomposition, contributing to the complex hydrological behaviour of weathered profiles (Swart et al. 2019; Dos Santos et al. 2022; Dos Santos et al. 2018; Bonnet et al. 2022).

The pore geometry and orientation, which is controlled by the relict rock structure, has been shown to be a critical parameter for the strength of the material (Day 1981; Buttrick 1986; Letey 1991; Rocchi et al. 2017; Rabot et al. 2018; Swart et al. 2019; Silva et al. 2022; Dos Santos et al. 2022; Bonnet et al. 2023; Wang et al. 2024). The relict rock structure is thought to provide strength and stiffness to completely weathered rock; however, it cannot accurately be assessed using standard microscopy methods and hand samples. These methods characterise the structure in 2-dimensions and the structure needs to be broken to begin the evaluation.

The continued decomposition of rock and absorption of carbonic acid during weathering forms an integral part of the carbonate-silicate cycle on earth (Mackenzie and Garrels 1966; Raymo and Ruddiman 1992; Berner 2004; Kasting 2019). It has been hypothesised that a negative feedback loop on the Earth's climate exists between fluxes of atmospheric CO_2 and the weathering intensity of silicates (Berner et al. 1983; Deng et al. 2022).This negative feedback loop regulates the global climate and stabilizes the habitability of the planet over long timescales.

The bases of the negative feedback loop are as follows: warmer, higher pCO_2 climates accelerate silicate weathering rates and drawdown of pCO_2, causing a cooling effect, hindering silicate weathering and allowing pCO_2 build up and warming. Silva et al. (2022) stated consumption of CO_2 by silicate weathering in completely weathered rock is not clearly understood, for many reasons including the role of varying pore geometry, and water flow and storage through the profile.

As the weathering front moves deeper down into the ground profile, completely weathered rock decomposes and weakens with increased weathering to the point where the relict rock structure, and the governing characteristic of this structure, is lost. This is the transition point where completely weathered rock transforms into residual soil within a weathering rock profile. Weathering fronts are generally parallel to the ground surface, and weathering profiles are typically vertical. However, in steep natural slopes, weathering profiles can also develop laterally (Phillips et al. 2006). Completely weathered rock exposed in large man-made excavations undergoes rapid weathering, leading to the decomposition of meta-stable minerals and ultimately altering or destroying the relict rock structure (Obermeier and Langer 1986). It is clear the relict rock structure and fabric is highly dependent on the chemical weathering intensity it is exposed to, and therefore the parameters that this structure governs are influenced by the weathering.

A relevant example is the excavation of completely weathered rock for material utilisation as general fill in road construction which is often the case in South Africa. Initially, the excavated material may grade as a silty sand and be competent for G8 or G9 material with low plasticity. However, the metastable minerals breakdown into smaller grains, increasing the total surface area, during removal, placement, and compaction in engineering layer works. The minerals are expected to undergo rapid weathering once exposed to Earth surface conditions, thereby increasing the clay content, resulting in unanticipated changes in the material's engineering properties. This differs from targeting transported soils for material utilisation because the minerals are weathering products, and generally stable on the surface of the Earth. The primary cause for high fill settlement is the lack of sorting and selecting appropriate filling material from multiple sources, causing zones of soil with unfavourable grading and plastic behaviour to be placed in the earthworks (Liang et al. 2022). This occurs due to materials excavated from weathering profiles are stockpiled and allowed to weather before being placed into layer works.

Unsaturated soil mechanics, particularly the concept of matric suction, is fundamentally based on the mathematics of circle circumference and radius where pore size influences the capillary forces within the soil matrix. This mathematical relationship underpins the behaviour of water in unsaturated soils and governs how moisture is retained and transmitted through the pore spaces of geological medium and other weathered materials.

Naturally occurring pores in residuum are almost always non-spherical, resulting in the need to make many assumptions of spatial orientations when basing soil structure on unsaturated tests (Baveye et al. 2022). Being able to confidentially model 3-dimensional porosity geometry will allow for more accurate pore modelling assumptions and further development in unsaturated soil mechanics and numerical modelling in water management.

1.2 Research aims

Residual soils and completely weathered rock are often associated with tropical climates where intense leaching occurs. *Tropical* soils are not normally associated with South Africa but due to the ancient and stable landscape, deeply weathered rock profiles do exist and are currently forming in the eastern parts of the country. The impact of chemical weathering on the mechanical, chemical and physical parameters has been intensely studied on igneous weathering profiles in high rainfall areas around the world (Hall et al. 2012; Rocchi et al. 2017; Riebe et al. 2021; Bonnet et al. 2022; 2023; Dos Santos et al. 2022; Liu et al. 2022; Wang et al. 2024). However, very little work has been done of investigating the influence of decomposition on mechanical and hydraulic properties through a weathered rock profile in South Africa, especially in the past decade (Van der Merwe 1964; Blight and Leong 2012).

This is especially true for residuum forming above dolomite bedrock, which is surprising considering the impact the overburden has on the formation or sinkholes and subsidence. The majority of the research focusing the residuum products of dolomite were conducted in the 1980s due to the increase in occurrence of sinkholes within residential areas and critical infrastructure (Day 1981; Buttrick 1986). Swart et al. (2019) focused on influence of the manganese and iron quantities on the material's hydromechanical properties and how it changes as the material undergoes weathering or anthropogenic alteration. The research showed the manganese oxide content, and the extremely low dry density of the wad were the most crucial parameters to consider when investigating dolomite residuum.

The *soil-end* of a weathering profile comprising completely weathered rock and residual soil is the most intricate portion of the profile. It is encountered the most often in geotechnical projects due to it being the closest to the ground surface and furthest away from the weathering front. The properties that seem to govern completely weathered rock are the parent rock origin and stress history and the weathering state of the completely weathered rock.

This research aims to:

- Investigate the influence of relict rock structures on the porosity, strength, and hydraulic conductivity of completely weathered rock.
- Determine the influence chemical weathering has on the porosity and mechanical behaviour of completely weathered rock and residual soil.
- Determine a method to quantify these changes to better understand and predict the evolving porosity and soil structure of completely weathered rock and residual soil.
- Determine the use of state-of-the-art X-ray imagery to identify and analyse the porosity in completely weathered rock and residual soil.
- Develop a method for reliably determining soil behaviour and texture on-site when working with meta-stable materials, such as completely weathered rock.

By thoroughly investigating the aims thoroughly, the study seeks to contribute to a better understanding of the engineering characteristics of a weathered rock profile and the soil-rock interface, and how this evolves through further decomposition and anthropogenic interactions. Furthermore, test the usability of x-ray scanning to be used to assess extremely weak rock and residual soil which is too friable to be tested using conventional rock testing methodologies, such as thin sections.

2 Hydromechanical behaviour and testing of unsaturated porous medium

2.1 Overview

In semi-arid countries a significance thickness of the ground profile is in the unsaturated zone, above the groundwater table, known as the vadose zone. This zone generally extends to great depths within the bedrock, leaving the transported and residual material in an unsaturated state. Negative pore-water pressures or matric suctions are prevailing components of the variably saturated soil behaviour in this zone. Changes in soil pore-water content led to variations in matric suction, which can result in significant to substantial changes in permeability, shear strength, and the volume of the unsaturated soil mass (Rahardjo et al. 2019). The potential for change will be variable in completely weathered rock with relict parent structure present. The theory of unsaturated soil mechanics, when the moisture content is less than the air entry value as will be seen in this chapter, is grounded in mathematics of a circumference and radius of a circle. The theoretical circle exists within the pore spaces of similar sized spheres in either a cubic or tetrahedral packing, which can be confidently related to a clean, well-sorted, sand or pure clay with near-homogenous pore sizes. However, this is of course an oversimplification mainly due to the constraints faced in quantifying pore geometry in natural soils (Lu 2020).

The climate and the boundary flux condition at the ground surface greatly impacts the soil moisture content and the depth to the groundwater table. The change in global climate patterns and anthropogenic alterations of the ground surface and excavations will induce unwanted and unexpected changes in matric suctions within the soil. To understand the alterations to the behaviour of soil with a change in moisture, and vertical and confining pressures, a good knowledge of unsaturated soil mechanics is needed.

2.2 Theory of unsaturated soil mechanics

The Principle of Effective Stress, as presented by Terzaghi (1943), is used to describe forces transmitted through the soil skeleton in fully saturated soils only and where the stress state is considered a two-phase system. The key distinguishing factor between saturated and unsaturated soil mechanics is the presence of air pore spaces and the contractile skin (Fredlund and Morgenstern 1977; Fredlund et al. 2012). The four phases forming unsaturated soils and the relationship between them is shown in Figure 2-1.

Figure 2–1 presents the components that result in the thin membrane that is interwoven throughout the voids of the soil. This is termed the contractile skin and forms to equilibrate changes in volume, water content and shear strength. Matric suction acts across the interface due to the pressure differences, while the surface tension acts along the membrane (u_a - u_w) (Fredlund et al. 2012).

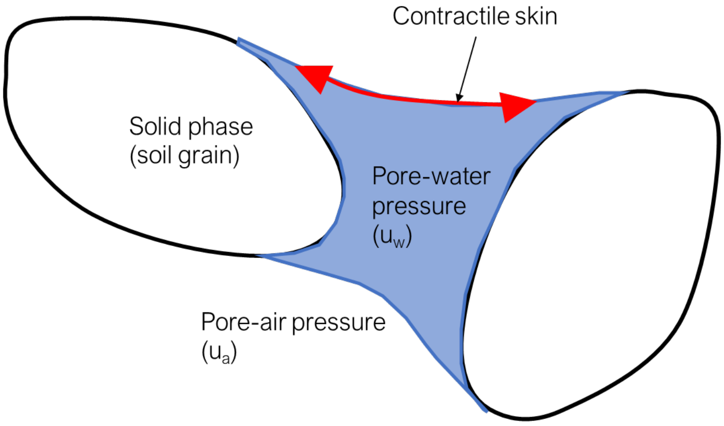

Figure 2-1 Components of unsaturated soils

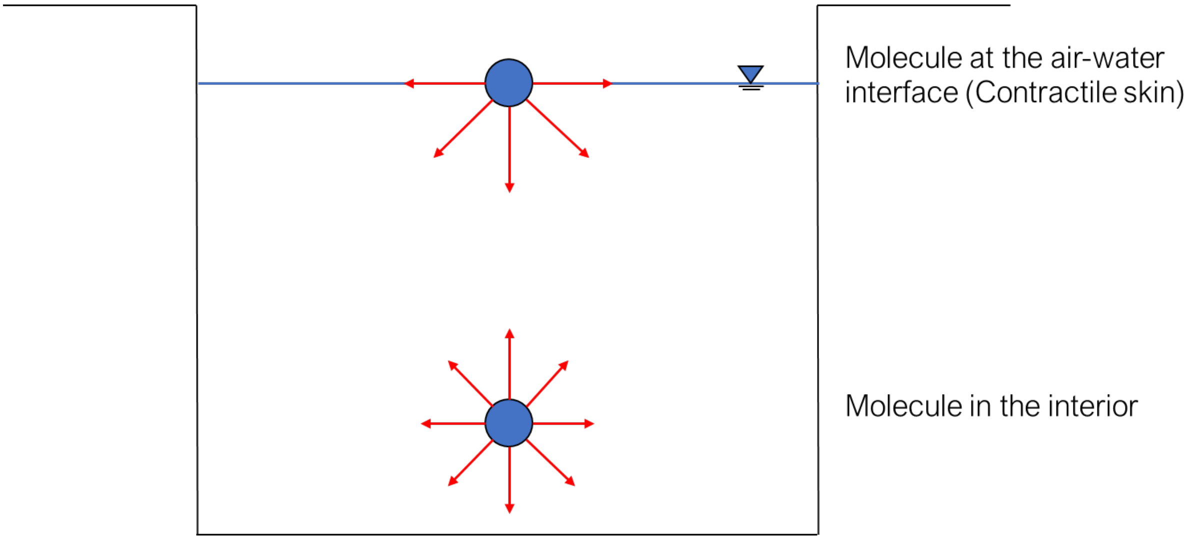

Figure 2-2 Intermolecular forces acting on contractile skin at the air-water interface (adapted from Fredlund et al. 2012)

The skin of a balloon will always orient itself concave toward the high-pressure gaseous phase inside the balloon. In the case of unsaturated soils, the air-pressure is assumed to be atmospheric ($u_a = 0$) and the pore-water pressure is generally assumed to be negative ($u_w < 0$), therefore the membrane will be concave towards the open pore side (Fredlund et al. 2012). The pressure difference across the membrane can be related to the surface tension and radius of curvature of the membrane.

The pressure difference can be related to the radius of curvature (R_S) of the meniscus and surface tension (T_S) acting along it as shown in Figure 2-3. The pressures acting on either side of the meniscus are u and ($u + \Delta u$).

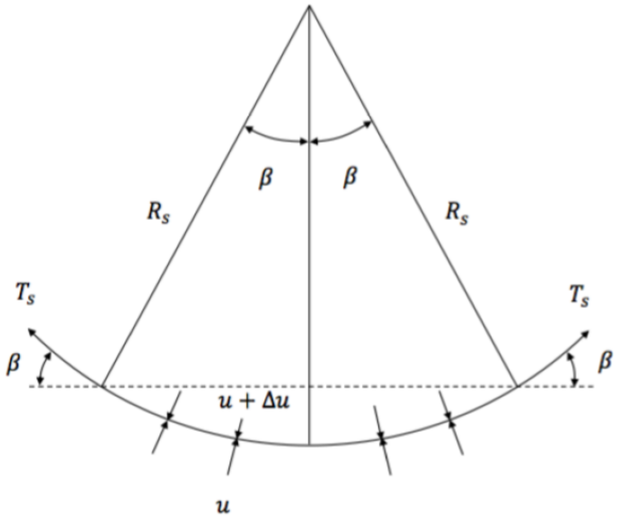

Figure 2-3 Forces acting on the concaved surface (taken from Fredlund et al. 2012)

Assuming force equilibrium in the vertical along the interface, therefore ΣFy = 0, Equation 2-1 can be written as.

$$2T_S sin\beta = 2\Delta u R_S\, sin\beta \tag{2-1}$$

Where:

$2T_S sin\beta$ = length of the membrane projected onto the horizontal plane.

Rearranging Equation 2-1 gives Equation 2-2.

$$\Delta u = \frac{T_S}{R_S} \tag{2-2}$$

Equation 2-2 can be extended using the Laplace equation for a three-dimensional membrane, as shown in Equation 2-3 (Fredlund et al. 2012).

$$\Delta u = T_S(\frac{1}{R_1} + \frac{1}{R_2}) \tag{2-3}$$

Where:

R_1, R_2 = radii of curvature of a warped membrane in two orthogonal principle curves

If the radius is assumed to be the same in all directions (R_1 = R_2 = R), Equation 2-3 becomes Equation 2-4.

$$\Delta u = \frac{2T_S}{R_S} \tag{2-4}$$

The contractile skin in an unsaturated soil is subjected to a pore-air pressure (u_a) which is greater than the negative pore-water (u_w). The pressure difference that causes the air-water interface in an unsaturated soil to bend to a curvature shown in Equation 2-5 (Fredlund et al. 2012).

$$u_a - u_w = \frac{2T_S}{R_S} \qquad \textbf{2-5}$$

Matric suction is the pressure difference across the contractile skin in an unsaturated soil and the concept is used to quantify the behaviour of these soils in geotechnics $(u_a - u_w)$. As the matric suction of the soil decreases the radius of curvature of the contractile skin decreases (Equation 2-5). When no pressure differences exist, the matric suction value is zero and the radius of curvature becomes flat, and a planar air-water interface will develop. The surface tension will remain at a constant value at these conditions (Fredlund et al. 2012).

The matric suction component of total suction includes the effects of both capillarity and short-range adsorption (Lu and Likos 2004). Figure 2-4, presented by Janssen and Dempsey (1980), best illustrates the concept of capillarity where soil pores are interpreted as capillary tubes partially submerged in a container of water. The combined effect of adhesion, between soil (solid) surface and water, and cohesion, in the water, result in capillarity in the glass tubes and soil pores.

The adhesion forces manifest the rise in water and the intermolecular cohesion force provokes all the water molecules to follow the upward pull (Sophocleous 2010). This model is an over-simplification of actual unsaturated soil behaviour but still provides a good explanation of mechanics of unsaturated soil behaviour (Fredlund et al. 2012).

The height of water rises in a capillary tube and radius of curvature of the air-water interface have direct implications to the water content-matric suction relationship in soils. Fredlund et al. (2012) provides a concise explanation for the capillary phenomenon occurring in unsaturated soils. Consider a narrow-radius, glass tube being placed into water under atmospheric conditions, as shown in Figure 2-5.

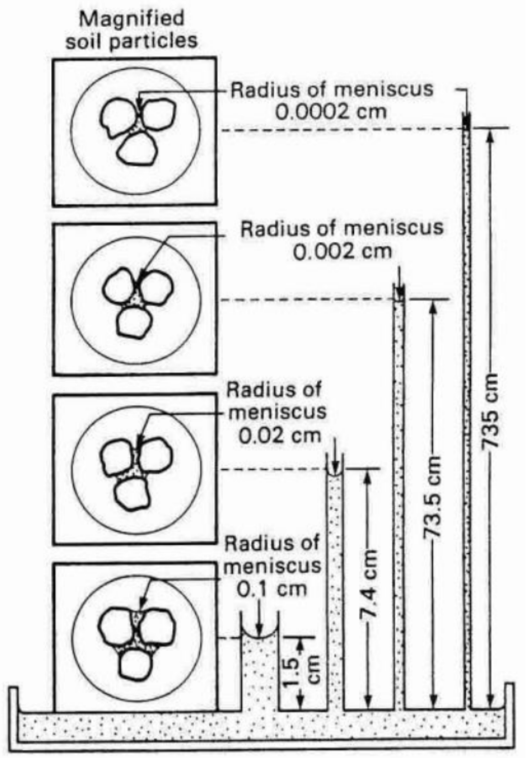

Figure 2-4 The effect capillarity in soil pores illustrated by capillary tubes (Janssen and Dempsey 1980)

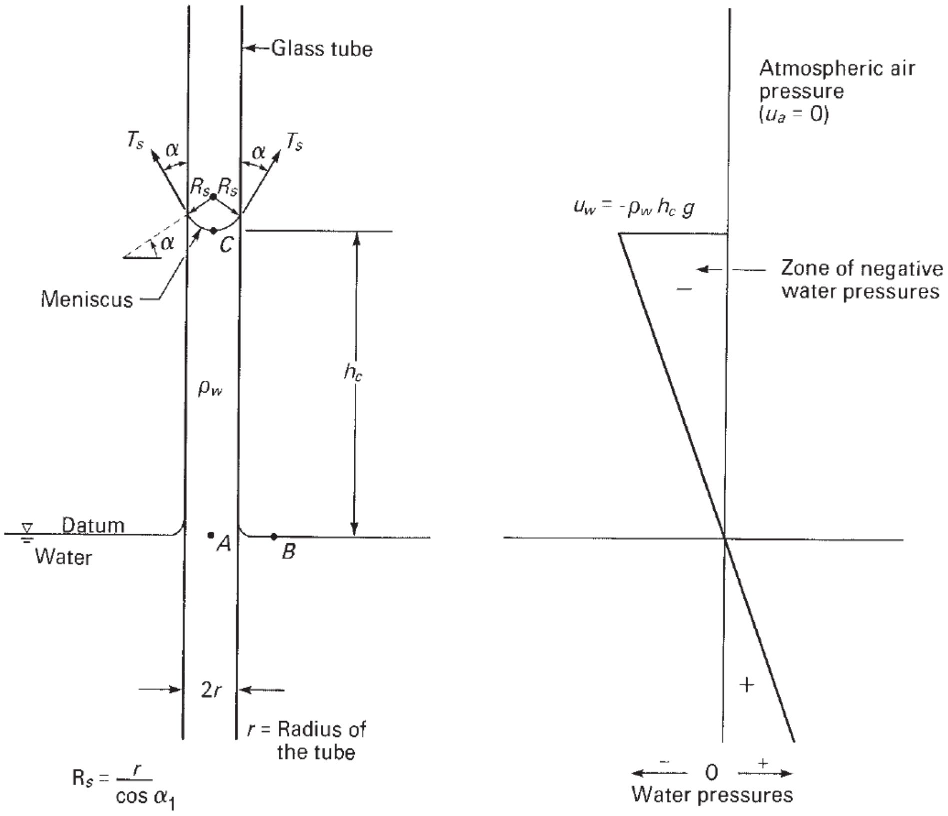

Figure 2-5 Model of capillarity in thin glass tubes (taken from Fredlund et al. 2012)

The capillary rise can be analysed by considering the surface tension (T_s) acting around the circumference of the meniscus. Equation 2-6 can be written as shown, assuming force equilibrium in the vertical along the interface (ΣFy = 0).

$$2\pi r T_s cosa_1 = \pi r^2 h_c \rho_w g \qquad \textbf{2-6}$$

Where:

r = radius of the capillary tube

T_s = surface tension of water

a_1 = contact angle

h_c = capillary height

g = gravitational acceleration

The left-hand side of the equation represents the vertical component of surface tension responsible for holding the weight of the water column. The height of the water column is shown by the right-hand side of the column. Equation 2-6 can be rearranged to Equation 2-7 to give the maximum height of water in the capillary tube (h_c).

$$h_c = \frac{2T_s}{\rho_w g R_s} \qquad \textbf{2-7}$$

Where:

R_s = radius of curvature of the meniscus (i.e., $r \,/\, cosa$)

In an ideal scenario, the contact angle between the contractile skin of pure water and clean glass is zero (i.e. $a_1 = 0$). When this angle is zero, the radius of curvature (*R*$_s$*)* is equal to the radius of the tube (*r*). Therefore, the capillary height in the ideal scenario is shown in Equation 2-8.

$$h_c = \frac{2T_s}{\rho_w g r} \tag{2-8}$$

Equation 2-8 shows as the radius of the tube reduces, the capillary height increases. This is also true for the capillary height in soils as the soil pores get smaller (Fredlund et al. 2012).

Referring to Figure 2-5, points A, B, and C are in hydrostatic equilibrium, and therefore the hydraulic heads at all three points are equal. The water pressures at points A and B are atmospheric and have an elevation of zero (i.e., datum assumed to be at the water level). This results in the hydraulic heads of points A and B to be zero. Point C is located at a height h_c above the datum, but the hydraulic head of point C must also equal zero. For this to be true, the pressure head at point C is equal to the negative value of the elevation head at point C (Fredlund et al. 2012). The water pressure at point C can be defined by Equation 2-9.

$$u_w = -\rho_w g h_c \tag{2-9}$$

Where:

u_w = water pressure

The water pressures above point A are negative and can be said to be in tension. At point C the air pressure is atmospheric (u_a = 0), therefore the matric suction at point C can described as shown in Equation 2-10.

$$u_a - u_w = -\rho_w g h_c \tag{2-10}$$

Substituting Equation 2-7 into Equation 2-10 allows matric suction to be written in terms of surface tension as shown in Equation 2-11.

$$u_a - u_w = \frac{2T_S}{R_S} \tag{2-11}$$

Equation 2-11 applies to the pressure difference across a contractile skin. The radius of curvature (R_s) can be considered analogous to the pore radius (*r*) in a soil by assuming a contact angle equal to zero as shown above. Assuming this, it can be seen as the pore radius gets smaller, the matric suction in the soil gets larger (Fredlund et al. 2012).

The surface tension carries the weight of the water column in a capillary tube. This done by the contractile skin transferring the forces onto the walls of the capillary tube, as shown in Figure 2-6, resulting in compressive stresses on the tube. The contractile skin results in an increased compression on the soil structure in the capillary zone. As a result, the presence of matric suction in an unsaturated soil can produce a volume decrease and an increase in the shear strength of the soil (Fredlund et al. 2012).

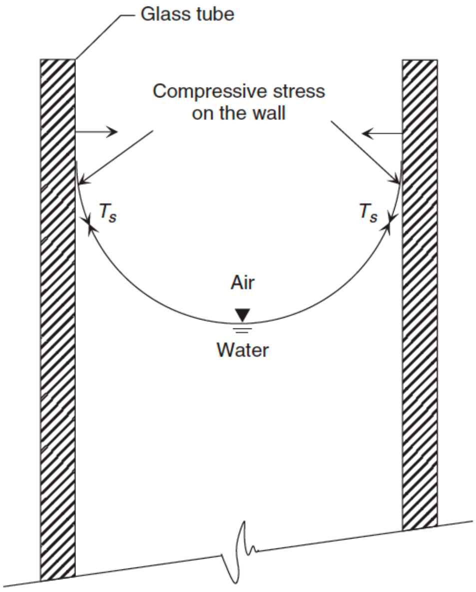

Figure 2-6 Forces acting on capillary tube (taken from Fredlund et al. 2012)

As mentioned above, the capillary tube analogy is an over-simplification of suction behaviour in soil. The capillary tube *opening* represents the pore spaces in the soil. The meniscus shape will vary in a soil due to nonuniform pore space and shape distribution in the soil. Furthermore, the contact angle of the meniscus on the soil grain will differ during a drying cycle and a wetting cycle for the same soil specimen. This is referred to as hysteresis and exists for a variety of reasons. Hysteresis is best represented by the Soil Water Retention Curve (SWRC), defined as the relationship between soil water content and suction in a soil, and this will be discussed in Section 2.3.

The ranges of suctions which relate to field descriptors are shown in Table 2-1. However, this table is only indicative. Soils will have limiting suctions depending on the texture or structure. The maximum suction that can be sustained in a pore of a soil will depend on the pore size. Referring to Equation 2-11, a meniscus requiring a radius less than the minimum pore radius cannot be sustained. Therefore, the maximum sustainable suction will be reached when the radius of the meniscus equals the minimum radius of the pore (Toll 2012).The effect of this in soils can be seen when comparing dried out clean sand, which will have lost all strength due to complete loss of suctions (sustainable suctions in order of < 5.0 kPa), and clayey soils which *harden* and possesses a high strength due to extremely high (> 1000 kPa) suctions sustained when dried out.

Table 2-1 The Suction Scale (adapted from Toll 2012)

Suction (kPa)	Component of suction	Reference points	Moisture content
1,000,000	Osmotic suction	Oven dry	Dry
100,000			
10,000			Practically dry
1,000	Matric suction	Wilting points for plants Plastic Limit	Slightly moist
100			Moist
10			
1		Liquid Limit	Wet
0.1		Saturated	

2.3 Soil Water Retention Curve

The Soil Water Retention Curve (SWRC) has been studied and used by many respected researchers (Lu and Likos 2004; Toll 2012; Fredlund et al. 2012). The shape of the SWRC is dependent on the pore size distribution, grain size distribution, density, organic material content, clay content and mineralogy of the soil (Lu and Likos 2004).

The typical SWRC, as shown in Figure 2-7, has a primary drying curve and primary wetting curve. A SWRC is commonly presented using gravimetric water content (ω), as it is easy to measure weight / mass, or volumetric water content (θ), which is simple to convert from ω, or as degree of saturation (S).

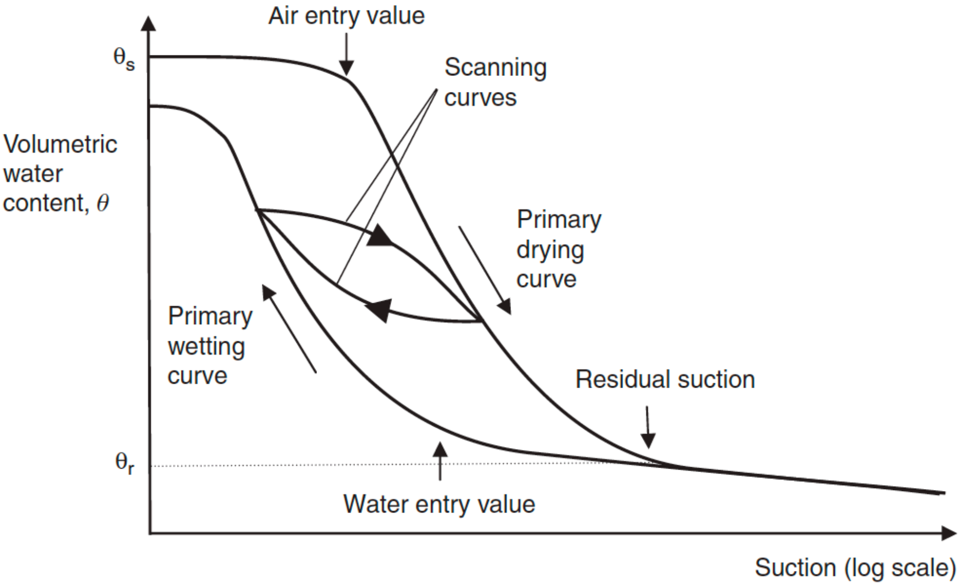

Figure 2-7 Typical Soil Water Retention Curve (taken from Toll 2012)

A soil undergoing drying from a saturated state (θ_s) will follow the drying curve. The soil will remain saturated before the *air entry value* (AEV) is reached and will have negative pore pressures due to the presence of suctions as drying occurs. This region of the SWRC closely represents a capillary fringe or zone in a ground profile above the groundwater table. The AEV value indicates the limiting suction values at which the larger pores in the soil remain saturated, meaning these pores will start to desaturate and air will occupy a percentage of the pores. A higher AEV general indicates a pore size distribution of fine pores within the soil. If desaturation occurs after the AEV, the soil will go through a reduction in water content as finer and finer pores progressively desaturate The residual suction, occurring after the residual suction value (θ_r), indicates the region where water is held as adsorbed water on clay particles surfaces (McQueen and Miller 1974). Before the θ_r is reached, pore water is held as capillary water in the meniscus and is referred to the matric suction as explained above (Toll 2012). Most geotechnical problems occur with changes of moisture in the matric suction range, which exists between θ_s and θ_r in Figure 2-7.

For the same soil specimen, which is wetted from an oven dry state, the primary wetting curve will be followed. The *water entry value* indicates the suction value at which the pores will start filing up with water as capillary water. When the suctions are zero, the final θ will be less than the original initial θ_s due to trapped air bubbles in the pores and the irrevocable volume decrease which happened during the drying cycle. The two primary curves represent an envelope in which the soil suctions can exist. The difference between the two curves is primarily a result of hysteresis as mentioned above. If a soil undergoing a drying cycle is exposed to an increase in moisture, the soil will follow a *scanning curve* until the primary wetting curve is reached, and vice versa. Soil found in the vadose zone is typically found to exist on a scanning curve (Toll 2012).

The SWRC, also referred to as the Soil Water Characteristic Curve (SWCC), is a fundamental part of understanding unsaturated behaviour of a soil as it can give indication of pore size distribution, among other properties of the soil, and it can be used to estimate unsaturated soil property functions (USPFs) (Fredlund et al. 2012). The hydraulic conductivity function (HCF) is commonly used to estimate the hydraulic conductivity (m/s) of a soil at a certain suction value (kPa) as testing for this requires specialised equipment. Section 2.4 will discuss unsaturated hydraulic conductivity of soil found in the vadose zone.

2.4 Movement of moisture through soil

The ease of soil to transmit water at saturation is described by the hydraulic conductivity (*K*) or coefficient of permeability of the soil. Darcy's Law defines the hydraulic conductivity (*K*) as a function of the hydraulic gradient (*i*) between two points and the cross-sectional area (*A*) through which the flow will happen. Darcy's Law is defined by Equation 2-12.

$$Q = -KiA = -K\frac{\Delta h}{\Delta l}A \qquad \textbf{2-12}$$

Where:

Q = Total discharge ($\frac{\mathrm{l}^3}{\mathrm{t}}$)

K = hydraulic conductivity ($\frac{\mathrm{l}}{\mathrm{t}}$)

Δh = difference in pressure head between observation points (l)

Δl = distance between observation points (l)

A = cross-sectional area (l^2)

Equation 2-12 defines the volume of water that flows through a specific area and does not determine the speed at which the water flows. Specific discharge (q) is the discharge rate through a cross-sectional area and is determined as shown in Equation 2-13.

$$q = \frac{Q}{A} = -Ki = -K\frac{\Delta h}{\Delta l} \qquad \textbf{2-13}$$

Equation 2-13 assumes that the total cross-sectional area permits flow, including both connected pores and solid grains. Average linear flow velocity (v) is defined as the flow through the cross-sectional area occupied by the connected pores only and is described in Equation 2-14.

$$v = \frac{q}{n_e} = \frac{-Ki}{n_e} \qquad \textbf{2-14}$$

Where:

n_e = Effective porosity (dimensionless)

The hydraulic conductivity (K) is used for the measure of flow of water through the soil and is a property of the soil. When other fluids are considered, intrinsic permeability (k) is used to determine the flow and is shown in Equation 2-15.

$$K = \frac{k\rho g}{\mu} \qquad \textbf{2-15}$$

Where:

ρ = fluid density

g = gravitational acceleration

μ = fluid’s dynamic viscosity

The theories of fluid flow through moisture are primarily based on saturated material occurring in the phreatic zone. Darcy’s Law is still applicable for flow of moisture through unsaturated material in the vadose zone. The hydrology of the vadose zone has been intensely investigated, with authors describing various flow mechanisms in a soil region where pore pressures are lower than atmospheric, and the system is governed by forces of capillarity and gravity (Lu and Likos 2004; Fredlund et al. 2012; Dippenaar et al. 2022).

The behaviour of water flow through unsaturated soil can be summed up by *water can only flow where there is water*. In a saturated medium, effective porosity is the portion of total porosity that can transmit water. In a partially saturated medium, the available pore space contributing to flow is reduced as the moisture content is reduced. Figure 2-8 best represents this relationship where at higher degrees of saturation a higher hydraulic conductivity is achieved, and saturated hydraulic conductivity is always greater than unsaturated hydraulic conductivity (Dippenaar 2014; Dippenaar et al. 2022).

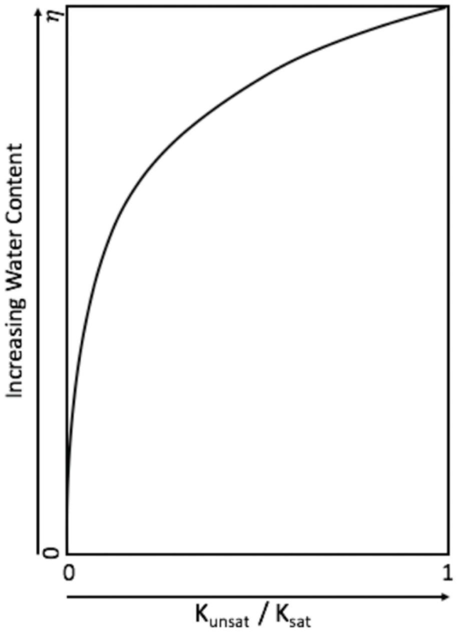

Figure 2-8 Influence of water content on relative hydraulic conductivity (adapted from Fitts 2013)

The coefficient of permeability is dependent on the fluid properties and the pore structure, effective porosity, and void ratio of the soil. In unsaturated soils, the function of the initial water content creates a variability in the flow dynamics. In other words, unsaturated hydraulic conductivity exhibits hysteresis. The hydraulic conductivity is a function of matric suction and, as exhibited in the SWRC, this parameter will also show characteristics of hysteresis (Lu and Likos 2004).

The secondary / structural porosity, namely fractures and discontinuities that persist from the original rock structure, are usually the preferred flow paths for moisture movement (Talib et al. 2016; Dippenaar et al. 2022). Completely weathered rock is expected to be a dual porosity system with a high matrix / primary porosity (and variable permeability) and a high secondary porosity (Van der Hoven et al. 2003). The presence of double porosity within a weathering profile becomes increasingly important to recognise at lower moisture contents as the flow through finer pores in the matrix may dominate over the larger pores existing in the secondary / structural porosity.

Since the characteristics of the relict rock structure, which governs the total porosity, of the completely weathered rock has the greatest influence of the material's hydromechanical properties, the next section will discuss the state of the art on soil structure with reference to unsaturated soils.

2.5 Porosity

Pores have been defined as "the *sine qua non* of soil" (Clothier 2008). In other words, the intrinsic characteristic which soil cannot be without. Pores are open spaces of the soil that are not occupied by solid grains. The porosity of a soil is distributed across a wide range of pore sizes and shapes, ranging from spaces between clay platelets to large open root or burrow channels. The pore size ranges, as defined by Brewer (1965), and updated by Bouma (1981) are presented in Table 2-2.

The class limits stated are derived from the surface-tension-capillary size equations and are equivalent pore size classes. It is recommended these classes should only be used for communication purposes and does not have much practical relevance.

The equivalent pore diameter in soil science and geotechnics is a conceptual measure representing the diameter of an idealized cylindrical pore that exhibits similar hydraulic or physical properties as the real pores in the soil or rock matrix. This parameter is commonly used to estimate permeability, air and water movement, and soil structure behaviour.

According to the review by Wang and Zhang (2024), equivalent pore diameter is defined as the pore size equivalent to a certain soil water suction. It is often determined using indirect methods such as the soil water retention curve, where the capillary rise formula relates soil suction to an equivalent cylindrical pore diameter.

From Dimitrovski (2019), the equivalent average pore diameter is defined as the diameter of cylindrical pore structures that allow the same air permeability as a real porous medium with the same number of pores and thickness. This concept accounts for internal pore structure features such as tortuosity, pore walls, and throat size, making it useful in permeability analysis.

Table 2-2 The size classification scheme of pore size developed by Brewer (1964) (adapted and taken from Bouma 1981)

Class	Subclass	Class limits (equivalent diameter - μm)	Method of measurement
Macropores	Coarse	>5000	Hand specimen; X-Ray Computed Tomography (XRCT)
	Medium	2000 – 5000	
	Fine	1000 – 2000	
	Very fine	75 – 2000	Microscope; hand specimen; water retention curve; XRCT
Mesopores		30 – 75	Microscope; water retention curve; XRCT
Micropores		5 – 30	
Ultra-micropores		0.1 – 5	Scanning electron microscope
Crypto-pores		<0.1	Water retention curve

The most basic form to define porosity is the ratio of total volume (V_T) of the soil mass to the volume of the voids (V_V) present, as shown in Equation 2-16.

$$\eta = \frac{V_V}{V_T} \qquad \textbf{2-16}$$

Soils are suspectable to volume change when under load, and with the removal or addition of moisture in the unsaturated state. Engineers often use the void ratio (e) to overcome the impact this change in volume will have on the porosity. The void ratio is defined in Equation 2-17.

$$e = \frac{V_V}{V_S} \qquad \textbf{2-17}$$

Where:

V_S = volume of solids

These simple ratios are based, and can be readily used for, well-sorted, transported, sands of similar particle size. To quantify the void space in this soil, the assumption is made the particles are spheres with the same effective grain size diameter (D_e) and are in a cubic packing arrangement (Fredlund et al. 2012; Dippenaar 2014). This is represented by the Figure 2-9.

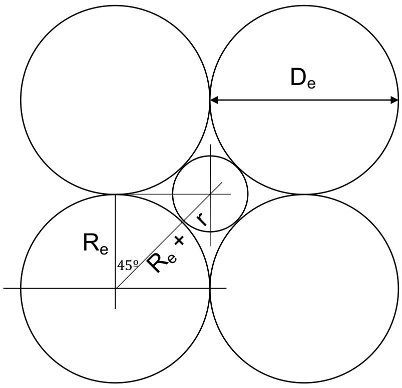

Figure 2-9 Cubic arrangement of particles used to calculate open space between particles (adapted from Fredlund et al. 2012)

A relationship between the effective radius of spheres (R_e) and the inner pore space radius (r) can be written as follows:

$$r = \frac{R}{cos45} - R \tag{2-18}$$

The relationship in Equation 2-18 is also used to describe the matric suction at air-entry point of the soil when substituted into capillary equation (Eq. 2-11), as shown in Equation

$$u_a - u_w = \frac{2T_S}{\frac{R}{cos45} - R} \tag{2-19}$$

The porosity and air-entry value will change when the packing configuration of the spherical grains change. Figure 2-10 shows the spheres with the same effective diameter in a denser, tetrahedral, packing and consequently a reduction in porosity and an increase in the air-entry value.

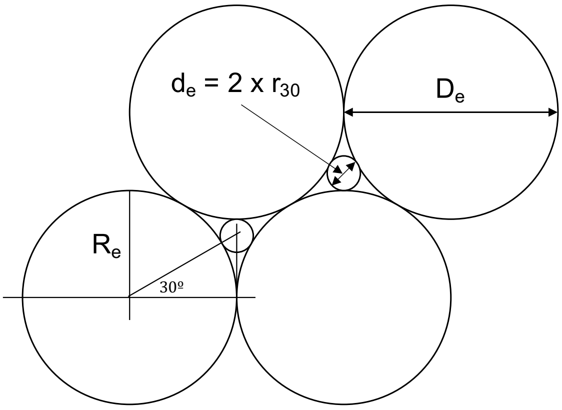

Figure 2-10 Tetrahedral arrangement of particles used to calculate open space between particles

The concept of spherical grains with an effective diameter is used for the basic understanding of primary porosity in most research fields dealing with soils in saturated and unsaturated states. The limitations of this idealised model have been discussed by many authors over a wide range of disciplines (Lu and Likos 2004; Fredlund et al. 2012; Dippenaar 2014). Notably that most natural soil comprise a range of particles sizes with the fines generally clogging the larger pores, greatly reducing, and causing variability, of the porosity.

Secondary porosity differs from primary porosity as it includes openings in geological material that originate as structural formations such as factures, bedding planes, and discontinuities. These features typically govern the weathering process of the host rock and may persist till the material has weathered to a residual soil. This type of porosity is difficult to quantify as each structure has its own properties, infill or aperture along its length, and history of influence. Typical idealised models have been suggested by Lu and Likos (2004).

Dippenaar (2014) conducted a detailed review of porosity present in both soil and rock, and how these are defined and quantified across multi-disciplinary applications. A fundamental concept in hydrology needs to be highlighted, namely the connectivity of porosity. Two types of pores exist in soil, non-effective porosity meaning there is no contribution to the movement of gas or liquids, and effective porosity which are drainable pores and govern the hydraulic conductivity. Both types of porosity contribute to mechanical behaviour of consolidation or collapse when the soil is placed under load. However, only the effective porosity is important in determining fluid flow through soil and measuring the SWRC of an unsaturated soil. Dead end pores can be saturated while most of the drainable pores are near the water entry value. To the remove the water in the non-effective pores, without having to destroy the structure, the sample can be oven-dried, which may lead to sesquioxides precipitating out of the porewater and oxidize resulting in a reduction of total porosity value (Huat et al. 2012).

Natural soils comprise non-homogeneous pore size and shape distributions for both primary and secondary porosities. The larger open void spaces are termed pores and the narrow sections connecting pores are termed throats. The varying diameter size along the length of a throat and a pore becomes important when the material is partially saturated, meaning voids are occupied by air and water.

At low moisture levels, the movement or storage of water is dependent on the size of the pore and throat. As moisture decrease (i.e. drainage occurs), water tends to retreat into smaller pore spaces and is held in as capillary water, as briefly discussed in Section 2.4. This phenomenon has been called the *ink-bottle* effect and is believed to contribute to the hysteresis behaviour in soil (Lu and Likos 2004; Fredlund et al. 2012). This behaviour is demonstrated in Figure 2-11.

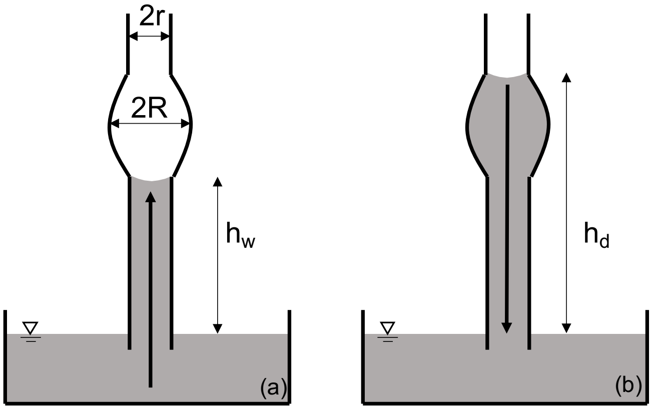

Figure 2-11 Capillary tube model for demonstrating ink-bottle effect (adapted from Lu and Likos 2004)

During imbibition, shown by image (a), the capillary rise will occur until point h_w is reached, which is a function of the smaller capillary tube radius (r). Assuming a zero-contact angle, the matric suction at this point can be determined by substituting the smaller tube's dimensions into Equation 2-11, as show in Equation 2-20.

$$u_a - u_w = \frac{2T_S}{r} \tag{2-20}$$

During drying of an initially full tube, shown by Figure 2-11(b), the meniscus at equilibrium at h_d will have the same matric suction as at point h_w shown by Equation 2-20. However, the total amount of water content in the capillary tube is larger during the drying cycle.

The porosity, macroporosity, pore distances and pore connectivity (effective porosity) are important indicators for several soil functions but are difficult to describe and define in a single or series of models. For this reason, many authors suggest pores should be characterised based on their function to store and transport water, and the impact they have on several other soil functions (Bouma 1981; Skopp 1981; Dippenaar 2014; Rabot et al. 2018). Samardzioska and Popov (2005) developed and tested three conceptual models to solve flow through a porous medium, namely equivalent continuum, dual porosity, and non-homogenous / discrete factures. The models do not specifically define and model the actual porosity of the medium, but the study shows the conceptual models can be confidently used to determine the function the porosity provides.

Residual soil and completely weathered rock usually possess relict rock structure and texture which influences the primary, secondary, and tertiary porosities and may govern the behaviour in-situ to a greater extent than the soil texture alone (Collins and McGown 1974; Dippenaar 2014; Swart et al. 2019). Griffiths et al. (2017) determine that the pore orientation has a significant influence on the rock strength and stiffness. If the pore aspect ratio is high, meaning elongated, such as a microcrack, the orientation has the biggest impact compared to a pore that is near spherical. Being able to map the pore orientation and geometry can only be done in 3-dimensional view.

Wesley (2010) proposed a classification for residual material, both soil and weathered rock, based firstly on the degree to which the mineralogy influences the behaviour of the material. Group A comprises residuum where there is minimal mineralogical influence, and this is group is further subdivided into materials with strong influences of macrostructure and microstructure. The macrostructure is identifiable with the naked eye and is expected to provide stiffness and strength to the material when under load. The microstructure cannot be seen with the naked eye and exists between grains as bonding. The presence of the bonding can be determined if the material exhibits high sensitivity when comparing undisturbed and remoulded samples under load. This classification does not definitively characterise the porosity in the residuum, but it does define the extent with which the relict rock structure, that governs the porosity, impacts the expected behaviour under load.

2.6 Soil architecture

Much of the fundamental understanding of unsaturated soil mechanics is based on work done by soil scientists. Though, geotechnics is more concerned with rock, weathered geological material, deeper profiles, shear strength, flow around infrastructure etc., much of the understanding of theories in unsaturated soil mechanics is based on work hypothesised and tested / proven by soil physicists and soil scientists. This section will mainly focus on the state of the art in the study of soil structure, and unsaturated soil function research in the field of soil science.

In soil, environmental and agricultural sciences, a strong consensus exists that soil function is closely linked to soil structure. So much so, the word *structure* is now more frequently defined as soil *architecture* to “emphasize the close relationship between the arrangement of soil physical constituents in space and the functions that such arrangement enables” (Vogel et al. 2022). The soil architecture is a complex, 3-dimensional (3D), heterogenous, bio-geochemical system that forms the essential building blocks for soil function such as water storage and movement, shrink-swell behaviour, and responses under load and changes in moisture conditions (Totsche et al. 2010; Vogel et al. 2022).

There are generally two schools of thought in soil science about the characterising soil architecture, one focuses on the pore structure and pore-solid interface, and the other focuses on aggregates as the building blocks (Baveye et al. 2022; Vogel et al. 2022).

The former requires the studied soil samples to be undisturbed, or at least only slightly disturbed, to ensure the openings and arrangement of pores are positioned correctly within a 3D complex soil system. The latter investigates the arrangement of isolated solid fragments, how these separate into structural aggregates and the compositions and stability of these building blocks.

The aggregate (latter) approach can be used on both disturbed and undisturbed samples and is the simpler approach as it can be done in the field and with hand samples in the laboratory. The pore approach (former) is typically the more costly method and requires careful sampling, more complex testing, and, since very recently, requires specialised testing equipment. The conflict between the two approaches became more apparent when the understanding of soil function shifted towards a more holistic analysing approach (Baveye et al. 2022; Vogel et al. 2022).

However, considering the extensive possibility and variability of soil type and behaviour, there is ample evidence in utilising both approaches together with changing balance depending on soil type and site conditions (Rabot et al. 2018). The history, difference and thoughts on each approach are discussed in detailed in Vogel et al. (2022) and Baveye et al. (2022).

Letey (1991) wrote: *Science is based on quantitative measurements which can be reproduced. Soil structure does not lend itself to quantification*. He carried on stating the state of the art in the study of soil structure only provided index values for the soil functionality and these were dependent on how the functionality was measured (Letey 1991). At the time of writing up this study, the opportunities to measure soil architecture have significantly increased in the field of soil science (Golparvar et al. 2021; Daneshian et al. 2021; Vogel et al. 2022; Baveye et al. 2022; Wang and Zhang 2024).

Rabot et al. (2018) published a comprehensive review to evaluate the potential of observable soil structural attributes, for both the pore and aggerate approaches, to be used in the assessment of soil functions. As in geotechnics, the interest in soil structure is to infer the soil characteristics, which can form due to soil texture or chemistry (i.e. swelling / shrinking clays) or it may govern the soil hydromechanical behaviour to a greater extent than the soil texture alone (Swart et al. 2019; Vogel et al. 2022; Baveye et al. 2022). Rabot et al. (2018) divided the methods into field and laboratory methods for the aggregate approach, and indirect and direct methods for the pore approach. Many of these methods were similar to techniques used in geotechnics to determine soil structure and porosity, such as test pit profiling in the field, and grading (texture) analyses and bulk density determination in the laboratory for the aggregate approach. In the pore approach, indirect methods discussed are gas adsorption and soil water retention curves and derived indicators, which is commonly used in unsaturated soil mechanics. Rabot et al. (2018) discusses the limitations and ambiguities in testing experienced when using the methods mentioned above, and some of these are similarly well-understood in geotechnics.

The direct methods for the pore approach include imaging techniques such as optical microscopy and scanning electron microscopy (SEM) (Rabot et al. 2018). These are commonly used in geotechnics, but these methods require sample preparation, such as cutting of thin sections, oven-drying and carbonization of sample surface that will disturb the soil structure before any evaluation takes place.

When analysing undisturbed soil samples to identify indicators of soil architecture, the most reliable and repeatable imaging technique is X-Ray Computed Tomography (XRCT) (Mees et al. 2003; Wildenschild and Sheppard 2013; Helliwell 2013; Cnudde and Boone 2013; Banerjee et al. 2016; Rabot et al. 2018; Daneshian et al. 2021; Golparvar et al. 2021; Vogel et al. 2022; Baveye et al. 2022)

XRCT is a non-invasive, non-destructive, imaging technique developed for the visualisation and quantification of the interior structure of an object in the 3-dimensions. A sample is placed within the scanner and exposed to a beam of X-rays, generated from an X-ray tube, while the sample is rotated a full 360°. The X-rays are absorbed or scattered by, or passed through, the sample materials causing attenuation of the beam. The degree of attenuation is proportional to the atomic number of the material, the photon energy of the incident beam and the thickness of the material. The degree of X-ray attenuation is acquired by the detector from the numerous 2-dimensional (2D) radiographic images, often called projections.

The key principle of the XRCT imaging technique is based on the differential attenuation of X-rays as they interact with the minerals and pore spaces within the sample. The ability of differing materials to adsorb and scatter incident photons is referred to as the linear attenuation coefficient (Huda and Abrahams 2016). At a given photon energy and sample thickness, a higher density material (i.e. larger linear attenuation coefficient) will absorb or scatter more X-rays, increasing the attenuation, resulting in a darker appearance on the CT projection. Using relevant software depending on the application, the CT projection is converted into a slice where the denser materials appear lighter and air appears darker (Li and Tang 2019; Sturrock 2022). The process of X-ray attenuation in sample materials before photons reach the detector in a XRCT scanner is shown in Figure 2-12.

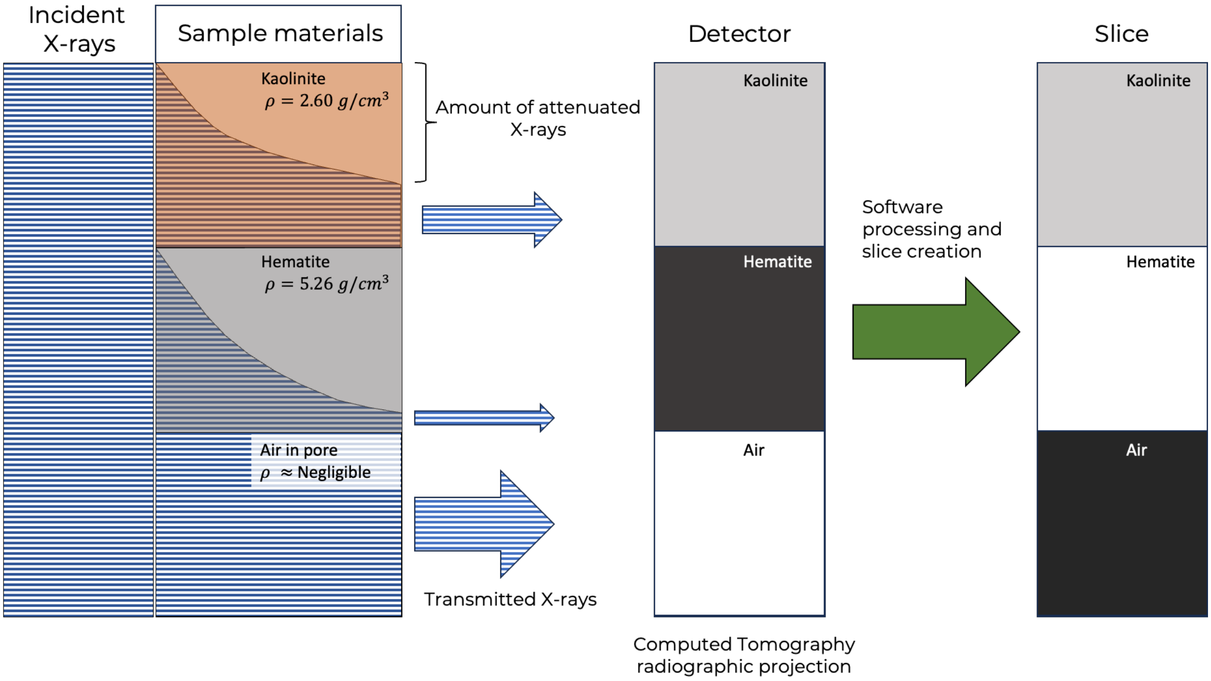

Figure 2-12 X-ray attenuation contrast of solid mineral grains compared to open pore spaces in soil

Wang and Zhang (2024) provide a comprehensive review of soil pores and the importance on the soil structure, and how to measure them effectively. The paper provides methods to study pores and soil structure and categorizes them into traditional and advance techniques. The traditional methods are further divided into indirect and direct methods. Indirect methods include soil water retention curves, mercury intrusion, mathematical modelling and interpretation from permeability data. Direct methods include mainly observation of the soil at varying scales with the addition of tracer dyes and soil slicing. Although cost-effective, these methods can be limited by complexity and accuracy issues.

The most recent advances in imaging techniques includes XRCT scans that enable the quantification of porosity, pore distribution and pore connectivity. With the use of available image analysis software, such as VG Studio Max 2.2, the data retrieved during the CT scan can be used to determine number of pores, equivalent pore diameter, surface area and volume, as well as the 3D pore model reconstruction. The 3D model can be used to determine the pore tortuosity, connectivity, node density, and network density (Wang and Zhang 2024). Pore network modelling or pore scale modelling is used to create a relativity cost effective approach to characterise pore networks. XRCT scans have successfully been used to provide a basis for the microscale features to better characterize pore scale modelling (Blunt 2001; Golparvar et al. 2018; Wang and Rahman 2023).

Disadvantages do exist with this imaging technique notably the cost to hire and use the equipment and the availability of it as well. A limiting factor of the XRCT is the inability to differentiate between minerals with similar density near one another, as well as differentiating air and water in pores. To overcome this, sample preparation is required by means of an additive into the soil sample which *stains* certain soil features or pore water depending on the required application. The *staining* of specific features alters the density and enhances the contrast between certain minerals, liquids, or soil structures (Li and Tang 2019; Terribile et al. 2022).

The voxel resolution of the scan is dependent on the size of the sample and the size of the detector. Depending on the nature of the investigation, a suitable sample size and positioning of the sample relative to the detector and X-ray beam should be determined. By decreasing the distance between the sample and the X-ray source or increasing the distance between the X-ray source and the detector, the magnification increases. The shifting of these distances changes the magnification, which is inversely proportional to the field of view or allowable sample size. Therefore, the smaller the sample, the greater the magnification and higher the voxel resolution (Terribile et al. 2022; Wang and Zhang 2024).

No dedicated soil-based CT scanner or software exists and most XRCT research conduct on soil structure has been done using medical or industrial CT equipment. For this reason, this method does not fully appreciate the irregularity and heterogeneity of the pore structure. Even with the disadvantages stated above, this imaging technique remains the most reliable and accurate of all widely used indirect and direct methods (Wang and Zhang 2024).

2.7 Conclusion

This chapter discusses the properties that govern the behaviour of a porous medium, namely residual soil and completely weathered rock, at varying saturation. The porosity, pore distribution, pore shape, and pore connectivity, which is closely linked to the material's structure, control the response to changes in moisture, volume strain and when placed under load. The mathematical and theoretical models to quantify this behaviour has been discussed and is fundamentally based on the capillary model and the SWRC for unsaturated soils. The most advanced and reliable imaging technique to quantify the pore structure is the XRCT scan and relevant software.

3 Geology

3.1 Overview

According to literature and the author's experience, the geology that typically creates deep weathering profiles are metamorphic and igneous rocks and dolomite (Van der Merwe 1964; Weinert 1980; Buttrick 1986; Blight and Leong 2012; Dos Santos et al. 2018; Swart et al. 2019; Bonnet et al. 2022; Dos Santos et al. 2022). Metamorphic rocks tend to have highly heterogeneous rock profiles with a mixture of hard rock lineations between completely weathered rock and soil (Blight and Leong 2012). This rock type was excluded from the study for these reasons that are discussed in Section 5.

The primary need of the study was to evaluate well developed weathering profiles that weather to fine-grained, mainly silt, residuum and have very minimal metamorphic rock features. Therefore, the rock types that were targeted comprised intrusive igneous rocks, ranging from felsic, intermediate and mafic. The rock units that were initially investigated during the desktop planning had to either be of significantly old, namely older than 120 million years old and therefore have been exposed to previous weathering cycles (Partridge 1998), or are currently exposed to a climate that results in chemical weathering or both.

The weathering profiles that were sampled were in the eastern escarpment of South Africa. This area falls within a moisture-surplus climatic area where decomposition dominates (Weinert 1980; Makhubela et al. 2021).

The Malmani dolomites formed through dolomitization and chertification processes are of limestone during the late Archean and early Proterozoic (Obbes 1995). Beukes et al. (1999) stated the weathering products of dolomite observed today formed during ancient climate conditions (~180 Ma). The conditions were humid and warm resulting in moderately acidic to weakly alkaline and oxidizing conditions. These conditions formed residuum material from dolomite, even if the weathering profiles exist in climate areas that aren't consider as a moisture surplus.

The focus of this research is the rock in a completely weathered state; however, the structure, porosity, texture and mineralogy are greatly influenced by the parent rock from which it forms. The specific parent rock units from which the completely weathered to residual material samples were retrieved will be discussed here. Section 6 discusses the field methodology used to identify silt on site. The Salnova Formation was sampled and incorporated into the study to illustrate the impact soluble salt contamination has on the hydrometer test results. Table 3-1 summarises the age and generalised lithology of the sampled geological units.

Table 3-1 Summary of geological units sampled

Age	Supergroup	Group	Subgroup	Formation	Intrusion	Rock / Soil Type
Quaternary	-	-	Algoa	**Salnova**	-	Pebbly coquina; semi-consolidated calcareous sandstone (Hassan et al. 2022)
Proterozoic	-	Rooiberg	-	**Dullstroom**	-	Andesite, dacite, rhyolites
	-	-	-	-	**Diabase**	-
	Transvaal	Chuniespoort	Malmani	-	-	**Dolomite** and chert
Neoarchean	-	-	-	-	**Granite**	Leucogranite

3.2 Intrusive igneous

3.2.1 Granite intrusions

Granites and granite-gneisses of the *Basement Complex* outcrop extensively over portions of Southern Africa. The collective term for these rocks is usually granites which can be considered any intrusive or hypabyssal felsic, igneous or metamorphic rock composed of predominantly quartz and feldspar (orthoclase and plagioclase) (Brink 1979; Dippenaar and Van Rooy 2014). These complex mineralogical make-ups range from alkali feldspar granite, granite, granodiorite and tonalite. The range of compositions which encompasses granites is shown in the Quartz-K-feldspar-Plagioclase-Feldspathoid (QAPF) diagram, developed by Streckeisen (1974), are presented as Figure 3-1. The plutonic igneous rocks commonly referred to as granites are shaded in orange.

The weathering profile sampled at the R528 site formed from chemical weathering of the Duivelskloof Leucogranite. The Duivelskloof Leucogranite forms a large batholith-like intrusion and underlays most of Tzaneen's town centre. This rock unit can be off-white, massive, medium grained rock which occurs in pockets or large masses and can grade into a pegmatoidal variety with foliation; or appear fine-grained and darker when in close contact with the confining greenstone to the north. The main constituents are sodic plagioclase, quartz, orthoclase, microperthitic microcline, biotite and muscovite. Biotite shows partial alteration to chlorite and lesser to garnet. The leucogranite varies from syenogranite to a monzogranite and is peraluminous in character (Robb et al. 2006).

The samples for the field identification testing, discussed in Section 6, was retrieved from the Duivelskloof Leucogranite and Turfloop Granite.

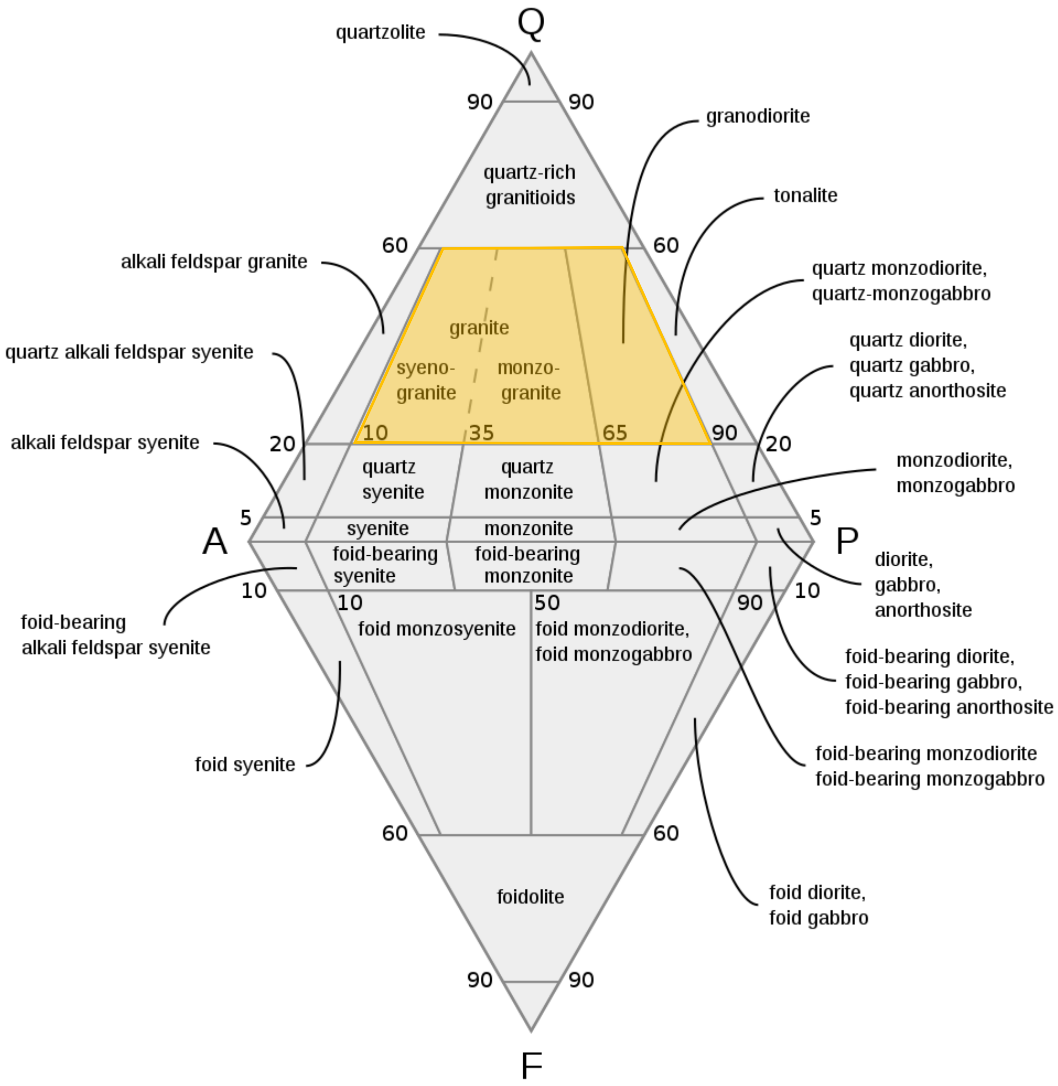

Figure 3-1 QAPF diagram (Streckeisen 1974)

The contact between the Duivelskloof Leucogranite and Turfloop Granite is not well defined The Turfloop Granite forms part of younger granitoid intrusions during the Neoarchaean ranging in age of 2800-2500 Ma. The TG is a large, northeast trending, batholith with a composition that is varied, ranging from granodioritic and monzogranitic. The dominant variant is light grey to pinkish grey, medium to coarse grained with trace amount of porphyritic phases. The TG comprises mainly plagioclase, quartz, orthoclase/microcline, biotite and some muscovite. The TG is metaluminous to slightly peraluminous in character (Robb et al. 2006).

3.2.2 Intrusive diabase

Mafic intrusions in South Africa, comprising dykes and sills of dolerite and diabase, are widespread throughout the Kaapvaal Craton (Anhaeusser 2006). Weinert (1980) stated the term dolerite is used to differentiate the Karoo-aged diabase from the older Proterozoic and Archean intrusions. However, these two terms are given to the same rock with similar chemical compositions and is only used to emphasise the expected difference in engineering behaviour due to the generally more deeply weathered, and possibly altered, diabase.

The sampled diabase residuum forms part of the Proterozoic (~1.90 Ga) NE-trending mafic dyke swarm occurring in the granitoid intrusions near Tzaneen. Klausen et al. (2010) found that these intrusions are mostly basaltic tholeiites, however some intrusions have undergone alteration resulting in amphibolites. The chemical composition of these intrusions is typically a series of actinolite, hornblende, epidote, calcite and recrystallized plagioclase.

3.2.3 Dullstroom Formation

The Dullstroom Formation was originally included in the Pretoria Group, however Schweitzer et al. (1995) proposed the Dullstroom Formation forms part of the lowermost unit of the Rooiberg Group. This geological unit comprises andesite to dacite, as well as rhyolites which are collectively referred to as the *Dullstroom lavas*. These volcanic units comprise fine-grained, groundmass with variable proportions of phenocrysts, porphyroblasts and amygdales. The Dullstroom Formation groundmass constitutes lath-shaped feldspar (mostly plagioclase), amphibole, anhedral quartz and opaque phases, including iron-oxide and ilmenite. The plagioclase can exist as phenocrysts characterised as euhedral to subhedral with composition of that of anorthite-rich (Ca-plagioclase) with minor albite (Na-plagioclase) (Lenhardt and Eriksson 2012). The geological rock type will be classed in this thesis as an andesite for simplicity.

The andesite was sampled at the Dullstroom site and retrieved for the field identification techniques discussed in Section 6.

The geological units sampled represent a range of varying rock types with different chemical constitutes. The expected major chemical components for each sample site are approximately shown by the arrow ranges in Figure 3-2. The green, orange and red arrows shown the expected chemical ranges of the Duivelskloof Leucogranite, diabase and Dullstroom Formation andesite, respectively.

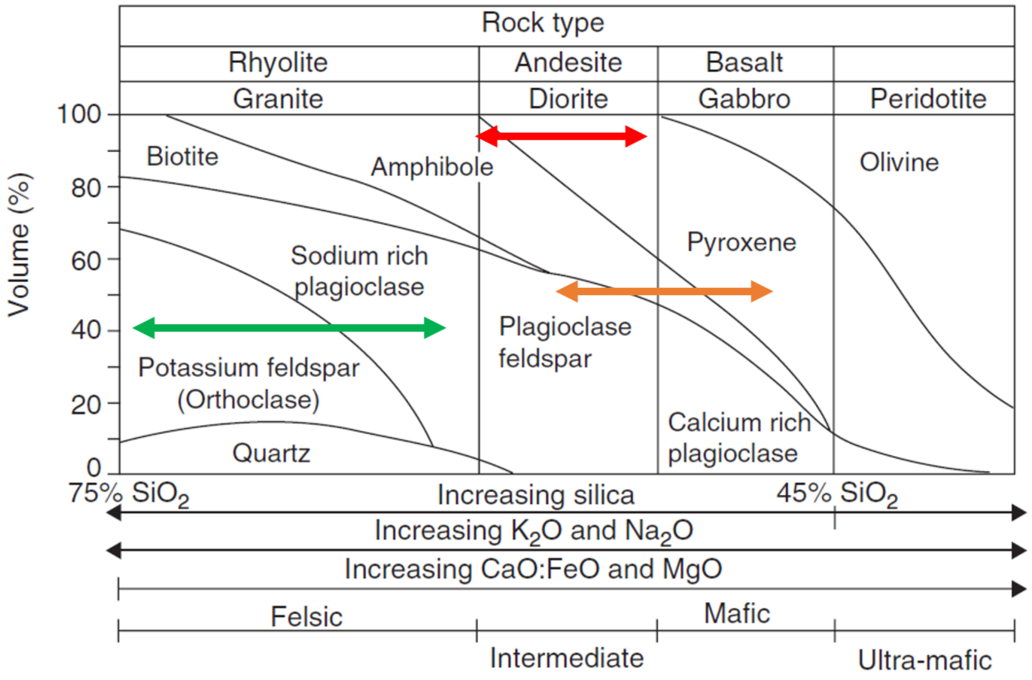

Figure 3-2 Classification of igneous rocks (taken and adapted from Singh and Huat 2013)

3.3 Dolomite

The dolomitic areas investigated in this research belong to the Malmani Subgroup of the Chuniespoort Group, which is part of the Transvaal Supergroup. The dolomite bedrock has been studied by numerous researchers (Brink 1979; Obbes 1995; Eriksson et al. 2006; Dippenaar et al. 2019), and is of significant importance due to the weathering process forming cavities that may lead to the formation of sinkholes. The dolomite bedrock outcrops in the eastern and western limbs of the Transvaal Supergroup as well as in the area south of Pretoria, as illustrated in Figure 3-3. The Malmani Subgroup comprises five formations, namely the Oaktree, Monte Christo, Lyttleton, Eccles, and Frisco Formations. These formations are differentiated by their chert content as well as the presence and morphology of stromatolites (Obbes 1995).

Dolomite rock contains more than 90% dolomite mineral and lesser secondary silica termed chert, and calcite and detrital minerals. The best representation of the range of the dolomite compositions that forms, namely calcian to magnesian dolomites, is $Ca_{(1+x)}Mg_{(1-x)}(CO_3)_2$ as dolomites are rarely stoichiometric ($CaMg(CO_3)_2$) (Warren 2000). Trace amounts of iron (Fe) and manganese (Mn), in the range of less than 2% can be found in the dolomites (Brink 1979; Buttrick 1986; Eriksson et al. 2006). These trace elements typically determine the weathering products that forms.

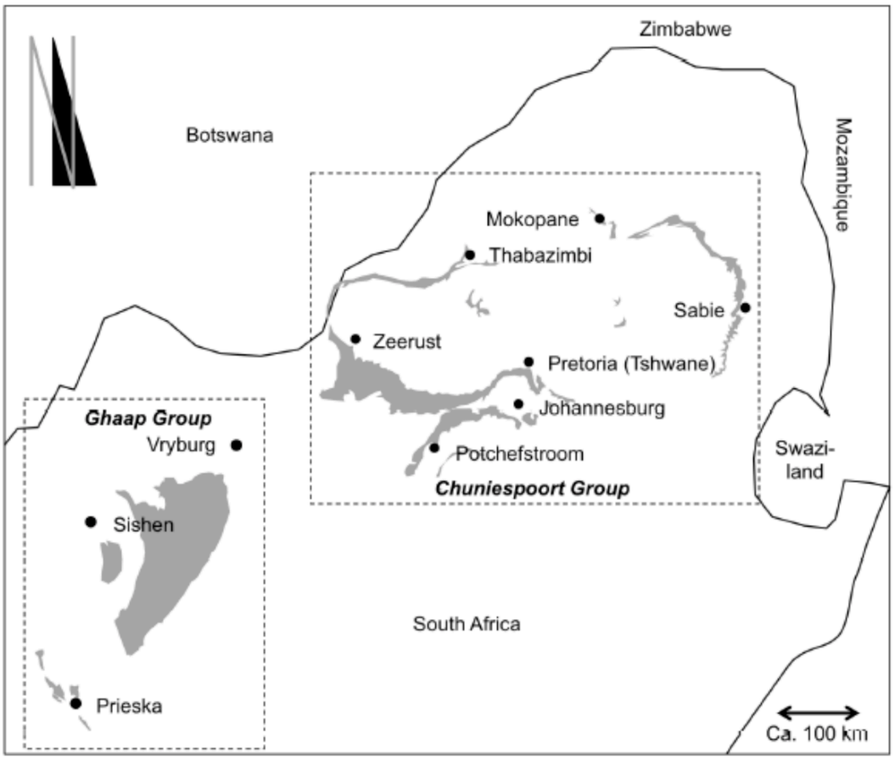

Figure 3-3 Distribution of outcropping dolomite bedrock within South Africa shown in grey shading (taken from Dippenaar et al. 2019)

3.4 Conclusion

The geology underlying deep weathering profiles plays a pivotal role in shaping the characteristics of completely weathered rock and residual soils. This chapter briefly summarised the parent rock types, namely fine-grained intrusive igneous rocks, including granites, diabase, and volcanic units of the Dullstroom Formation, as well as dolomite from the Malmani Subgroup. Each rock type contributes uniquely to the texture, mineralogy, and weathering behaviour of the residuum.

The fine-grained intrusive igneous rocks, particularly the Duivelskloof Leucogranite and Turfloop Granite, exhibit chemical weathering profiles influenced by their quartz and feldspar compositions. Similarly, the diabase and Dullstroom Fm units provide insights into the weathering processes of mafic to intermediate materials. The susceptibility of the Malmani Dolomites to cavity formation emphasizes the complexity of chemical weathering in carbonate rocks and highlights the importance of thoroughly understanding the weathering profile in dolomite stability investigations.

Overall, the chapter establishes the significance of parent rock composition, age, and environmental conditions in determining the development and characteristics of weathering profiles, laying the groundwork for more detailed understanding of how various types of weathering profiles form on these parent rock units.

4 Completely Weathered Rock and Residual Soils

4.1 Overview

The saprolite forms the lower part of the regolith which is described as the transition zone from surface soil to fresh rock. The term saprolite is generally applied to chemically altered rocks where all or part of the primary minerals are transformed to new ones while retaining most of the original parent grain texture and volume. The saprolite forms in erosion limited environments (weathering rates exceed erosion rates) where products of weathering have remained in-situ and is associated with low relief topography and humid, tropical to sub-tropical environments. This zone generally comprises a mixture of clays, Al and Fe oxides and hydroxides, and any other minerals largely resistant to weathering (quartz, existing clay minerals) with traces of the rock structure still intact. The term is generally used when dealing with igneous or metamorphic rocks with deep weathered profiles. The saprolite comprises different zones or horizons that vary from profile to profile. These include completely weathered rock below becoming residual soil as you move towards the surface or up the profile. These zones can support variably weathered rock fragments (corestones) in the matrix (Riebe et al. 2021; Silva et al. 2022; Dos Santos et al. 2022; Bonnet et al. 2022; Hu et al. 2023; Wang et al. 2024).

The term saprolite is commonly used in literature and has been defined by many authors and institutions (National Research 2001; Richardson 2017; Frings and Buss 2019; Silva et al. 2022). To keep to international standards in geotechnics and geology, for the remainder of this thesis, the definitions of residual soil and completely weathered rock will be used in place of the saprolite (ISRM 1981; Dippenaar et al. 2024). ISRM (1981) defines these two weathering states as follows:

- **Completely weathered rock**: “All rock material is decomposed and/or disintegrated to soil. The original mass structure is still largely intact.”
- **Residual soil**: “All rock material is converted to soil. The mass structure and material fabric are destroyed. There is a large change in volume, but the soil has not been significantly transported.”

Dippenaar et al. (2024) defines the completely weathered rock with the same diagnostic features as the above ISRM (1981) definition. The residual soil definition is slightly different and stated as follows by Dippenaar et al. (2024):

- **Residual soil**: “Rock weathered to the state where original minerals, structures and textures have been altered or removed by weathering.”

The boundary between the completely weathered rock and residual soil is defined by the loss in relict rock structure and a significant change in chemical mineralogy, namely the alteration of most to all primary rock forming minerals to secondary minerals, and the increase in pedogenic iron oxides and aluminium, and relative increase in silica.

The formation of these two horizons is dependent on parent material, rainfall, temperature / radiation, evaporation, vegetation cover, time, and topography, with different intensities of each resulting in different profiles and geotechnical conditions. This section will discuss the formation of completely weathered rock and residual soil, which will collectively be called residuum, in a humid climate and will elucidate the alterations the material goes through both from a chemical and structural aspect (Bonnet et al. 2022). These changes will impact on the geotechnical properties namely the porosity and plasticity of the material which will be discussed.

4.2 Formation of the weathering profile

The residuum forms by weathering via physical, chemical and biological processes. Physical processes mechanically disintegrate rock that will expose fresh rock to chemical weathering, increase permeability and surface area of bedrock to allow flow and increased interaction with chemically active fluid. Chemical weathering alters rock minerals through hydration, hydrolysis, carbonation, dissolution, cation exchange and oxidation, forming clay minerals with lower energy states that are more stable (Mitchell and Soga 2005). The process through which a rock weathers is dependent on the climate and will result in different profile depths and characteristics, as shown in Figure 4-1.

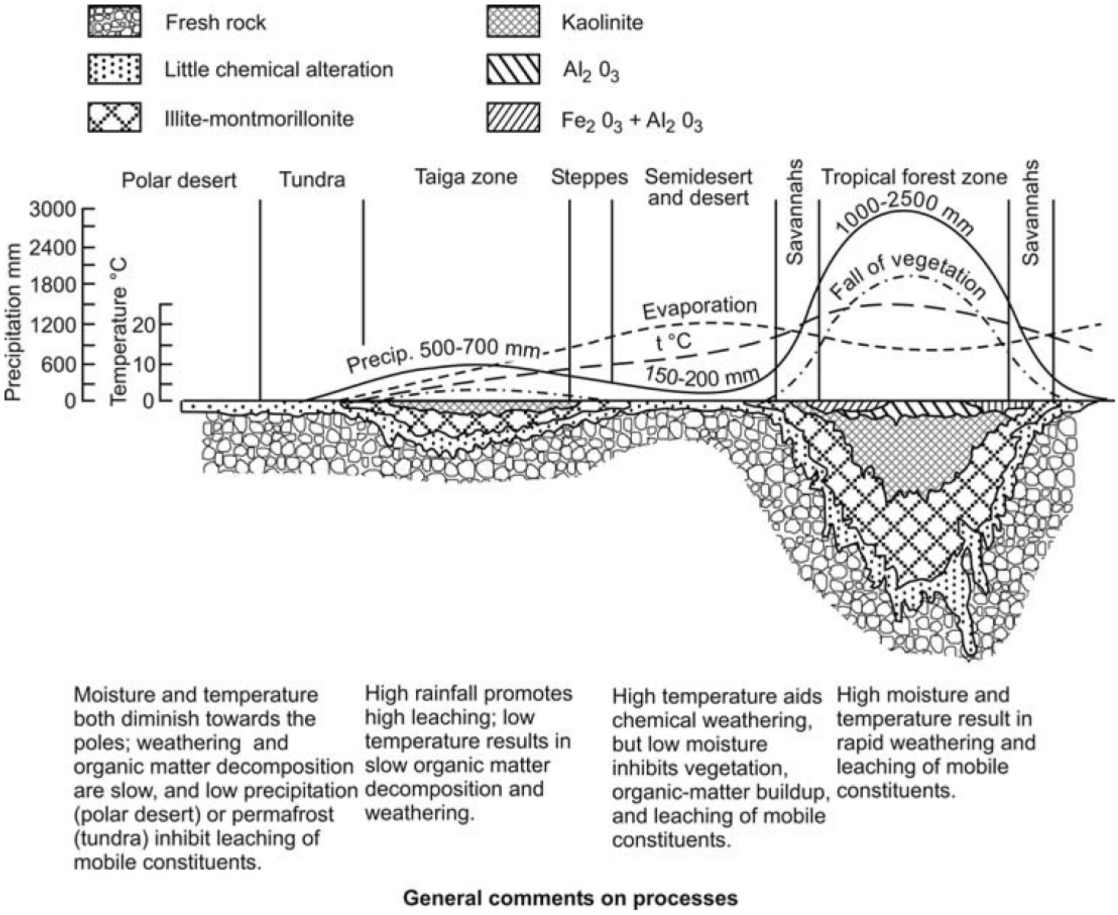

Figure 4-1 Influence of global climate on depth of weathering and weathering products (adapted from Strakhov 1967; taken from Blight and Leong 2012)

Climate determines the amount of water present, the temperature, and character of vegetation cover, and these, in turn, affect the biological complex. Some of the general influences of climate are (Mitchell and Soga 2005):

- For a given amount of rainfall, chemical weathering proceeds more rapidly in warm than in cool climate. At normal temperatures, reactions rates approximately double for each 10°C rise in temperature.
- At a given temperature, weathering proceeds more rapidly in a wet climate than in a dry climate provided there is good drainage.
- The depth to the water table influences weathering by determining the depth to which air is available as a gas or in solution and by its effect on the type of biotic activity.
- Type of rainfall is important: short, intense rains erode, and cause run off, whereas light-intensity, long duration rains soak in and aid in leaching.

Topography has a lesser impact on the formation of a weathered bedrock profile, but its influence can either foster chemical weathering or entirely suppress it. For deep weathering profiles to occur, many authors agree a low or flat relief is required so that erosion takes place slower than chemical alteration (Strakhov 1967; Summerfield 2014; Dippenaar and Van Rooy 2014). With greater variations in relief, mechanical denudation becomes more intense, reducing the impact of deep chemical alteration. A point can be reached where the ground surface is steep enough and the rate of erosion exceeds the rate of chemical weathering. Therefore, the latter is completely suppressed even in conducive climate conditions.

The ancient topography and surface age of southern Africa (~100 million years) resulted in deeply weathered residual profiles which are now exposed in steep valleys along the eastern escarpment of South Africa. This implies that the ancient topography has influenced the formation of the soil profile more over than recent or current topography.

The resultant soil texture and chemically constitutions of residuum are dependent on parent rock characteristics (grain size and structure, fabric texture, chemical components, rock mass features etc.), long term climate conditions and trends, vegetation and bioturbation and regional topography. All the factors contribute to the type and intensity of weathering that occurs.

The parent rock characteristics are important to consider in the initial stages of weathering in warm, humid environments to form a completely weathered rock horizon (Wilson 2004; Bonnet et al. 2023).

Alkali and alkaline cation content of parent rocks are important factors in determining parent rock weathering products. Rocks containing no alkalis can only produce kaolinite or lateritic weathering products. Rocks containing alkalis and alkaline earth cations will produce a variety of weathering products. Parent rocks with high amounts of iron and magnesium (mafic) tend to form dark coloured soils of high clay content. Felsic parent rocks with high proportions of iron and silica tend to be form light coloured clays with large, typically sandy, quartz component (Yong et al. 2012).

Biological weathering contributes to both physical (burrowing insects) and chemical weathering (organic decay). Physical and chemically weathering usually occur simultaneously. Riebe et al. (2021) concluded anisovolumetric weathering, change in volume due to physical weathering, produces more porosity when compared to chemical mass loss only.

Anderson (2019) found microfractures in rock form from low applied stress, such as volume change from mineral alteration, known as subcritical cracking. Physical breakdown or disintegration forms smaller rock fragments and increases surface area. This allows for chemical decomposition of fresh minerals which typically produces clay minerals, oxides, hydroxide and free silica depending on the factors discussed below.

4.2.1 Chemical weathering of primary rock minerals

Chemical decomposition is the most intense at ground surface and along rock joint faces, with it usually decreasing in intensity with depth from ground surface and reduction of jointing. Chemical weathering occurs at surface due to the differing of conditions, compared to deep earth conditions, causing primary rock minerals to react with the new environment and produce new secondary minerals that are stable, or at least more stable, at surface.

The type of primary rock mineral is crucial to consider because the rock matrix's pores and micro-cracks, which allow water to interact with exposed surfaces, typically occur at mineral grain boundaries, cleavage structure, and preexisting defects within the minerals. These openings are influenced by the rock mass's stress and strain history. As decomposition progresses, fresh mineral surfaces are exposed, which exponentially increases the potential for weathering and leads to varying chemical and physical conditions in the weathering profile (Wilson 2004).

These new surface conditions to consider are as follows:

- Lower temperature,
- Lower pressure,
- Presence of organics,
- Higher amount of free water, and
- Higher amount of free oxygen in the atmosphere.

The main agent responsible for chemical weathering reactions is water and weak acid formed in water. Rainwater falling from above the ground surface, infiltrates and eventually percolates to the bedrock becomes slightly acidic due to the particle pressure of carbon dioxide in the atmosphere, decaying vegetation and other acids in the soil, to form a weak carbonic acid (H_2CO_3) as shown in Equation 4-1.

water + carbon dioxide → carbonic acid → hydrogen ion + bicarbonate ion

$$H_2O + CO_2 \rightarrow \quad H_2CO_3 \quad \rightarrow \quad H^+ + HCO_3 \qquad \textbf{4-1}$$

H$^+$ is a small ion (proton) and can easily enter crystal structures releasing other ions into the water (Nelson 2017), furthering chemical weathering as shown in Equation 4-2. Therefore, carbonation in silicates is accompanied by the liberation of silica (Yong et al. 2012). This is an important aspect to consider when realising the excess of carbon being ejected into the atmosphere due to anthropogenic activities and the increase occurrence of acidification of rainwater.

The rate of chemical weathering is based on temperature, moisture, composition, potential for leaching and composition of the leaching solution (Yong et al. 2012).

Chemical reaction processes can be categorized into hydrolysis (decomposition), leaching and redeposition, and dehydration. These processes can occur simultaneously, cyclically, or sequentially, depending on climatic conditions and exposure time or intensity (Fourie et al. 2012).

Hydrolysis is the reaction between a rock mineral, hydrogen ion and water forming two or more products from the mineral, as shown in Equation 4-2.

orthoclase + hydrogen ion + water → potassium ion + kaolinite + quartz

$$4KAlSi_3O_8 + 4H^+ + 2H_2O \rightarrow 4K^+ + Al_4Si_4O_{10}(OH)_8 + 8SiO_2 \qquad \textbf{4-2}$$

This reaction is a main driver for the weathering of silicates, which are the primary rock forming minerals. For hydrolysis reactions to cause weathering of rocks, it is necessary for the weathering products to be removed continuously by a constant supply of fresh water (Yong et al. 2012). Hence, these reactions occur along rock joints, mineral boundaries and defects, and near to the surface where continuous water supply is available.

Hydration is the chemical uptake of water by silicates, oxides of iron and aluminium, and sulphates in rock (Yong et al. 2012). The minerals in the rock form hydrous compounds and an increase in volume occurs. This differential volume expansion causes fragmentation of rock and increases rock surface area, whereby increasing potential for more chemical weathering.

Solution (or *dissolution*) is the process of a mineral decomposing, when slightly acidic water acts as the solvent, forming a solution. The extent to which minerals will dissolve into water is dependent on the temperature and pH of the environment and is known as equilibrium solubility. For example, quartz is practically insoluble in pH ranges below 10, while halite is very soluble in earth surface environments. Ferrous iron (FeO) is soluble below pH of about 7, while ferric oxide (Fe_2O_3) is insoluble except below under high acidic conditions (pH < 3.5) (Summerfield 2014). The rock type of significancse in South Africa that weathers through dissolution is dolomite which a calcium magnesium carbonate mineral and collectively a rock by the same name. The dissolution process is simply presented by Equation 4-3 (Buttrick 1986).

Dolomite + carbonic acid → calcium bicarbonate + magnesium bicarbonate

$$CaMg(CO_3)_2 + 2H_2CO_3 \rightarrow Ca(HCO_3)_2 + Mg(HCO_3)_2 \qquad \textbf{4-3}$$

It must be noted that all major components of dolomite go into solution with very little to no residual material remaining. This causes the formation of cavities in the rock which becomes receptacles, for overburden to fall into, forming sinkholes at surface.

Leaching occurs when ions are removed by dissolution into water. For example, K^+ ion in Equation 4-2 will be carried away by free water. The mobility of ions depends upon their ionic potential. Ca^{2+}, Mg^{2+}, Na^+, K^+ are easily leached by moving water, Fe^{2+} is more resistant, and Al^{3+} is immobile. *Redeposition* may occur in another part of the profile where leached ions (Fe^{2+}) are removed from the free water, usually due to evaporation, resulting in an accumulation of oxides and hydroxides of sesquioxides in the accumulation zone (e.g. ferricrete horizon) (Blight and Leong 2012).

Oxidation occurs at surface as abundant free oxygen is present, in air and water, and will react with minerals to change the oxidation state of the ion (loses an electron). The tendency for oxidation to occur is based in the redox potential (Eh) of the environment. It is measured in unit s of millivolts (mV), with the positive values registering an oxidizing potential and negative values a reducing potential (Summerfield 2014). This most commonly occurs with Fe bearing minerals, since Fe can have several oxidation states, namely *Fe*, Fe^{2+}, Fe^{3+}. This is shown in Equation 4-4.

pyroxene + oxygen → magnetite + quartz

$$3Fe^{+2}SiO_3 + \frac{1}{2}O_2 \rightarrow Fe_3O_4 + 3SiO_2 \tag{4-4}$$

Oxidation of minerals by gaseous oxygen occurs by the intermediary action of water (Yong et al 2012). Depending on the partial pressure of gaseous oxygen and acidity of the water, gaseous oxygen dissolved in water renders the resulting solution an oxidizing potential (i.e. positive redox potential) (Yong et al. 2012).

Dehydration alters the composition and distribution of the sesquioxides in a manner that is not reversible upon wetting. The reaction forms very stable iron and aluminium oxide minerals in soil such as hematite and gibbsite, respectively as shown in Equation 4-5.

goethite → hematite + water

$$2FeO \cdot OH \rightarrow Fe_2O_3 + H_2O \tag{4-5}$$

Rock minerals are not equally susceptible to chemical breakdown and mineralogic change. Typically, the minerals that form at the highest temperature, meaning the first minerals to form during cooling of magma, forming igneous rocks, are the least stable at low temperature at ground surface. An example of this is olivine and calcium-rich plagioclase, which is the highest temperature forming minerals on Bowen's reaction series (Bowen 1929). Similarly, the mineral to form at the lowest temperature, which is quartz, is typically the most stable primary rock-forming mineral at Earth surface conditions in the series. This is represented by Goldich's mineral stability series, which is shown in Figure 4-2, by the most commonly occurring primary rock minerals occurring in igneous rock. Other less common minerals have not been shown here.

All the above reactions occur to form, and occur in, weathering profiles depending on internal and external conditions. Many of the by-products from the various reactions are clay minerals, oxide minerals and quartz (from rock matrix and oxidation reaction). If the weathering is highly intensive, the primary rock mineral can completely decompose without the formation of by-products forming openings in the rock mass (Wilson 2004; Bonnet et al. 2023). The clay minerals occupy the fine-grained portion of the residuum, while quartz and iron oxides tend to occur in the coarse-grained portions, as well as coatings. Gibbsite, and other amorphous aluminous material, is commonly found as fillings in pores and voids in concreted particle aggregations (Fourie et al. 2012). It is important to understand each major component of the residuum before considering the vertical heterogeneity and complexity of the material.

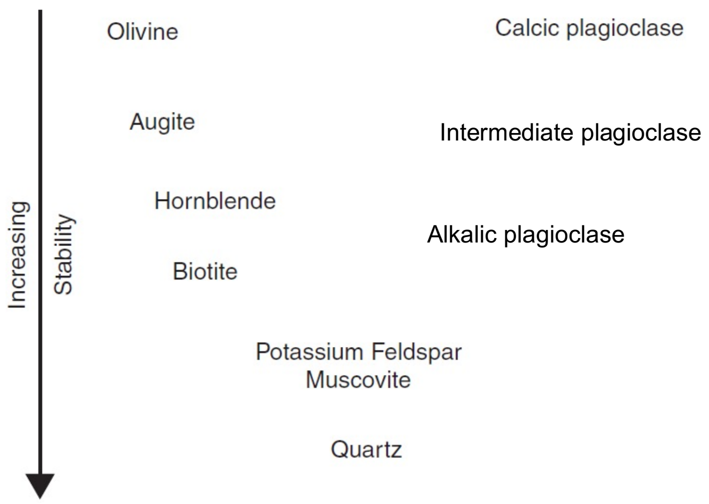

Figure 4-2 Goldich's mineral stability series (adapted from Goldich 1938)

4.3 Products of primary rock mineral decomposition

Soil comprises a four-phase system, gaseous, fluid, soil phases and contractile skin, as discussed in Section 2. The solid phase can be further separated into two sub-groups of importance. Inorganic crystalline material includes primary minerals; clay minerals; oxides and hydrous oxides of iron, aluminium, and silica; carbonates, sulphates, phosphates, and sulphides Inorganic non-crystalline material consist of hydrous oxides of iron, aluminium, and silica (Yong et al. 2012). Understanding the properties, role and typically proportion of each will give a good understanding of the unified behaviour of residual soil and especially completely weathered rock.

4.3.1 Clay minerals

Clay minerals form from reactions during chemical weathering of primary rock minerals. The composition of the solution during the reactions and the degree of leaching (removing ions from environment) result in a particular clay mineral (Yong et al. 2012). Feldspar may weather to montmorillonite first and then to kaolinite, or directly to kaolinite depending on the conditions during weathering. Limited leaching environments where cations are retained tend to form illite and montmorillonite, where leaching favourable environments tend to form kaolinite. However, with excess leaching of silica, iron and aluminium oxides tend to form.

Clays are a major contributor to behaviour of intensively weathered igneous and chemical sedimentary profiles, and it is important to understand the differences of each major type of phyllosilicate.

4.3.1.1 Kaolinite group (1:1 layer type)

The kaolinite mineral is made up of a single silica tetrahedral sheet and one aluminium-hydroxyl octahedral (similar to the structure of gibbsite). The combined silica-gibbsite sheets are held together by strong hydrogen bonding. The layers are electronically neutral and are attracted to other clay minerals by weak, short-range, van der Waals forces. Kaolinite is the most common clay mineral group and has a chemical formula of $Al_2Si_2O_5(OH)_4$. Kaolinite crystals are usually 0.20 to 2.00 micrometres (μm) in size and have hexagonal crystal structure (Singh and Huat 2013).

It forms from weathering (hydrolysis) of feldspar-rich (aluminosilicates minerals) rocks and is the most common weathering product of feldspars (Wilson 2004). It is typically the end member of a weathering series from multiple rock types in highly leaching environments (Summerfield 2014). In order to form, ions like Na, K, Ca, Mg, and Fe must first be leached away by the weathering or alteration process. This leaching is favoured by acidic conditions (low *pH*). Kaolinite does not absorb water due to surface neutrality and only shows very limited shrink or swell when in contact with water.

4.3.1.2 Illite group (2:1 layer type)

Illite group comprises minerals with two silica tetrahedral sheets with a single aluminium-hydroxyl octahedral sheet set in between. The illite group has a layer charge of approximately 1 per ½ unit cell (Singh and Huat 2013). The combined sheets are linked together by relatively weak bonding due to non-exchangeable potassium held between them.

However, due to charge imbalances, the K ion can be exchanged for Mg and Ca. The presence of the *K* ion (and other ions) between the sheets and the high layer charge prevents the adsorption of water between the sheets and results in this clay mineral group to be non-expansive. Illite type clays are formed from weathering of K- and Al-rich rocks under high pH conditions. Thus, they form by alteration of minerals like muscovite and feldspar. Though, micas minerals in the parent rock remain relatively unaffected by weathering (Singh and Huat 2013). The chemical formula of illite is $KAl_2(Si,Al)_4O_{10}(OH)_2$. Partial substitution of Si by Al in the silica sheet can occur, but at a much lesser extent compared to the smectite group. This group occurs as greyish-white or silvery-grey, sometimes greenish-grey, in colour.

4.3.1.3 Smectite group (2:1 layer type)

Smectite has a similar structure to the illite group but has a much lower layer charge of 0.2-0.6 per ½ unit cell (Singh and Huat 2013). In the gibbsite sheet there is partial substitution of Al by Mg and Fe, and partial substitution of Si by Al in the silica sheet. The most important aspect of this group is the ability for H_2O molecules to attach to hydroscopic surfaces, and to occupy the space, between the sheets (due to the lower layer charge). This absorption of the molecule causes a significant increase in the volume of the soil. Therefore, the clay group is considered active (shrink-swell) clays with a change in moisture content in the soil. Montmorillonite is the most common of this group, with a chemical formula of $(Na,Ca)_{0.33}(Al,Mg)_2Si_4O_{10}(OH)_2$ and usually forms microscopic-size, platy, micaceous crystals (Singh and Huat 2013).

4.3.1.4 Vermiculite group (2:1 layer type)

This group consists of 2:1 clays that have a layer charge between 0.6 to 0.9 per ½ unit cell. They form from weathered micas when K^+ ions between the molecular sheets are replaced by Mg^{2+} and Fe^{2+} ions (Singh and Huat 2013). Therefore, the chemical formula is $(Mg,Fe,Al)_3(Al,Si)_4O_{10}(OH)_2$. Due to the relatively lower charge, this group can absorb water but not as readily as the smectite group. This group is considered active clays but not as intense as the smectite group.

4.3.1.5 Chlorite group (2:1:1 layer type)

This group has the same 2:1 layer as the above groups with an octahedral sheet adjacent to the 2:1-layer sheets. This group comprises four micaceous phyllosilicate end members based on their substitution of Mg, Fe, Ni and Mn, with the two most common minerals being clinochlore ($(Mg_5Al)(AlSi_3)O_{10}(OH)_8$) and chamosite ($(Fe_5Al)(AlSi_3)O_{10}(OH)_8$). Chlorite group minerals are commonly found as low-grade metamorphic and igneous rocks. It can form from alteration of mafic minerals biotite, hornblende, pyroxene and garnet.

4.3.2 Mica

Mica, usually occurring as muscovite and biotite, are essential rock forming minerals of granite and gneiss. It typically consists of minerals characterised by highly perfect cleavage which allows the mineral to be separated into very line leaves (Singh and Huat 2013). This group differs widely in composition and vary in colour. Muscovite is the most common of this group with a chemical formula of $KAl_2(AlSi_3O_{10})(OH_2)$. It is resistant to chemical weathering and results in soil by breaking down into smaller particles, easily identifiable by its lustre in a soil profile.

It can also form in soil from the breakdown of feldspars where it forms as fine-grained aggregates collectively called sericite (Singh and Huat 2013).

4.3.3 Oxide and hydroxide minerals

Metal oxides and hydrous metal oxides are common components of weathered rock and soils in general. They form from weathering of common rock forming minerals. Oxides in soil exist as crystalline (mineral) or amorphous forms. It is important to distinguish between the two. Amorphous forms of oxides have the ability to coat mineral particles surfaces because of the net electric charges on the surfaces of both the clay mineral particles and amorphous material. The charge of the coating amorphous material is dependent on the pH conditions of the porewater and becomes important when studying interactions between coated soil particles (Yong et al. 2012). Al, Fe and Mn oxides and hydroxides are the most common minerals (Singh and Huat 2013). Gibbsite is the most common of the Al (hydro)oxides. Goethite, hematite, magnetite and lepidocrocite are among the most common Fe (hydro)oxides.

4.3.3.1 Gibbsite

This mineral has a clay-like layered structure formed from stacked sheets of linked octahedrons of aluminium hydroxide with a chemical formula of $Al(OH)_3$. The sheets are only held together by weak residual bonds and these result in very soft, easily cleaved, mineral. It forms mainly in intense leaching environments (hot and cold temperatures and high rainfall) where most secondary minerals have weathered away resulting in a relative enrichment of gibbsite. It can be observed in early stages of weathering where an abundance of feldspars is present.

4.3.3.2 Goethite

It is a common hydrous oxide of Fe found in soil and has a chemical formula of $FeO(OH)$. It forms in conditions of continuous moisture and aeration within intense leaching environments (hot temperatures and high rainfall), exhibiting a yellowish to blackish brown colour. It forms from weathering of iron-rich minerals (Banerjee et al. 2016). It commonly forms pseudomorphs of cubic pyrite and other minerals.

4.3.3.3 Hematite

Forms in highly oxidizing environments and in the mineral from of iron (III) oxide. *Rust* on metal is also a form of iron (III) oxide. This mineral commonly gives tropic soil profiles the bright red colour. The chemical formula is Fe_2O_3 and occurs in high leaching environments (hot temperature and high rainfall) where other minerals are weathered away resulting in relative enrichment of this mineral. Hematite commonly forms coatings on clay minerals and quartz grains giving the clays a red colour (White 2006). Iron oxides typically coat joint infill or can completely seal joints that existed in the fresh parent rock (Banerjee et al. 2016).

4.3.4 Silica mineralogy

Quartz is generally inert and resistant to chemical weathering and will typically only break down to finer particles through physical weathering. Thus, the quartz found in soil usually grades in the sand and possibly silt portion of the soil and influences the behaviour based on grading alone. The quartz particles are generally coated by clay minerals and (hydro)oxide minerals.

4.3.5 Residual dolomite and wad

The weathering product of dolomite is a special case when it comes to understanding the mechanism through which it forms and the implications of the behaviour. Dolomite rock contains more than 90% dolomite (mineral) and less than 10% calcite, secondary silica (chert) and detrital minerals. Dolomite can be *enriched* in iron (Fe) or manganese (Mn), but these are usually in trace amounts (less than 2%) in the overall rock (Buttrick 1986).

The completely weathered rock forms through the removal of soluble dolomite and can result in an extremely low-density residuum that is enriched in Fe and Mn oxides. When the resulting residuum is Mn-rich, it is usually dark purple to blue in colour and is termed wad. This material is further split into two types, namely structured wad and non-structured wad. The former possesses a highly porous, low-density, usually lower than that of water, structure that is inherited from the parent rock. The latter is often described as powdery and does not have a *prominent* structure, however, relic rock structure is still present. Structured wad typically has a void ratio double that of non-structured wad and has been found to have a void ratio as high a 13. To keep continuity on the material type across the weathering profiles, the term completely weathered rock will be used for wad. The material will be defined as wad when necessary. Residual dolomite forms in the same manner as residual soils of other rock types.

The Fe oxides are typically goethite and hematite in residuum forming on dolomite (Buttrick 1986; Swart et al. 2019). The Mn oxides that form in wad and residual dolomite are dependent on the prevailing environment (Dowding et al. 2005). The most common Mn minerals to form in wad are birnessite, lithiophorite and todorokite (McKenzie 1972; Post 1999; Dowding et al. 2005; Swart et al. 2019).

Birnessite [(Na,Mg,Ca,$Mn^{2+)}Mn_7O_{14}$] (simplified to δ-MnO_2 in geochemical literature) is the most common Mn oxide in soil. The mineral has typically a sponge to coral type structure and contributes greatly to the water holding capacity of the material to an extent that is far greater than its quantity of weight percentage (wt.%) in the soil (McKenzie 1972; Post 1999; Swart et al. 2019).

Lithiophorite [(Al,Li)$MnO_2(OH)_2$] has a similar structure as birnessite but differ with the presence of alternating Al-hydroxy sheets layers, between the MnO_6 octahedra (Dowding et al. 2005). The mineral typically occurs as a clay and dominates the mineralogy of the clay fraction in the highly acidic soils of the humid Graskop area in Mpumalanga (Post 1999; Dowding 2004).

Todorokite [(Na,Ca,K,Ba,$Mn^{2+})_2Mn_5O_{12}.3H_2O$] is made up of triple chains of edge-sharing MnO_6 octahedra that link up to form 3x3 tunnels (Post 1999). Golden et al. (1986) suggests that todorokite will not be expected in highly weathered, acid environments due to the fibrous morphology and influence of magnesium in the formation of the mineral. Post (1999) concluded when the material is encountered in highly weathering environments, the todorokite is an important phase in Mn coatings and varnishes.

Fe and Mn oxides in wad have recently been shown to influence the variable and high liquid limits to a much greater extent than previously thought, especially the presence of the certain Mn oxides (Swart et al. 2019). Jenne (1968) stated that the chemical influences that Mn oxides have on the surrounding environment and aqueous solutions far outweighs their concentrations. The type of Mn mineral is usually difficult to identify due to the poor-crystallinity of the material. This is further complicated due to Mn minerals having similar x-ray diffraction (XRD) diagnostic peaks to common clay minerals (Dowding 2004).

4.4 Chemical weathering profile

A typical weathering profile consists of a combination of all the minerals mentioned above and other less common ones. There are generalisations of expected weathering products (secondary minerals) based on the parent rock and weathering environment. However, there is no suitable method to fit a blanket classification system to all possible quantities and forms for each secondary mineral that make up completely weathered rock and residual soil. This section will investigate clarifying the accepted generalisations to better understand the formation of secondary minerals that occupy a weathering profile.

The basic weathering profile is best described by soil scientist concept of soil pedon. The weathering profile is divided in defined horizons based on the extent and type of pedogenic processes which generally exist parallel to the soil surface (Shaw 1927). The upper portion of the soil profile is known as the solum and includes all horizons altered or formed from pedogenic process (Kellogg 1930).The solum lies on top of the C horizon, which is designated as the transition layer between the solum and bedrock (Schaetzl and Thompson 2015). Kellogg (1930) defined this horizon as “parent material that has been unaltered by soil-building forces”. However, for the bedrock to weather and alter via various chemical reactions, rainwater must infiltrate and percolate through the surface soils and flow into and through the bedrock.

This percolated water will most certainly have solids and solutes, picked up in the atmosphere and surface soils, which will essentially alter the parent bedrock through illuviation and other pedogenic processes. For this reason, defining the upper boundary of the completely weathered bedrock from chemical observations alone may be challenging. The idea of a D horizon exists, and it represents the lower, completely unaltered, weathered bedrock, while the C horizon includes the upper, slightly influenced by pedological formations and alterations in volume (Kellogg et al. 1936; Schaetzl and Thompson 2015). Geologists and geotechnical engineers tend to focus on the macro structure characteristics during logging and will often refer to the C and D horizons as a singular completely weathered rock horizon.

Futai et al. (2004) studied a profile of weathered gneiss in Brazil. The mineral distribution of the profile is shown in Figure 4-3. The mineral distribution is typical of igneous and metamorphic rocks with high amounts of quartz and kaolinite and an increase of oxides present close to the ground surface.

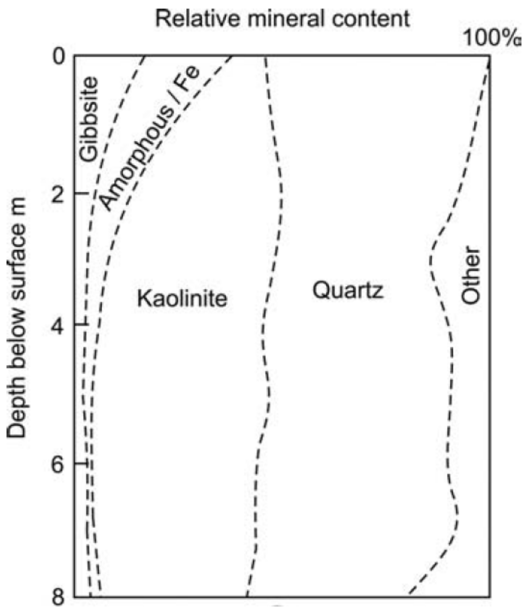

Figure 4-3 Mineral distribution in a profile of weathered gneiss (taken from Blight and Leong 2012)

Van der Merwe (1964) observed nine (9) chemical weathered igneous rock profiles in various locations in South Africa with annual rainfall of between 600 mm and 1100 mm. The study focused on the chemical compositions, Atterberg limits, and excavated soil texture. There was a generally increase in plasticity and clay content as weathering increased. The completely weathered rock possessed relict structure with pedogenic staining and generally graded as a silty sand to sand. The vertical chemical profile varied but the generally trend showed feldspar, quartz, chlorite, existed in the lower portion of the completely weathered rock. As weathering increase, montmorillonite and kaolinite became more prominent while the feldspar and chlorite decomposed, until eventually kaolinite and quartzite and lesser montmorillonite existed. Much of the residual profiles were logged as red in colour and therefore it can be deduced that Fe-oxides were present.

The movement of Mn in a weathering profile has been investigated by many authors from various backgrounds (Van der Merwe 1942; Buttrick 1986; Dowding et al. 2005; Dowding and Fey 2007; Bourgault and Rabenhorst 2011). Mn can exist in multiple different oxidation states in soil but can only be dissolved if Mn (III) or Mn (IV) is reduced to Mn (II) or Mn (II) is released from the crystal lattice. This process is controlled by the pH value and the oxidation-reduction equilibrium of the soil. Mn compounds are much more soluble in acid soils than in neutral or alkaline soils, and much more soluble in reducing than in oxidising soils. The greater susceptibility of Mn to undergo different forms of oxidation, compared to Fe, makes the Mn oxides readily dissolve into solution when exposed to further leached, acidic, environments. This can be seen in weathering profiles where Mn oxides, typically birnessite and lithiophorite which form wad, in highly weathered soils are normally confined to the C horizon or completely weathered rock, in which the pH may be more alkaline and reduction subdued enough, to allow precipitation.

Swart et al. (2019) sampled and tested residuum formed from dolomite of the Malmani Subgroup that outcropped in the northern portion of South Africa. The study showed behaviour of wad, which is a form of completely weathered dolomite, occasionally incorrectly termed weathered altered dolomite, is governed by the relict rock structure and presence of Mn oxides. If the wad experiences more weathering, the material will eventually densify, destroying the relict structure. The Mn content will gradually be replaced by Fe ions as weathering continues turning the soil red in colour and forming goethite and hematite as well as gibbsite in highly weathering environments. Once this has occurred, the material will have a higher weight percentage of Fe oxides than Mn oxides and the material is defined as residual dolomite. The relative enrichment of the Fe will cause the metal oxides' crystal structure, namely the Mn oxides, to tend towards an amorphous state reducing the originally large reactive surface area. This chemical change has the biggest impact on the material's unsaturated behaviour leading to lower liquid limits and water holding capacities (Swart et al. 2019).

Formation of a weathered profile starts at the concept of a weathering front. A weathering front is assumed to be approximately parallel to the ground surface, however this is a simplification and is typically geometrically irregular (Phillips et al. 2019). Weathering is most intense at the ground surface and along rock fractures (i.e. joints and faults) and decreases with an increase in depth and reduction in jointing. As the weathering front moves down the ground profile, the degree of alteration increases towards the ground surface as indicate in Figure 4-4.

This degree of weathering will usually result in a typical sequence of mineral occurrences with depth, as shown in Figure 4-1. The mineral which forms at a certain depth within a profile is dependent on the composition of the pore water, mineralogy of the parent rock, intensity of leaching and prevailing Eh-pH conditions at that depth (Summerfield 2014). Summerfield (2014) best represents the formation sequence of secondary minerals, based on leaching intensity (i.e., exposure time and depth in profile), from original primary minerals, and is presented in Figure 4-5.

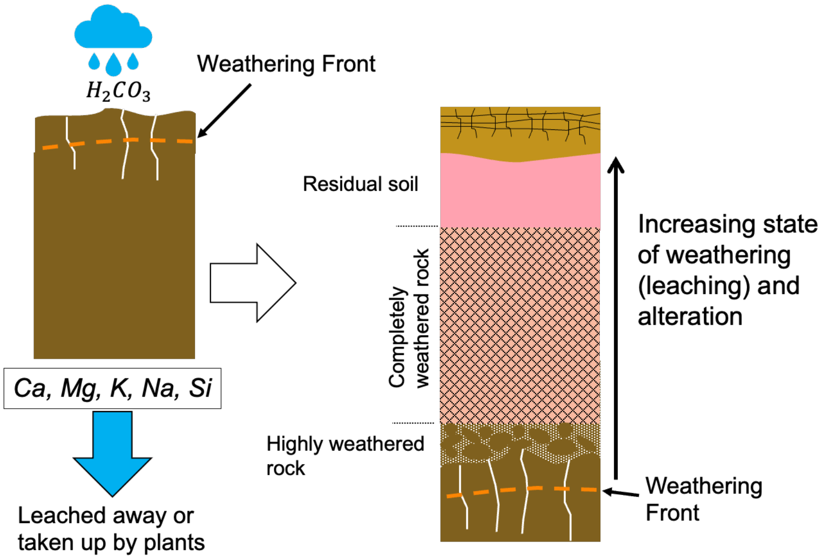

Figure 4-4 Movement of weathering front forming typical soil profile

Generally, all feldspars and mafic minerals weather to kaolinite in free draining profiles in areas that class as Weinert N-value of less than 2 in Southern Africa (Weinert 1980). Usually following the path of primary mineral to montmorillonite to eventually kaolinite or directly decompose to kaolinite. Decomposition of primary mineral grains will vary in the profile, but generally increase from being a minimum in the parent rock and maximum in the upper residual soil. Additionally, Ca-rich feldspars and pyroxenes can completely dissolve resulting in an open pore while leaving no weathering products (Wilson 2004).

Chemical weathering indices are used to quantify the state of weathering by assessing the quantities of mobile ions such as Ca^{2+}, Na^{+}, and K^{+}, and the relative accumulation of immobile ions such as Fe^{3+} and Al^{3+}. Various methods have been put forward and successfully used in literature (Nesbitt and Young 1982; Fedo et al. 1995; Meunier et al. 2013; Liu et al. 2022; Cho and Ohta 2022; Sergeev 2023).

Many of these chemical weathering indices have their limitations and need to be adjusted based on the state of the weathered material and parent rock under investigation.

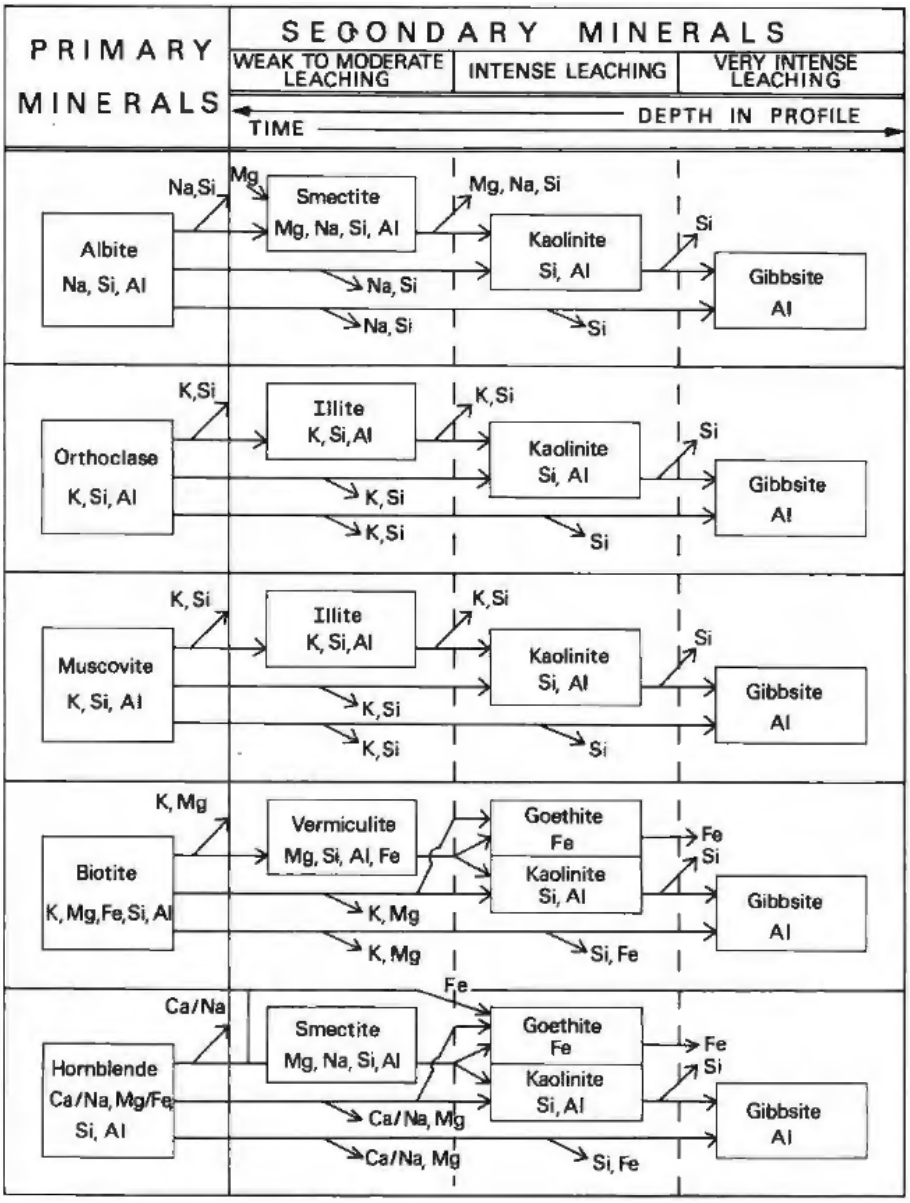

Figure 4-5 Schematic representation of the relations between leaching intensity and types of minerals formed (taken from Summerfield 2014)

The most frequently used method to measure the degree of weathering is the chemical index of alteration (*CIA*). This method is based on the changes in chemical compositional associated with the decomposition of feldspar and formation of clay minerals. Since kaolinite is a common clay mineral into which most igneous rocks weather to, this method has been widely adopted (Cho and Ohta 2022). The *CIA* is calculated as presented in Equation 4-6.

$$CIA = \frac{Al_2O_3}{Al_2O_3 + CaO^* + Na_2O + K_2O} \times 100 \qquad \textbf{4-6}$$

*CaO** denotes the amount of *CaO* incorporated in the silicate fraction of the rock. The resulting value indicates the degree of weathering and typical values are between 30% and 45% for basalt, 45% and 55% for granites, and near 100% for kaolinite (Nesbitt and Young 1982). The range of the *CIA* for fresh rock is dependent on the chemical constitutions of the parent rock, and the calculated value has a possibility of reflecting a change in the source rock composition and not the degree of weathering (Meunier et al. 2013).

Meunier et al. (2013) proposed a method where the M^{+}-$4Si$-R^{2+} system is used and takes the amount of silica into account, which the *CIA* does not. This method has been termed the weathering intensity scale (WIS) and estimates weathering by quantifying the loss in silica and the accumulation of less mobile elements during weathering (Bonnet et al. 2022). Each component of the M^{+}-$4Si$-R^{2+} system is calculated, and the three values normalised to 100% and plotted onto a ternary diagram as stated in Meunier et al. (2013). Both the *CIA* and *WIS* methods can be successfully used for various igneous and sedimentary rock.

Cho and Ohta (2022) stated the *CIA* method has limitations due to chemical components used to calculate the degree of weathering. To fully utilise the method, the parent rock type and chemical data needs to be known which is often not the case. Therefore, a new weathering index method was derived and proposed, called the robust weathering (*RW*) method. The *RW* method can determine the degree of weathering of rock from a near fresh state to an intensely weathered, completely weathered rock and residual soil. The method does not make use of SiO_2, CaO, and P_2O_5 in the calculations but, of the six elements in the equation, the largest influence to determine the weathering is the leaching out of Na_2O and accumulation of Al_2O_3.

The type of weathering to form deep weathering profiles is mainly the alteration of chemical components in the rock. The chemical and structural properties of the weathered material is closely linked and will evolve simultaneously as primary rock minerals change to secondary minerals, microcracks and openings will form, whereby increasing surface area and permeability to further the weathering process (Liu et al. 2022; Bonnet et al. 2022; 2023).

4.5 Structural weathering profile

Throughout the decomposition of the parent rock, the structure is largely retained (Kellogg 1936; Schaetzl and Anderson 2005), however a weathered rock profile does undergo continuous volumetric strain as the degree of weathering increases (Banerjee et al. 2016; Hayes et al. 2019; Riebe et al. 2021; Liu et al. 2022; Dos Santos et al. 2022; Bonnet et al. 2022; 2023). Chemical weathering of rock implies the alteration of primary rock minerals to secondary minerals, but also its physical properties such as total porosity, tortuosity of pore network, aperture of the pores and relative permeability, water flow, diffusivity, and mechanical strength will change. At the initial stages of weathering, micro pores will form as etching and defects along mineral cleavage breaks and imperfections (Wilson 2004). At macro scale, the knowledge of porosity evolution during weathering is one key parameter for predicting water storage capacity and water flow in the completely weathered and residual soil horizons (Bonnet et al. 2023).

Hencher (2024) stated residual soils above an igneous bedrock form when the original rock texture is destroyed through leaching out and transformation of parent rock minerals or volume change and densification due to collapse under self-weight. The resulting material is typically a red, clay-rich, soil with discontinuous, localised, zones having remnants of parent rock structure. This results in a reduction of the dry density as the weathering front pushes deeper into ground profile. As weathering depth increases the upper portion of the completely weathered rock will collapse, whereby increasing dry density and reducing void ratio, destroying any existing relict parent structure, and forming residual soils (Hencher 2024). This process is shown in Figure 4-6.

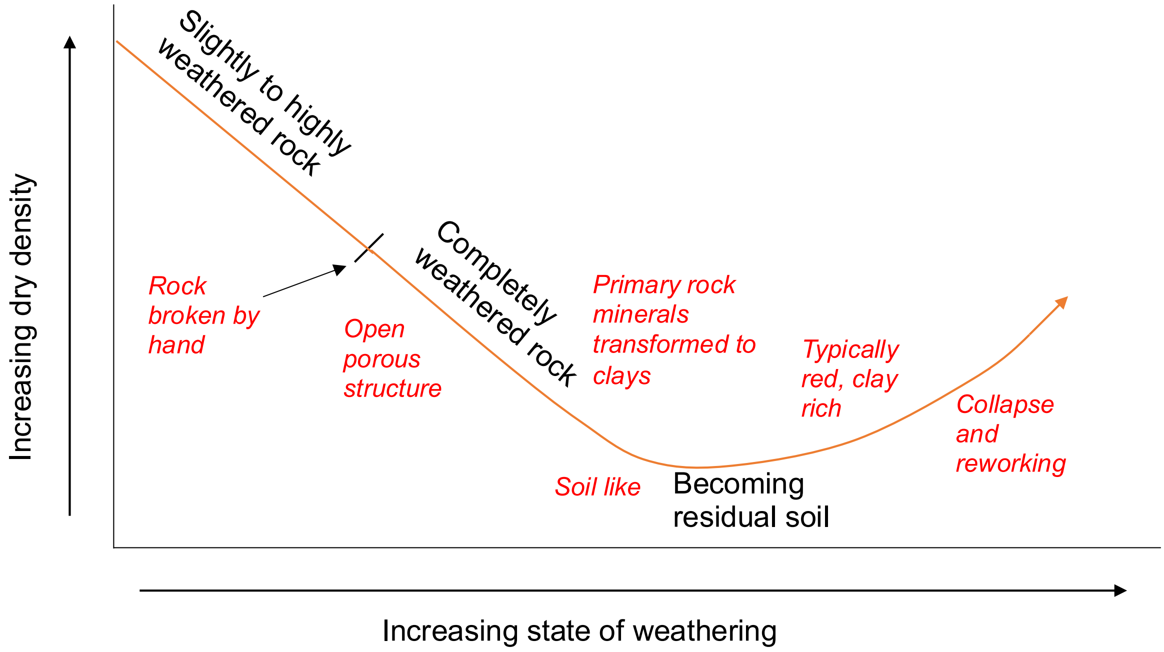

Figure 4-6 Change in dry density in relation to decomposition (adapted from Dippenaar et al. 2024; Hencher 2024)

Bonnet et al. (2022) study how the chemical weathering process impacts the Viamão granodiorite rock profile in South Brazil. The degree of chemical weathering, grain fragmentation, and development of connected porosity intensifies toward the upper layers of the completely weathered rock. Dissolution pits in feldspar grains form a network of intergranular micropores, while the expansion of biotite due to chemical weathering results in dense intergranular macrocracks. Both total porosity and macroporosity increase as you move upward in the completely weathered rock profile. Cracks formed during weathering and relict rock structure is often filled with clay and Fe-oxides. At the surface of the residual soil, grains become dislodged, causing the rock structure to break down and form a soil-like structure shaped by seasonal swelling and shrinkage cycles (Bonnet et al. 2022; Hencher 2024).

Swart et al. (2019) investigated the influence the relict rock structure and chemical components on the hydromechanical behaviour of wad and residual dolomite. The definitions and differentiation of wad and residual dolomite are based firstly on the chemical composition of the material, be it *Mn*- or *Fe*-rich, and secondly on the presence of structure. Wad is divided into two groups based on the structure, to either structured wad or non-structured wad. Structured wad is the insoluble residue that occupies a similar volume to the parent rock after the soluble rock leached away resulting in a high porosity and low permeability material. The structure observed in the wad is inherited from the parent rock, and it could be said wad is a form of a completely weathered rock. Structured wad possesses more than double the average void ratio value than non-structured wad. The void ratios are generally greater than 1.00 and have been found to be as high as 16.0.

The inherent fabric present in the residual dolomite is the major influencer of the water holding capacity and unsaturated soil behaviour.

The natural moisture content of structured wad usually exceeds the liquid limit (Buttrick 1986; Wagener 1982; De Beer 1985; Brink 1979; Swart et al. 2019).

Breaking down of the structure through intense weathering or external factors results in a decrease of water holding capabilities and may cause the material to liquify in-situ without a change in moisture content.

The relict rock structure and macro grain relations that survive the weathering process and persist in completely weathered rock provide strength and stiffness to the material (Wesley 1990; 2010; 2019; Bonnet et al. 2023; Wang et al. 2024). The relict rock structure can be lost through continued weathering in-situ, through rapid weathering once exposed to the Earth's surface and through anthropogenic influences (Obermeier and Langer 1986; Rabot et al. 2018; Dos Santos et al. 2022; Liu et al. 2022). An oedometer test can be used to determine the influence the structure has on the compression behaviour of soil. When testing residual soils, the concept of the pre-consolidation pressure and over-consolidation ratio are not applicable as the material has formed through chemical weathering and not consolidation (Wesley 1990; 2010; 2019).

Wesley (2019) suggests the data should be plotted on a linear pressure scale and the soil compressibility should be determined. Examples of how oedometer data plots on a strain to linear pressure scale plot is presented in Figure 4-7. Soil with structure is expected to yield if the yield pressure is reached under load and weaken. Non-structured soil is expected to compress and strengthen as loading continues.

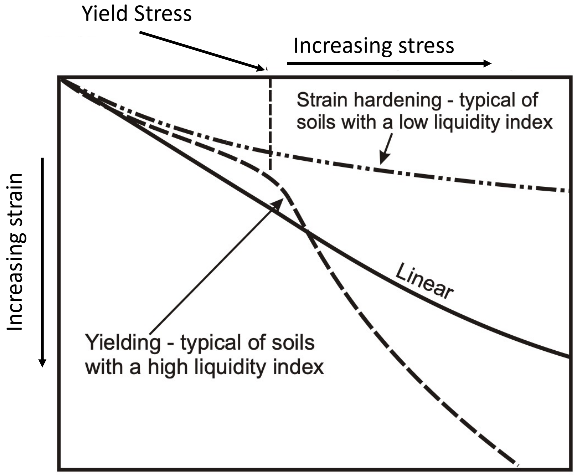

Figure 4-7 Recommended analysis for soil compressibility behaviour when testing residual soils (adapted from Wesley 2019)

The liquidity index is a key indicator of structured residuum behaviour, particularly in terms of sensitivity and strength. Soils with a high liquidity index, a value of 1 or greater, often experience significant strength loss when the structure is destroyed. A soil with a high liquidity index is at a natural moisture content near or greater than the liquid limit. The structure of the soil allows it to have a water holding capacity greater than the liquid limit. When the structure breaks down, the material will liquefy, resulting in a massive loss in strength. When testing soils with high liquidity indices, they may exhibit a well-defined yield stress under loading, though this is not always the case. Some sensitive soils have a strong structure that resists remoulding and failing under load, requiring significant energy to cause the structure to break down, and may not display a clear yield pressure on the strain graph. Understanding these properties is essential for evaluating soil performance in engineering applications (Wesley 2010; 2019).

Rocchi et al. (2017) investigated the influence of weathering on the physical and mechanical properties of igneous rocks and found that the presence of the relict rock structure provided additional strength which decreased with an increase in weathering. The study also found that weathering generally causes a decrease in grain size as rock minerals decompose to clays and silts which reduces the shearing resistance of the material.

Hu et al. (2023) provided a comprehensive review of soil structural vulnerability, with a focus on how soil compaction and aggregate breakdown influence soil functions and ecosystem services. A key factor affecting soil structural degradation is the pore network, which directly impacts soil functions like water and nutrient transport. The research proposes a model to clarify distinctions between susceptibility (inherent structural tendency to degrade), vulnerability (ability to resist stress under specific conditions), and risk (likelihood of degradation under real-world pressures). Soil structural condition is the measurement of the structure in-situ, and structural vulnerability is the possibility of the structure to alter due to external stresses. High resistance and resilience imply low vulnerability. The resistance reflects the ability of the soil to retain its structure when exposed to stress, namely continued weathering and the material being placed under load when the models are applied to completely weathered rock.

Obermeier and Langer (1986) found that highly decomposed completely weathered rock undergoes rapid weathering when exposed in an excavation, and the material can change from a medium hard rock to an extremely weak rock within 48-hrs. According to Hu et al. (2023) this material will be seen as having a high structure vulnerability. Townsend et al. (1969) and Saha et al. (2024) investigated the impact of destroying the soil structure and remoulding of soil samples have on the compressibility and strength of the material. Both studies found that breaking down the structure formed through pedogenic processes, results in a decrease in strength and an increase in compressibility.

Future research should concentrate on evaluating the connection between soil structural vulnerability and possible loss or changes in key soil functions indicators, such as the pore network and hydraulic conductivity.

Initially, the risk of soil structure degradation and the related changes in essential soil structure indicators, such as hydraulic properties based on pore networks, should be assessed, taking into account soil structural vulnerability (Hu et al. 2023).

4.6 Conclusion

The development of the weathering profile is mainly driven by chemical decompositions of the rock. The alteration of primary rock minerals will cause volumetric changes resulting in micro cracking forming. Therefore, chemical and physical weathering are closely linked and will occur simultaneously throughout the weathering process. Primary rock minerals tend to follow certain weathering series depending on the mineral's composition and intensity of weathering assuming the rock profiles are free draining. The chemistry of the material influences the unsaturated behaviour which is often not appreciated in geotechnics to the extent that the grain size distribution and macrostructure of the soil is. The chemical weathering indices can be used to quantify the degree or state of weathering for different lithologies to be used in a comparative assessment.

During the initial weathering stages of rock, the porosity that forms tend to be at the grain boundaries, cleavage planes or minerals surface defects. Thereafter, microcracks form due to various processes which increases the porosity and connectivity of the completely weathered rock. These cracks will continue to propagate and can be filled with clay minerals or sealed with Fe-oxides. Under intense weathering conditions the completely weathered rock will have a high structure vulnerability and may lose the structure and, therefore, the strength and pore network through external stresses such as rapid weathering or external loads.

The vulnerability and sensitivity of completely weathered rock and residual soil should be assessed and placing the material through a testing regime of traditional soil testing techniques. The degree of weathering of the samples can be quantified and compared through chemical weathering indices and be used to assess if there is a link between the state of weathering, which influences the structure, and the materials' behaviour.

The best way to characterise the weathered induced changes to the structure and chemical components is with the use of XRCT scans. Deducing the state of the structure in a weathering prolife and comparing it to results of traditional, well-understood, mechanical testing methods will allow for the comparative study to determine the alteration of the hydromechanical behaviour through weathering, and to determine the vulnerability of the soil to further degradation and sudden changes in the environment.

5 Materials and Methods

5.1 Overview

The selection of sample locations was guided by the necessity to find weathered rock profiles that included both residual soil and completely weathered rock near the surface, ensuring accessibility, analysis and sampling through conventional machine excavation methods, and existing manmade cuttings and excavations. The completely weathered rock needed to exhibit properties that would allow it to excavate as a silt. Consequently, the focus was placed on fine-grained igneous rock and dolomite rock, as the chemical weathering products from both rock types are often fine-grained soil. These lithologies were ideal because, through intensive weathering, most of the primary rock minerals either completely transformed into secondary minerals or dissolved, leaving behind pore spaces. This ensured that the relict rock structure was maintained without the influence of slightly weathered fragments or hard, altered, lineations formed during metamorphism.

The critical criterion was to avoid coarse-grained material or any slightly weathered rock fragments that might influence the rock's porosity or skew the mechanical properties of the silt-like material being studied. The rock profiles had to represent a consistent state of complete weathering to allow for accurate evaluations of hydraulic and mechanical properties. However, a significant challenge arose when trying to classify the excavated material as a silt on site. The *Guidelines for Soil and Rock Logging in South Africa* (2001) did not provide adequate techniques for identifying silt or mixtures of silt, sand, and clay, making the classification process ambiguous. The process, testing and findings to derive a testing methodology to be used on site to identify silt quantities in soil is discussed in Section 6.

The testing methods chosen for this research was aimed to investigate how the structure, which governs the porosity, changes through the weathering process and the implications it has on the material's mechanical strength and permeability across various lithologies. Undisturbed samples were taken at each sample location and wrapped and stored in a manner to minimise loss of moisture and alteration of the structure as far as practically possible.

An oedometer was chosen to assess the influence of the presence and absence of relict rock structure in completely weathered soil and pedogenic structure in residual soils due to its availability in industry, cost-effectiveness, and recommendation as stated in Wesley (1990; 2010). Placing the undisturbed material under load will assess the vulnerability of the material. The saturated permeabilities were tested in a triaxial cell. Every undisturbed sample tested, was remoulded back to in-situ density, as similarly as possible and retested under the same conditions. A change in the behaviour and testing results were expected due to the influence of remoulding (Townsend et al. 1969; Hu et al. 2023; Saha et al. 2024). The remoulding of the material and testing under the same conditions will test the materials sensitivity. The state of weathering for each sample was determined using appropriate chemical weathering indices and therefore chemical components needed to be determined.

For limited samples as will be discussed, the porosity and structure of the samples was visually assessed in 2D and 3D by means of the XRCT scan and associated software. The qualitative assessment was used to determine the state of chemical and physical conditions of the samples that was linked back to the degree of weathering.

The aim is to determine and compare the mechanical and hydraulic behaviour of samples taken from various weathering profiles and how the state of weathering, presence of relict rock or pedogenic structure, chemical constitutes, and pore geometry of the sample, influence the expected behaviour. A comparison is done with samples forming from the sample lithology and weathering profile, as well as samples from different lithologies in a similar state of weathering.

5.2 Locality

The study area spans the eastern escarpment and the western, central, and eastern Highveld regions, located across the North West, Gauteng, Mpumalanga, and Limpopo provinces. The top of the eastern escarpment represents an area where intensive chemical weathering and low erosion rates take place, and it is covered by a thin surficial transported horizon (Makhubela et al. 2021). This typical ground profile facilitates access to residual soil and completely weathered rock material for sampling and logging by in freshly excavated trial pits. Sample locations were selected based on expected bedrock geology, primarily dolomite and igneous rocks, and accessible weathering profiles.

The primary research and testing were conducted at the Tzaneen, R533, Dullstroom, Graskop, and Highveld sites. Data and sample material from these locations, as well as findings from Swart's (2019) study on dolomite weathering and its residual products, were incorporated into this study. The sampling objective was to collect completely weathered rock that breaks down and sieves into a silt-grade material. The field identification methods used to confirm the presence of silt is discussed in Section 6.

The sample locations, named after the nearest town, road, or suburb, are shown in Figure 5-1. The sampled geology is colour coded as shown in the legend.

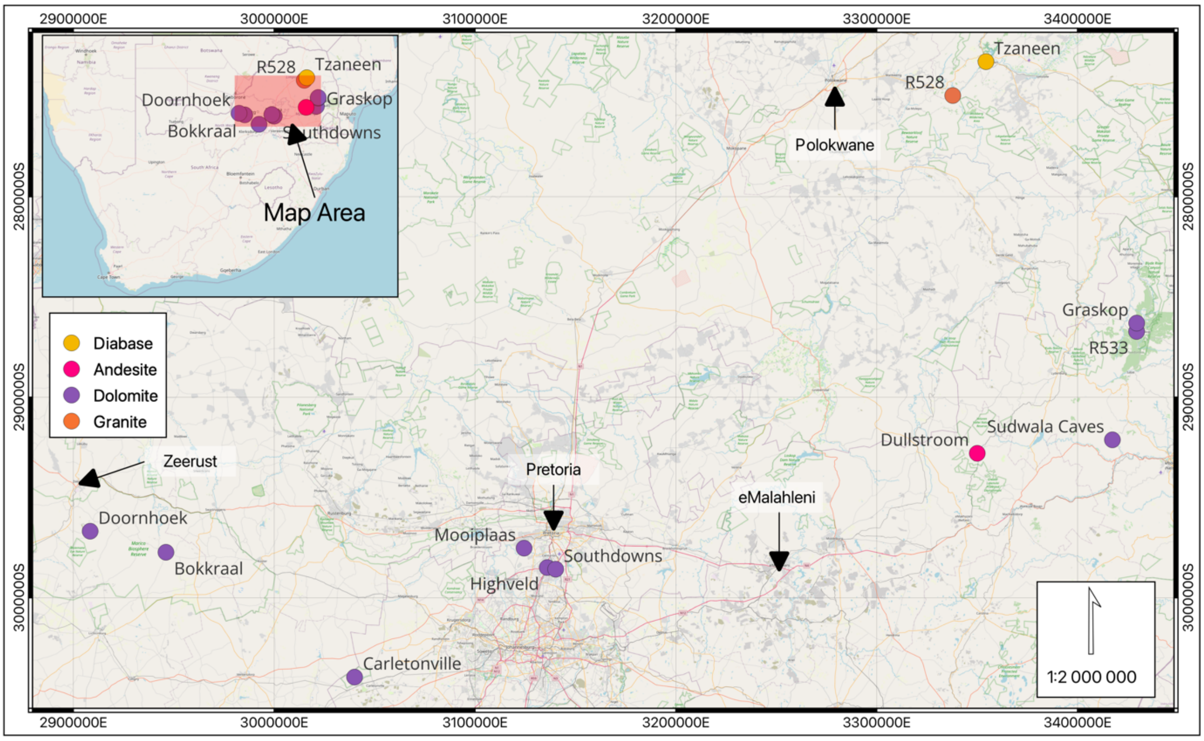

Figure 5-1 Locations for sample retrieval

5.3 Sampling

The exposed ground profile at each location was logged according to the methodology as stated in Dippenaar et al. (2024) and Swart et al. (2023). The ground profile was either exposed in existing, recently dug, borrow pits, or exposed by means of machine excavation using an industry standard Tractor Loader Backhoe (TLB) (model: JCB 3DX or similar).

This research occurred over several phases of site visits and sampling campaigns. It is such that not all samples went through the same testing methodology, however, were put through testing regimes that were appropriate considering the sample condition. Table 5-1 summaries the sample data and provides the sample identification (ID) to be used in this thesis. Table 5-2 summarises the testing methodologies conducted on the appropriate sample. Each test methodology is explained in Section 5.4.

Table 5-1 Summary of samples retrieved at each location

Location	Geology	Sample material description	Sample ID	Data Reference
Tzaneen	Diabase	Residual soil	2828	-
		Completely weathered rock	2829	-
R528	Granite	Residual soil	2830	-
		Completely weathered rock	2831	-
Dullstroom	Andesite	Residual soil	2842	-
		Completely weathered rock	1357	-
		Completely weathered rock	1354	-
		Completely weathered rock	2835	-
Graskop	Dolomite	Residual soil	2832	-
		Completely weathered rock (non-structured wad)	2833	-
Highveld		Completely weathered rock (structured wad)	2930	Swart (2019); Bester (2021)
		Completely weathered rock (structured wad)	2850	
		Completely weathered rock (structured wad)	2820	
		Completely weathered rock (structured wad)	2860	
		Completely weathered rock (structured wad)	2840	
		Completely weathered rock (structured wad)	2880	
		Residual dolomite	2870	
		Residual dolomite	2790	
		Residual dolomite	2730	
R533		Completely weathered rock (non-structured wad)	1510	Swart (2019)
Doornhoek		Completely weathered rock (non-structured wad)	1520	
Sudwala Caves		Completely weathered rock (non-structured wad)	1530	
Carletonville		Residual dolomite	1540	
Southdowns		Residual dolomite	1560	
Bokkraal		Residual dolomite	1570	
Mooiplaas		Residual dolomite	1580	

Table 5-2 Summary of sample types and testing conducted on the various samples

Sample ID	Geology	Sample material description	Test					
			FI	Oedometer	Chemical	Permeability	XRCT	SWRC
2828	Diabase	Residual soil	•	•	•	•	•	
2829		Completely weathered rock	•	•	•	•	•	
2830	Granite	Residual soil	•	•	•	•		
2831		Completely weathered rock	•	•	•	•		
2842	Andesite	Residual soil	•	•	•	•	•	
1357		Completely weathered rock	•				•	
1354		Completely weathered rock	•				•	
2835		Completely weathered rock	•	•	•	•	•	
2832	Dolomite	Residual soil	•	•	•	•	•	
2833		Completely weathered rock (structured wad)	•	•	•	•	•	
2930		Completely weathered rock (structured wad)	•	•	•			•
2850		Completely weathered rock (structured wad)	•			•		
2820		Completely weathered rock (structured wad)	•	•				
2860		Completely weathered rock (structured wad)	•	•				
2840		Completely weathered rock (structured wad)	•	•				
2880		Completely weathered rock (structured wad)	•			•		
2870		Residual dolomite	•	•				
2790		Residual dolomite	•	•				
2730		Residual dolomite	•			•		
1510		Completely weathered rock (non-structured wad)	•		•			
1520		Completely weathered rock (non-structured wad)	•		•			
1530		Completely weathered rock (non-structured wad)	•		•			
1540		Completely weathered rock (non-structured wad)	•		•			
1560		Residual dolomite	•		•			
1570		Residual dolomite	•		•			
1580		Residual dolomite	•		•			
Notes:	FI – Foundation Indicator; XRCT – X-Ray Computed Tomography; SWRC – Soil Water Retention Curve							

5.4 Testing methodology

5.4.1 Particle size analysis and Atterberg limits

The samples underwent particle size analysis according to SANS 3001 GR1 (2013). The Atterberg limits testing was conducted using the one-point method as stated in SANS 3001 GR10 (2013). These two tests combined is commonly referred to in South Africa as a Foundation Indicator (FI) test. In this standard the liquid limit (LL) and plastic limit (PL) are determined using the Casagrande cup and the thread rolling method, respectively. The Atterberg limits testing was duplicated to ensure accurate readings were achieved. The laboratory Unified Soil Classification System (USCS) description was determined as stated in the ASTM D2487 – 17e1(2020).

5.4.2 Oedometer testing

One-dimensional consolidation testing is widely used and is seen as a fundamental soil behaviour test. The oedometer test applies a series of predetermined loads onto the sample and the deformation response is measured. The consolidation of a soil is dependent on its stress history, density, and porosity (Terzaghi 1943). Wesley (1990; 2010) recommends using the oedometer as a compression test to assess the fabric of residuum. The oedometer was chosen due to the availability in industry compared to the triaxial shear testing equipment at the time of writing this thesis. Lead times were more than 6 to 8 months and undisturbed samples were desiccated when removed from wrapping after standing for this period.

Humans frequently use the completely weathered rock in a profile as a founding medium and will apply loads that may or may not cause deformation to take place. Furthermore, the completely weathered rock is often ripped and recompacted at the founding level thereby changing the density and porosity. The change in volume will impact the porosity value and therefore flow characteristics of the soil and completely weathered rock profile.

Undisturbed samples were placed in an oedometer to undergo a one-dimensional consolidation test guided by the method stated in the BS 1377-5 (1990) code. These samples underwent a full compression test before the material was removed and remoulded to destroy any remaining soil structure. The remoulded soil material was placed back into the oedometer cell and compacted to achieve the in-situ density. The remoulded porosity values and moisture content was brought as close as practicably possible to the in-situ values, however, due to the loss in structure, this was not always achievable. Therefore, the in-situ density value was governing parameter for the remoulded sample condition. The behaviour of the undisturbed and disturbed samples was assessed and compared in this study.

Bester (2021) sampled and tested material from the same profile encountered at the Highveld site, and these results were used to supplement the testing regime conducted on the material. Therefore, no samples from this site underwent remoulding and only the in-situ condition of the material was tested.

The interpretation of the oedometers was guided by the recommendations as stated in Wesley (2019). No attempt was made to determine the pre-consolidation pressure or over consolidation ratio. The material formed through weathering and leaching of rock and not by consolidation of sediments under load. Therefore, the above-mentioned parameters do not apply to the material and can be misinterpreted due to the log stress curve. Therefore, the data taken from the oedometer test results will be plotted on a linear stress strain curve to assess the compressibility of the soil (Wesley 1990; 2010; 2019).

The coefficient of volume compressibility (m_v) is defined as the volume change per unit volume per unit increase in effective stress. It defines the ratio of volumetric strain to applied stress of a soil and is the inverse of soil stiffness. Soil stiffness is also termed the constraint modulus (E'_{oed}) and is defined by Equation 5-1 (Knappett et al. 2012).

$$E'_{oed} = \frac{1}{m_v} = \left(\frac{\mathrm{MN}}{\mathrm{m}^2}\right) = \mathrm{MPa} \qquad \textbf{5-1}$$

The m_v value was used to quantify the stiffness the soil structure provided to the sample in the undisturbed state. It was also used to compare the difference in compressibility of the samples before and after remoulding.

5.4.3 Triaxial Permeability

The permeability values of the samples were tested according to the methodology as stated in BS 1377-6 (1990) code. The samples were statured and placed under a confining pressure of 100 kPa and allowed to consolidate before the test was conducted. To ensure the testing methodology was normalised between samples the consolidation pressure was limited to 100 kPa to ensure the sample does not yield and undergo any significant loss of pores structure. Determining the permeability values for heterogeneous soils is extremely challenging and highly dependent on the scale of the samples and the representative elementary volume (REV) being tested (Koestel et al. 2020). The purpose of testing permeability was not to establish a definitive value for each material type but rather to investigate how the weathering state within a profile and the disturbance of the in-situ structure influence the results. The difference in strain experienced during the consolidation between the samples was used to assess the vulnerability of the undisturbed samples and sensitivity of the material when remoulded.

The samples underwent falling head tests due to the material grading as mostly silt and clay and lesser sand. Each sample were cut into a cylindrical specimen capped by porous disks and enclosed in a flexible membrane to prevent lateral leakage. The test involved applying a hydraulic gradient of 10 kPa, and the reduction in water head over time was measured to calculate the coefficient of permeability.

The Tzaneen, Dullstroom, R533 and Graskop undisturbed and remoulded samples underwent permeability testing. The testing data for Highveld samples, and the Doornhoek, Bokkraal and Mooiplaas samples were retrieved from Bester (2021) and Swart (2019), respectively. Therefore, these samples were only tested in the undisturbed state.

5.4.4 XRF and XRD

The chemical compositions of each sample were determined by means of an x-ray fluorescence

(XRF) spectroscopy which provides the elemental composition. X-ray diffraction (XRD) analyses were undertaken to provide information on the unit cell dimensions of the crystalline material in the soil

The Bokkraal, Mooiplaas and Doornhoek samples were determined at the University of Pretoria X-Ray Analytical Facility housed in the Stoneman Building. The remainder of the samples were tested at UIS Analytical Services in Centurion. The samples from each locality were milled and prepared in the laboratory.

The former XRF samples were analysed using the ARL Perform'X Sequential, and the latter using the ARL ADVANT'X Series, XRF instruments and Quantas software. The XRD samples were prepared according to the standardized Panalytical back loading system, which provides nearly random distribution of the particles. The samples were analysed using a PANalytical X'Pert Pro powder diffractometer in θ–θ configuration with an X'Celerator detector and variable divergence- and fixed receiving slits with Fe filtered Co-Kα radiation (λ=1.789Å). The phases were identified using X'Pert Highscore plus software. The relative phase amounts (weight%) were estimated using the Rietveld (1969) method.

5.4.1 X-Ray Computed Tomography

The sampling methodology for X-Ray Computed Tomography (XRCT) samples comprised undisturbed block and tube samples. The tube samples, taken at Dullstroom and Graskop, were retrieved by pushing a PVC pipe (30.0 mm x 150.0 mm) into the sidewall of a freshly dug test pit. These tube samples were wrapped and caped to ensure minimal loss of moisture. At the Tzaneen site, the tubes refused on the sidewall surface and therefore, undisturbed block samples were retrieved and were wrapped in plastic and waxed appropriately to ensure moisture loss was minimal before being tested in the laboratory. Materials such as tin foil and other metals cannot be used as wrapping because these materials will distort the x-rays passing through the sample.

The tube samples were scanned at X-Sight X-Ray Services by means of their Nikon XT H225 ST system. The scans were conducted at 180 kV and 330 uA where approximately 2985 images were acquired of each sample while the samples rotated a full 360 degrees. Two-dimensional (2D) and three-dimensional (3D) slices were constructed using the Phoenix Datos acquisition and reconstruction software. The software processing focused on the sample material only and excluded a 2.00 mm space between the sample material and the tube's inner wall and 2.00 mm at the top and bottom portion of the sample. This was done to exclude areas where displacement and density alteration would have occurred at the sample and tube interface during sample retrieval. The density contrast and pore space analyses were performed with use of VOLUME GRAPHICS (VG) STUDIO MAX software.

As discussed in Section 2, the behaviour of porous material is dependent on the 3D pore geometry and connectivity, which is directly linked to the parent rock and weathering intensity as discussed in Section 4. The purpose of obtaining images using the XRCT scanner was to characterise the pore space orientation and size distribution, and the persistence of the relict rock structure and infill material of undisturbed samples.

The scan could be done with no sample preparation, which ultimately preserves the structure and minerals from deforming or alternating during drying or saturation which is required in other imaging techniques.

After the tubes were scanned, the PVC pipes were cut open to assess the macro-relict-rock-structure. The same was done for the block samples. Finally, all samples were oven-dried to calculate the natural moisture content and dry density.

5.4.2 Soil Water Retention Curve

The influence of the highly porous, relict rock structure, observed in the wad sample (2930) retrieved at the Highveld site was tested by recording the suction pressures in both an undisturbed and remoulded state. The pore pressure tensiometer (PPT), as described by Jacobsz (2018), was used to measure two drying curves in each sample, respectively. This testing methodology and testing results have been discussed in Swart et al. (2021).

The tested structured specimen was cut from the undisturbed block sample and placed in a ring and saturated using de-aired water. The spoil after cutting the structured specimen was taken and the macro-structure was further broken down with a rubber spoon. The spoil was air dried and remoulded to fit the testing ring as close as practicably possible to the in-situ density. The remoulded specimen was brought to approximately full saturation using de-aired water. The measurement of the Soil Water Retention Curve (SWRC) for both samples took place along a drying path, starting close to saturation, and ending at the point of cavitation of the PPT.

A description of the tensiometer design is provided by Jacobsz (2018). The testing procedure implemented, referred to as the continuous tensiometer approach has been described by Gaspar et al. (2019). The PPT has been proven to accurately measure suctions in excess of 500 kPa (Jacobsz 2018). A datalogger and an electronic scale was used to record the change in suction and mass of the samples at a logging rate of 5 and 1 second intervals, respectively.

5.5 Conclusion

The methodologies outlined in this chapter were designed to comprehensively assess the hydraulic and mechanical properties of completely weathered rock and residual soil focusing on the influence of weathering on their physical, chemical, and structural characteristics. The detailed sampling strategy ensured that material representative of various weathering profiles was selected, while the combination of completely weathered rock and residual soils allows for in-depth investigations into the behaviour of these materials under varying conditions.

The integration of standardised testing, including oedometer and permeability testing, and advanced testing methods, namely XRCT imaging and SWRC, provides a robust framework to evaluate key properties such as porosity, strength, and permeability.

The use of remoulded and undisturbed samples enables a comparison of the materials' sensitivity to structural disruption, further enhancing our understanding of their response to mechanical loading and fluid flow.

These methodologies set the foundation for subsequent chapters, where the results from these tests will be presented, analysed, and discussed in relation to the study's objectives. By systematically linking the testing outcomes to weathering states, lithology, and relict structure, this research aims to contribute to the broader understanding of completely weathered bedrock behaviour in engineering and geotechnical context.

6 Field Identification of Silts

As mentioned in Section 5.1, a first phase site visit was conducted to develop a methodology to more precisely identify silt and mixtures of silt, sand, and clay in the field. The field identification techniques used in this study relied on the use of water, working hands, and common stationery brought to the site. This hands-on approach enabled the author to refine the classification of silts and mixtures of fine-grained materials to a maximum of 2.00 mm grain size, overcoming the limitations of existing standards. By implementing these methods in the field, we were able to accurately categorize materials for further testing and analysis without the need for in-situ or laboratory equipment on site.

This work is discussed and published in Swart et al. (2023) and is now referenced in the latest South African soil and rock description guidelines as the gold standard in texture identification on site (Dippenaar et al. 2024). The literature review and methodology will briefly be explained, and the detailed literature review and methodology can be obtained in Swart et al. (2023). The detailed methodologies for the laboratory testing have been explained in Section 5.

6.1 Literature review for soil texture determination

Natural soils are typically highly complex due to the wide ranges of textures possible and the presence of minerals with reactive surfaces. Soil classifications typically assume the sand and silt grain surfaces are inert, and plastic behaviour only originates from the clay portion. To effectively classify soil into a material type, more than one parameter or test result, is needed. Many authors discussed the difficulties in determining the silt and clay percentages using the hydrometer method. Therefore, authors have proposed to class soils based on their plastic behaviour, mineralogy and the grading, rather than the quantities of individual grain sizes only. (Savage 2007; Stott and Theron 2016; Moreno-Maroto and Alonso-Azcárate 2022; Swart et al. 2023)

The mechanical sieving to determine the gravel and sand percentages of a sample is usually simple and effective. However, when sampling completely weathered rock that excavates as a soil with weathered rock fragments present, the final sieving analysis results are dependent on the energy applied and methodology used during the sample preparation (Rabot et al. 2018; Swart et al. 2023).

The plastic behaviour is based on the Atterberg limits which determines the changes in material characteristics with a change in water content. From the grading results of the mechanical sieve and plasticity determined, a soil sample can be grouped using the Unified Soil Classification System (USCS).

The components of a fine-grained soil (fine sand, and silt) and the plasticity and quantity of clay material can be determined when using a series of field tests as described by Burmister (1949), Hunt (2005) and Norbury (2020), and as stated in ASTM D2488-09a (2009). The existing field tests recommend that the medium sand and coarser particle grains are removed before conducting the tests. Most natural soils, especially residual soils, comprise varying quantities of clay, silt, and fine to coarse sand, and therefore this preparation step cannot be practically done on-site.

The field tests are based on well understood characteristics and behaviours of a pure clay, silt, and fine to medium sand. A principal characteristic of clay is the high plastic behaviour that even a fat silt will not express. Silts are able to possess very slight plastic behaviour, but deform and typically dilate during deformation (Paniagua et al. 2013). Silts also tend to hold onto water though capillary tension where the clays do so with adsorption and capillary tension. Medium sands cannot hold onto water through either mechanism, and possesses no plastic behaviour.

This researched aimed to produce a methodology that uses the known reactions with changes in water content and loading to determine the soil texture. These methodologies should be used on soils with a particle size up to 2.00 mm. These tests should not need extra equipment and should only require a small amount of water (Swart et al. 2023).

6.2 Sample localities and testing methodology

To ensure the proposed methodology is thoroughly tested, a large amount of sample material was required comprising mainly silt mixtures of natural soils. Existing road cuttings allowed for easy sampling of material from weathering profiles forming in the Magoebaskloof-Tzaneen and Dullstroom-Mashishing areas. The sampled material retrieved formed from parent rock of the Duivelskloof Leucogranite, Turfloop Granites, and Dullstroom Formation. The sample locations are presented in Figure 6-1.

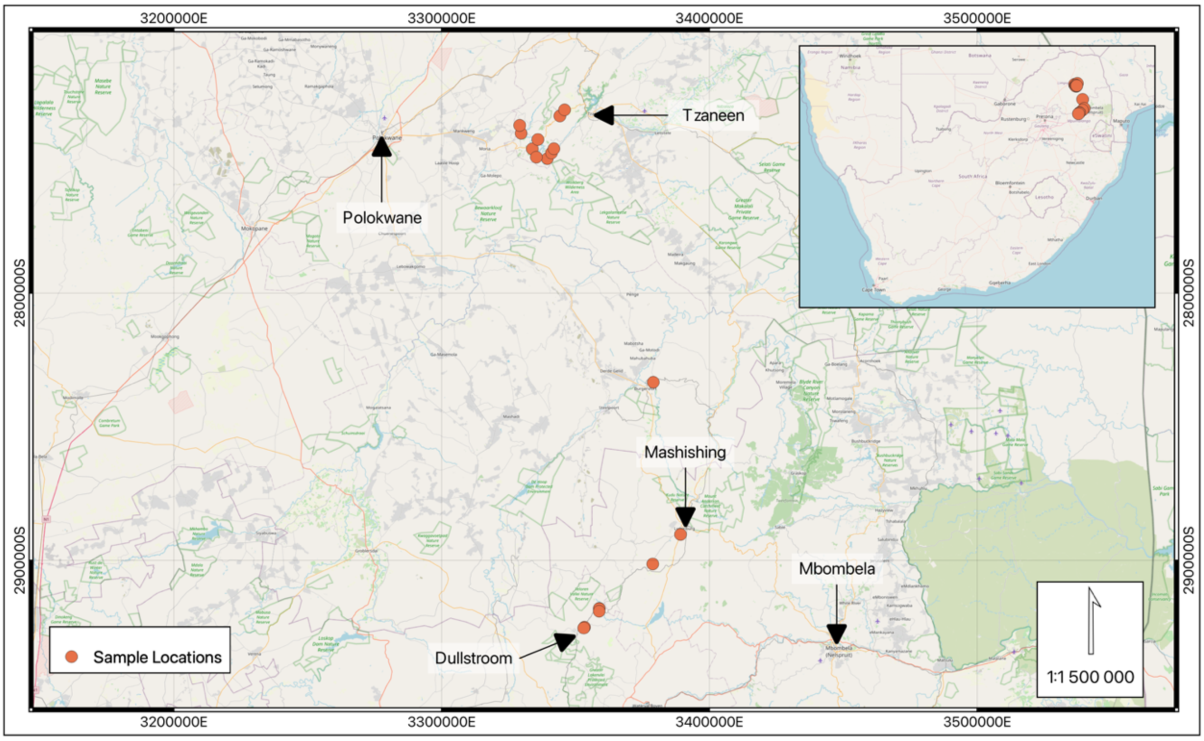

Figure 6-1 Sample points for field identification testing

All sampled material were placed into bags and transported to a single testing location. All the material was air dried and broken down using a rubber hammer to ensure all soil structures have been broken down. This was done to ensure all the materials are silt mixtures with varying quantities of clay and sand.

The Atterberg limits and soil grading were measured according to the testing procedure outlined in the SANS 3001 series, as described in Section 5.4.1.. Due to the uncertainties of the hydrometer test, these results were supplemented with the visual inspection of the soil grains using a stereomicroscope and a Scanning Electron Microscope (SEM).

A stereomicroscope is an optical microscope (model: Zeiss Stereo Discovery V20) designed for low magnification for observation of a sample's inter-particle relation, and shape and size of grains, using reflected light from the surface. The samples were analysed at various magnifications, and photographs of the most representative sections of the samples were taken. Undisturbed samples were oven-dried before being examined in the laboratory.

The soil grains of disturbed samples were observed using a Zeiss Gemini SEM under different magnifications best suited for the material. The SEM scans the material surface with the use of a focused beam of electrons, producing an image revealing the surface topography. Investigating the microscopic structure of the soil grain may build an understanding of the sample grading and typical minerals present.

Sample preparation includes oven-drying samples before being placed on a sticky carbon disk. The material was coated with a layer of carbon to create a conductive surface on the soil sample. Thereafter, the sample was placed in a vacuum within the SEM equipment and the sample was analysed. The preparation process essentially renders the sample as disturbed.

The samples were tested using chemical analysis techniques, namely X-Ray Fluorescence Spectroscopy (XRF) and X-Ray Diffraction (XRD). These tests were done to determine the influence mineralogy has on the plasticity.

Included in this study are samples of the Salnova Formation retrieved from an open excavation near Gqeberha, South Africa. These samples did not undergo as rigorous testing as the samples discussed above, however it is included to show how the influence of soluble salt content impacts on the particle size analysis, namely the hydrometer test results (Picornell et al. 1990; Lorefice and Malengo 2006; Wuddivira et al. 2023). These samples, as will be discussed, do not grade as a silt mixture but illustrates the importance for the need to have more than one soil classification methodology during an investigation.

6.3 Field tests

The guidelines and methodologies for each field test discussed here has been published in Swart et al. (2023). The description and methodology of these tests have been excluded from this thesis. The methods are stated in a factual manner and to change the descriptions would be to change the possible results. For all the detailed testing procedures, refer to Swart (et al. 2023).

Table 6-1 has been included and shows the range of results for each inferred soil class. Once all the testing has been done, the results are compared to each table column. The column with the highest results is therefore the soil texture and inferred soil class.

Table 6-1: Identification table for inorganic, fine to coarse grained, soils from field tests (Swart et al. 2023)

Inferred USCS class	CH	CL, MH, CL-ML	MH, ML, CL-ML	ML	SC, CL	ML	SC, SW-SC, SP-SC	SM, SW-SM, SP-SM	SW, SP
Texture	CLAY	Silty CLAY	Clayey SILT	SILT	Sandy CLAY	Sandy SILT	Clayey SAND	Silty SAND	SAND
Test	Soil response								
Dilatancy	None	None to slow	Slow	Slow to rapid	Slow to none	Rapid, weak ball formed with some difficulty	Slow to rapid	Rapid, weak ball formed with difficulty	Rapid or material to coarse for test. Weak ball formed with difficulty
Ball pickup / drop	-	-	-	-	Readily picked up between finger and thumb	Readily picked up between finger and thumb (breaks after more than 3 drops)	Readily picked up between finger and thumb	Picked up with difficulty, breaks when picked up after drop (~20% silt). Picked up readily, breaks after few (~3) drops (35 - 50% Silt)	Medium to fine sand forms weak ball. Cannot be picked up. Medium sand only cannot form ball
Thread pickup	Readily picked up at <3 mm diameter	Readily picked up at 5 mm diameter to picked up with difficulty at 3 mm	Readily picked up at 5 mm diameter to picked up with difficulty or breaks at at 3mm	Picked up with difficulty or cannot be picked up at 5 mm	Readily picked up at 5 mm	Breaks, cannot be picked up at 5 mm	Picked up with difficulty or cannot be picked up at 5 mm	Only thread >5 mm can form. Breaks, cannot be picked up	-
Plasticity	High	Medium	Low	Non-plastic	Low to medium	Non-plastic	Low to non-plastic	Non-plastic	-
Toughness	High	Medium	Low to medium	Low or thread cannot be formed	Medium	Very low	Low or thread cannot be formed	Very Low or thread cannot form	-
Dry Strength	High to very high	Medium to high	Low to medium	None to low	Low to high	None to very low	None to low	None to very low	-
Feel	Smooth, sticky (when wet)	Smooth and slightly sticky; possible chance of slight gritty sound	Silky to smooth, sounds slightly gritty	Silky, sounds gritty	Smooth with slight 'sand paper feel', slightly gritty	Sliky with slight 'sand paper feel', gritty	Smooth to sliky with gritty feel	Gritty, sandy	-
Behaviour in air	Dries slowly with shrinkage	Dries slowly with shrinkage	Dries quickly, brushes off	Dries quickly, brushes off	Dries slowly with shrinkage	Dries quickly, brushes off	Dries quickly, brushes off	Dries rapidly, brushes off	-
Cohesion	Deforms without rupture.	Deforms without rupture. Maintains shape during handling	Rupture	Rupture. Difficult to shape when very dry	Deforms, rupture possible. Maintains shape during handling	Rupture. Difficult to shape when dry	Rupture. Difficult to shape when very dry	Rupture. Difficult to shape when dry	-
Drain test	Maintains moisture during handling. No moisture front	Maintains moisture during handling. Very small mositure front	Moisture drains slightly during handling. Small mositure front	Moisture drains readily during handle. Moderate moisture front	Maintains moisture during handling, small mositure front possible.	Moisture drains quickly during handling. Moderate to large moisture front	Moisture drains slightly during handling. Small mositure front.	Moisture drains rapidly. Large water front.	-

6.4 Results

Most of the samples were retrieved from existing road cuttings along the eastern escarpment of South Africa. The sample material was generally desiccated residuum and completely weathered rock. The ground profiles were logged and photographed by the author with a typical photograph presented in Figure 6-2.

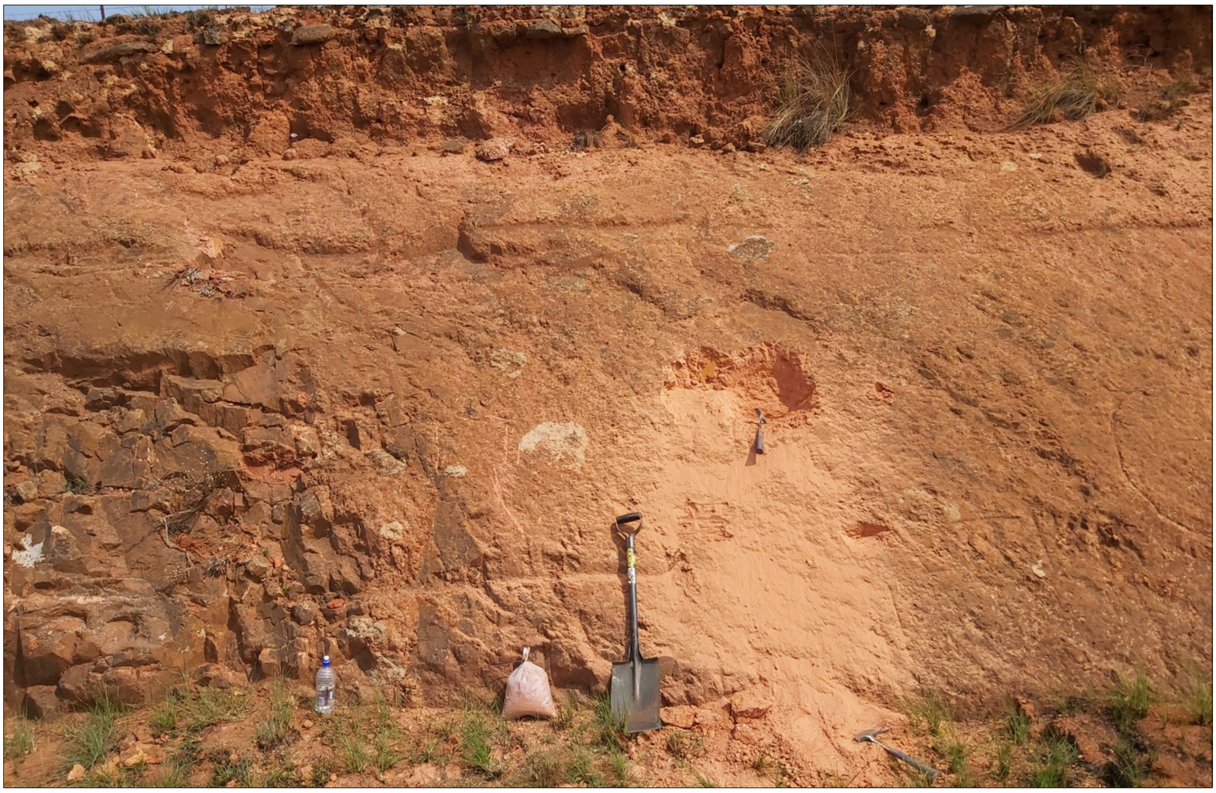

Figure 6-2 Typical sampled and logged road cutting profile (photograph taken by D Swart)

Two (2) samples, namely 686 and 687, were taken from a test pit dug in the Salnova Formation are beach, nearshore and estuarine in origin and comprises varying levels of salinity (Hassan et al. 2022). These sample underwent only sieve, hydrometer and Atterberg limits testing. However, these sample test results are included in the study to illustrate the impact of soluble salt contamination of the hydrometer solution can skew clay content results. A photograph taken of the, excavated and sampled, silty sand is presented in Figure 6-3.

Figure 6-3 Excavation spoil from the Salona Formation comprising silty sand in a dry state (photograph taken by D Swart)

6.4.1 Soil grading and Atterberg limits

The particle size percentages (%), Atterberg limits test results, and the laboratory assigned USCS classes for each sample are summarised on Figure 6-4. Moreno-Maroto and Alonso-Azcárate (2018, 2022) proposed the use of the *clay factor* which is the ratio of plasticity index (PI) and the liquid limit (LL) (i.e. PI/LL), which is an indicator of clay characteristic in the soil. Soils with values greater than 0.50 indicate the presence of plastic clays; values between 0.33 and 0.50 indicate moderate to slightly plastic behaviour in soils made up of clay, silt, and sand; and values less than 0.33 suggest the soil comprises silts and sand with low to non-plastic behaviour. The clay factor and summary of particle size for each sample is presented in Figure 6-5.

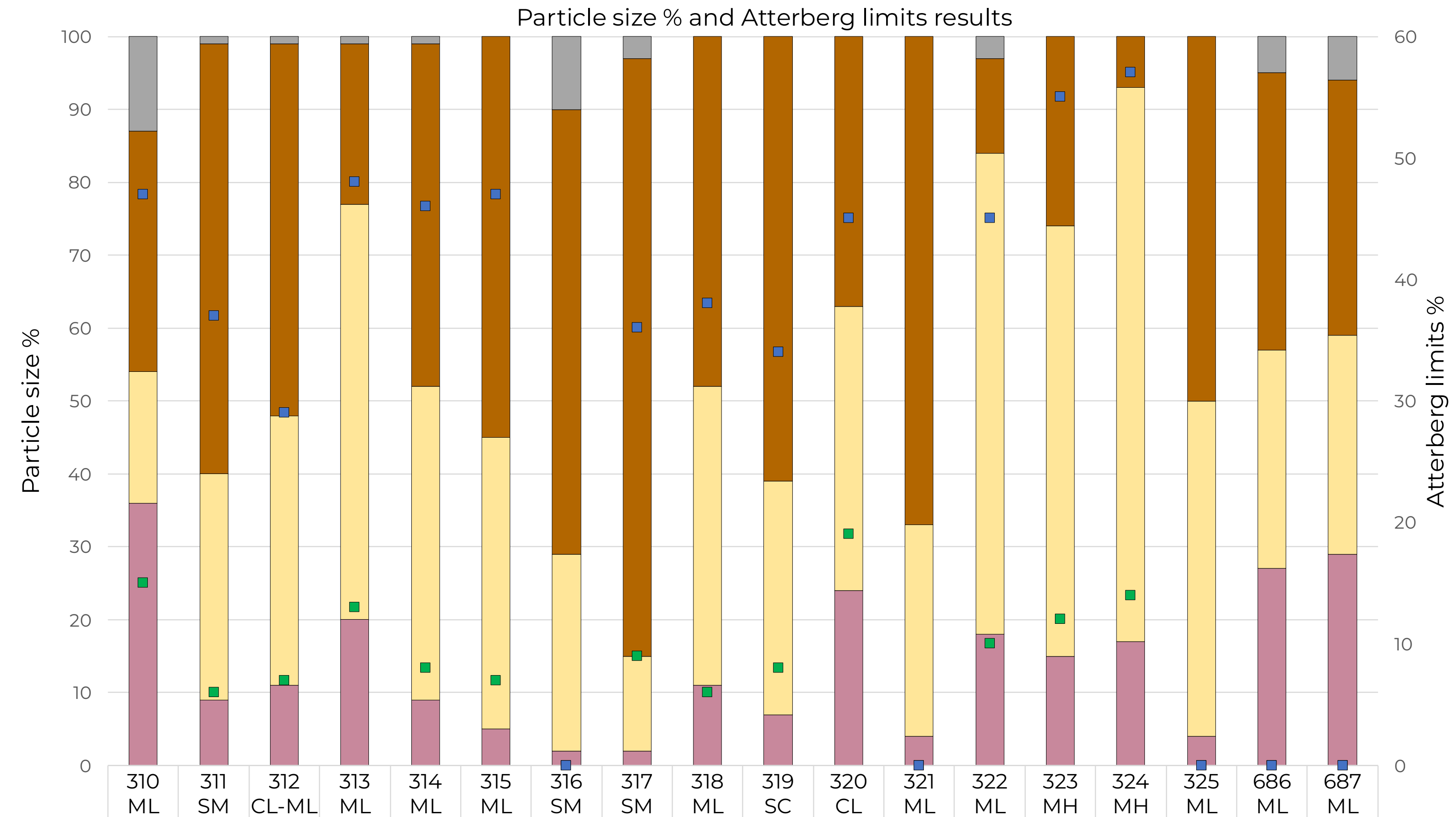

	310 ML	311 SM	312 CL-ML	313 ML	314 ML	315 ML	316 SM	317 SM	318 ML	319 SC	320 CL	321 ML	322 ML	323 MH	324 MH	325 ML	686 ML	687 ML
■ Gravel	13	1	1	1	1	0	10	3	0	0	0	0	3	0	0	0	5	6
■ Sand	33	59	51	22	47	55	61	82	48	61	37	67	13	26	7	50	38	35
■ Silt	18	31	37	57	43	40	27	13	41	32	39	29	66	59	76	46	30	30
■ Clay	36	9	11	20	9	5	2	2	11	7	24	4	18	15	17	4	27	29
■ Plasticity Index	15	6	7	13	8	7	0	9	6	8	19	0	10	12	14	0	0	0
■ Liquid Limit (%)	47	37	29	48	46	47	0	36	38	34	45	0	45	55	57	0	0	0

Figure 6-4 Summary of soil grading

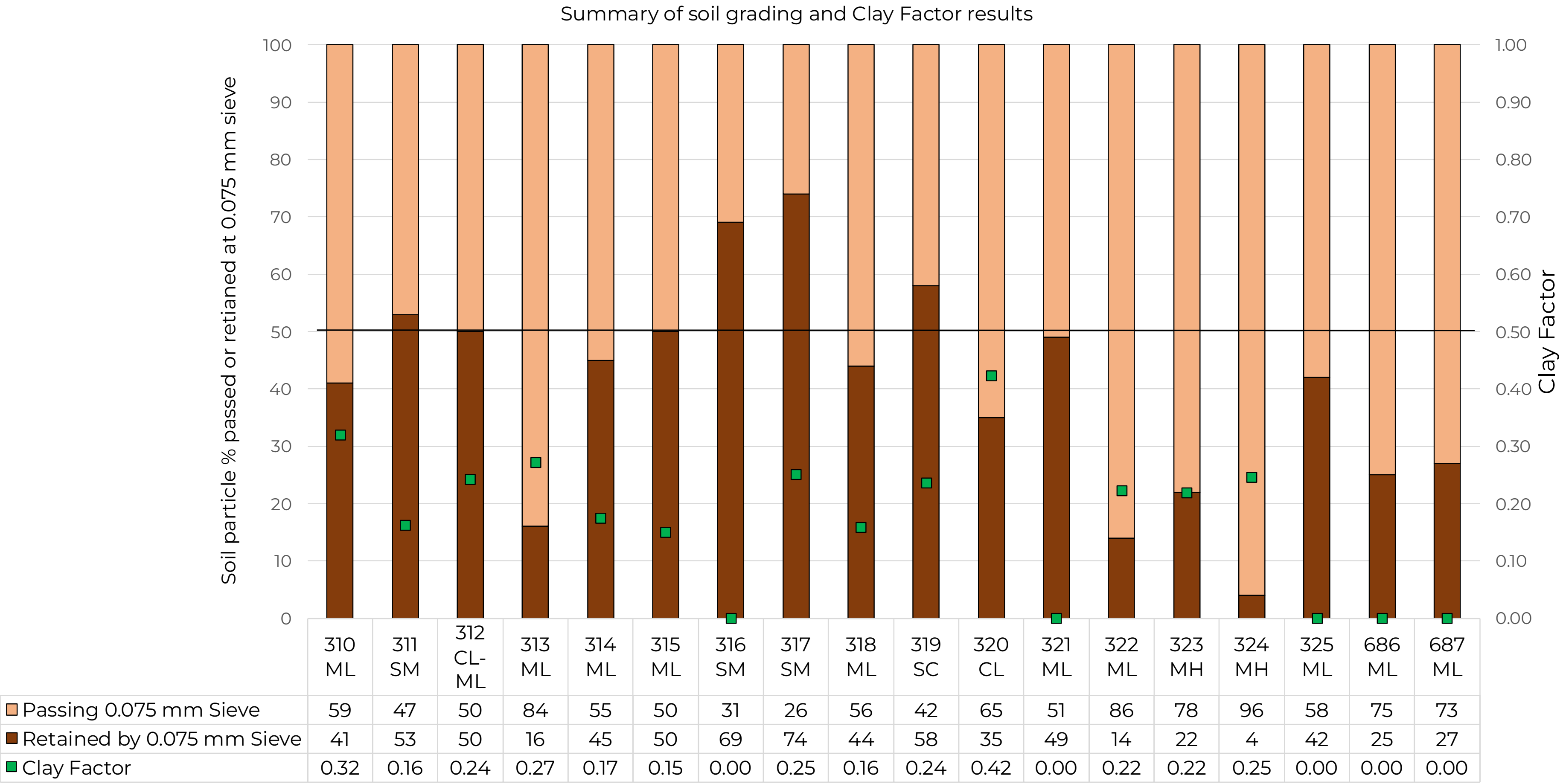

	310 ML	311 SM	312 CL-ML	313 ML	314 ML	315 ML	316 SM	317 SM	318 ML	319 SC	320 CL	321 ML	322 ML	323 MH	324 MH	325 ML	686 ML	687 ML
🟧 Passing 0.075 mm Sieve	59	47	50	84	55	50	31	26	56	42	65	51	86	78	96	58	75	73
🟫 Retained by 0.075 mm Sieve	41	53	50	16	45	50	69	74	44	58	35	49	14	22	4	42	25	27
🟩 Clay Factor	0.32	0.16	0.24	0.27	0.17	0.15	0.00	0.25	0.16	0.24	0.42	0.00	0.22	0.22	0.25	0.00	0.00	0.00

Figure 6-5 Summary soil particle % passing or retained at 0.0 75 mm sieve and clay factor test results

6.4.2 *XRF and XRD results*

The XRF results revealed the samples are generally made up of SiO_2 and Al_2O_3, typical of highly weathered soils, and lesser MgO, Fe_2O_3 and K_2O. The XRD test results are presented in Figure 6-6. The samples are generally made up of quartz and kaolinite which is typical of deeply weathered residual soils that formed from felsic bedrock. Varying quantities of original parent rock minerals, such as muscovite, microcline, albite and rutile, still exist in the soil, and these are expected to occupy the silt and sand portions of the soil. Gibbsite, hematite, and goethite are typical of highly weathered soils and are expected to occupy the clay portion of the soil and as surface coating of silt and sand size particles.

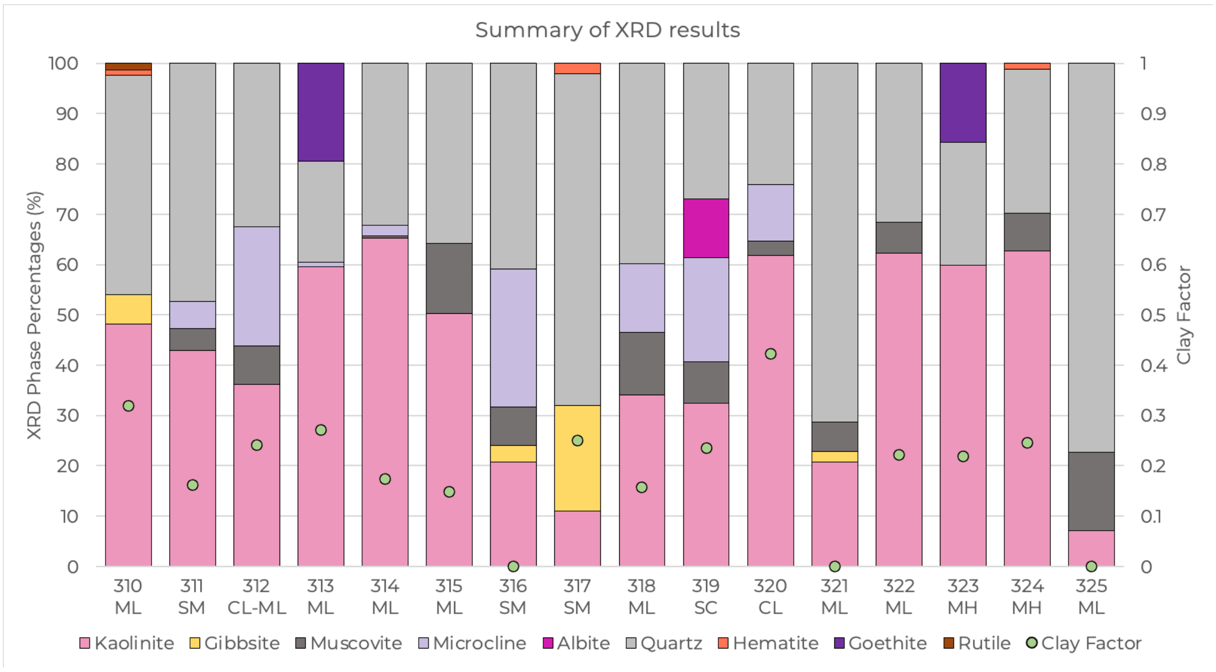

Figure 6-6 Summary of XRD results and clay factor

6.4.3 *Stereomicroscope*

Each soil sample was visually analysed to support the findings of the laboratory and field-testing results. This was done by qualitatively examining the coarse silt to sand particle size distributions, which minerals exist as either a silt or sand, and the possible surface coating of the sand and silt particles. Photographs taken of representative samples indicates all the soils are dominantly made up of silt, clay, and fine sand material. The silt and sand are mainly quartz grains and other rock forming minerals such as microcline and muscovite, and they are typically coated by clay minerals (kaolinite) and metal oxides creating a reddish hue. Figure 6-7 shows a photograph taken of typical grains found in the residual soils formed from felsic bedrock. Figure 6-8 shows a photograph of a highly weathered soil sample that has undergone pedogenic alteration with relatively large amounts of metal oxides.

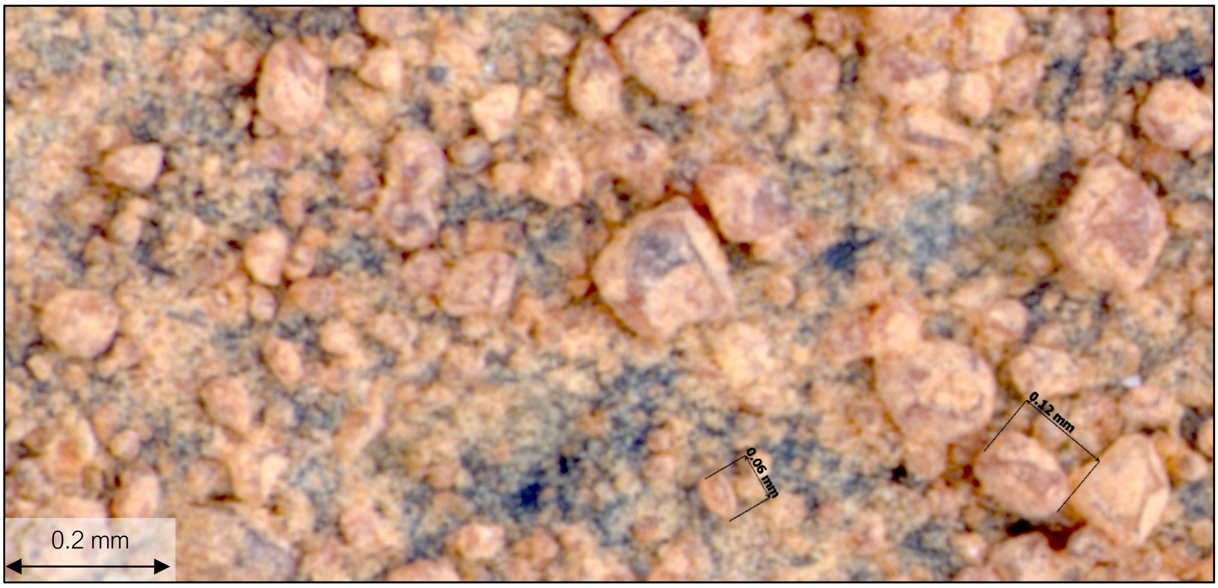

Figure 6-7 Photograph taken of sample 311 particles comprising kaolinite and quartz (photograph taken by D Swart)

Figure 6-8 Photograph taken of sample 310 comprising metal oxides nodules and coating (photograph taken by D Swart)

6.4.4 SEM

Similar to the stereomicroscope, the SEM was used to qualitatively assess the soil grains in the clay and silt portions of the samples. Figure 6-9 and Figure 6-10 present scans taken at high-magnification and it shows that the fine-grained portion of the soil comprises an assemblage of kaolinite clays and other similar clays.

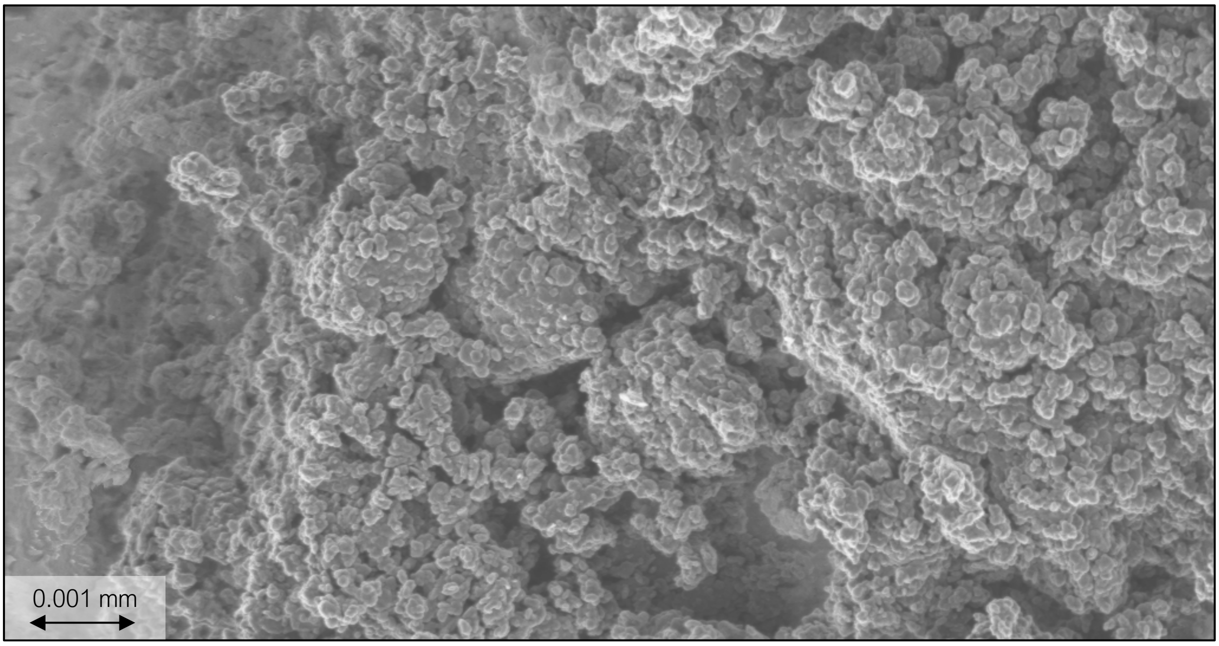

Figure 6-9 Scan taken at 11.27K magnification (photograph taken by D Swart)

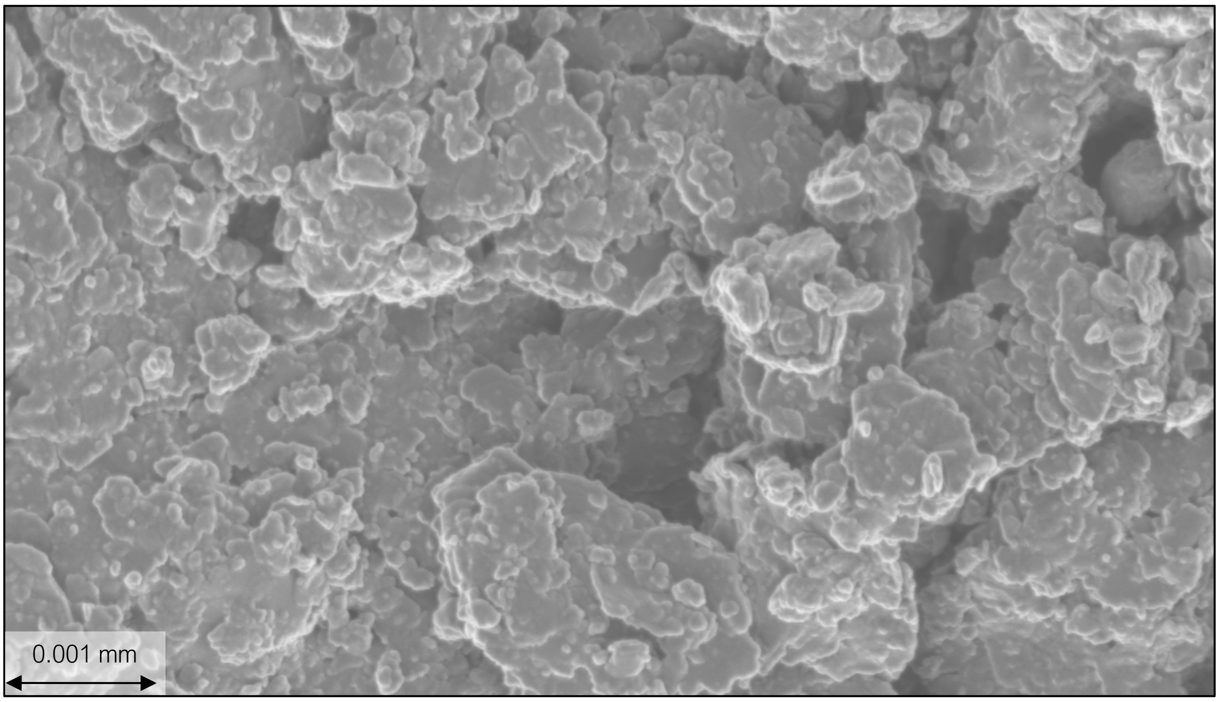

Figure 6-10 Scan taken at 14.61K magnification (photograph taken by D Swart)

6.4.5 Field test results

Every sample underwent all recommended field tests described in Section 6.3 and the response of each sample during all tests were documented and photographed. Figure 6-11, Figure 6-12 and Figure 6-13 show the range of typical test responses of a SM, ML and CL soil, respectively. The soil threads presented in the photographs are the thinnest thread that could be rolled for that sample.

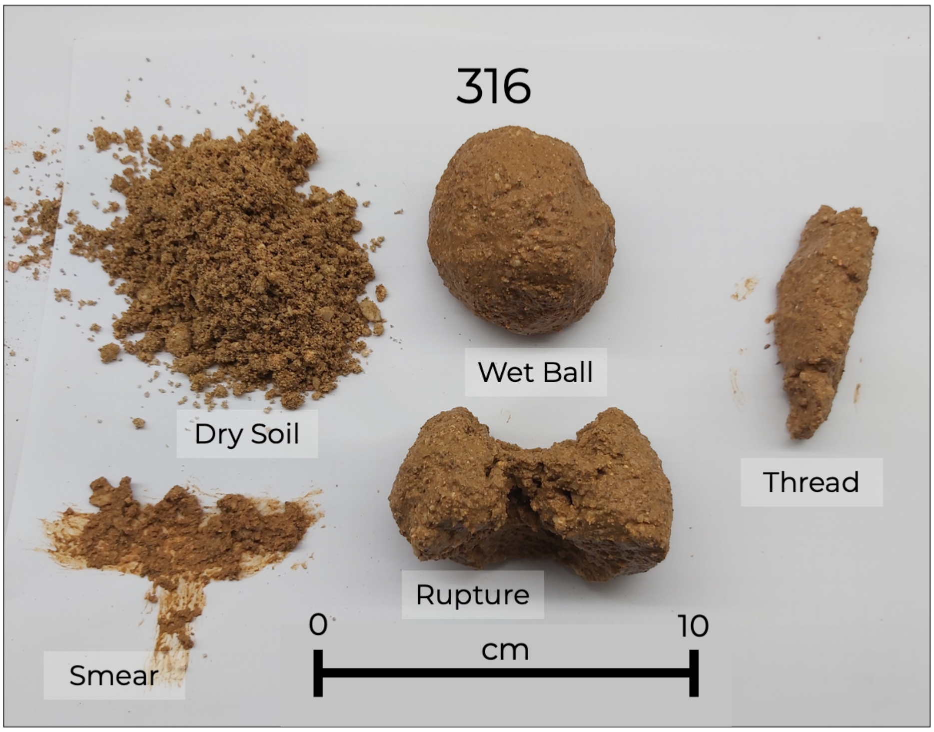

Figure 6-11 Typical soil responses of SM; Sample 316 (photograph taken by D Swart)

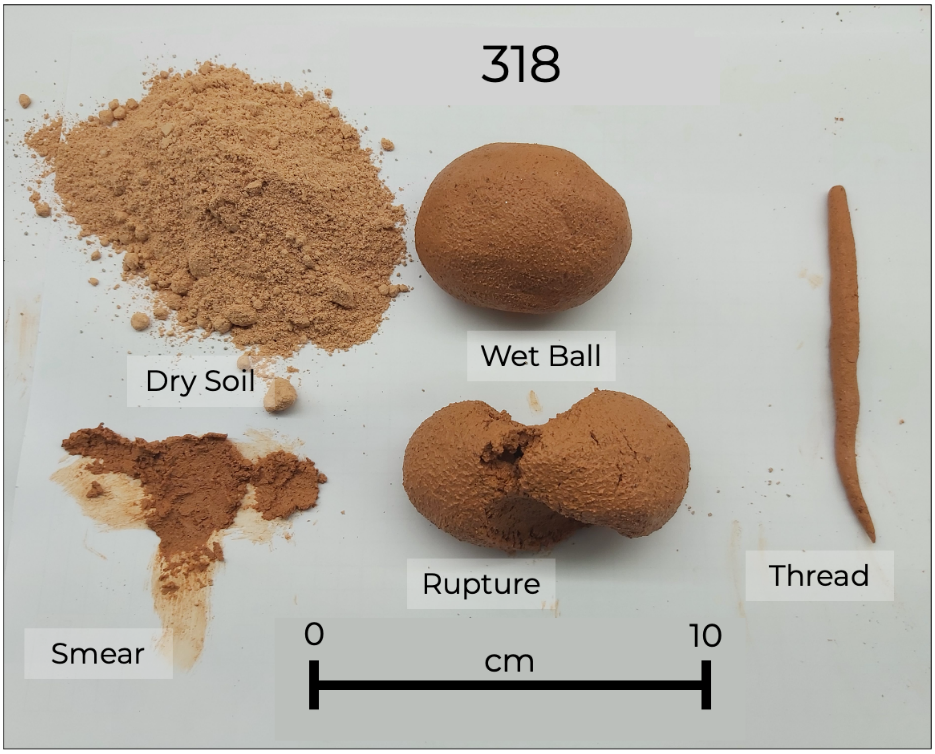

Figure 6-12 Typical soil responses of ML; Sample 318 (photograph taken by D Swart)

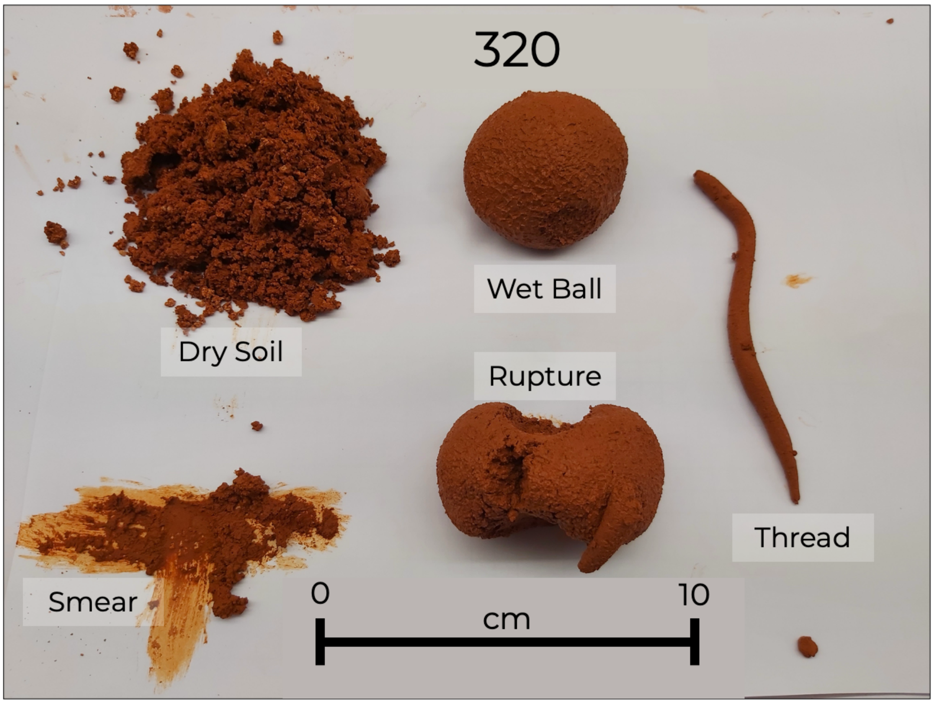

Figure 6-13 Typical soil responses of CL; Sample 320 (photograph taken by D Swart)

The final soil responses were *scored* using the identification table presented in Table 6-1, and the scoring results are summarised in Figure 6-14. There are ten (10) tests with defined criteria for each possible response listed in Table 6-1. The *ball pickup / drop test* is only used for samples where rapid water movement is observed in the *shaking / dilatancy test*, or a weak ball is formed during the *ball forming test*. The *ball forming test* is not listed in identification table and is the eleventh (11th) test.

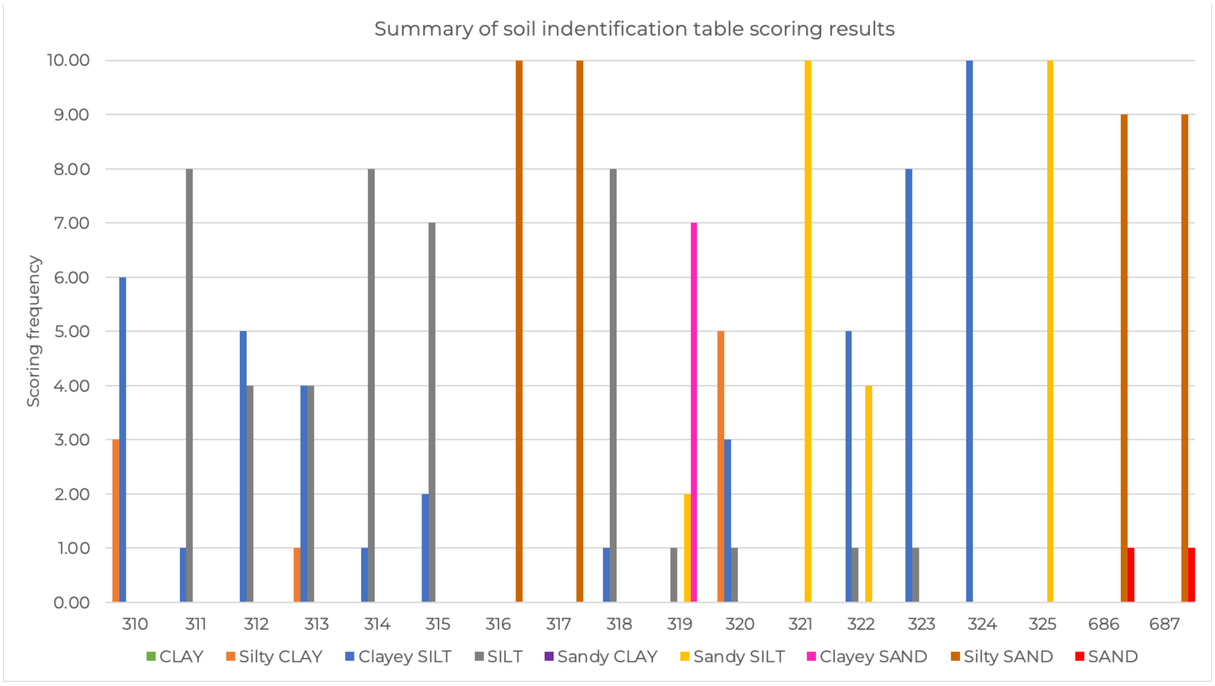

Figure 6-14 Summary of soil identification scoring results

Typically, weak balls and rapid water movement will occur in samples where silt and sand are the major components with very little clay. Therefore, the *ball pickup / drop test* will not be conducted on soils with majority silts or clays only. A tested sample with majority silt with lesser clay and sand can therefore have either a total scoring of nine (9) or ten (10) with the inclusion or exclusion of the ball pickup / drop test. A sample with majority medium sand only and very little silt will only undergo one (1) test which is the *ball forming test* and no ball is expected to be formed. If the sand component becomes a fine-grained sand or there is an increase in coarse silt, the sample can undergo a maximum of two (2) tests, namely the *ball forming test* and *ball pickup / drop test.*

6.5 Discussion

Only the key points will be discussed here, and the detailed version can be obtained in Swart et al (2023).

All non-duplicated tests described and recommended in Burmister (1949), Hunt (2005,) and Norbury (2016) were first reviewed to determine its usability in this study. Any test that required the operator to place soil in the mouth was not used and not included in the testing list. Soil contamination is not well understood, and the operator could be exposed to harmful contaminants found on brownfield and greenfield sites. Any tests requiring compounds not typical of site investigations, such as hydrochloric acid (HCl) to test for calcium carbonate content, was excluded for practicality purposes. The remaining list of tests were assessed using the soil samples.

The test descriptions were modified to ensure all different silt mixtures sampled can be assigned a test results. Once a test description or methodology was altered, all samples were retested to ensure the descriptions are still applicable. Tests such as the *smear test* and *behaviour in water* test were excluded from the final test list due to the unreliable test results and excess need for water, respectively.

The tested sample can be assigned an inferred USCS class as the plasticity and general grading are tested using changes in water content and load application. These responses are well understood in literature (Swart et al 2023). The actual USCS is based on quantitative grading percentages. The inferred USCS based on the field tests are not meant to replace the steps required to class the soil using the USCS in the laboratory. For most soil textures in Table 6-1 a range of possible USCS classes are given and therefore is termed as the inferred USCS class.

The field test soil texture for each sample was assessed by comparing the soil texture based on the clay factor, and the sand percentage (retained by the 0.075 mm sieve), presented in Figure 6-15, as proposed by Moreno-Maroto and Alonso-Azcárate (2018, 2022).

To illustrate the impact of soluble salts on the hydrometer test results, as discussed by Picornell et al. (1990), Lorefice and Malengo (2006), and Wuddivira et al. (2023), the same data has been plotted on the traditional soil texture triangle in Figure 6-16 (U.S.D.A. 2017). The two samples to note are the blue dots in Figure 6-15 and Figure 6-16 which are samples 687 and 686 taken of the marine sediments. There is an overestimation of the clay content due to skewed results of the hydrometer test caused by soluble salt content on the marine sediments. The salts present on the marine sediments have caused the hydrometer solution to become denser than expected and caused the hydrometer to indicate a high amount of clay Picornell et al. (1990).

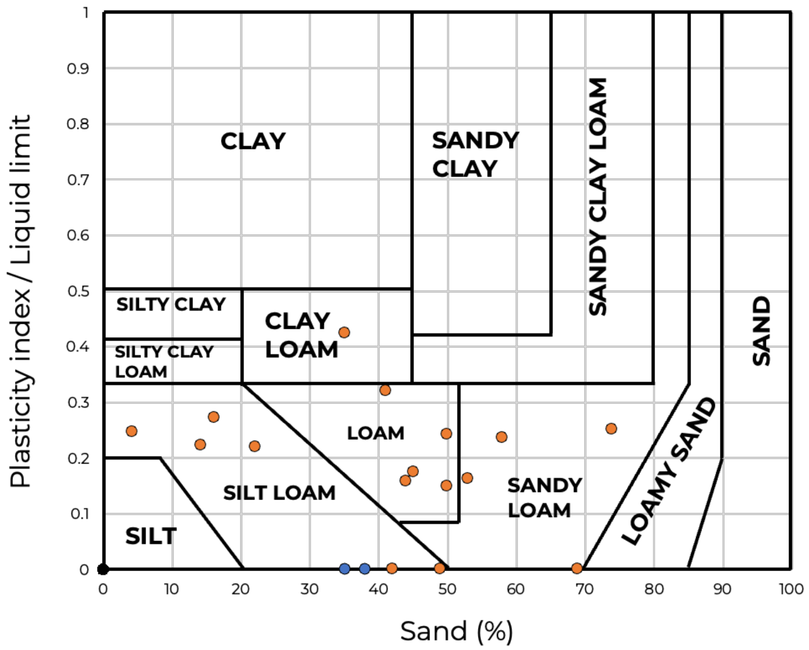

Figure 6-15 Classification based on clay factor and sand percentage (Moreno-Maroto and Alonso-Azcárate, 2018, 2022) (adapted from Swart et al 2023)

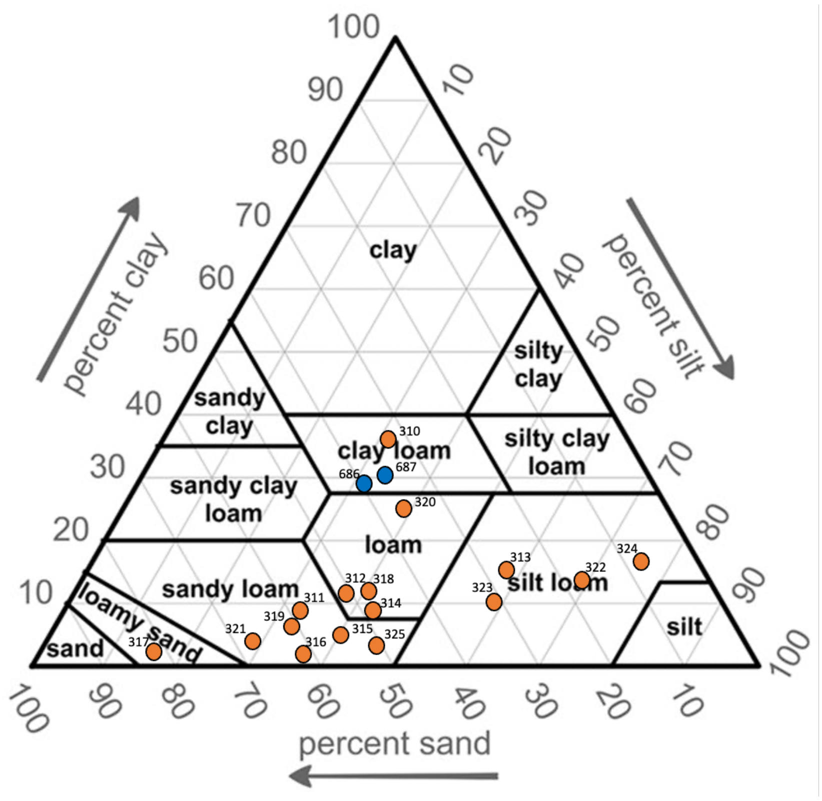

Figure 6-16 Representation of soil texture according to the soil texture triangle using the laboratory test results (U.S.D.A. 2017)

The traditional texture triangle indicates the two (2) samples are clays where the texture classification presented by Moreno-Maroto and Alonso-Azcárate (2018, 2022) indicate the material is a silt mixture. The field identification tests suggest the material behaves as a fine sand to silt-sand mixture. The two latter identification techniques assess the materials plasticity and should have very similar results.

Table 6-2 presents the summary of results for each sampled material. Though this a qualitative comparison of results, it can be seen the field test soil texture compares well with the soil texture based on the clay factor and sand percentages, respectively. Both soil identification systems make use of the plastic behaviour and not the grading of the particle sizes (Swart et al. 2023).

Table 6-2: Identification table for inorganic, fine to coarse grained, soils from field tests (adapted from Swart et al. 2023)

Sample	Laboratory USCS	Field test inferred USCS	Clay factor	Sand particle % (retained by 0.075 mm sieve)	Field test soil texture	Texture based on texture triangle (%)	Texture based on clay factor and sand (%)
310	ML	MH, ML, CL-ML	0.32	41	Clayey SILT	Clay Loam	Loam
311	SM	ML	0.16	53	SILT	Sandy loam	Sandy loam
312	CL-ML	MH, ML, CL-ML	0.24	50	Clayey SILT	Loam	Loam
313	ML	MH, ML, CL-ML	0.27	16	Clayey SILT	Silt loam	Silt loam
314	ML	ML	0.17	45	SILT	Loam	Loam
315	ML	ML	0.15	50	SILT	Loam	Loam
316	SM	SM, SW-SP, SP-SM	0.00	69	Silty SAND	Sandy loam	Sandy loam
317	SM	SM, SW-SP, SP-SM	0.25	74	Silty SAND	Loamy sand	Sandy loam
318	ML	ML	0.16	44	SILT	Loam	Loam
319	SC	SC, SW-SC, SP-SC	0.24	58	Clayey SAND	Sandy loam	Sandy loam
320	CL	CL, MH, CL-ML	0.42	35	Silty CLAY	Loam	Clay loam
321	ML	ML	0.00	49	Sandy SILT	Sandy loam	Silt loam
322	ML	MH, ML, CL-ML	0.22	14	Clayey SILT	Silt loam	Silt loam
323	MH	MH, ML, CL-ML	0.22	22	Clayey SILT	Silt loam	Silt loam
324	MH	MH, ML, CL-ML	0.25	4	Clayey SILT	Silt loam	Silt loam
325	ML	ML	0.00	42	Sandy SILT	Sandy loam	Silt loam
686	ML	SM, SW-SP, SP-SM	0.00	38	Silty SAND	Clay Loam	Silt loam
687	ML	SM, SW-SP, SP-SM	0.00	35	Silty SAND	Clay Loam	Silt loam

A flow chart is presented to show the recommended testing sequence in Figure 6-17 (Swart et al. 2023).

Flow chart to determine typical plasticity and texture using field test

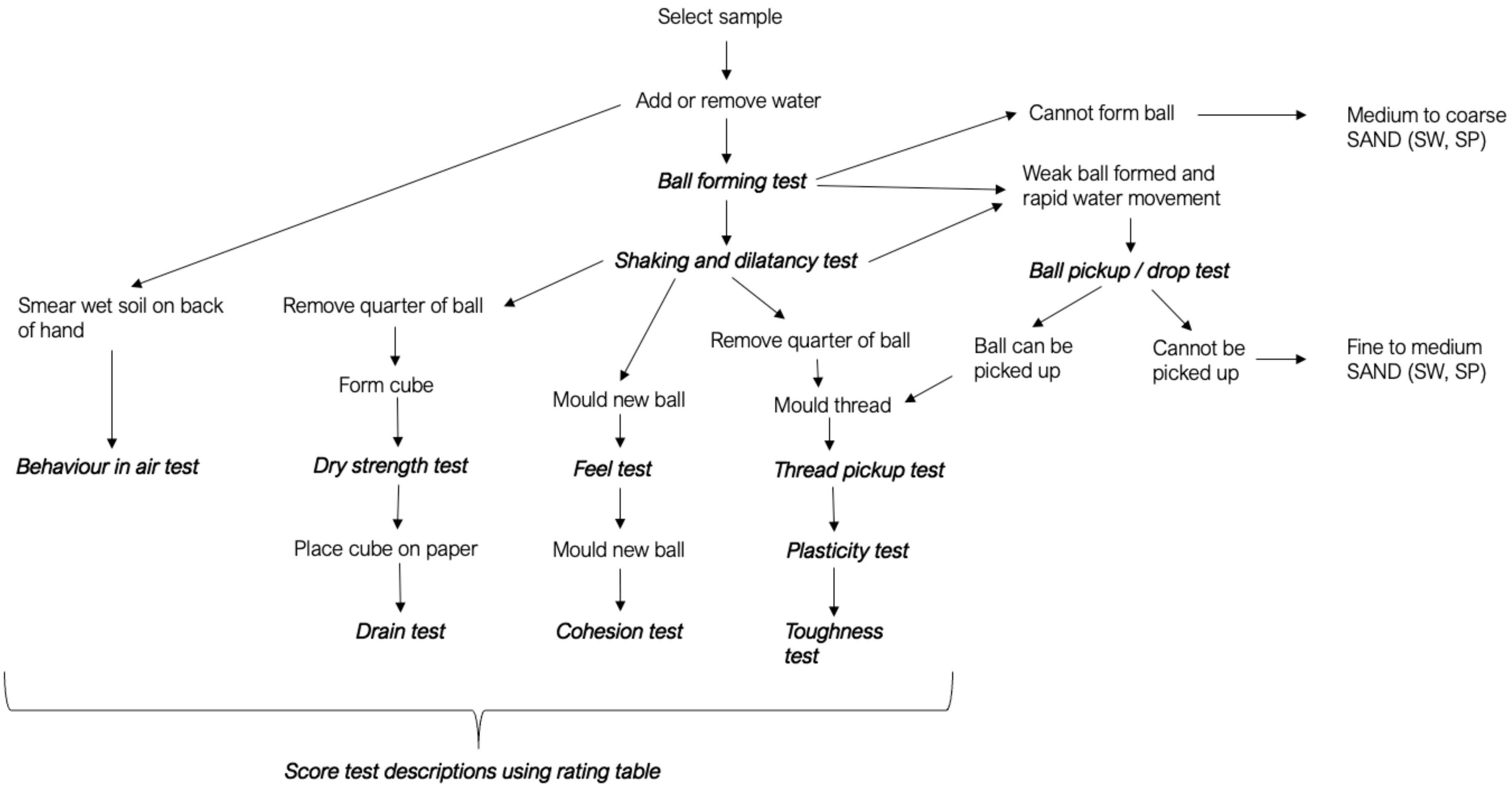

Figure 6-17 Recommended sequence of testing for effective soil identification using field tests (Swart et al. 2023)

6.6 Conclusion

The field identification tests provide a practical and convenient approach to assess soils on any site where soils have particle sizes up to 2.00 mm. By employing a single list of field tests that only necessitate water and commonly available stationery materials on-site, this research has presented a valuable tool for on-site determination of soil texture and inference of the Unified Soil Classification System (USCS) (Swart et al. 2023).

The description of possible soil responses listed in each test allows for the assessment of low to high plasticity clays and silts, and completely inert silts and sands, as well as a wide range of particles sizes typically found in natural soils. The recommended test sequence opens the possibility to conduct multiple tests simultaneously, resulting in effective soil identification while on site (Swart et al. 2023).

Additionally, the field techniques introduced in this study serve as a valuable cross-check against laboratory results, particularly hydrometer analyses, which can be affected by operator error or solution contamination. Soluble salts on the soil particle surfaces may alter the hydrometer solution and skew the clay content readings. By referencing field observations, these techniques help validate laboratory findings and mitigate potential errors.

These techniques, once reviewed and approved by industry through a journal article, were used to identify appropriate weathering profiles that excavated as low-plasticity silt mixtures to be logged and sampled for detailed testing a discussed in Section 5. The results of this testing are presented in Section 7.

7 Results

7.1 Overview

The results of the detailed on-site sampling campaign and laboratory testing will be reported in this Section of the thesis and be divided based on parent geology and location. The results will be assessed and compared across the various geologies and weathering states in Section 8. The field identification techniques as discussed in Section 6 and Swart et al. (2023) were used to ensure the tested material is of low-plasticity silt mixtures when excavated.

7.2 Field investigation and sampling

7.2.1 Tzaneen

The sample area was identified as an existing excavation to create a levelled platform just to the north of the Tzaneen town centre. The south facing excavation sidewall was chosen to be logged and sampled as this face was shaded and not desiccated. The existing sidewall was excavated by pick and shovel until the material showed no signs of excessive weathering due to exposure and was cool to touch, indicating moisture was retained in the material.

The residual diabase was logged as slightly moist, orange red mottled red, soft, open root channels, fissured, slightly sandy clayey silt. The field identification technique indicated the soil had an inferred USCS of a MH. The completely weathered diabase was logged as slightly moist, yellow brown, speckled and stained black on relict fractures, extremely weak rock, jointed, relict rock structure, sandy clayey silt. The field identification technique indicated the soil had an inferred USCS of an ML.

A schematic of the approximate sample positions as well as photographs and basic details of the undisturbed block samples is presented in Figure 7-1. The dry density (ρ_d) and moisture content (m), which is the same parameter as water content (w), values shown are the in-situ parameters that were determined in the laboratory.

Undisturbed block samples and disturbed bag samples were retrieved and sent to the laboratory for appropriate testing. The influence of the roots was kept to a minimum in the sampled residual soil, and the schematic is only an indication to provide context to the reader. Due to the tube samples refusing against the sidewall surface, undisturbed block samples were carefully cut of out the profile and sent to the laboratory for XRCT scans.

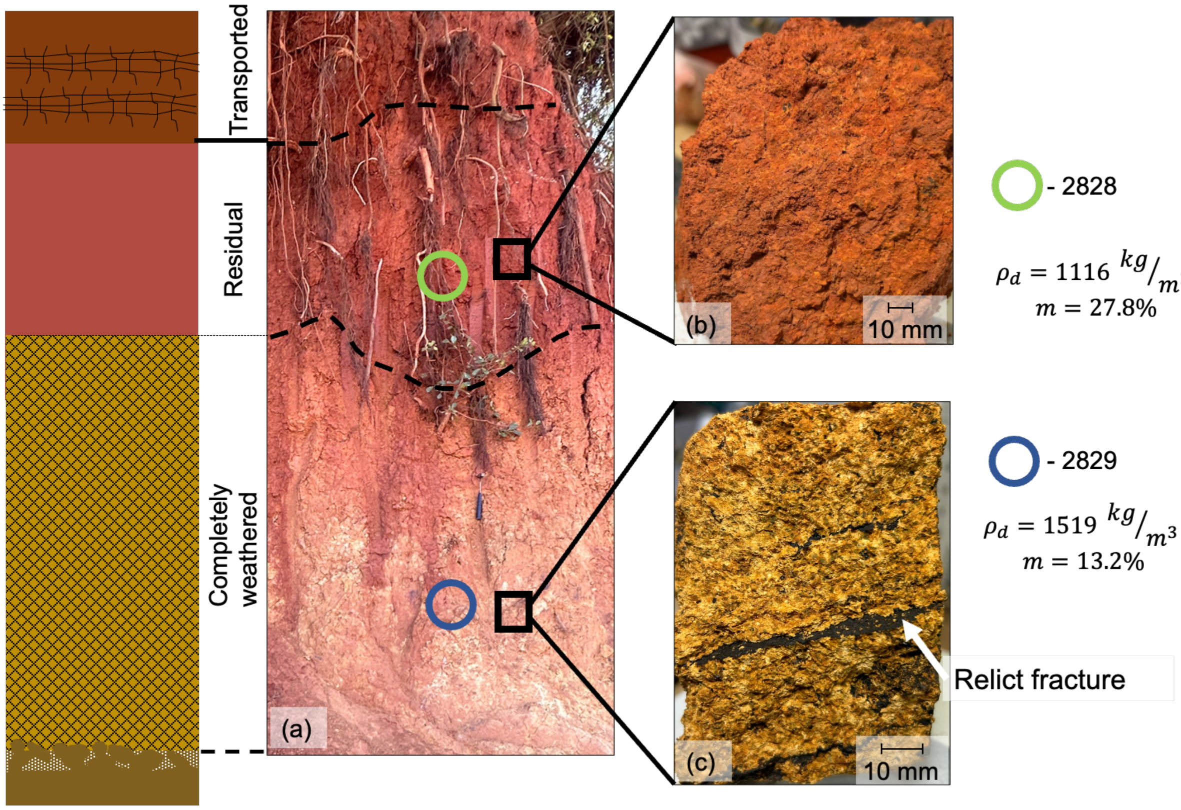

Figure 7-1 (a) Existing excavation face at Tzaneen (photograph taken by MA Dippenaar); (b) Macro soil structure in residual soil (c) Macro relict rock structure and pedogenic infill on relict fracture in completely weathered rock (photograph taken by D Swart)

7.2.2 Dullstroom

The Dullstroom site is characterised by an open field with an existing 3.00 m to 4.00 m deep borrow pit present at the site. A photograph of the borrow pit sidewall is presented in Figure 7-2(a). The approximate depths of which the samples were taken is presented. It must be noted that these samples were taken in freshly dug pits as well as in the existing borrow pit sidewall. The test pits were dug at random until a well-developed weathering profile was observed. The 2D macro structure of the residual soil and completely weathered rock are shown in Figure 7-2(b) and Figure 7-2(c), respectively.

The residual andesite was logged as slightly moist, light orange, firm, open structured, fissured, silty clay. The field identification technique indicated the soil had an inferred USCS of a CL. The completely weathered andesite was logged as moist, light orange blotched pink, stained black, extremely weak rock, jointed, relict rock structure, clayey silt. The field identification technique indicated the soil had an inferred USCS of a ML.

Undisturbed block samples and disturbed bag samples were retrieved and sent to laboratory for appropriate testing. Four (4) tube samples were pushed into moist sidewalls, with one (1) in the residual and three (3) in the completely weathered rock with the general depth of each sample shown. The sample details were calculated using the tube sample data.

Sample 2835 represents the deepest and least altered of the completely weathered rock samples at the Dullstroom site. The tube samples were sent to the laboratory for XRCT scans. Figure 7-3 shows the cut open tube samples with sample ID indicated. It can be seen the macro rock structure becomes less prominent with an increase in the state of weathering.

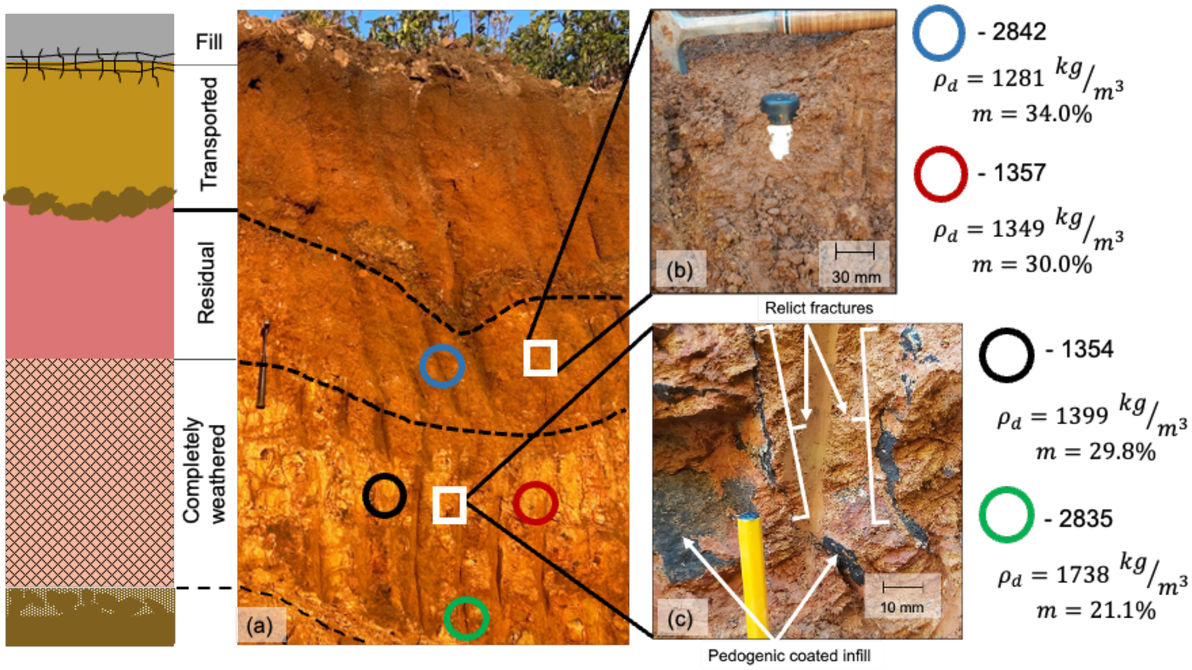

Figure 7-2 (a) Existing excavation face at Dullstroom (photograph taken by MA Dippenaar); (b) Macro soil structure in residual soil with tube sample (c) Macro relict rock structure and pedogenic infill on relict fractures in completely weathered rock (photograph taken by D Swart)

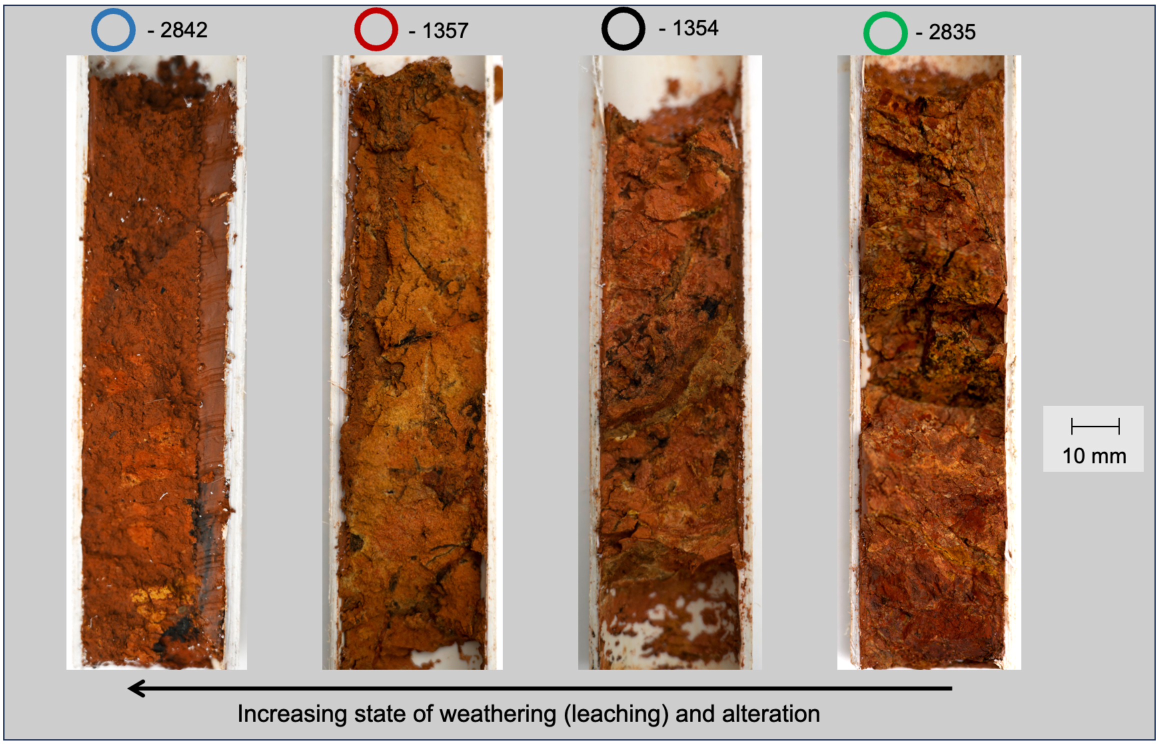

Figure 7-3 Cut open tube samples showing the condition of the relict rock structure with increase state of weathering

7.2.3 R528

The R538 sample site is an open borrow pit sidewall face adjacent to the mentioned road. It has been opened up to be used as an informal borrow pit for the surrounding forestry roads. As can be seen in Figure 7-4(a), the profile is dry, and the residual soil horizon is dry and desiccated at the sidewall surface. Great care was taken to ensure the sidewall is excavated deep enough by pick and shovel to a point where the material was at an in-situ moisture which allowed the structure to be retained. Figure 7-4(b) shows the macro relict rock structure of the completely weathered rock, especially the rock texture grain relations.

The residual granite was logged as slightly moist, reddish brown, firm, fissured, open structure, silty sandy clay. The field identification technique indicated the soil had an inferred USCS of a CL. The completely weathered granite was logged as Slightly moist, light orange, speckled white and green, extremely weak rock, relict rock structure, slightly clayey silty fine sand. The field identification technique indicated the soil had an inferred USCS of a SM.

The undisturbed block samples and disturbed bag samples were taken of the residual soil and completely weathered rock, and the details of these samples are shown in Figure 7-4. No tube samples were taken as the tubes refused on the sidewall surface.

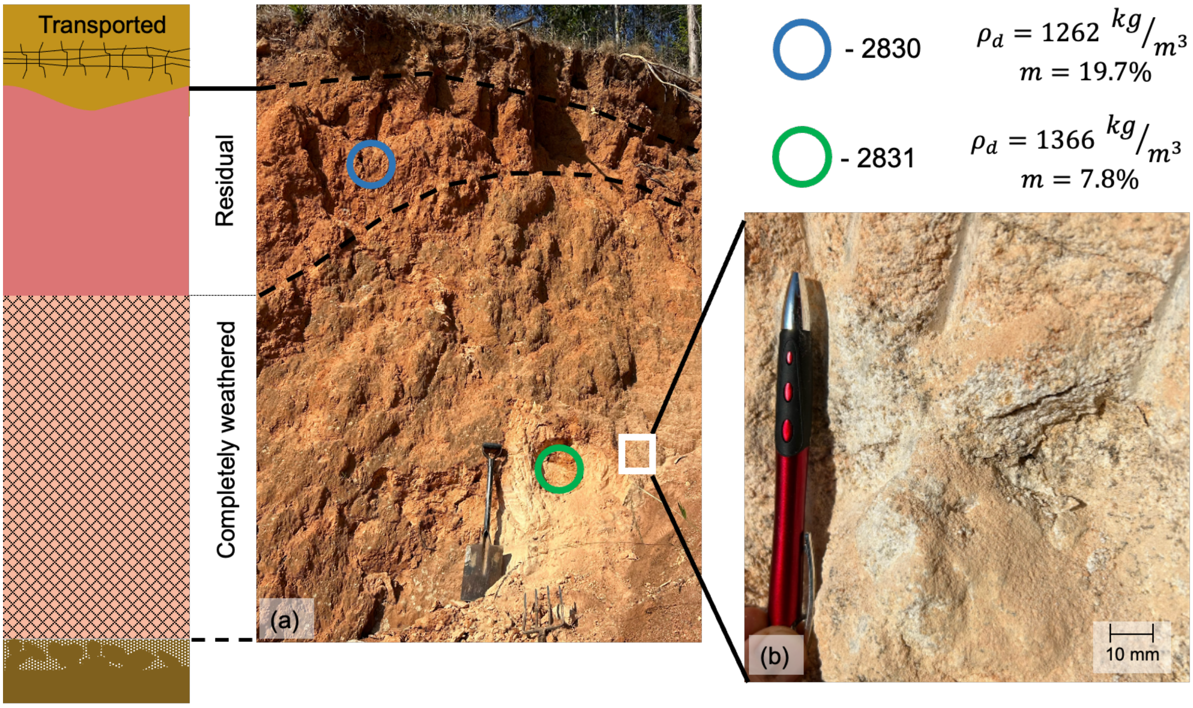

Figure 7-4 (a) Existing excavation face at R528; (b) Macro relict rock structure in completely weathered rock (photographs taken by D Swart)

7.2.4 Graskop

The Graskop profile was found at an existing box cutting for an access road in the forestry area to the north of Graskop. This profile was investigated thoroughly by Dowding and Fey (2007). The sampled profile exists under a thick canopy of trees and was easily excavated due to the high in-situ moisture content of the profile. The profile was opened up by pick and shovel and is presented in Figure 7-5.

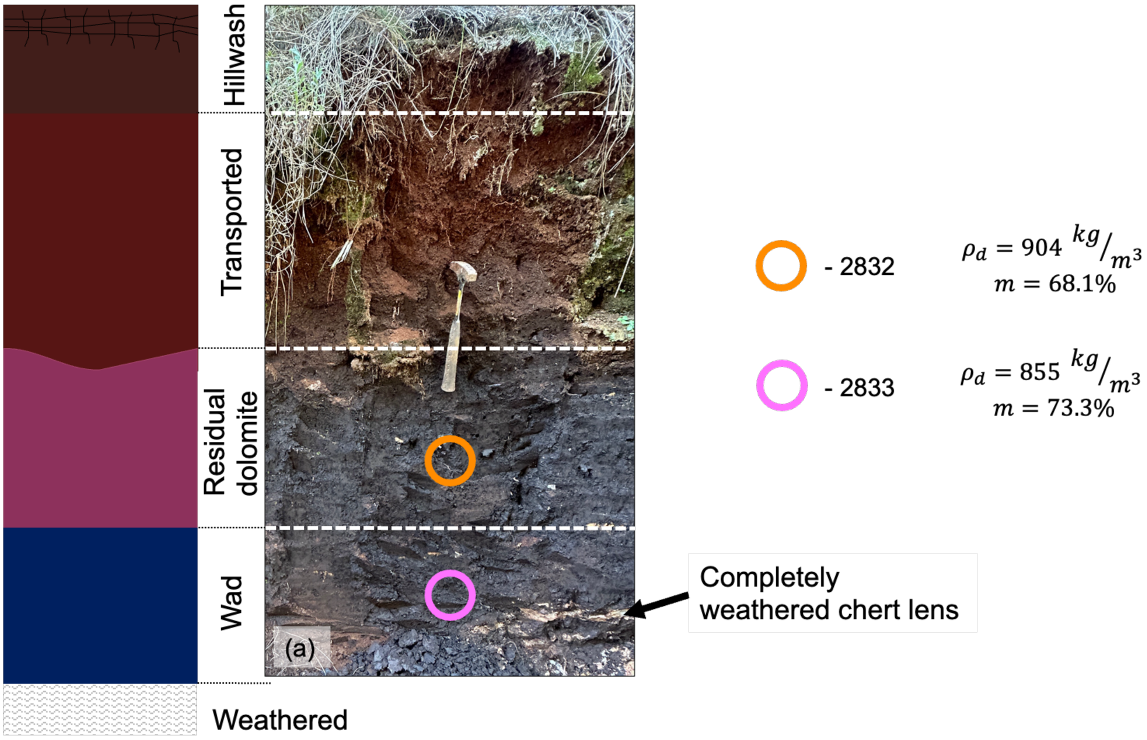

Figure 7-5 (a) Existing excavation face at Graskop (photograph taken by MA Dippenaar)

The residual dolomite was logged as moist, dark purple to grey, stiff, shattered and fissured, silty clay with abundant moderately cemented Fe & Mn nodules. The field identification technique indicated the soil had an inferred USCS of a ML. The completely weathered rock, also termed wad, was logged as wet, dark bluish grey, firm, open structured, silty clay with trace amount of grey and blue stained pink completely weathered chert lenses. The field identification technique indicated the soil had an inferred USCS of a ML. The presence of the nodules and chert lenses results in a slightly higher than anticipated gravel and sand content.

The factors that differentiate the residual dolomite and completely weathered rock was the high amount of pedogenic nodules and fissuring in the former horizon. The latter horizon had notably a much higher in-situ moisture content, to the point where if the material was remoulded and structure broken down, free-water would appear on the palm of the hand and the soil was liquified. This suggests that the structure of the soil allows it to have a water holding capacity greater than the liquid limit of the particle size distribution. Dowding and Fey (2007) noted the wad material is highly porous and had a large water holding capacity.

The completely weathered rock horizon also has completely weathered chert lenses which suggests the relict rock structure has survived in this horizon. Undisturbed block samples and disturbed bag samples were taken of each horizon. One (1) tube sample was retrieved from each horizon and sent to the laboratory for XRCT scans.

7.2.5 Highveld

The Highveld site details have been discussed in Bester (2021) and Swart (2019) and is located to the south of Pretoria. The samples were retrieved from freshly dug pits that were opened by means of machine excavation. The site existed near a drainage channel and the impervious dolomite bedrock was shallow, which resulted in the soil profile having a high moisture content.

It must be emphasised the schematic in Figure 7-6 is for illustration purpose to provide context to the reader on the properties of the weathering profile. The sample location is not the actual location of the samples but provide a good indication on the sample positioning relative to one another. Testing results of the oedometer, permeability, and particle size grading data gathered at the site has been provided in Bester (2021). The Soil Water Retention Curve, chemical data and particle size grading data has been taken from Swart (2019). The data has been interpreted and processed in a different manner, and only novel findings generated during this research will be presented.

The residual dolomite was logged as dark brown speckled orange and black, slightly clayey sandy silt. The completely weathered rock was logged as dark grey to black, relict rock structure, slightly sandy silt. The completely weathered rock is also defined as structured wad and was sampled at the bedrock to soil interface. The sampling at this site was conducted in 2019 and the field identification techniques had not yet been written, therefore no inferred USCS was assigned to the material.

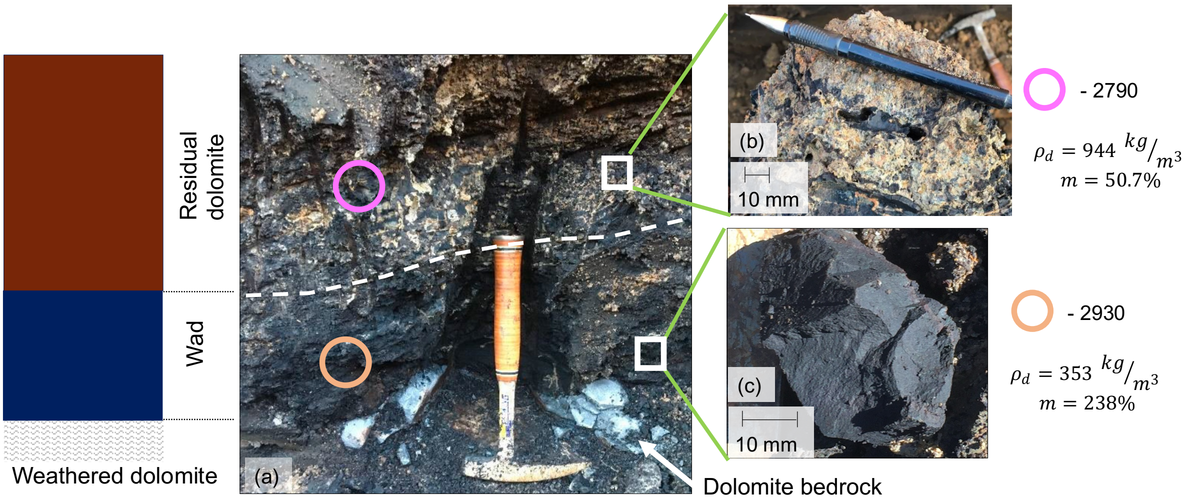

Figure 7-6 (a) Freshly dug pit at Highveld site (photograph taken by D Bester); (b) Macro structure in residual dolomite (photograph taken by D Bester (Bester 2021)) (c) Macro relict rock structure in completely weathered rock defined as wad (photograph taken by D Swart)

7.2.6 *Dolomite residuum sites*

The remaining sample sites all exist on dolomite and the residuum present at the site was sampled. The detail of each site is presented in Swart (2019). For completeness the detail of each site is summarised in Table 7-1. Undisturbed block and disturbed bag samples were taken at each site location. The test results of the chemical and imagery analyses, and particle size grading will be used from these sites to supplement the testing done of the dolomite residuum a the Graskop and Highveld sites to illustrate how weathering alters wad and residual dolomite. The undisturbed testing results included triaxial shear and permeability testing, and SWRC testing and are presented in Swart (2019).

Table 7-1: Summary of residuum samples sites as presented in Swart (2019)

Sample site	Sample ID	Sampled material	Dry density (kg/m^3)
R533	1510	Completely weathered rock (non-structured wad)	464
Doornhoek	1520	Completely weathered rock (non-structured wad)	539
Sudwala Caves	1530	Completely weathered rock (non-structured wad)	894
Carletonville	1540	Completely weathered rock (non-structured wad)	898
Southdowns	1560	Residual dolomite	-
Bokkraal	1570	Residual dolomite	1237
Mooiplaas	1580	Residual dolomite	1034

7.3 Laboratory testing results

7.3.1 *Particle size analysis and Atterberg limits*

The grading and Atterberg limits testing were conducted on disturbed bag samples at commercial laboratories. Three different laboratories were used over the course of this study and therefore, some biases in the Atterberg limits results as discussed in Section 6. The testing results for the particle size grading analyses and Atterberg limits are summarised in Figure 7-7. The USCS class presented was determined from the laboratory results.

7.3.2 *Oedometer testing*

The material was loaded at intervals of 6 kPa, 12 kPa, 25 kPa, 50 kPa, 100 kPa, 200 kPa, 400 kPa, 800 kPa, 1600 kPa as stated in the relevant standard. However, only the strain and void ratio between 6 kPa and 800 kPa will be assessed. Analysing the behaviour of soil when under a loading of 1600 kPa is not a realistic scenario and testing results become unreliable at this stage of the test (Wesley 2010). The strain curves for the undisturbed (*Undis*) and remoulded (*Remo*) samples retrieved at the Tzaneen site is presented in Figure 7-8. The testing results summary for each sample is presented in Table 7-2. The value of m_v is not constant for a soil but depends on the stress range for which it is calculated. It is calculated using data from the oedometer test results as the change in height can be measured with the change in stress known. Therefore, the m_v value calculated for the stress increment between 50 kPa to 100 kPa is given.

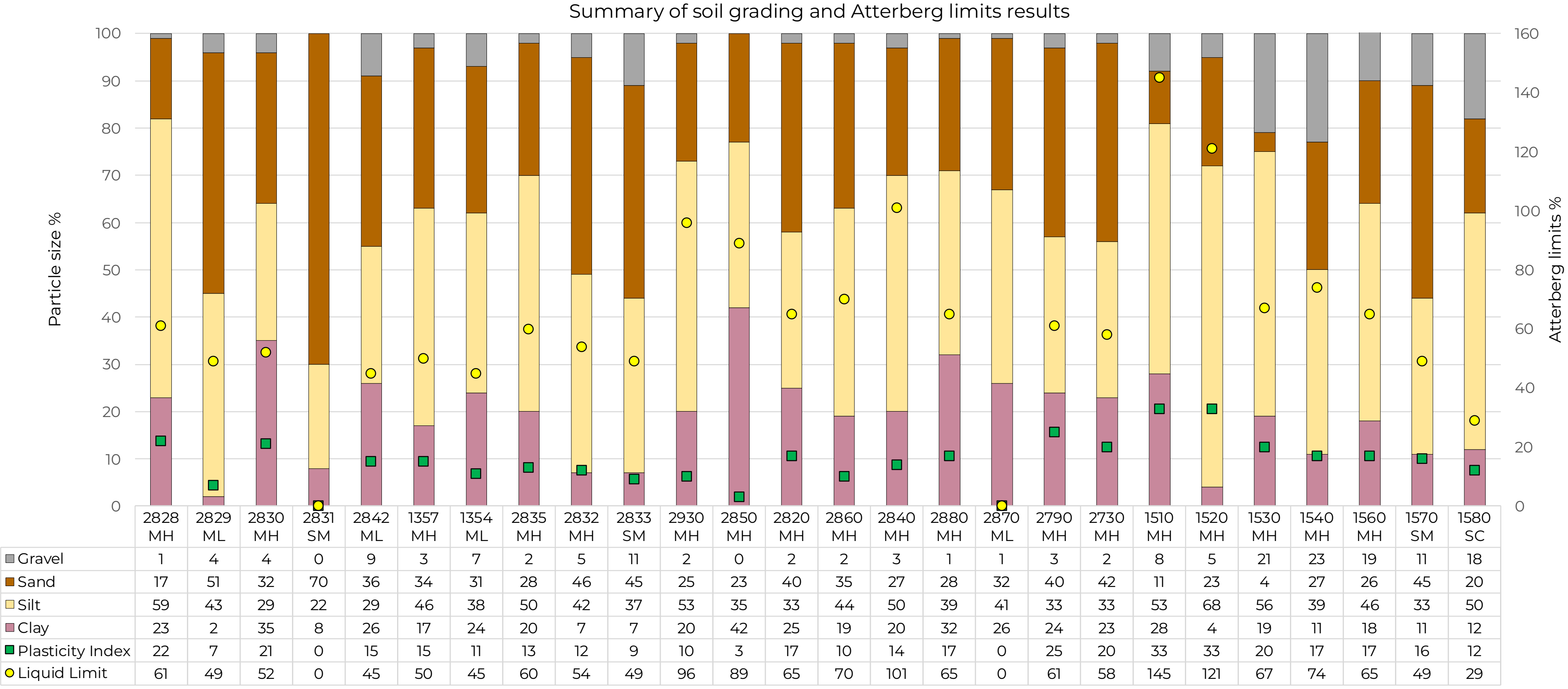

	2828 MH	2829 ML	2830 MH	2831 SM	2842 ML	1357 MH	1354 ML	2835 MH	2832 MH	2833 SM	2930 MH	2850 MH	2820 MH	2860 MH	2840 MH	2880 MH	2870 ML	2790 MH	2730 MH	1510 MH	1520 MH	1530 MH	1540 MH	1560 MH	1570 SM	1580 SC
■ Gravel	1	4	4	0	9	3	7	2	5	11	2	0	2	2	3	1	1	3	2	8	5	21	23	19	11	18
🟫 Sand	17	51	32	70	36	34	31	28	46	45	25	23	40	35	27	28	32	40	42	11	23	4	27	26	45	20
☐ Silt	59	43	29	22	29	46	38	50	42	37	53	35	33	44	50	39	41	33	33	53	68	56	39	46	33	50
🟪 Clay	23	2	35	8	26	17	24	20	7	7	20	42	25	19	20	32	26	24	23	28	4	19	11	18	11	12
🟩 Plasticity Index	22	7	21	0	15	15	11	13	12	9	10	3	17	10	14	17	0	25	20	33	33	20	17	17	16	12
🟡 Liquid Limit	61	49	52	0	45	50	45	60	54	49	96	89	65	70	101	65	0	61	58	145	121	67	74	65	49	29

Figure 7-7 Soil grading and Atterberg limits testing results

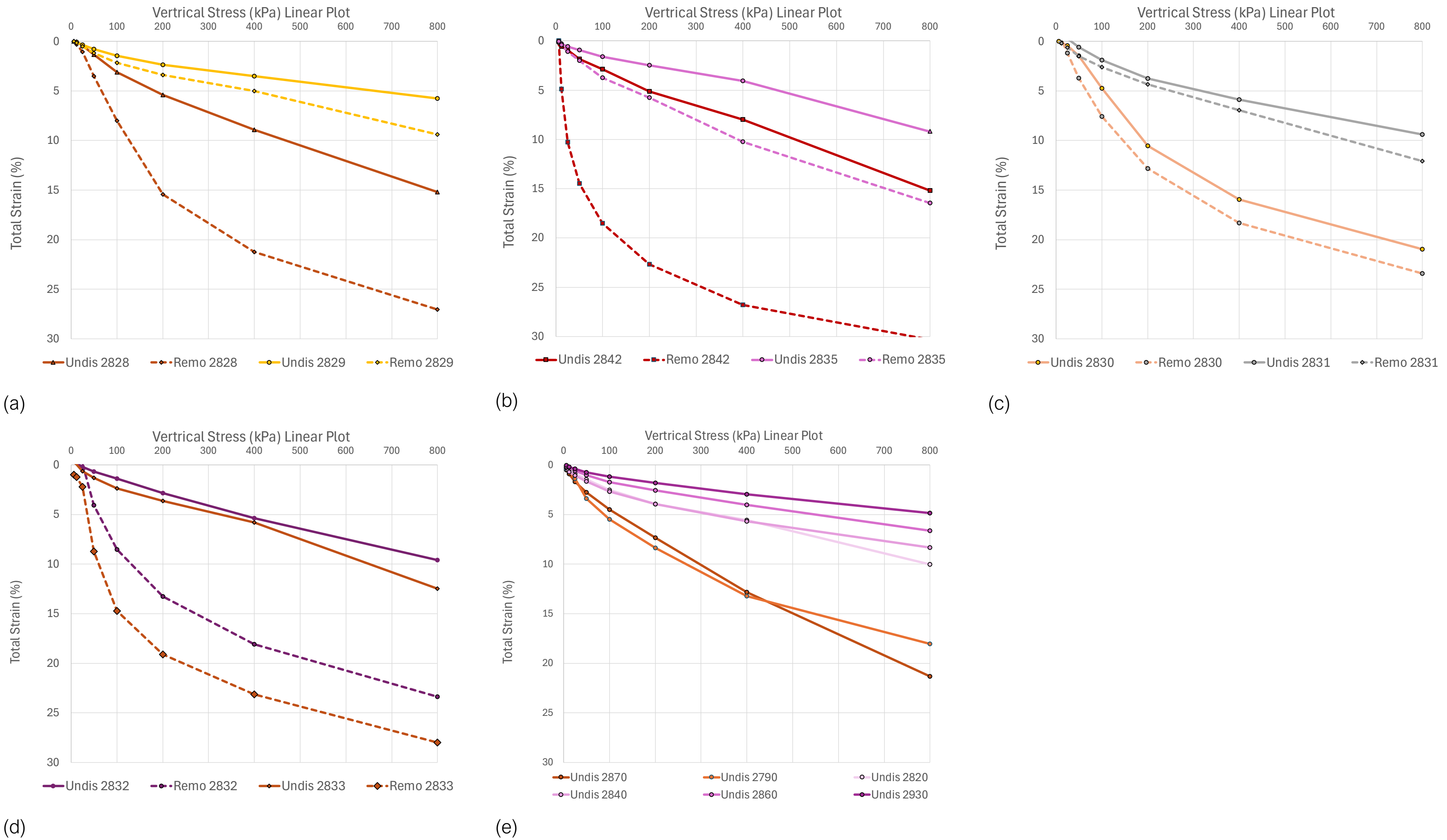

Figure 7-8 Oedometer linear stress strain curves for a) Tzaneen, b) Dullstroom, c) R528, d) Graskop, and e) Highveld samples

Table 7-2: Oedometer testing results summary

Sample ID	Initial dry density (kg/m^3)		Initial void ratio		m_v (1/MPa) at 100 kPa	
	Undisturbed	Remoulded	Undisturbed	Remoulded	Undisturbed	Remoulded
2828	1116	1104	1.581	1.610	0.356	0.913
2829	1519	1517	0.867	0.871	0.131	0.192
2830	1262	1259	1.123	1.127	0.656	0.800
2831	1366	1365	0.903	0.905	0.223	0.265
2842	1114	1065	1.542	1.579	0.216	0.985
2835	1012	1170	1.729	1.253	0.140	0.354
2832	904	893	2.293	2.334	0.137	0.926
2833	855	842	2.444	2.500	0.217	1.316
2860	572	-	4.115	-	0.141	-
2930	353	-	7.268	-	0.082	-
2820	722	-	3.059	-	0.165	-
2860	572	-	4.115	-	0.160	-
2840	715	-	3.228	-	0.207	-
2870	1141	-	1.483	-	0.362	-
2790	994	-	2.215	-	0.429	-

7.3.3 Triaxial permeability testing

The triaxial permeability testing was conducted by a single commercial laboratory for all samples, including the Highveld sample from which the data was taken from Bester (2021). The samples were consolidated at a confining pressure of 100 kPa and was placed under a 10 kPa hydraulic pressure. The remoulded samples typically underwent double the volumetric strain when compared to the undisturbed samples. The summary of the triaxial permeability results is presented in Table 7-3.

It must be noted here, the permeabilities were conducted after the oedometer test results were received. There were significant differences in the compression behaviour after remoulding. It was decided to remould the permeability samples as well to see if there was an expected influence of a change in permeability which could be driving the force of increase compression as water dissipates out of the sample.

Table 7-3: Saturated triaxial permeability testing results summary

Sample ID	Initial dry density (kg/m^3)		Initial void ratio		Average Coefficient of Permeability (*K*) (m/s)	
	Undisturbed	Remoulded	Undisturbed	Remoulded	Undisturbed	Remoulded
2828	1239	1119	1.325	1.574	5.13E-08	5.08E-08
2829	1434	1477	0.979	0.921	2.30E-07	2.69E-07
2830	1380	1285	0.941	1.085	6.72E-07	1.88E-07
2831	1155	1392	1.251	0.868	2.38E-06	8.41E-07
2842	-	1124	-	1.444	-	4.15E-07
2835	1045	974	1.640	1.837	1.78E-07	1.29E-07
2832	1013	928	1.939	2.206	1.20E-08	6.67E-08
2833	951	880	2.130	2.382	1.90E-09	7.82E-08
2860	529	-	-	-	2.83E-06	-
2850	296	-	-	-	1.73E-06	-
2880	760	-	-	-	7.74E-07	-
2730	1168	-	-	-	9.44E-08	-

7.3.4 XRD and XRF testing

The chemical testing, comprising the XRD and XRF analyses, was done to determine the weathering state of the samples. Only the required data to plot the chemical weathering indices are presented in Table 7-4. The XRD tests were conducted at numerous commercial laboratories and institutions. The interpretation of a mineral type is done by assessing *XRD* diffraction patterns and peaks, and these can shift and change due to amorphous crystal structures. Less common soil minerals of similar structures or peaks are often grouped together with more common soil minerals, such as kaolinite and birnessite, and muscovite and lithiophorite, if no additionally testing is done to confirm the presence of either mineral (Swart et al. 2019). These limitations result in the XRD results to be influenced by operator bias. Notwithstanding, the Tzaneen, Dullstroom, and Graskop XRD results were reviewed after the XRF results became available and the XRD results were updated based on the elemental composition. Only minerals, based on the XRF and XRD results, of significant importance to the study will be presented in Table 7-5.

Table 7-4: Summary of XRF test results

Sample ID	Weight percentages (wt.%)								
	SiO_2	Al_2O_3	Fe_2O_3	MgO	MnO	CaO	K_2O	P_2O_5	Na_2O
2828	41.8	19.6	22.9	0.65	0.19	0.14	0.66	0.26	0.01
2829	48.9	16.3	17.1	2.31	0.19	3.45	1.99	0.25	0.61
2830	53.8	23.8	8.42	0.31	0.13	0.05	1.51	0.23	0.01
2831	66.9	19.1	1.18	0.06	0.09	0.04	4.96	0.20	0.32
2842	57.0	16.3	14.9	0.46	0.25	0.03	0.53	0.31	0.01
2835	56.5	25.9	9.43	1.70	0.06	0.12	4.46	0.31	0.12
2832	24.9	25.8	16.4	1.13	11.0	0.03	2.98	0.22	0.14
2833	27.4	25.6	16.1	1.08	9.88	0.02	2.88	0.22	0.17
2930	5.78	0.76	33.9	0.52	45.8	2.13	0.25	0.09	0.01
1510	24.5	6.57	23.7	0.48	29.4	0.08	0.92	0.03	0.07
1520	45.9	2.67	25.5	0.73	9.35	0.08	0.11	0.04	0.01
1530	35.7	12.4	13.3	0.73	22.8	0.07	2.57	0.12	0.08
1540	68.6	4.24	10.1	0.69	8.26	0.76	0.86	0.03	0.01
1560	72.0	3.14	12.3	0.29	6.58	0.13	0.72	0.08	0.01
1570	62.0	3.57	16.5	0.35	8.78	0.13	1.18	0.01	0.01
1580	82.0	5.09	5.61	0.28	2.60	0.20	0.25	0.01	0.01

Table 7-5: Summary of XRD test results

Sample ID	Weight percentages (*wt.*%)											
	Quartz	Kaolinite	Microcline	Gibbsite	Muscovite	Goethite	Albite	Actinolite	Pyrochroite	Todorokite	Lithiophorite	Smectite
2828	30.0	60.4	-	-	9.60	-	-	-	-	-	-	-
2829	9.10	19.9	14.0	-	-	-	17.2	25.0	-	-	-	9.6
2830	41.9	41.6	10.2	1.00	5.30	-	-	-	-	-	-	-
2831	51.8	7.20	39.8	-	1.20	-	-	-	-	-	-	-
2842	55.5	37.8	-	-	4.90	1.80	-	-	-	-	-	-
2835	20.5	24.1	12.7	-	15.6	0.04	-	-	-	-	-	-
2832	16.3	-	-	28.2	32.9	-	-	-	3.00	15.8	3.80	-
2833	23.7	-	-	27.3	32.9	-	-	-	2.20	11.4	2.60	-
2930	36.9	11.9	-	-	29.3	19.0	-	-	-	-	-	-
1510	59.9	4.11	-	-	29.4	6.63	-	-	-	-	-	-
1520	80.3	4.40	-	-	2.46	12.8	-	-	-	-	-	-
1530	53.3	6.49	-	-	36.2	3.36	-	-	-	-	-	-
1540	91.3	-	-	-	5.89	1.11	-	-	-	-	-	-
1560	91.8	0.11	-	-	5.38	2.40	-	-	-	-	-	-
1570	80.5	2.48	-	-	5.20	11.8	-	-	-	-	-	-
1580	86.2	6.99	-	-	-	1.90	-	-	-	-	-	-

7.3.5 X-Ray Computed Tomography

The XRCT scans were conducted in two phases where the four (4) Dullstroom tube samples were sampled across the weathering profile and scanned in the first phase. The aim of this phase was to determine the usability of the XRCT scan projections to model the soil minerals and voids and see the influence of weathering on the structure, porosity and moisture flow indicators. The influence of using tubes that are pushed and tapped into the sidewalls to retrieve the samples was also assessed. The first phase test results indicated that tube samples are appropriate as moisture and structure is retained in the sample for several months after sampling. Notwithstanding, care must be taken when sampling as cracks can form along preexisting structures in the soil, which will influence the porosity 3D modelling. These types of cracks were identified in a sample of stiff residual soil that was later discarded and not included in the study.

During the analyses of the first phase, it was noted the sample sizes that were scanned resulted in a reduction of resolution and voxel size of the data. The entire tube sample, which is 150.0 mm long and 30.0 mm diameter was scanned. It was decided in the second phase of sampling, the sample sizes and scanning area would be smaller to improve the resolution. The second phase of sampling was done with a 100.0 mm long and 40.0 mm diameter tube sample. This tube sample was scanned twice with the top half being scanned first and bottom half second. These two scans were stitched together during the software processing phase. This resulted in a smaller voxel and pore sizes, as small as 0.06 mm in equivalent diameter, to be identified during the second phase. Tube samples were not used in the second phase when the material was stiff or dense and a block sample was taken instead. This ensure minimal disturbance to soil structure, however, samples had to be transported with more care and scanned immediately after sampling, which was done. The block sample was scanned by creating a *theoretical* tube in the block sample that had the dimensions of 100.0 mm long and 40.0 mm diameter. This *theoretical* tube section of the sample was used during the software processing. The second phase sample locations include Tzaneen and Graskop. Samples from R528 were disturbed to the point where no meaningful data could be used in this study and were therefore discarded.

The 2D slices and subsequent 3D porosity and density models were assessed, and figures produced using the VOLUME GRAPHICS (VG) STUDIO MAX software. The raw data is based on the density of the material scanned, and therefore a density colour contrast can be applied to identify the densest material in that sample. For continuity in analysing the samples, the upper 10% of the densest material was shaded in red when this method was applied. The orange shading was applied to the upper 20% of the densest material. The results for the Dullstroom site will be explained first, starting with the least weathered sample 2835 and progressively working towards the most weathered sample 2842. It must be noted the smallest pore that could be modelled for the Dullstroom samples was 0.16 mm.

To provide context to the reader, the images generated for each sample will be briefly discussed as they are presented.

Figure 7-9 (a) shows the 2D slice of sample 2835 from the top view and right view with the cross-sectional plane of the top view indicated. The yellow markers indicate a well-defined, tight, fracture of the relict rock structure present in the sample that persists both laterally and horizontally through the sample. The yellow brackets show the orientation of the same specific structure in the two adjacent images. Weathered rock grains, most likely microcline according to the chemical testing results, which are slightly denser (lighter) than the surrounding material less dense (darker) clay present. The difference in densities of the individual minerals allows for colour contrasts to be created based on relative density to the lowest density material in the sample. In Figure 7-9 (b) the denser minerals are highlighted in red and occur as discontinuous pockets within the relict rock structures and are denser than the weathered rock grains. To further evaluate the occurrence of the denser material, a 3D density contrast is presented in Figure 7-9 (c).

As mentioned, the scan area was relatively large and therefore the voxel sizes were too big to identify micropores between the rock mineral grains. No porosity models were generated for this sample.

Figure 7-10 (a) and (b) presents the 2D slices and 3D models for sample 1357 with the density contrast applied and indicates a horizontal and vertical structure, respectively. The 3D porosity model is presented in Figure 7-11 (a) and shows the pore geometry is governed by structural orientation of the completely weathered rock. The top view in Figure 7-11 (b) shows the pore orientation to be parallel to the vertical structure identified in this sample, as well as showing the structures comprising open pores and pedogenic material. The matrix has a more uniform greyscale, compared to sample 2835, with no indication of weathered rock minerals, suggesting all minerals in this sample have weathered to secondary clays and weathered quartz.

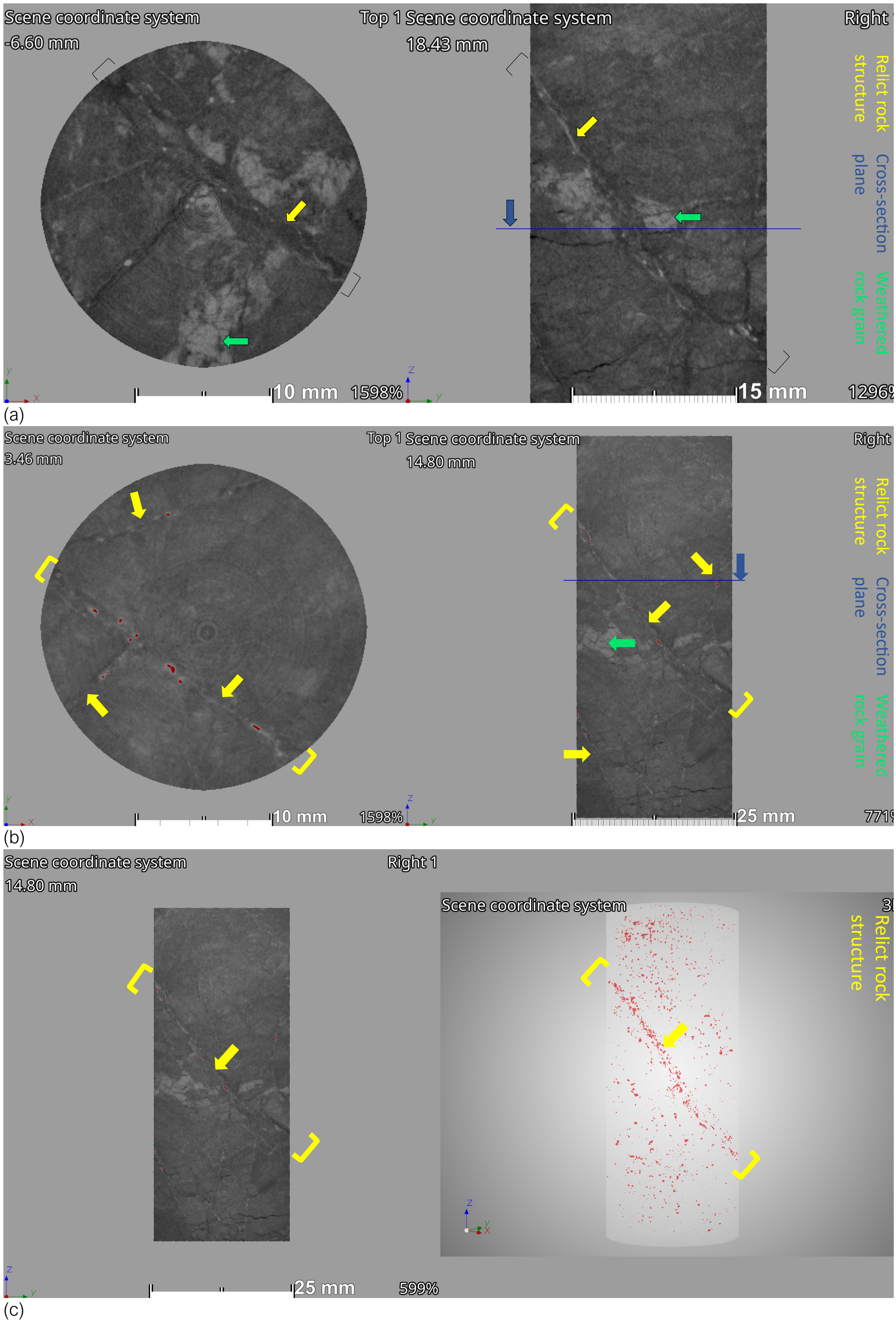

Figure 7-9 (a) Sample 2835 2D slices from top view (left) and right view (right); (b) with density colour contrast; (c) 3D distribution of denser minerals

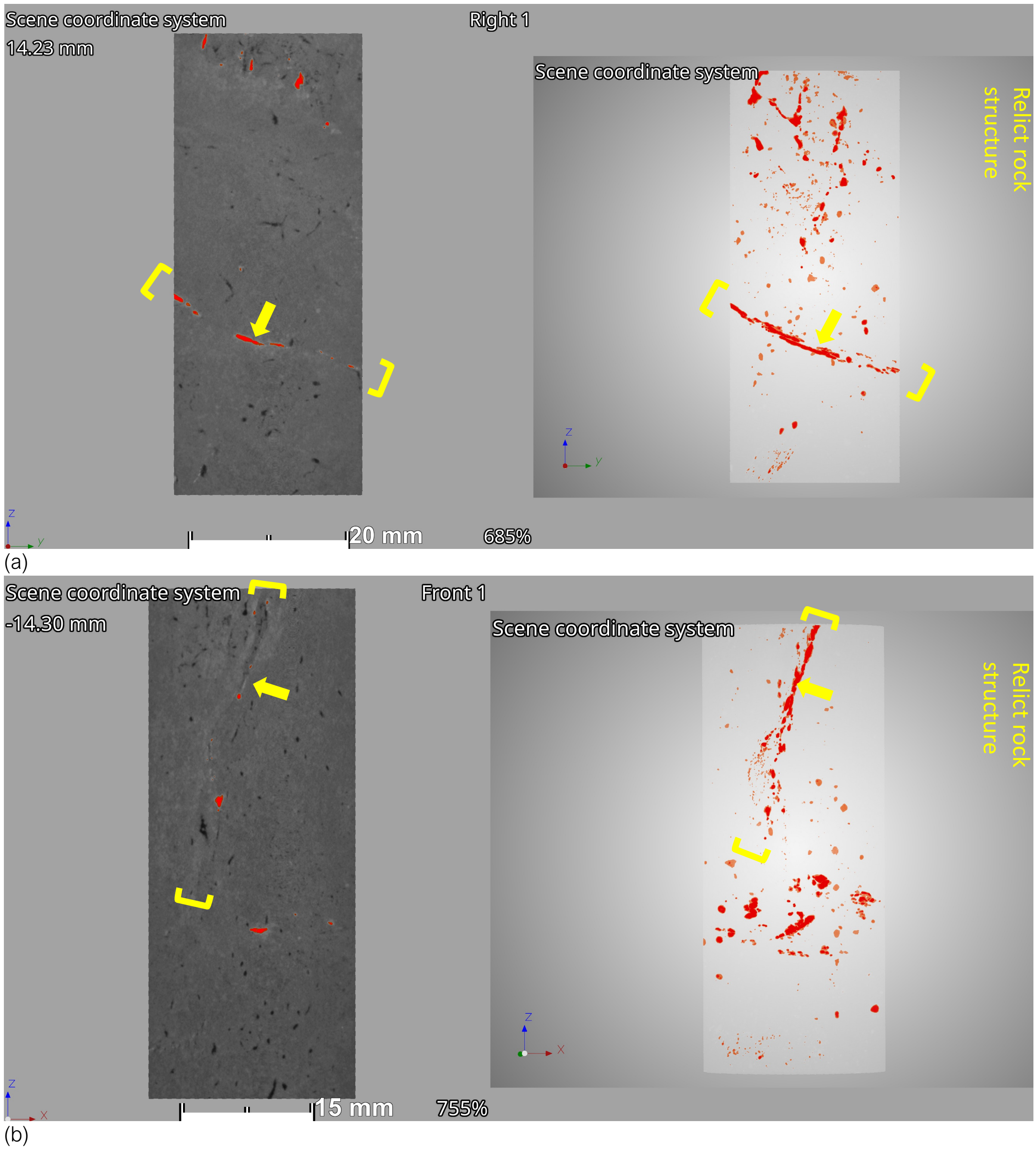

Figure 7-10 (a) Sample 1357 2D slice right view (left) and 3D density contrast (right); (b) front view (left) and 3D porosity distribution (right)

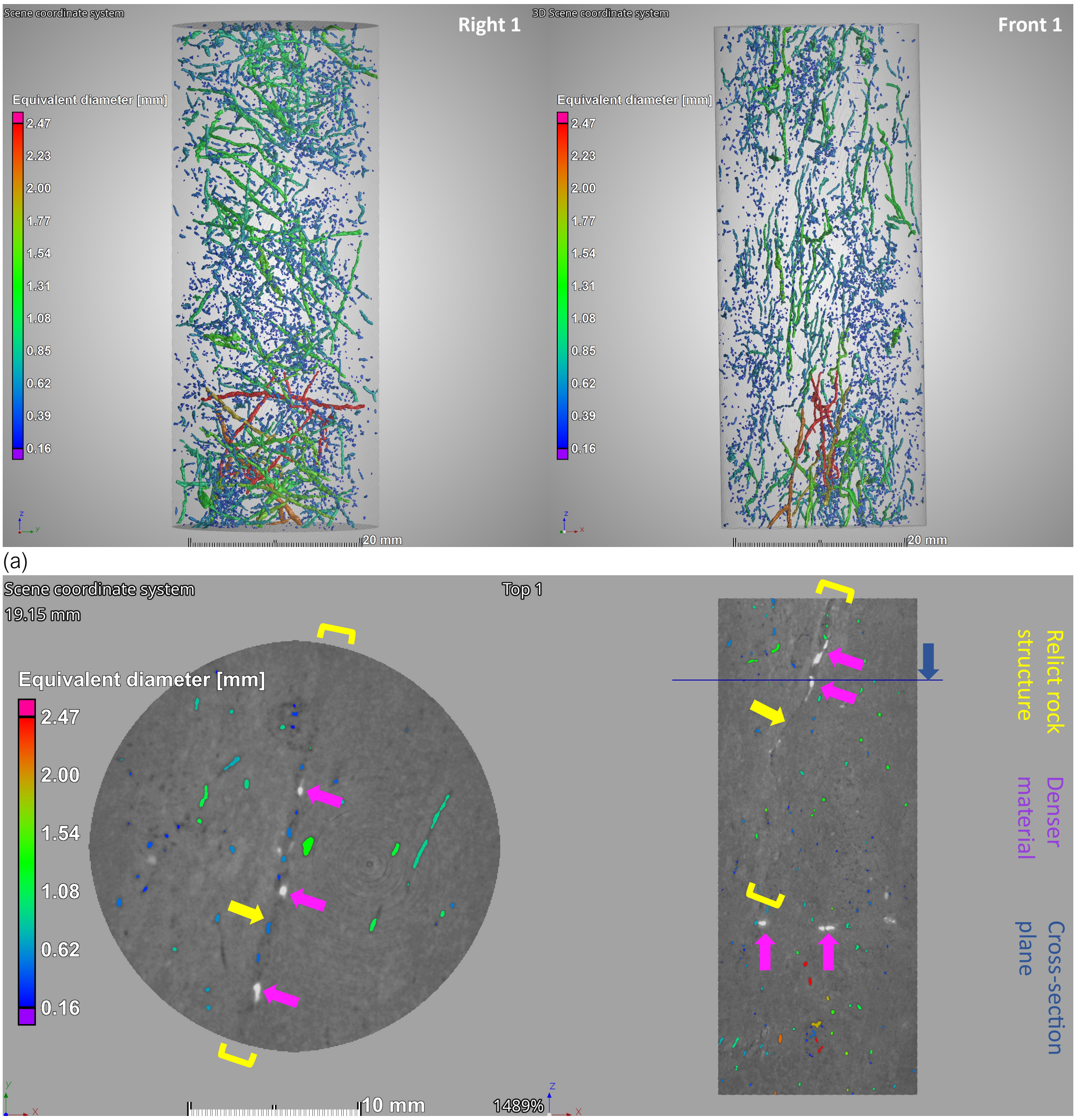

(a)

(b)

Figure 7-11 (a) Sample 1357 3D porosity model with right view (left) and front view (right); (b) with 2D slice overlay top view (left) and front view (right)

Figure 7-12 (a) and (b) show denser pedogenic formations in possibly a relict rock fracture that has eroded and changed shape over the weathering process. The density contrast has been stacked in Figure 7-12 (b) where the red is the densest and orange is slightly less dense. This was done to see if the denser material exists in the completely weathered rock matrix. The weathering has resulted in relatively thick infill material. This fracture could have formed through volumetric strain during the weathering of an existing major joint that was a preferred flow path in the original parent rock mass. The denser material occurs as 1.00 to 2.00 mm, rounded, nodules in the infill material with portions of the facture sidewall having pedogenic coatings. Other, subrounded to sub-angular grains can be seen in the infill material. Within the completely weathered rock matrix, weathered rock grains can be seen with very little to no material being highlighted in the density contrast.

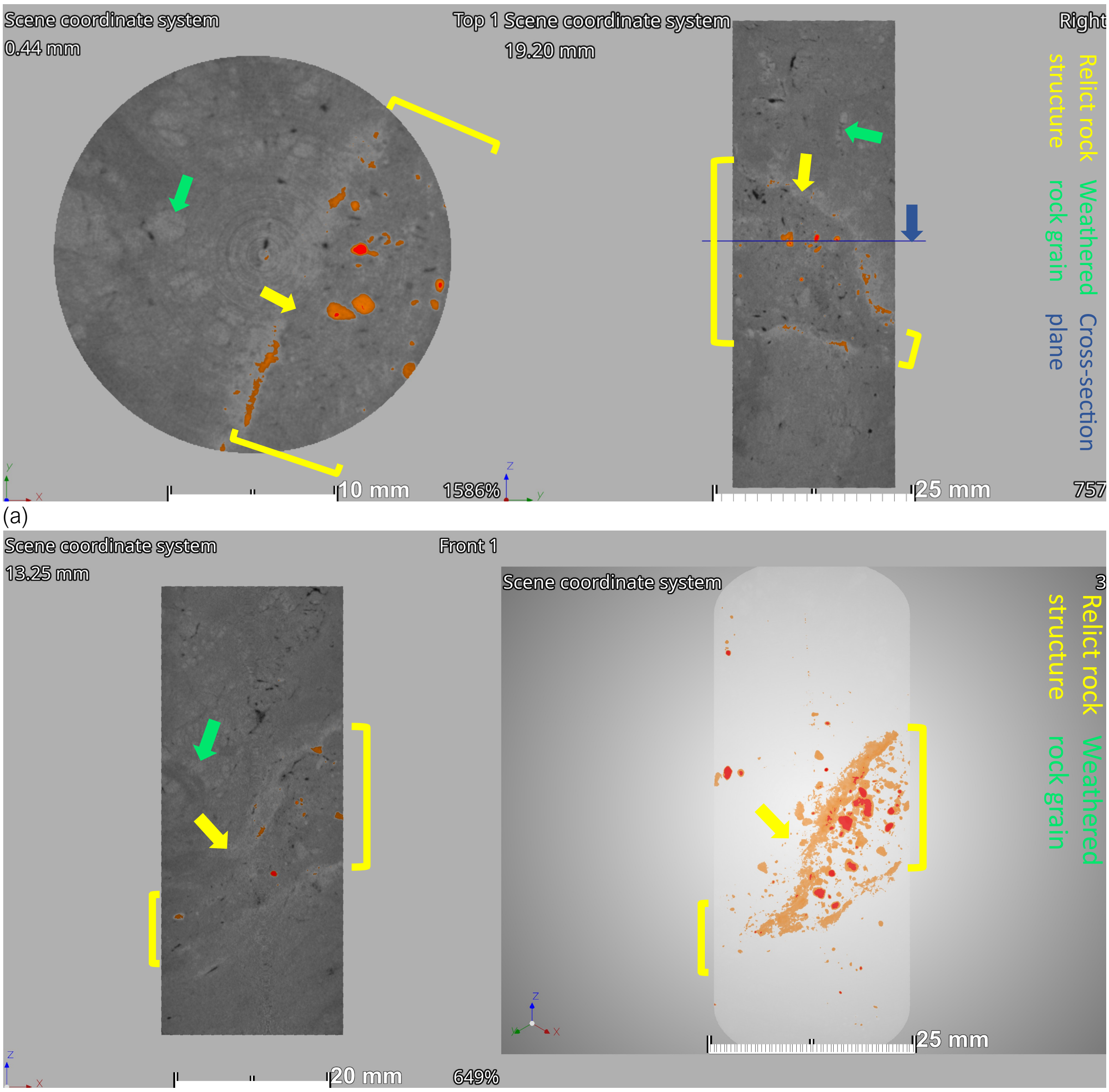

(a)

(b)

Figure 7-12 (a) Sample 1354 2D density contrast with top view (left) and right view (right); (b) with 2D slice front view (left) and 3D density contrast (right)

This sample provides a distinction of fabric characteristics of completely weathered rock and infill material within a possible preferred flow.

The 3D porosity model is shown in Figure 7-13 (a) and reveals there is a preferred pore orientation within the sample that follows the same direction as the infilled fracture. Focusing on the top portion of the sample, a distinction can be made on a possible open fissure as shown in Figure 7-13 (b). Here the fissure forms a series of connected and disconnected pores with no indication of dense material within the structure itself. It is expected the fissure has recently opened due to volumetric strain during weathering and therefore there has not been enough time for pedogenic deposits to occur within this fracture. The fissure is curvilinear in shape in both the vertical and horizontal directions.

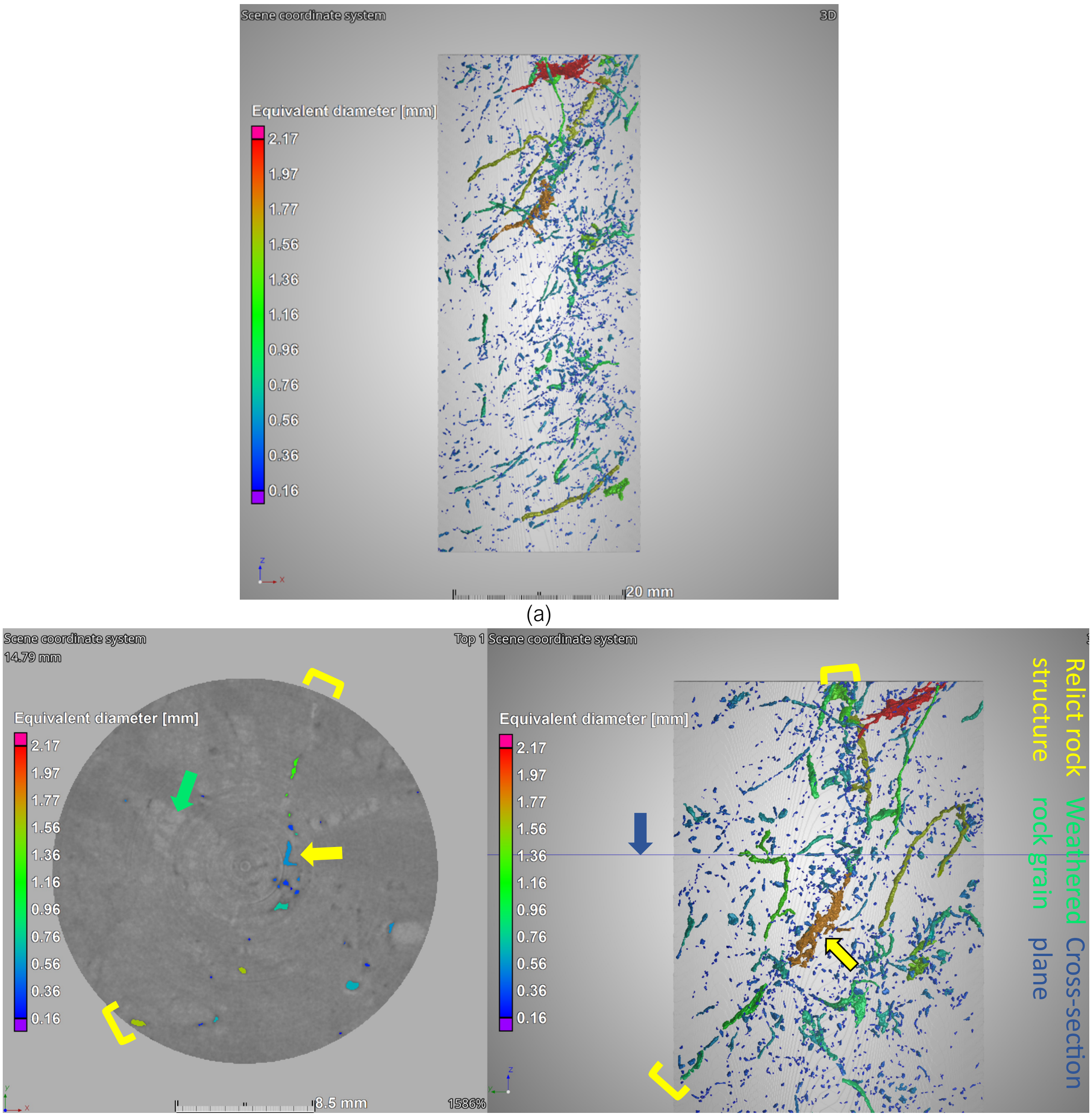

(a)

(b)

Figure 7-13 (a) Sample 1354 3D porosity model; (b) from top view (left) and 3D porosity model (right)

The 2D slice with the density colour contrast and 3D density model for sample 2842 is shown in Figure 7-14 (a). The sample has lost the majority of the relict rock structure and the pedogenic deposits are mostly rounded and do not follow or exist within a defined relict rock structure. A partial relict structure in the lower portion of the sample persists and is shown in Figure 7-14 (b).

Figure 7-15 reveals how highly voided the most weathered sample 2842 is compared to the less weathered samples retrieved from the same profile. The largest void, shaded in red, is seemingly a root that has propagated through the matrix and created an open root channel. The 2D slices and 3D models indicate the residual soil has lost the original rock structure that is maintained in the completely weathered rock.

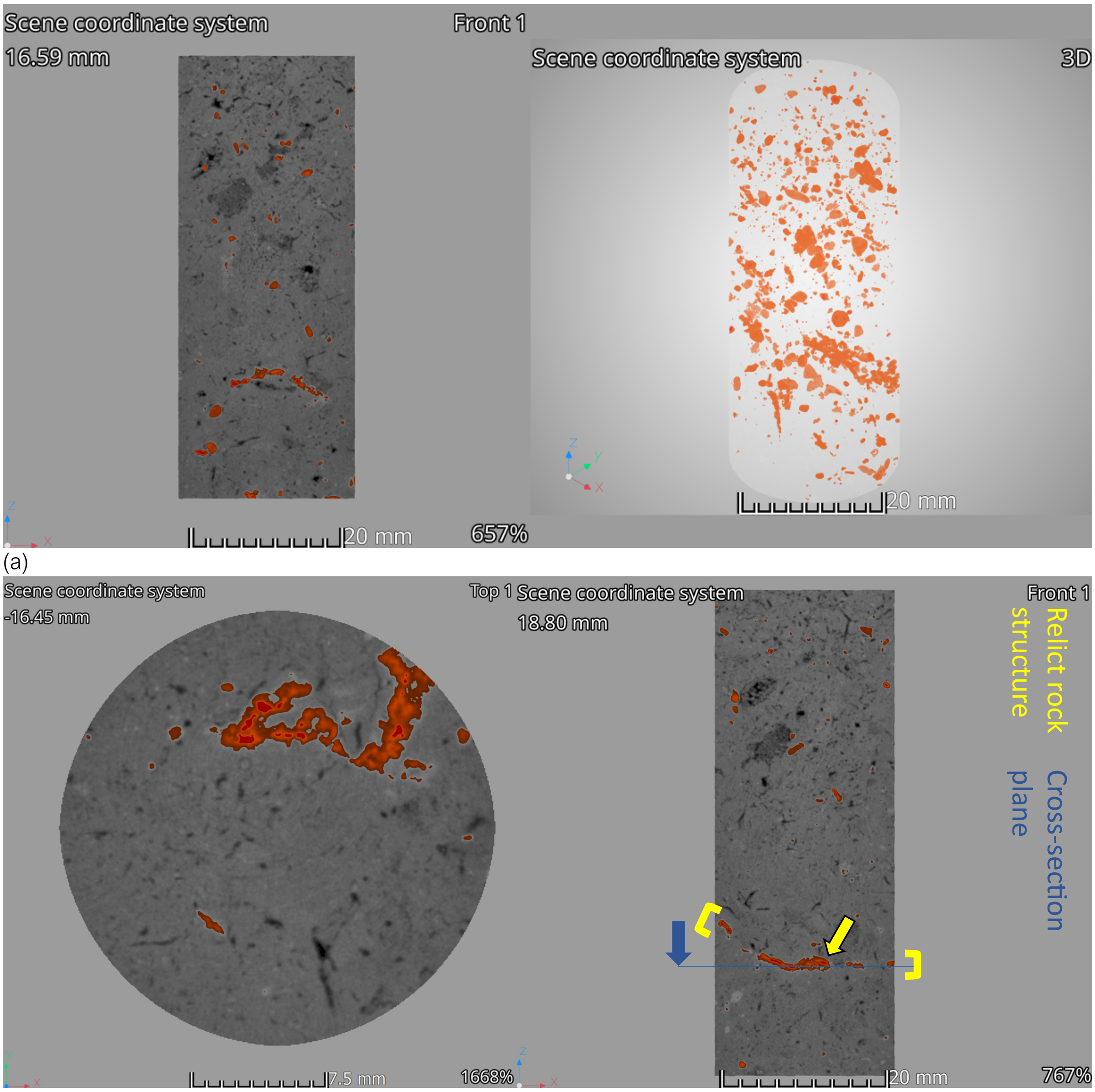

Figure 7-14 (a) Sample 2842 2D slice from front view (left) and 3D view with density contrast (right); (b) from front view (left) and 2D density contrast (right)

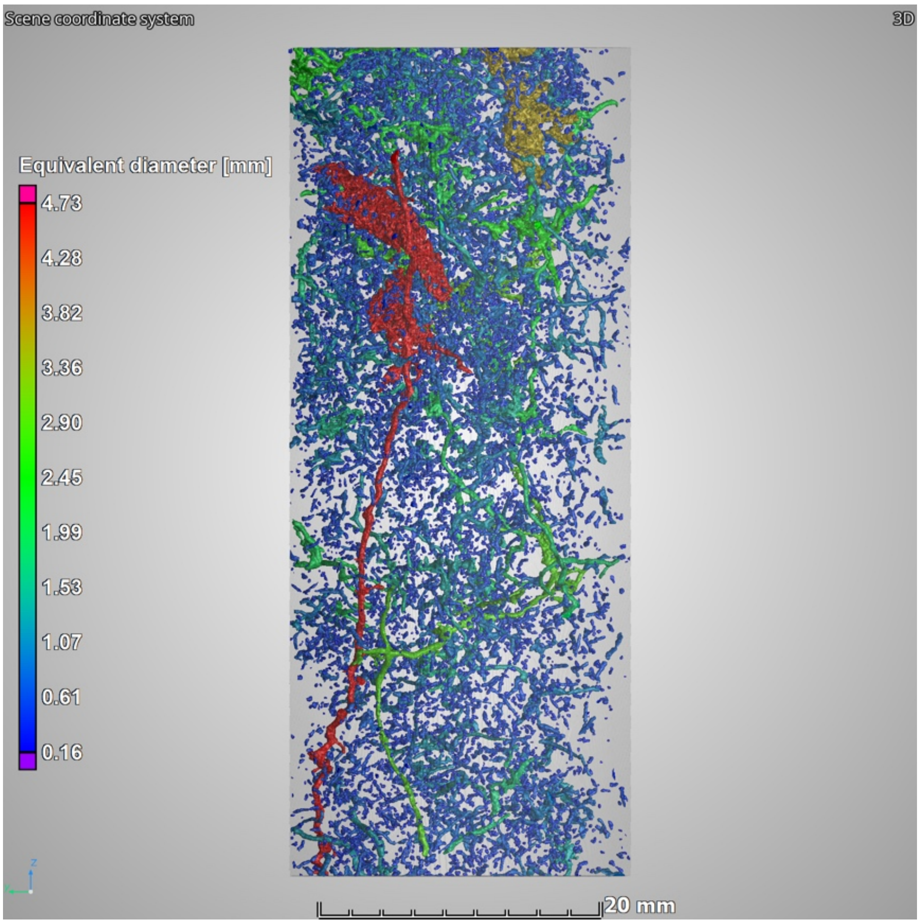

Figure 7-15 Sample 2842 3D porosity model

The XRCT samples at the Tzaneen site comprised two (2) block samples taken from the completely weathered diabase (sample 2829) and residual diabase (sample 2828), respectively. Figure 7-16 (a) presents a 2D scan of the sample 2829 with the density contrast applied, showing both top and front views. The densest portion of the material is shaded in red, which is surround by the lighter shaded areas representing varying quantities of possible albite and amphibole (actinolite) minerals that have survived weathering. The black-shaded regions indicate open pores. The outline of the modelled pores is shown in Figure 7-16 (b). The pores between the mineral grains, outlined in green and blue, have an orientation in the same direction of the vertical structure outlined in purple.

Referring to Figure 7-17 (a), the focus is placed on the micropores between the grains with the modelled pore outlined in green and blue. The pores have an orientation that is governed by the weathered rock mineral grains and forms linear or 90° cross shaped pores. The density colour contrast is applied in Figure 7-17 (b), and it can be seen the densest minerals, probably amphibole and albite, govern the shape of the pores. These two minerals have mineral cleavages of 120° to 60° and 90°, respectively, which is the orientation of the pores. The density contrast shows the densest portion in red is surrounded by a lighter shaded area which in turn is surrounded by the open pore. This indicates that the weathering of the mineral grains, is most intense at the grain boundaries or cleavage breaks and decreases inward towards the grain.

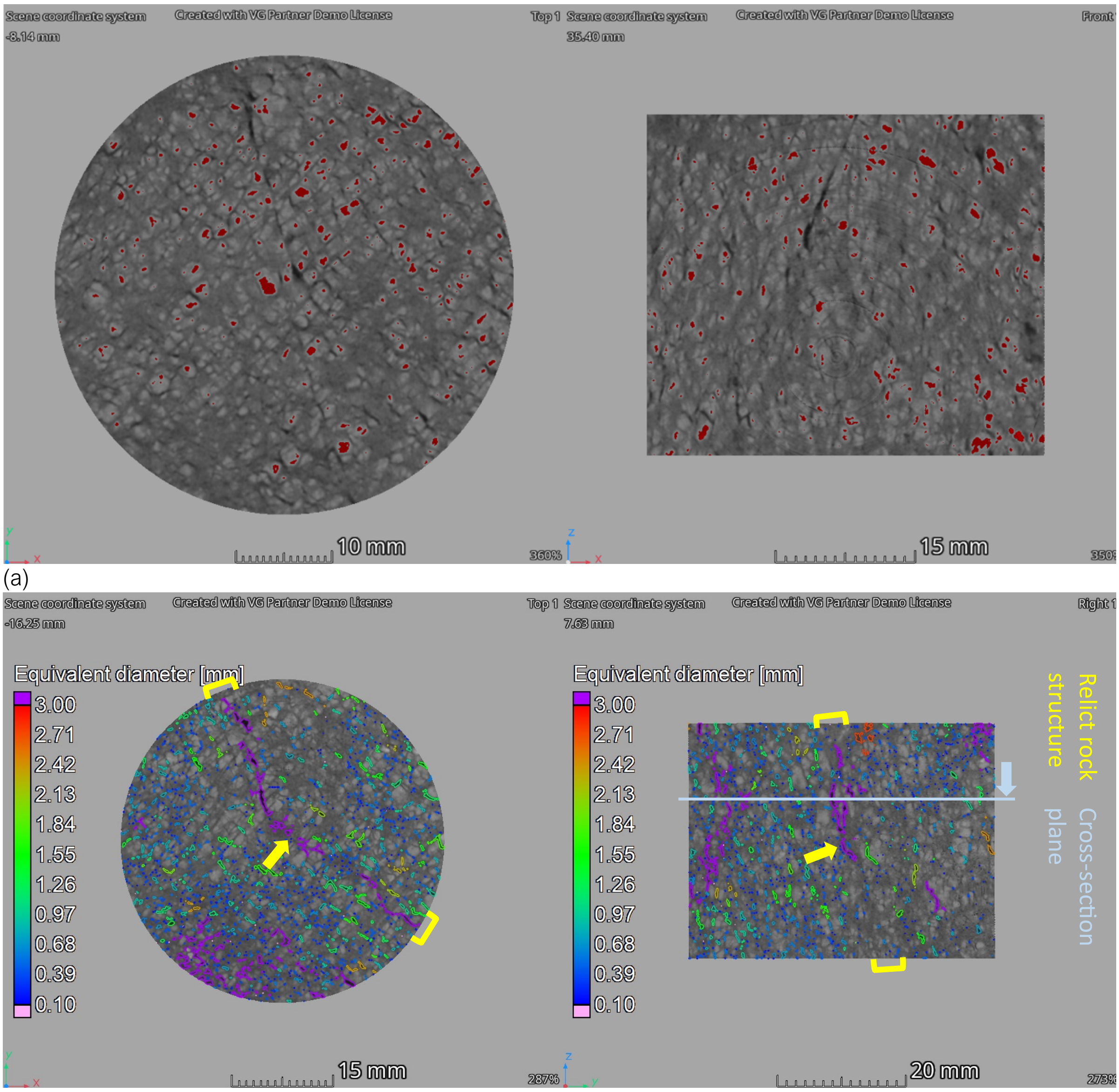

(a)

(b)

Figure 7-16 (a) Sample 2828 2D slices from top view (left) and front view (right) with density colour contrast; (b) 2D pore modelling for top view (left) and right view (right)

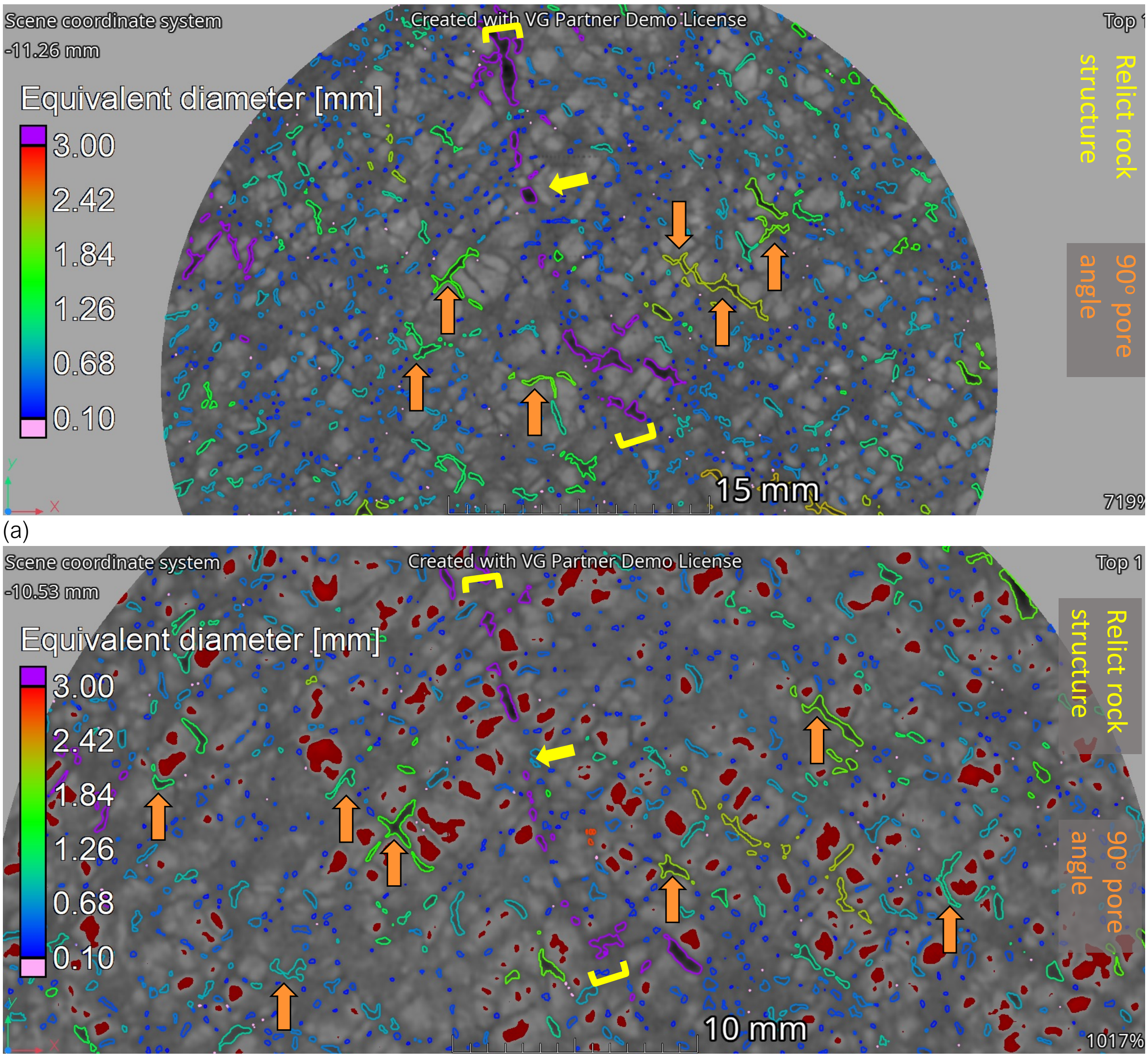

(a)

(b)

Figure 7-17 (a) Sample 2829 2D slices from top view with pore modelling; (b) 2D pore modelling for top view with density colour contrast

The 2828 sample is highly voided, and no remnants of relict rock structure is shown in Figure 7-18 (a). Figure 7-18 (b) shows evidence of fissures, as indicated, reworked areas from biotic activity and rounded open root channels. The 3D porosity model shows there is dual porosity system present, namely the large fissures and bioactivity openings and tunnels, greater than 18.0 mm equivalent diameter, surrounded by much finer, more spherical pores colours in blue. No pores between the equivalent diameter ranges of approximately 6.00 mm and 14.00 mm were identified.

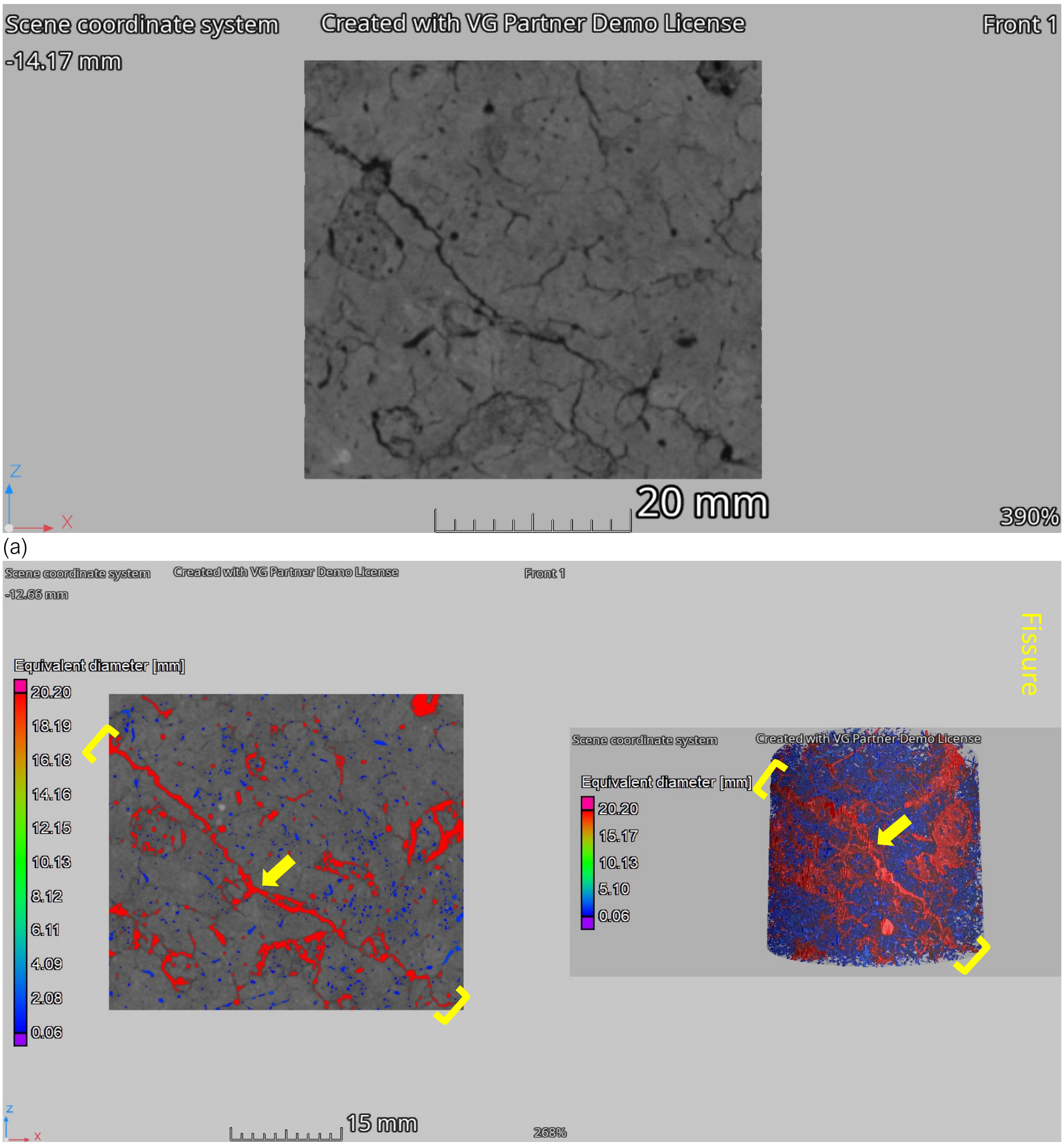

(a)

(b)

Figure 7-18 (a) Sample 2828 2D slice from front view; (b) 2D pore modelling for front view (left) with 3D pore modelling (right)

The two (2) tube samples retrieved at the Graskop site were within 300 mm from one another. The reason for separating the profile into completely weathered rock and residual dolomite on a short profile was due to the presence of pedogenic nodules and fissures in the residual soil. Referring to Figure 7-19 (a) and (b), the difference in the presence of the round pedogenic nodules is represented by the red coloured density contrast. The nodules are more abundant in the residual soil and are larger, suggesting the material has been under pedogenic processes for a longer period than the completely weathered rock.

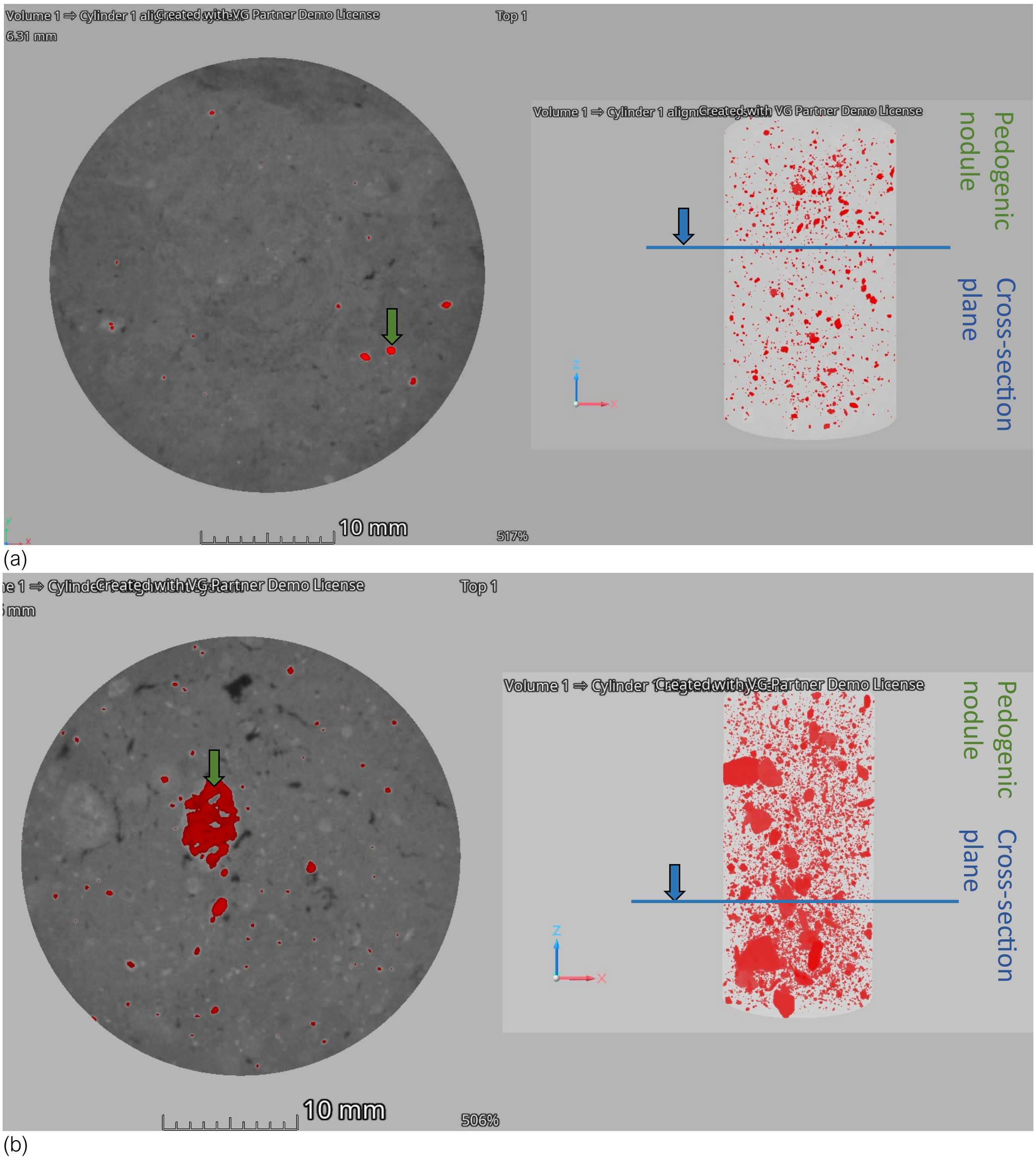

Figure 7-19 (a) Sample 2833 2D slice from top view (left) and 3D model (right); (b) Sample 2832 2D slice from top view (left) and 3D model (right) with density contrast applied

Figure 7-20 presents the top view of the two tube samples with the modelled pore spaces and density contrast applied. The completely weathered rock sample 2833 has scattered pores that are less than 1.00 mm in equivalent diameter and a few pore sizes between 1.50 mm and 1.00 mm equivalent diameter. It is expected the majority of the pores spaces in sample 2833 will be smaller than 0.06 mm in diameter which could not be identified and modelled by the XRCT equipment as this exceeds the smallest measurable voxel size. The residual dolomite sample 2832 has generally larger pores which are frequently greater than 1.00 mm and elongated in shape. No pore orientation seems to exist in either sample. The relict rock structure is expected to occupy the micropore space and will be too small to be modelled by the XRCT.

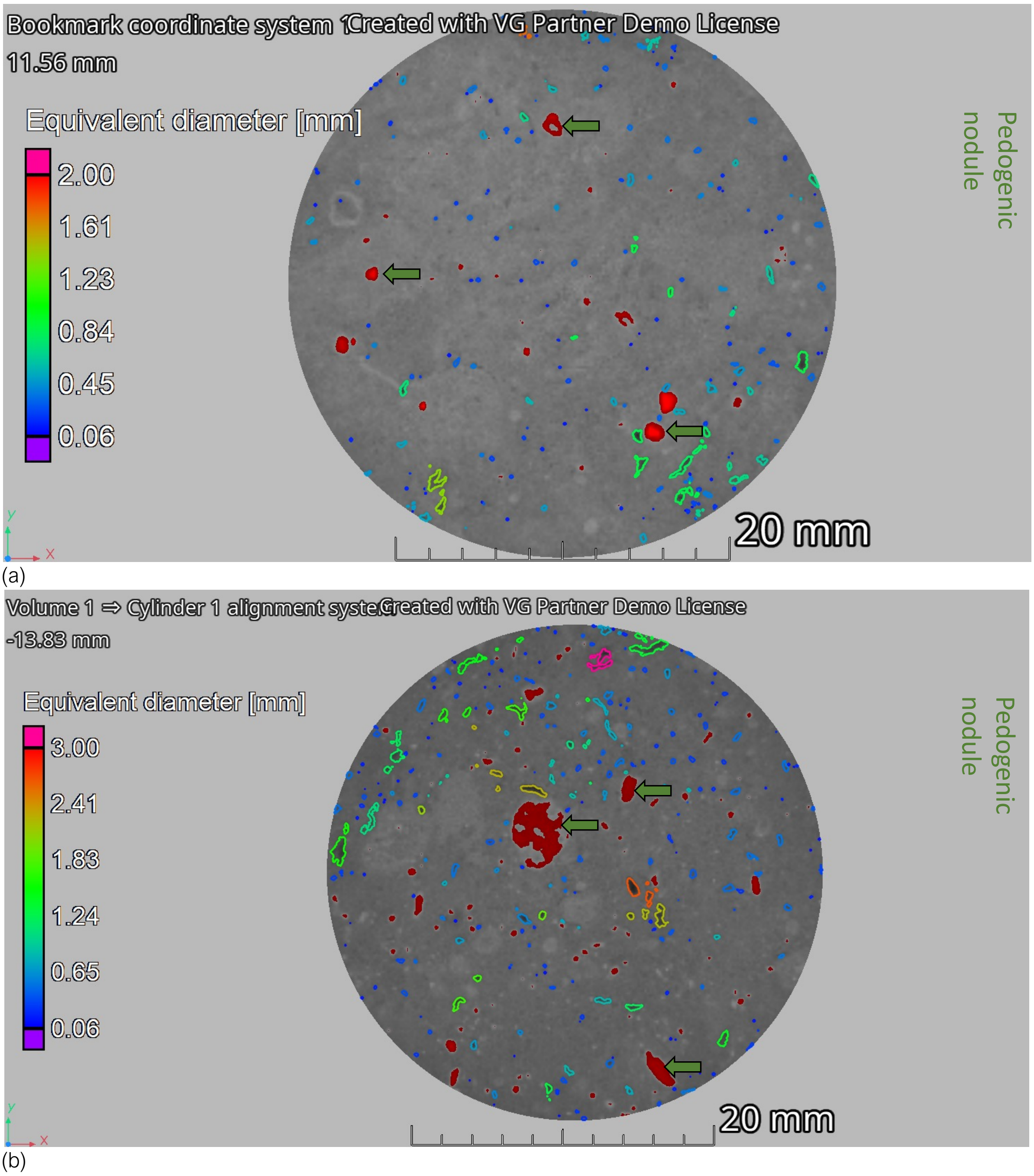

Figure 7-20 (a) Sample 2833 2D slice from top view; (b) Sample 2832 2D slice from top view with density contrast applied and pore modelling

7.3.6 Soil Water Retention Curve

The drying Soil Water Retention Curves (SWRCs) for the structured and remoulded samples are shown by plotting the measured suction values from the pore pressure tensiometer (PPT) against calculated degree of saturation (*Sr* – SWRC) in Figure 7-21. The specimens' parameters are summarised in Table 7-6.

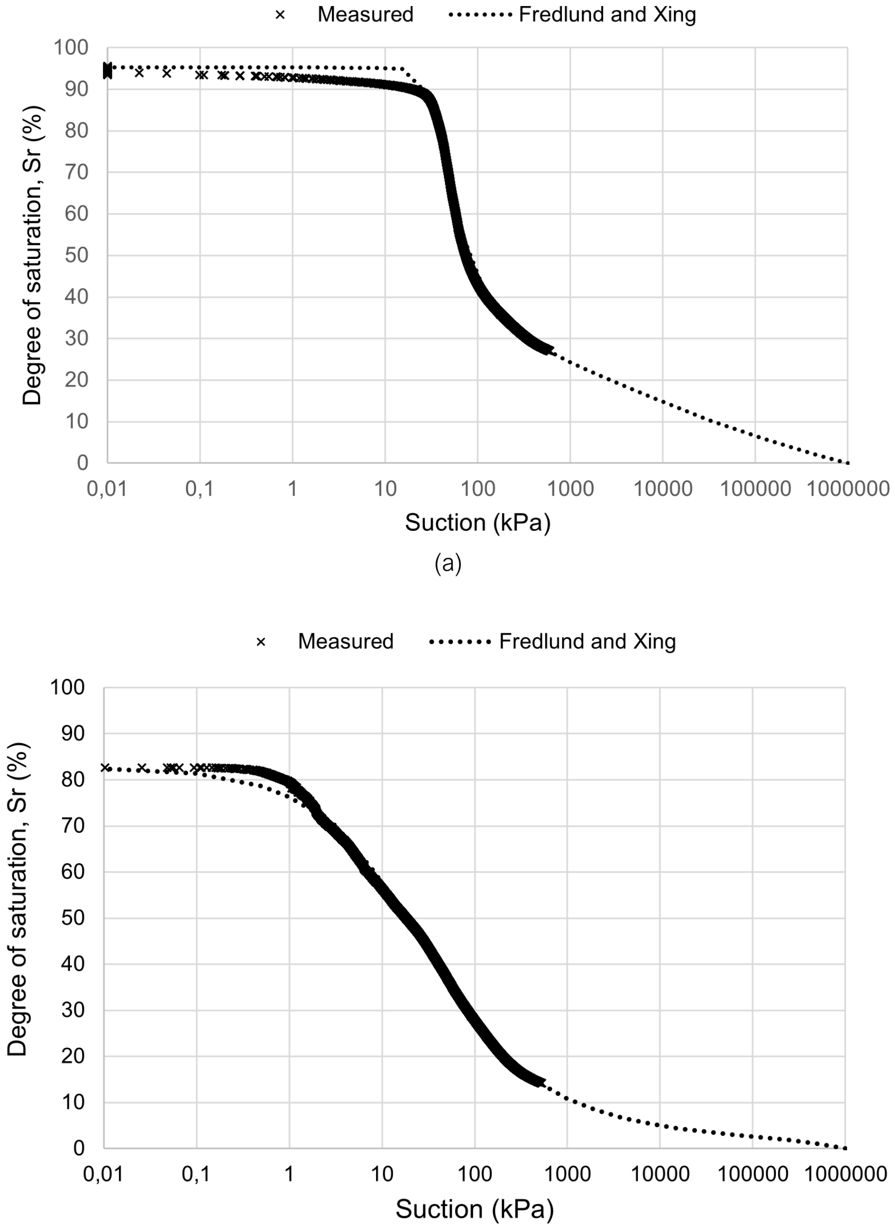

(a)

(b)

Figure 7-21 Suction values measured using PPT of (a) structured and (b) remoulded specimens with the fitted curve (taken from Swart et al. 2021)

The measured suction data has been used to determine fitting paraments, as discussed by Fredlund and Xing (1994), and these are presented in Table 7-7. The two fitted curves of the *Sr* – SWRC are plotted in Figure 7-22. The two fitted curves are plotted on suction versus volumetric water content (θ – SWRC) in Figure 7-23.

Table 7-6: Summary of SWRC test results (Swart 2019)

Sample ID	Sample condition	Dry density (kg/m^3)	Void ratio	Initial moisture content (%)	Air entry value (kPa)	Suction value (kPa) at degree of saturation (*Sr*)		
						40% saturation	60% saturation	80% saturation
2930	Structured	309	8.32	300	20	146	62	44
	Remoulded	746	2.18	87.6	0.8	146	32	5.5

Table 7-7: Summary of fitting parameters (Swart et al. 2019)

Sample ID	Sampled material	Fitting paraments		
		a	*n*	*m*
2930	Structured	35.7	5.13	0.46
	Remoulded	5.00	1.00	0.92

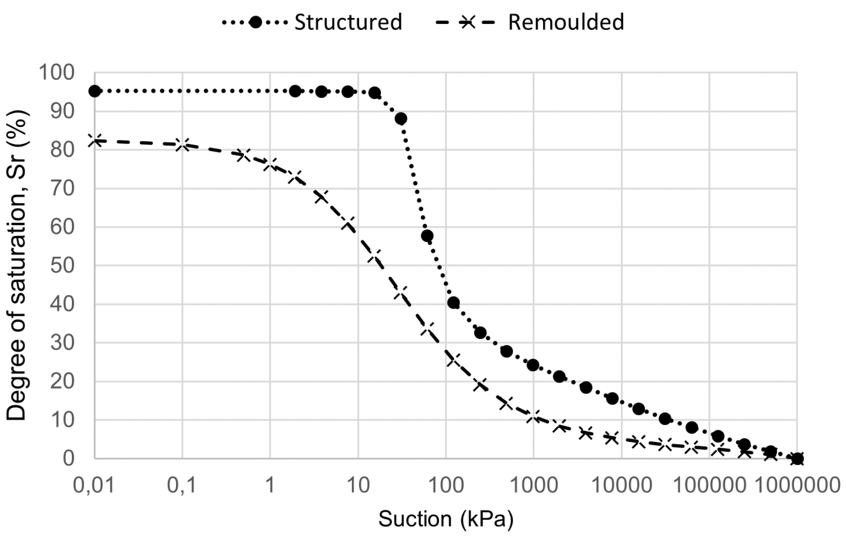

Figure 7-22 Fitted curves for structured and remoulded specimens on *Sr* - SWRC (taken from Swart et al. 2021)

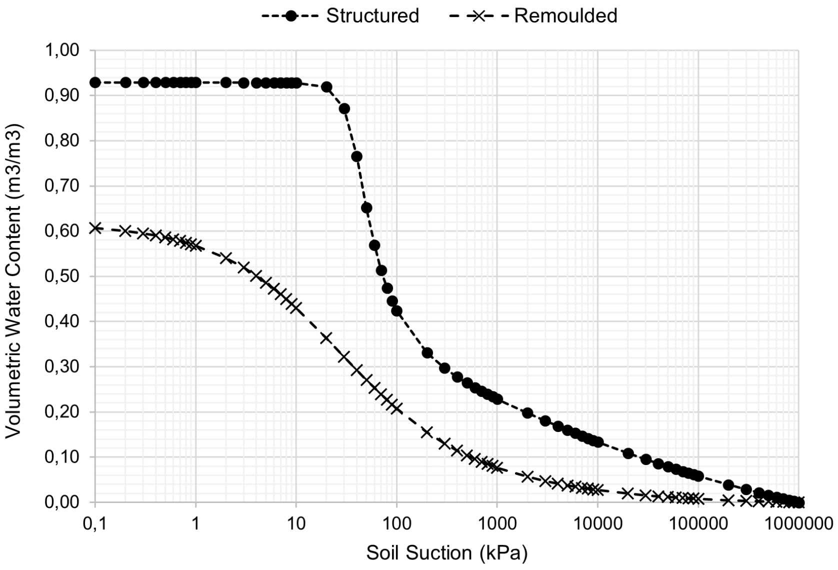

Figure 7-23 Fitted curves for structured and remoulded specimens on θ - SWRC (taken from Swart et al. 2021)

7.4 Conclusion

The testing framework provides results on the materials’ chemical, physical, and structural characteristics. The samples were taken from weathering profiles that were easily accessible via machine excavation or hand excavation with a pick and shovel. The exposed profiles were appropriately logged as guided by the latest logging standards in South Africa (Dippenaar et al. 2024). The testing results reveal all the samples break down to silt mixtures and generally have low permeability values. The testing comprised fundamental and well understood testing methodologies such as the compression test in the oedometer and saturated permeability testing in triaxial cells. These results are supplemented with advanced visual analysing techniques, namely the XRCT scan. The data from the XRCT scan was processed in the relevant software to assess the porosity, relict rock structure, if any, and to determine the usability of such investigation equipment in geotechnical projects. The behaviour of the residual soil and completely weathered rock under load was assessed and results reveal the presence of relict rock structure generally provides a positive influence on the strength and stiffness of the material.

8 Discussion and Observations

The findings of the literature review and test results of the sampled material will be discussed. To fully understand the impact of weathering, first the individual profiles will be assessed and observations elucidated. This will be followed by comparing the findings from each sample location and relevant literature for the igneous rock and dolomite rock profiles, respectively. The two major geology types will then be compared and determine the influence of weathering and anthropogenic remoulding of the materials from the profile.

The state of weathering of each horizon encountered in the igneous weathering profile during this study will be assessed based on the chemical weathering indices recommended in literature, namely the chemical index of alteration (*CIA*) and weather intensity scale (*WIS*).

The robust weathering (*RW*) method, as described in Cho and Ohta (2022) provides a chemical weathering indices that does not include SiO_2, CaO, and P_2O_5. The largest influence to determine the weathering in this method is the leaching out of sodium (*Na*) and accumulation of aluminium (*Al*). Completely weathered rock and residual soils typically have a near zero value for *Na* because all the *Na*-bearing minerals would have decomposed under moderately to intense weathering conditions. Furthermore, most of the samples are at the *soil-end* of the weathering process and have a high amount of kaolinite and therefore a high quantity of *Al.* The *RW* methods tends to indicate a very high decomposition value, approximately greater than 97%, for all the samples and may be an overestimation of the degree of weathering. The RW method was excluded from this study for this reason.

8.1 Weathering profiles at sample locations

8.1.1 Tzaneen weathering profile

Through the visual assessments on site and the pore modelling from the XRCT scan data, the completely weathered diabase is a highly structured soil with a strong presence of relict rock structure. Relict rock fractures with black staining on the surface, as shown in Figure 7-1, were observed in the rock profile and were detected in the pore modelling. The staining comprises metal oxides that formed through seasonal water flow (Van der Merwe 1964; Banerjee et al. 2016), but the metal oxide was not identified during the XRCT scan. It is expected the staining is extremely thin and was not determined to be of high-density material through x-ray attenuation, which is influenced by the thickness of the material which it passes through.

Figure 8-1 summaries the texture class based on the clay factor and sand content, degree of weathering according to the *WIS*, and percentage of *CIA* compared to the m_v value at 100 kPa for the undisturbed and remoulded 2828 and 2829 samples.

The chemical testing results show the completely weathered rock comprises a relatively large amount of primary rock minerals such as actinolite, microcline and albite. The presence of smectite suggests the material has been exposed to moderate weathering conditions according to Summerfield (2014).

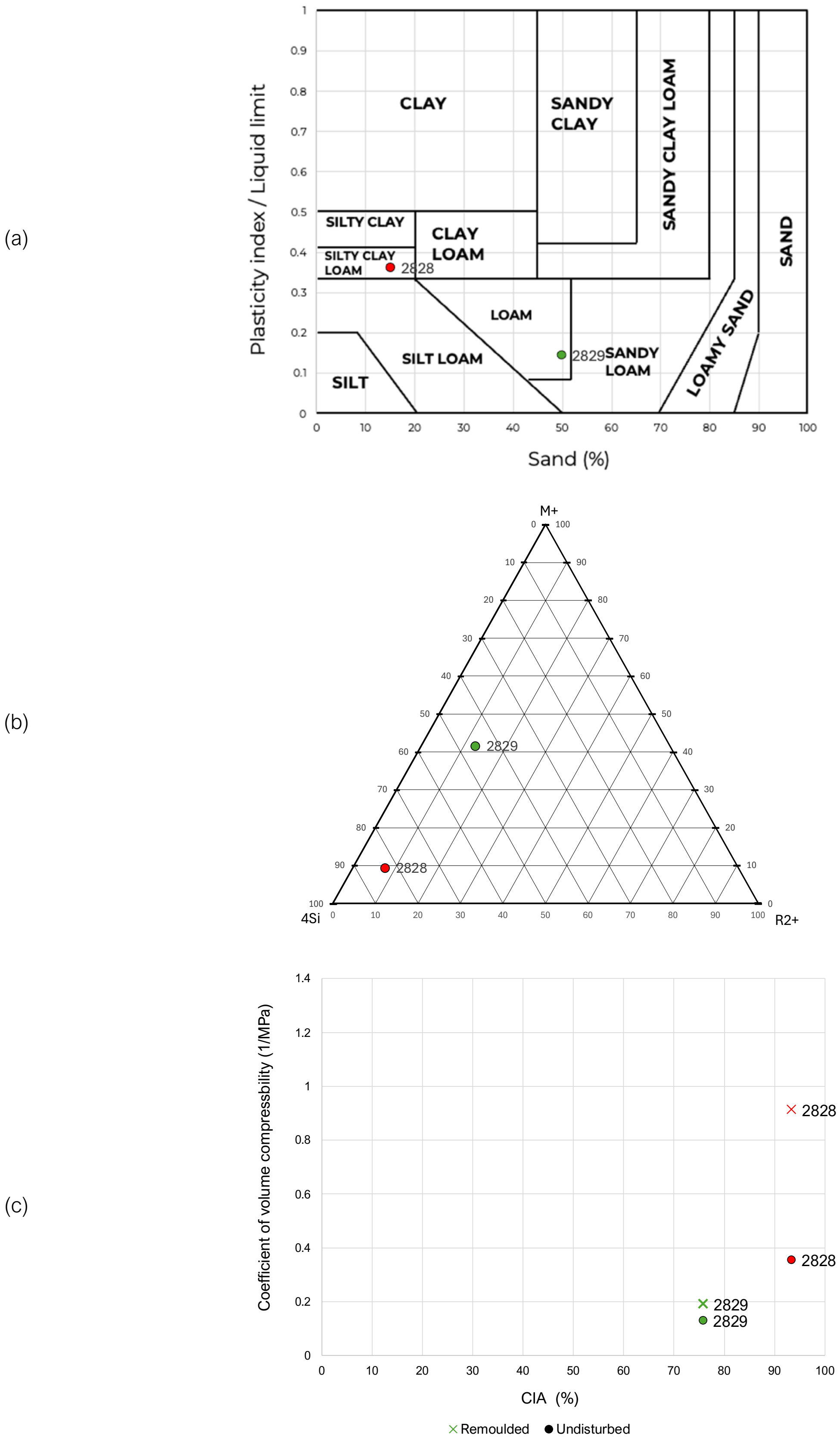

Figure 8-1 (a) Texture classification (Moreno-Maroto and Alonso-Azcárate 2018; 2022) (b) Weathering intensity scale (*WIS*) (Meunier et al. 2013) (c) m_v value calculated for stress increment from 50 kPa to 100 kPa vs chemical index of alteration (*CIA*) (Nesbitt and Young 1982) for the Tzaneen samples

This agrees with the weathering indices as presented in Figure 8-1. The presence of XRCT data agrees well with this and rock mineral grains can be identified based on the cleavages.

According to Wilson and Jones (1983) and Wilson et al. (2004), the dissolution of amphibole minerals, of which actinolite is a member of, is strongly influenced by the relict structure of the mineral grain, leading to surface etching and cleavage breaks that govern pore orientation during weathering. This is clearly seen in the near-perpendicular pore orientations within the moderately decomposed rock minerals, which has two cleavage planes intersecting at approximately a 90° to 120° angle, as shown in Figure 7-17. The centre of these mineral grains is the densest portion of the rock and suggest the least weathered for this sample. Moving outward from these centres, the surrounding region is shaded in a light grey before reaching the block open pore space.

Amphibole minerals decompose through surface reactions starting at the edges and progressing inward, often altering into secondary products like various clay minerals and Fe-oxides, or completely decomposing without leaving a weathering product, resulting in open pores (Colman 1982; Wilson 2004). The surrounding dark grey portions of the sample represent the weathering products of plagioclase and pyroxene that had formed the kaolinite. It is expected that the pores within the kaolinite portion of the sample are smaller than the voxel size and thus could not be detected. This indicates that the geometry of the initial porosity formed during the early stages of weathering is governed by the rock mineral's structure, chemical defects, and stress history. Most of the modelled pores are located near or on the mineral grain boundary. Preferred pore orientation has implications on the strength and stiffness of the material (Griffiths et al. 2017) and cause a variation in the permeability value depending on testing orientation (Dippenaar et al. 2022).

The visual and chemical assessments of the residual diabase show this material is far more decomposed, which no relict rock structure present on a macro and micro scale. Figure 8-1 shows the residual diabase is much more weathered than the completely weathered rock according to the *CIA* and *WIS* index systems. The largest structure identified in the sample is most likely a fissure which was encountered on site. The material comprises mostly quartz and kaolinite with lesser muscovite. The aluminium detected in the elemental chemical test forms part of the kaolinite and muscovite minerals. Surprisingly, no hematite or goethite was identified with the iron content being approximately 22% of the sample. The iron probably exists as an oxide grouped into the muscovite weight percentage, that provides strength to the intact sample as can be seen on the compression test results.

Both samples performed better in the undisturbed state when placed under a load in the oedometer. The remoulding of the samples caused more strain to be experienced after the structure was destroyed. The undisturbed completely weathered diabase underwent a slight strain hardening, according to Wesley (2019), with the coefficient of compressibility slightly decreasing as the load increased. No yield pressure was observed, and this suggests the structure, that was identified in the XRCT scan, remained intact. The residual soil underwent much more strain compared to the completely weathered rock but did not express a yield pressure.

The XRCT scan showed the material is highly voided and it is expected the material's structure, which is expected to have formed from pedogenic processes, provided some stiffness and the material consolidated into a slightly denser packing as the load increased.

The compression behaviour for remoulded samples from this profile is seemingly linked to the presence of structure and clay content which is influenced by the state of weathering, as shown in Figure 8-1 (c) (Rocchi et al. 2017; Bonnet et al. 2022). The higher the plasticity of a fine-grained soil, the more strain is expected once the material is remoulded (Saha et al. 2024). The higher compression experienced by the remoulded residual soil is a function of the loss of structure, higher plasticity and low initial dry density. The same can be applied to the remoulded completely weathered diabase, where it experienced relativity a much lower amount of strain due to the much lower plasticity and clay content and higher initial dry density.

8.1.2 Dullstroom weathering profile

The Dullstroom site comprised three (3) samples taken from the completely weathered rock. Samples 1354 and 1357 were taken near the completely weathered rock and residual soil interface, and sample 2835 was taken approximately 4.00 m below ground surface and is considered the least weathered of all the samples. This was done to visually assess the influence of weathering within the same horizon, based on geotechnical parameters, on the structure. The structure was easily broken down by moderate pressure from fingers into a silt, as shown in Figure 8-2. Note the black staining on the joint surfaces.

The chemical and visual assessments revealed the rock comprised primary rock minerals such as microcline. The light grey shaded areas in the XRTC scan are most likely decomposed microcline mineral. The black and *dense* material in the joints of sample 2835 is most likely goethite as this has a higher density at 3.8 g/cm^3 compared to the microcline at 2.6 g/cm^3. Goethite can form through pedogenic processes in preferred moisture flow channels such as joints (Van der Merwe 1964; Banerjee et al. 2016). The pedogenic deposits almost always occurred in the relict rock joints in the completely weathered rock. Assessing the tube sample material and the XRCT imagery, it is evident that the structure becomes less prominent with increased weathering when moving up the profile. The pore distribution generally stayed in orientation to the major rock fractures in all the completely weathered samples.

Figure 8-3 (a) indicates that all the completely weathered rock samples excavate as a silt mixture and the residual soil has slightly higher clay content and plasticity. This agrees with the XRD results that showed a much higher quantity of kaolinite. This is expected for a more weathered soil, as shown in Figure 8-3 (b) (Van der Merwe 1964; Bonnet et al. 2022; Wang et al. 2024). The XRCT imagery showed the material lost all relict rock structure and the pore structure was governed by pedogenic and biotic processes. According to the tube samples the dry density decreased as weathering increased moving up the profile, as shown in Figure 7-2. However, according to the oedometer samples, the completely weathered rock had lower than expected dry density which was lower than the residual soil. This may have occurred for a few reasons, namely sample disturbance or a less dense pocket was sampled in the completely weathered rock.

Figure 8-2 (a) Sample 2835 with structure intact (b) Sample 2835 after smeared with light finger pressure (photographs taken by D Swart)

It is expected that the completely weathered rock would have undergone a greater amount of strain since the initial parameters had a lower dry density and a higher initial void ratio compared to the residual soil. However, as can be seen in the oedometer results in Figure 7-8 and Figure 8-3, the completely weathered rock experienced less strain than the residual soil both for the undisturbed and remoulded samples. The structure in the undisturbed 2835 sample provided the stiffness to limit the total strain experience. Once the structure was lost through remoulding, the 2835 sample underwent a greater amount of strain compared to the residual soil undisturbed sample.

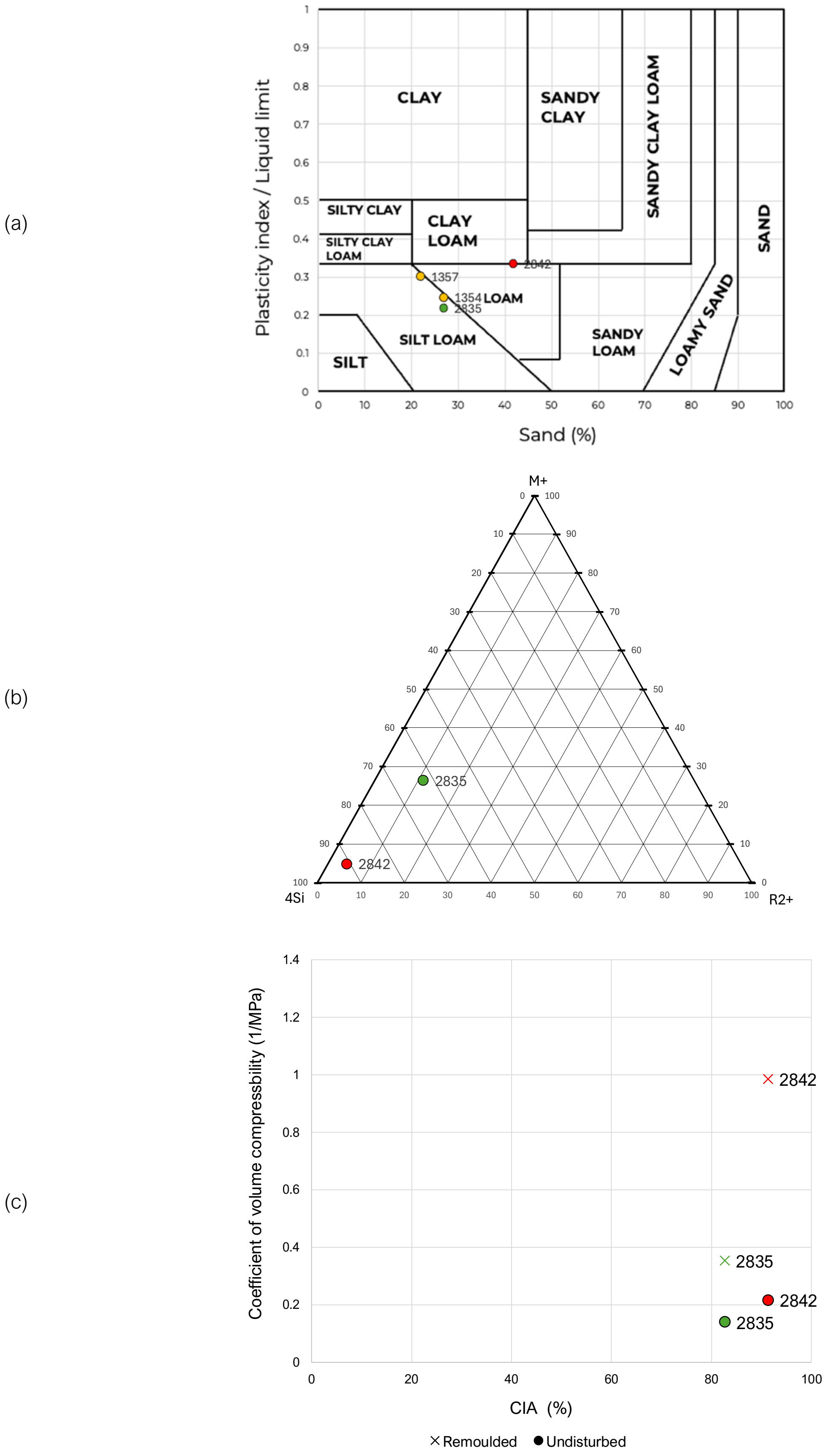

Figure 8-3 (a) Texture classification (Moreno-Maroto and Alonso-Azcárate 2018; 2022) (b) Weathering intensity scale (*WIS*) (Meunier et al. 2013) (c) m_v value calculated for stress increment from 50 kPa to 100 kPa vs chemical index of alteration (*CIA*) (Nesbitt and Young 1982) for the Dullstroom samples

8.1.1 R528 weathering profile

The 2830 and 2831 samples used in the XRCT scanner was too disturbed to gather any reliable data. The sample site was north facing, and the existing exposed surface was highly desiccated. A great deal of effort was put in to retrieved samples that retained moisture to preserve the soil structure. Referring to Figure 8-4, the residual soil has a moderate plasticity and comprises a mixture of clay and silt with lesser sand. The strength of the soil with the structure intact was low compared to other igneous rock weathered profiles. The sample underwent more strain once remoulded but not much more than the undisturbed sample, as shown in Figure 8-4. This is not expected considering the moderate plasticity of this sample. This may have happened as the structure in the undisturbed sample was already significantly broken which may have also caused the poor data quality in the XRCT scan.

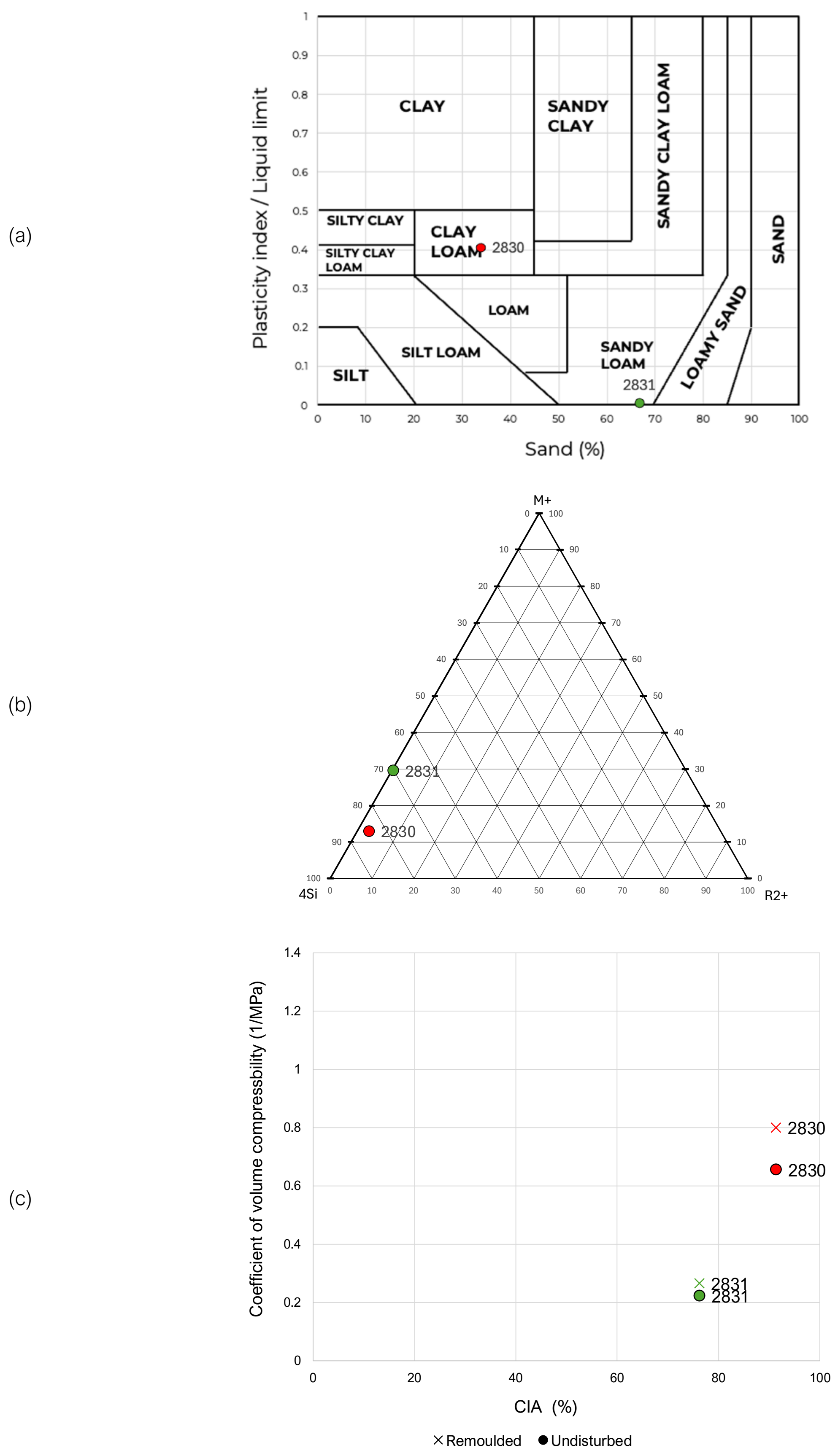

Figure 8-4 (a) Texture classification (Moreno-Maroto and Alonso-Azcárate 2018; 2022) (b) Weathering intensity scale (*WIS*) (Meunier et al. 2013) (c) m_v value calculated for stress increment from 50 kPa to 100 kPa vs chemical index of alteration (*CIA*) (Nesbitt and Young 1982) for the R528 samples

8.1.2 *Graskop weathering profile*

Dowding (2004) investigated the same profile and found both the wad and residual dolomite to be enriched in lithiophorite ($MnO_2(OH)_2$) with a relative increase in *Fe* content and pedogenic nodules in the residual dolomite.

The Graskop samples were retrieved within 500 mm of one another and as a result the two material types have very similar chemical components. Therefore, the degree of weathering is very similar according to chemical weathering indices, as shown in Figure 8-5. The grading is very similar; however, the sand content comprises two different material types. As was observed in the soil profile and the XRCT scans, the residual soil has a significantly higher quantity of moderately cemented pedogenic nodules. These nodules, which form in-situ, are expected to define the sand component of the sample. Highly weathered chert lenses, as shown in Figure 7-5, existed in the completely weathered rock that excavated as a sand. The XRD results show the completely weathered rock has approximately 7% more quartz, which can be interpreted as chert as they both comprise pure silica, compared to the residual soil.

Apart from the presence of nodules and fissures in the residual soil, the main difference between the two horizons, was the presence of a highly porous relict rock structure in the completely weathered rock. The pore geometry of the relict rock could not be identified in the XRCT. The average pore diameter of wad is typically in the range of micro- and nanometres in size (Swart et al. 2019). These pores are much smaller than the voxel size of the XRCT scanner and therefore could not be detected and modelled. When the structure was broken by hand in the field, free water was released from the structure and was present in hand. The broken-down material comprised a clayey silt which liquified in the free water, losing all strength. The in-situ moisture content recorded in the block samples and tube samples were higher than the determined liquid limit, which is typically of wad (Buttrick 1986; Swart et al. 2019).

Referring to Figure 7-8, the 2833 sample seems to yield at 400 kPa, suggesting the structure of the material has broken down (Wesley 2019). The remoulding of the completely weathered rock resulted in much higher strain being measured compared to the remoulded residual sample, however this is not expected as the plasticity and grain is similar. This indicates the completely weathered rock is highly vulnerable to the loss of structure.

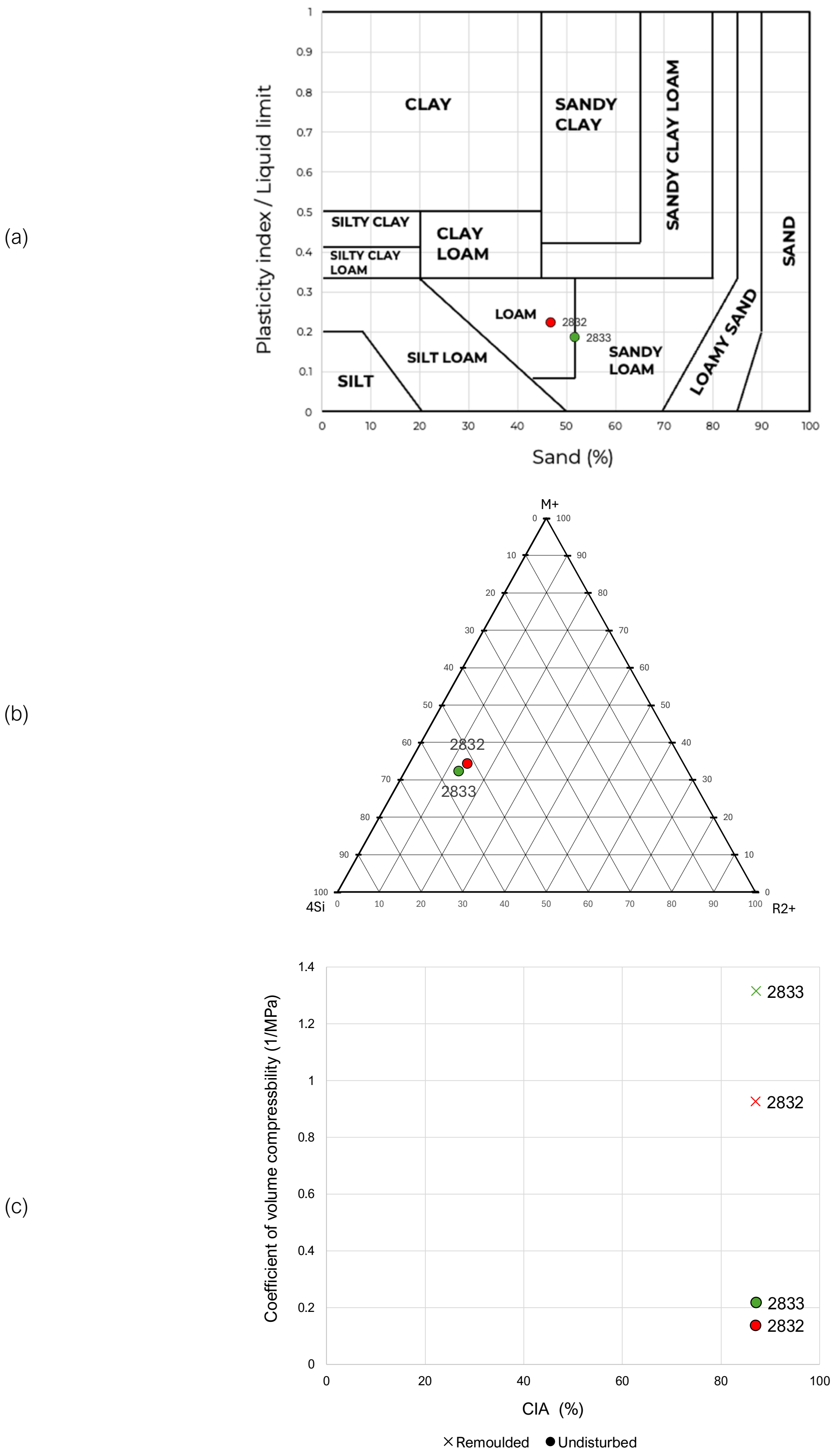

Figure 8-5 (a) Texture classification (Moreno-Maroto and Alonso-Azcárate 2018; 2022) (b) Weathering intensity scale (*WIS*) (Meunier et al. 2013) (c) m_v value calculated for stress increment from 50 kPa to 100 kPa vs chemical index of alteration (*CIA*) (Nesbitt and Young 1982) for Graskop samples

8.1.3 Highveld weathering profile

According to the grading analyses and Atterberg limits testing results, represented in Figure 8-6 as the clay factor to sand content, the structured wad samples are typically low to moderately plastic silts. Two (2) of the residual dolomite samples are clay and silt mixtures and one (1) sample is a non-plastic silt. The liquid limit of the wad is generally higher than the residual soil and ranges from 65% to 101% for the Highveld wad samples. The in-situ moisture for the wad samples was calculated to be between 89% to 238%. All the wad samples had in-situ moisture contents greater than the liquid limit. This is possible due to the presence of the structure and Mn oxides in the material (Swart et al. 2019).

The Highveld wad sample comprises mostly Mn and Fe oxides, accompanied by silica, in the form of quartz or chert and, to a lesser extent calcium (Ca) which probably forms part of dolomite still present in the material. The material has very little Al, approximately less than 1%, and relatively low amount of silica. This indicates the material is not highly weathered or leached.

Only one (1) wad sample from the Highveld site underwent chemical testing and therefore a comparison of materials tested cannot be done based on chemical weathering indices. Swart et al. (2019) found that through further alteration of wad, the material almost always has an increase in dry density and a reduction of void ratio as the structure breaks down and the Mn oxides are replaced with Fe oxides. For this reason, the dry density and void ratios are plotted against the m_v values at 100 kPa for each tested sample and presented in Figure 8-6. It can be seen the residual soil, represented by the red dots, have higher dry densities and lower void ratios but experience more strain at the same load as the wad samples. This contradicts the idea in classic soil mechanics that a material with a lower dry density and higher void ratio would undergo more strain with a similar grading (Terzaghi 1943; Fukue and Okusa 1987; Al-Khafaji and Andersland 1992; Wu et al. 2024). All wad samples underwent much less strain across the entire test range.

Sample 2820 yielded at 400 kPa as can be seen by the change in the gradient of the slope compared to the rest of the wad samples. This sample had the highest dry density and lowest void ratio of the wad sample, it also plotted the closest to the more clayey residual soil samples. Though it was not confirmed through chemical testing, it is expected sample 2820 is the *most* weathered of the wad samples and therefore the only sample that experienced yield pressure.

Referring to Figure 7-23, the difference in the slope of the Soil Water Retention Curves (SWRCs) below the 1 MPa suction range is apparent. This is indicative of the distinct differences in pore size distribution of the two samples, with the steeper gradient of the structured material being indicative of a more uniform pore size distribution. The difference in initial volumetric water content can be attributed to the large differences in initial void ratio of the structured and remoulded samples, namely 8.32 and 2.18, respectively. The influence of the structure on the material performance in an unsaturated state cannot be overlooked. Day (1981) cited soil structure as the most critical aspect governing the soil's compressibility.

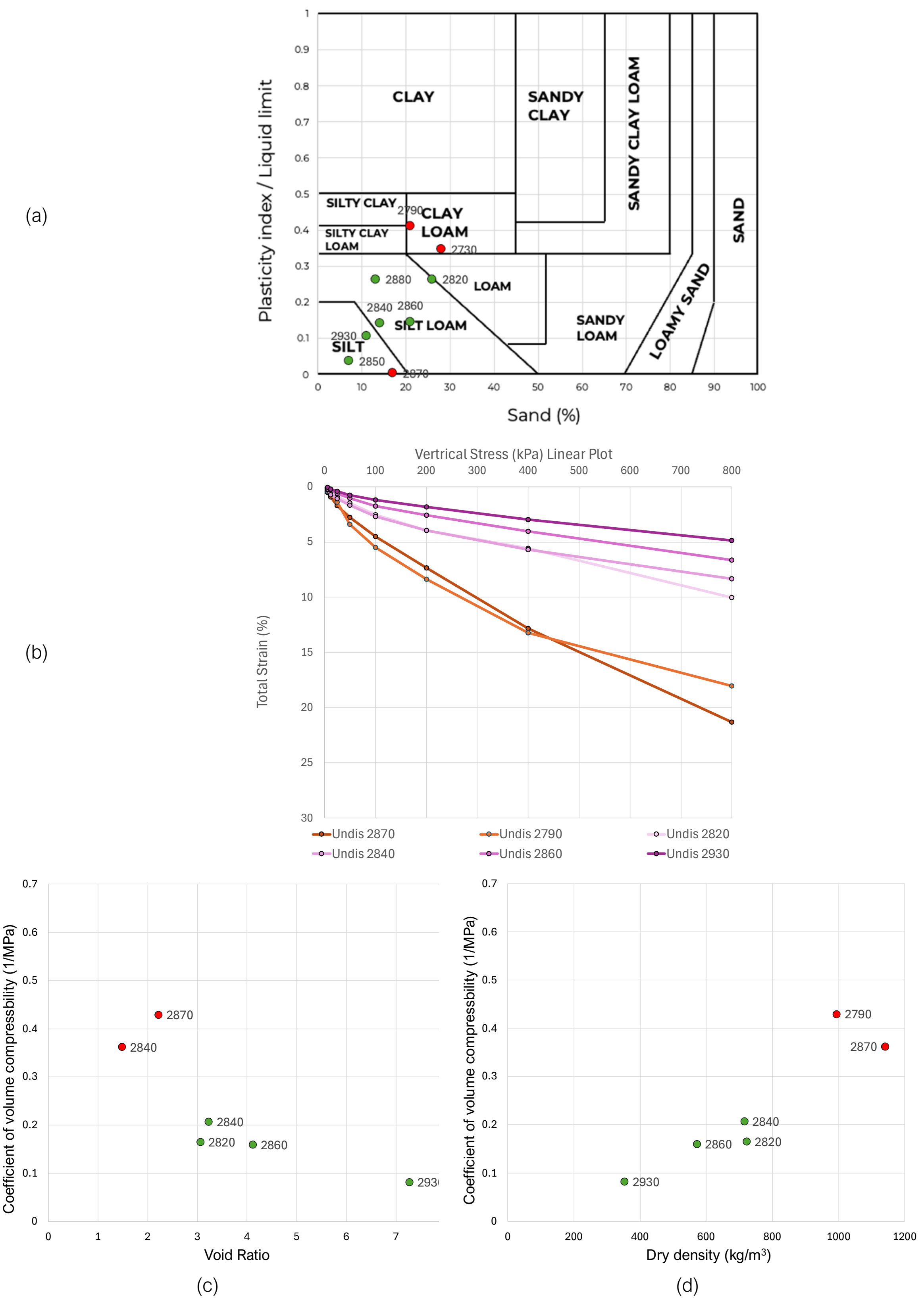

Figure 8-6 (a) Texture classification (Moreno-Maroto and Alonso-Azcárate 2018; 2022) (b) linear stress strain curves (c) m_v at 100 kPa vs void ratio (d) m_v value calculated for stress increment from 50 kPa to 100 kPa vs dry density for Highveld samples

8.2 Igneous weathering profile

The data and observations gathered from the Tzaneen, Dullstroom, and R528 weathering profiles will be compared and assessed together to find similarities to the materials' behaviour due to weathering. Figure 8-7 summaries the soil texture, behaviour under load and weathering state of residual soil samples (red coloured data points) and completely weathered rock (green coloured data points) samples taken from the igneous weathering profiles.

The soil texture based on the clay factor indicates all the residual soils are moderately plastic with a higher clay percentages compared to the completely weathered rock. Primary rock minerals progressively transforms into clay minerals as weathering intensity increases resulting in an increase in finer particle size percentages and plasticity (Rocchi et al. 2017; Dos Santos et al. 2018; Bonnet et al. 2022).

The on-site profile logging showed all the completely weathered rock horizons had relict rock structure that govern the mineral grain relations, macro-structure and flow channels indicated by pedogenic staining. The XRCT imagery revealed this influence of the relict structure controls the pore geometry, pore orientation, and flow channels which was closely linked to the chemical components of the material and become less prominent as weathering increased. The same visual assessments showed all the residual soils had lost any sort of pore orientation or relict structure and the pores were governed by pedogenic processes. The loss in structure is linked to the increase in chemical decomposition of the profile as the depth from the ground surface decreases.

The completely weathered rock samples experienced less strain than all the residual soil samples. This is primarily a function of the relict rock structure which has shown to contribute significantly to the stiffness of the material (Rocchi et al. 2017; Liu et al. 2022; Bonnet et al. 2023; Wang et al. 2024). The structure of sample 2835 seemingly broke down at the yield pressure of 400 kPa. This may be linked to the sample being the most weathered of the completely weathered rock samples according to the *WIS* and *CIA* weathering indices. On remoulding of the samples, sample 2835 has the highest plasticity according to the clay factor and as a result experienced the most compression. Sample 2829 plotted as the least weathered sample and performed the best in terms of volume change in the undisturbed and remoulded state. The XRCT imagery also indicates this material has not experienced a high intensity of weathering as the observed pores are governed by the cleavages and structure of the primary rock minerals (Wilson 2004).

Sample 2830 had the highest compressibility in the undisturbed state but the least in the remoulded state. As previously discussed, this sample probably underwent intense weathering once existing borrow pit was excavated and exposed the sample to the Earth surface conditions (Obermeier and Langer 1986). The sample seems to have yielded at 50 kPa and then underwent straining hardening which suggests, most of the structure was lost during yielding. The remoulding destroyed the remaining structure and resulted in slightly more strain during the remoulded state. Sample 2824 is the most weathered sample according to the weathering indices and underwent the most strain in the remoulded state. This sample is least plastic of the residual soil samples and had a similar dry density value to sample 2828. The reason for the significantly more strain experienced by the sample could not be determined. It is possibly a function of a larger quantity of fine-sands and silts in the sample.

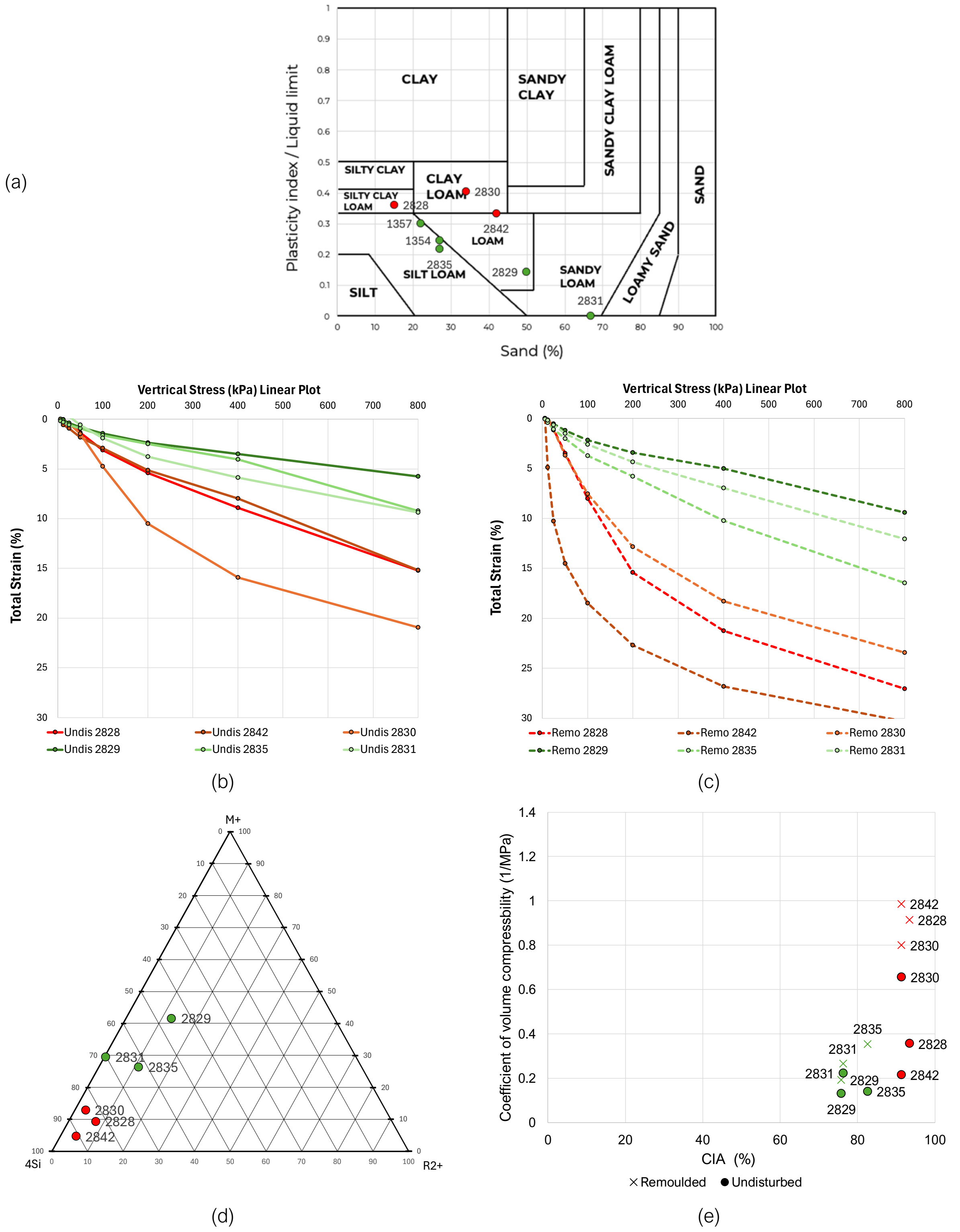

Figure 8-7 (a) Texture classification (Moreno-Maroto and Alonso-Azcárate 2018; 2022) (b) linear stress strain curves for undisturbed samples (c) linear stress strain curves for remoulded samples (d) Weathering intensity scale (*WIS*) (Meunier et al. 2013) (e) m_v value calculated for stress increment from 50 kPa to 100 kPa vs chemical index of alteration (*CIA*) (Nesbitt and Young 1982) for igneous weathering profile samples

Figure 8-8 presents plots for the coefficient of volume compressibility (m_v) against the sample's dry density (ρ), void ratio (e) and degree of weathering determined by the *CIA* and *WIS* methods. Typically, for soils that formed through consolidation and Terzaghi's (1943) theory of one-dimensional consolidation can be applied, many of the equations to predict compression of soil are based on the void ratio (Fukue and Okusa 1987; Al-Khafaji and Andersland 1992; Wu et al. 2024). Figure 8-8 (a) and (b) plot the m_v against the dry density and void ratio, respectively. As can be seen the data is fairly scattered with no relationship being shown between the compressibility of the soil and the density and volume parameters. Referring to Figure 8-8 (c) and (d), which plots the degree of weathering to the compressibility of the soil, a relationship does seem to appear. It must be noted that no correlation will be attempted to be made as the data set is limited. It seems the degree of weathering is a better predictor for compressibility of residuum than using initial void ratio or dry density due to the presence of the structure. The stiffness provided by the relict rock structure has been shown in this research and by many other authors. This positive influence has been shown to decrease with an increase in weathering (Rocchi et al. 2017; Liu et al. 2022; Bonnet et al. 2023; Wang et al. 2024).

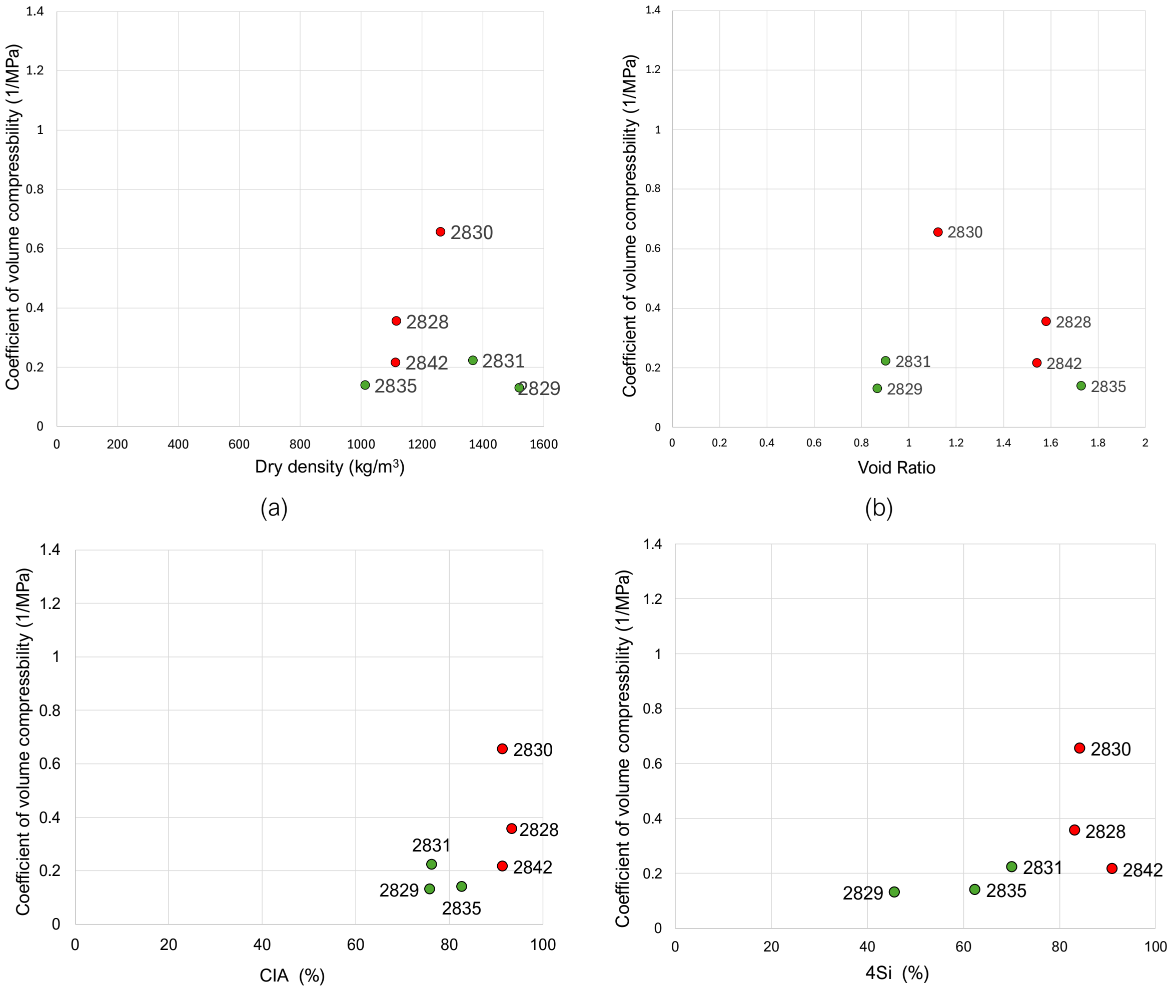

(a)

(b)

(c)

(d)

Figure 8-8 The m_v value calculated for stress increment from 50 kPa to 100 kPa plotted against (a) dry density, (b) void ratio, (c) chemical index of alteration value (*CIA*), and (d) 4Si value from the weathering intensity scale (*WIS*) for igneous completely weathered (green plot) and residual soil (red plot)

The XRCT scans conducted in this study showed the most *prominent* relict rock structure is present in the least weathered igneous rock and this *prominence* decreases with an increase in weathering until the structure is eventually destroyed to form the residual soil higher up the profile. This trend was confirmed by the chemical analyses, which was used to determine the degree of weathering. The compressibility of residuum, being residual soil and completely weathered rock, forming on igneous weathering profiles is expected to increase with an increase in weathering and subsequently a decrease in relict rock structure *prominence*.

The coefficient of permeabilities were measured in saturated triaxial tests to assess the influence of weathering on the movement of moisture. After the oedometer test results were received, it was decided to conduct remoulded permeabilities test for each sample to ensure there was not an influence of remoulded permeability values that was driving the greater compression in the remoulded samples. The coefficient of permeability (*K*) for each sample is plotted against the degree of weathering and void ratio in Figure 8-9.

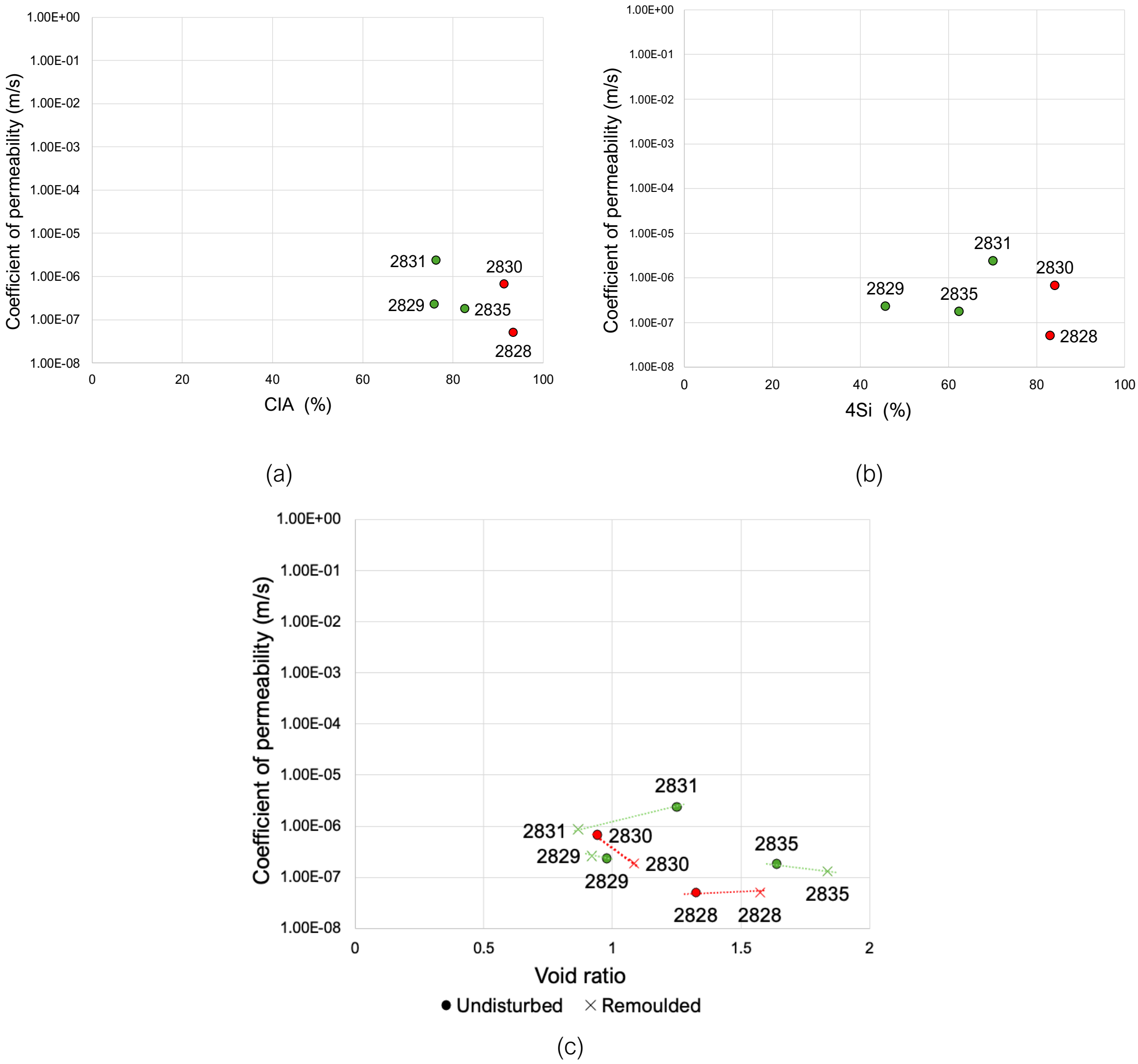

(a)

(b)

(c)

Figure 8-9 The coefficient of permeability *(K)* value plotted against (a) chemical index of alteration value (*CIA*), (b) 4Si value from the weathering intensity scale (*WIS*), and (c) void ratio for igneous completely weathered (green plot) and residual soil (red plot)

All samples had low permeabilities in the undisturbed state and no relationship seems to exist with a change in the degree of weathering. The movement of moisture is expected to occur primarily along relict rock structures and the evidence can be seen by the black and red staining of the relict faces and the denser pedogenic deposits in the XRCT scans. It is expected moisture movement will also occur within microcracks and through the rock matrix depending on the degree of saturated of the material (Van der Hoven et al. 2003; Talib et al. 2016; Dippenaar et al. 2022).

The remoulding did not seem to impact the coefficient of permeability values greatly with all remoulded sample retaining a low permeability and therefore would not have an impact on the consolidation in the oedometer tests. Referring to Figure 8-9, remoulding a sample back to in-situ parameters for a triaxial cell sample is difficult. The remoulded dry density and void ratio values differ greatly from the in-situ values. This operator difficulty seems to control the permeability value for sample 2831 where the remoulded sample had a much lower void ratio and therefore a lower permeability value. The remoulding is expected to change the path that the moisture travels in the completely weathered rock as the relict fractures have been destroyed.

8.3 Dolomite weathering profile

The influence of weathering on the residuum profile forms above dolomite bedrock will be discussed in this section by incorporating data form the Graskop and Highveld sites. The oedometer, grading and permeability testing results for the Highveld samples were retrieved from Bester (2021). Bester (2021) focused on logging, sampling and performing a rigorous testing regime on wad and residual dolomite from various sites underlain by dolomite in South Africa. Swart (2019) sampled the same material from the Highveld site but focused on the influence of the *Mn* and *Fe* content on the hydromechanical properties of the soil. Swart (2019) also sampled and tested residual dolomite from various dolomitic formations across South Africa and the data from these sites are also included in this section. Figure 8-10 summarises the texture, compression behaviour, liquid limit and dry density of all the available wad (green coloured data points) and residual dolomite (red coloured data points) samples.

Dolomite is a calcium-magnesium-carbonate rock that can completely dissolve into solution, resulting in no weathering product. This leads to the formation of elaborate cave formations found in areas around Gauteng. Residual products do often form as the dolomites are typically enriched in calcite, chert, and to a lesser extent metal oxides. Due to the very low permeability of the rock, the weathering occurs mostly at the joint faces and results in extremely drastic changes in properties over a short length (Buttrick 1986). The dolomite weathering profile is usually not as well developed, gradual or predictable as igneous weathering profiles. Therefore, no method to determine the degree of weathering of a dolomite exists.

Swart et al. (2019) concluded that alteration of wad usually results in an increase in dry density and lowering of the liquid limit. The dry density to liquid limit plot is shown in Figure 8-10. Residual dolomite generally has a lower liquid limit and higher dry density compared to the wad samples.

This is linked to the presence of the *Mn* and *Fe* oxides in the wad and residual dolomite, respectively. The *Mn* oxides in wad have large surface areas that govern the material's ability to take up large amounts of water before liquefying, therefore the Atterberg tests indicate high liquid limits. Continued weathering creates an unstable, acidic, environment and the *Mn* oxides are more readily available to dissolve into solution compared to *Fe*. This results in a relative enrichment of *Fe* as the *Mn* leaches away. The dissolution of this mineral greatly reduces the liquid limit of this material (Dowding and Fey 2007; Swart et al. 2019). The plasticity chart for the residual dolomite and wad samples are plotted with other residual soils with high liquid limits and is presented in Figure 8-10 (d) (Wesley 2010).

Residual dolomite typically still has a large amount of *Mn* present ranging from approximately 5% to 10%. As weathering occurs, the *Mn* oxides dissolve and redistribute to form nodules and coatings in the residual dolomite. This reduces the surface area of the Mn oxides and causes the soil to transform from a black to red colour as the *Fe* oxides are exposed. This reworking process reduces the influence the *Mn* oxides have on the hydromechanical properties of the weathered profile. To illustrate this weathering process photographs taken with a stereo microscope of wad and residual dolomite is shown in Figure 8-11. Note the sand size, black, nodules in Figure 8-11 (c).

Day (1981) emphasised how the structure of wad is essential when assessing the material's compressibility. In this publication, Day (1981) cited soil structure as the most critical aspect governing the soil's compressibility. Buttrick (1986) highlights the importance of preserving the relict parent structure when testing the material. Considering the importance of soil structure in the testing of this material, it may be desirable to conduct full-scale testing (Jacobsz 2015). However, as such tests are often not financially feasible, an in-depth understanding of the implications of element testing of wad is crucial.

The compression data of the Highveld and Graskop samples are presented in Figure 8-10 (b). All the Highveld wad samples experienced relativity low amount of strain. The wad and residual soil samples taken from Graskop performed very similar, however sample 2833, the wad sample, yielded at 400 kPa. Sample 2832, the residual soil sample, may still possess relict rock structure, as well as pedogenic structure due to the higher quantity of nodules present, that provided stiffness under load. The remoulding process caused both samples to undergo more compression, especially the wad sample. This is indicative of the high vulnerability and susceptibility of wad when the structure is lost. Breaking down of the structure occurred through intense weathering or external factors results mostly in an increase in dry density. Wad generally has a density less than water and a void ratio greater than 1. Any volume change will almost certainly cause the material to compact or densify, reducing the void ratio and reducing the water holding capacity. Through this loss in structure, the compressibility is expected to increase for the material, which is interesting because a soil with the same grading is expected to be less compressible as the dry density increases and void ratio decreases. The trend of compressibility for residuum forming on dolomite weathering profiles seemed to be governed by the degree of weathering.

As weathering increases, the relict rock structural *prominence* decreases, resulting in an increase in compressibility, seemingly regardless of the change in dry density or void ratio.

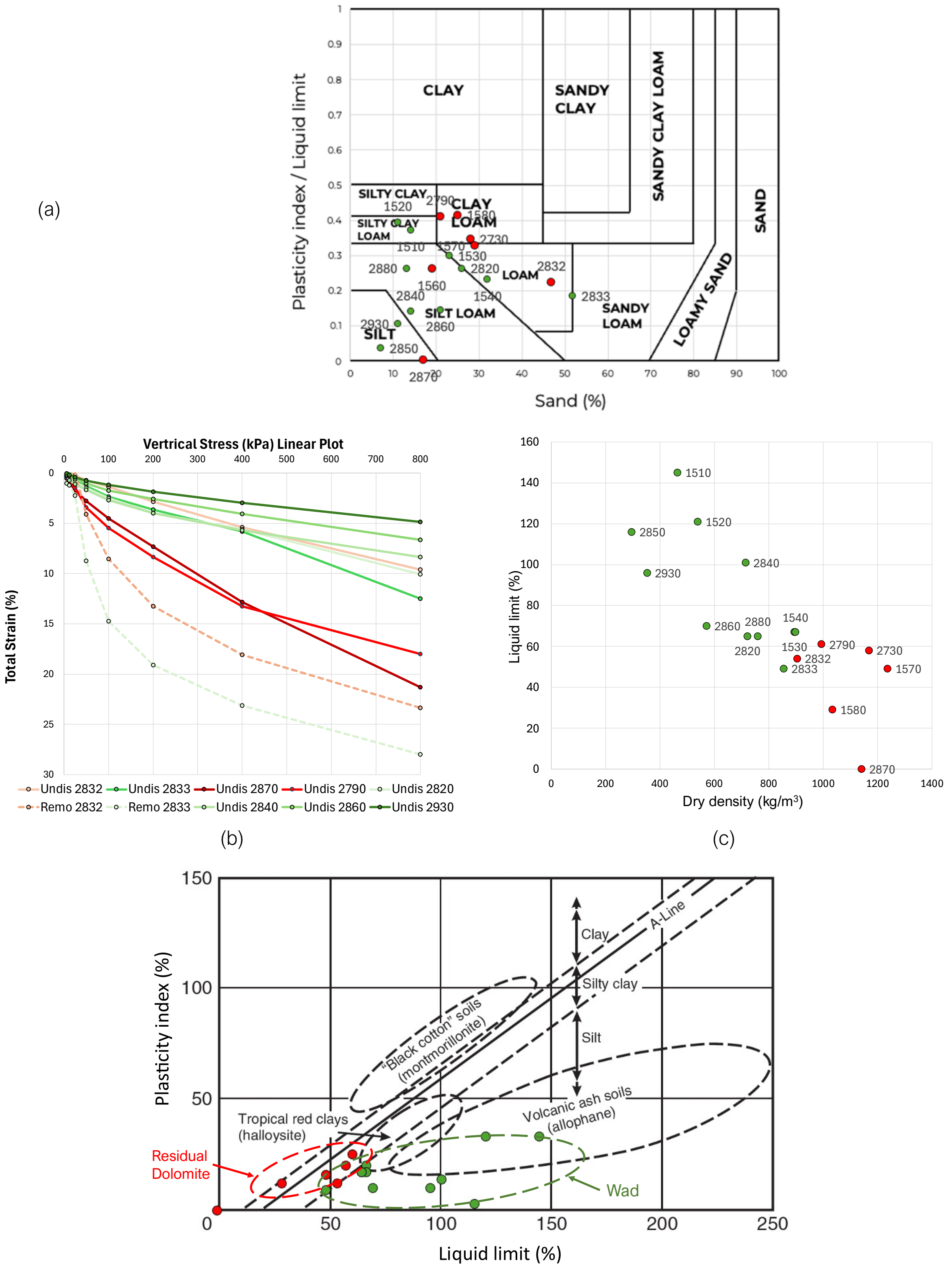

(a)

(b)

(c)

(d)

Figure 8-10 (a) Texture classification (Moreno-Maroto and Alonso-Azcárate 2018; 2022) (b) linear stress strain curves (c) dry density vs liquid limit (d) Plasticity chart for residual soils (adapted from Wesley 2010) including residual dolomite and wad samples

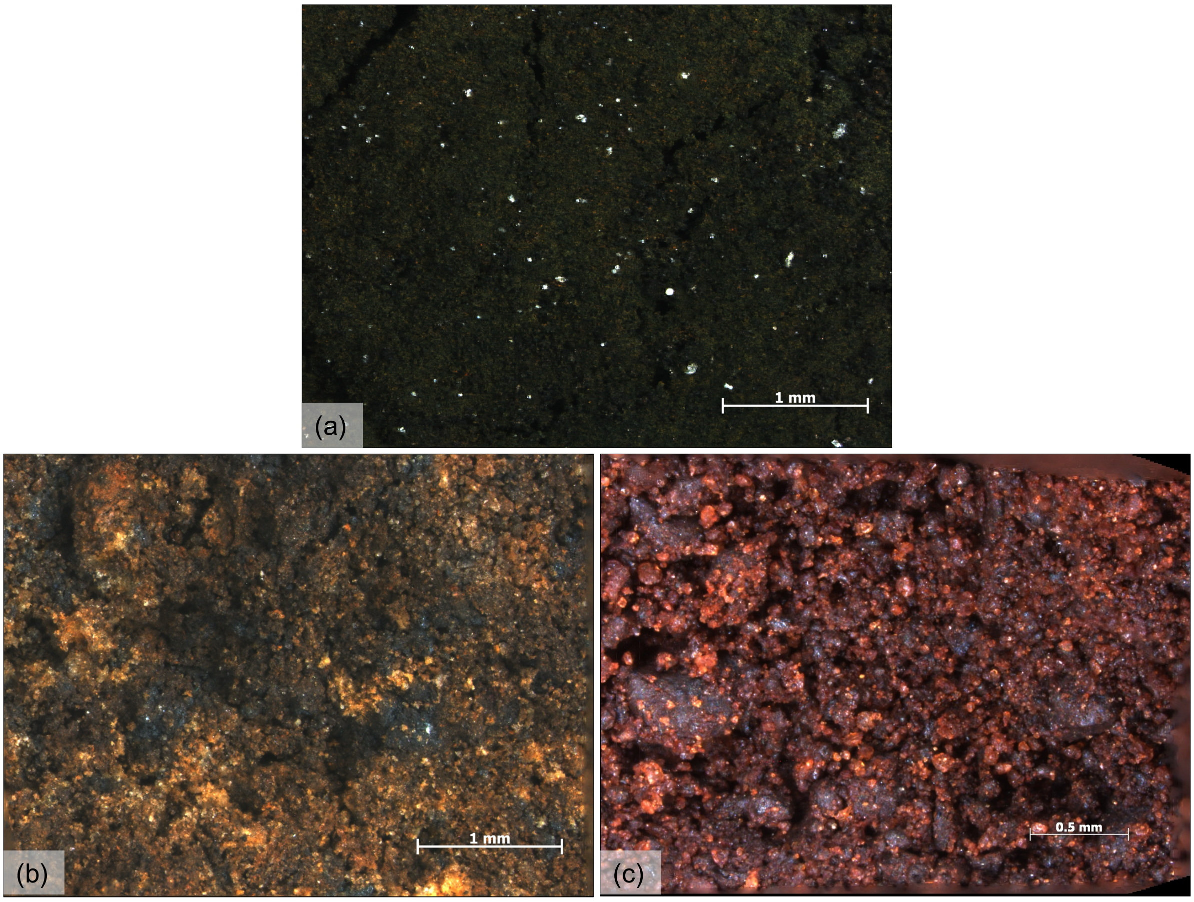

Figure 8-11 Stereo microscope photographs taken of (a) the least weathered sample 2930, (b) to intermediately weathered sample 1530, to (c) the most weathered sample 1570 (taken and adapted from Swart 2019)

Wad usually has a natural moisture content that is greater than the liquid limit (Day 1981; Buttrick 1986; Swart et al. 2019; Bester 2021). In this scenario, if the structure breaks down in-situ, the individual grains that govern the liquid limit, will behave as a liquid and have zero strength. Large sinkholes may form when a zone of wad near the dolomite bedrock interface liquifies, sloughs into a receptacle and this creates a void beneath the surface or the void propagates upwards, forming the sinkhole at surface (Jacobsz 2015).

8.4 Generalised weathering profile

Evaluating the impact of weathering on the individual profiles at each site and for the weathering profiles on the dolomite and igneous parent rocks, respectively, this research has shown the degree of weathering is closely linked to the chemical and physical state of the material, which seems to govern the structural *prominence* in the profile. The structural *prominence* decreases with an increase in weathering resulting in an increase in compressibility. Figure 8-12 presents the state of weathering and the compressibility behaviour for the completely weathered rock and residual soil sampled at all the profile sites. Sample 2832, the residual dolomite from Graskop, is the outlier on both plots separately, but if the two plots are evaluated together, the sample still follows the trend of structural *prominence*. This sample was logged as a residual soil but is much less weathered than the remaining residual soil samples, therefore it underwent relativity much less strain. The reasons for logging this sample as a residual sample has been discussed.

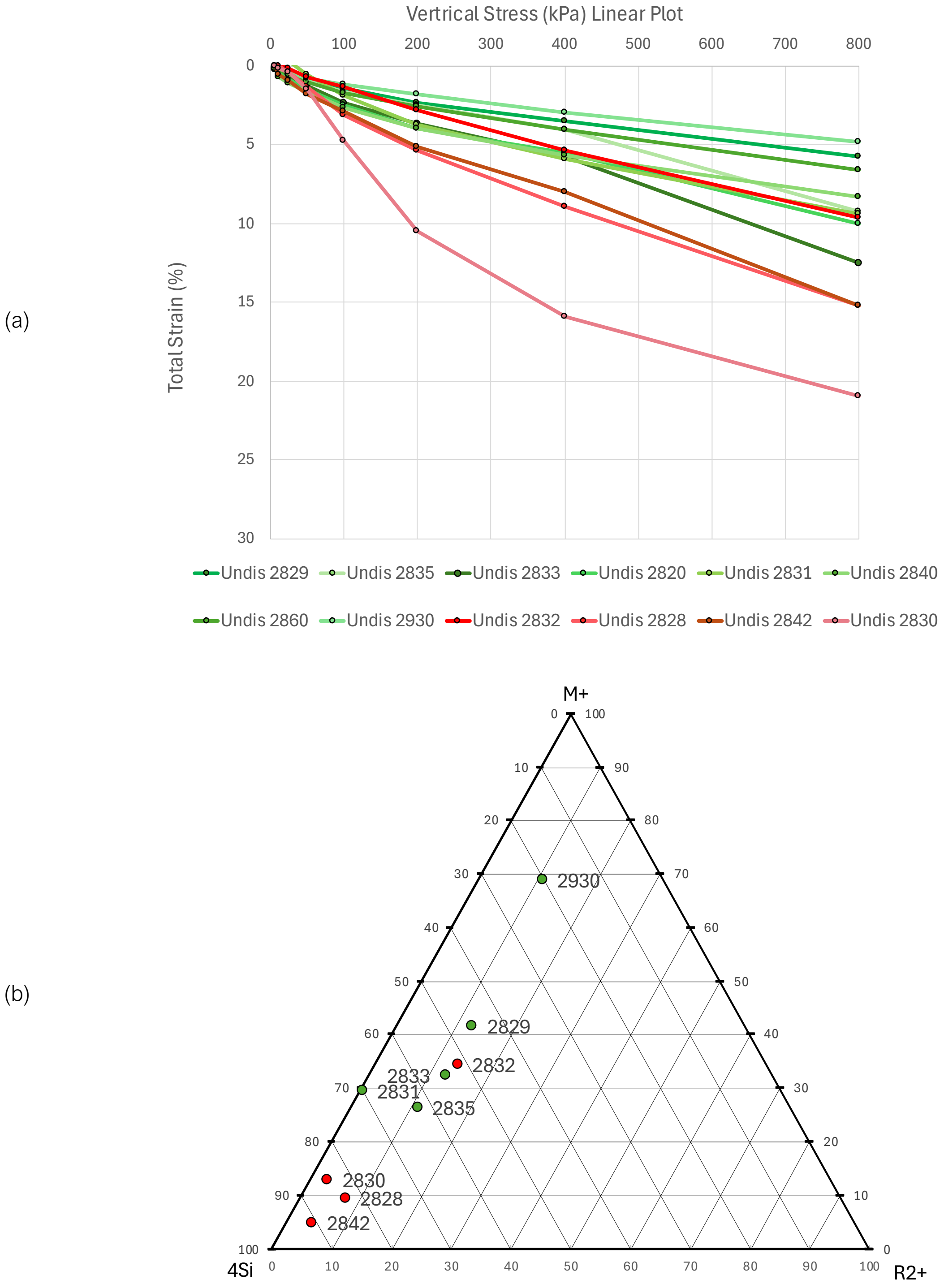

Figure 8-12 (a) linear stress strain curves (b) Weathering intensity scale (*WIS*) (Meunier et al. 2013) for dolomite and igneous completely weathered (green plot) and residual soil (red plot)

The sample was taken near the residual soil and completely weathered rock interface, and it may be that the sample still possesses relict rock structure that has provided the sample with the stiffness observed.

As shown by XRCT scans of the completely weathered rock samples 1354 and 1357, that were also taken near the above-mentioned interface, the influence of pedological structures is present in the completely weathered rock. The relict rock structure *prominence* may continue into some residual soils for a short distance. The observed loss of relict rock structure in a weathering profile may be the point where the relict rock structure becomes discontinuous and only localised zones of structural *prominence* exist.

Figure 8-13 (a) and (b) plot the coefficient of compressibility (m_v) values for each sample against the dry density and void ratio, respectively. A relationship between these parameters does exist on all the plots, though the data is slightly scattered, and no correlations can be made. In general, samples with a higher dry density, mainly comprising completely weathered rock, compressed more than samples with a lower dry density. Samples with a higher void ratio, compresses less than samples with a lower void ratio. Sample 2930, comprises wad, has the lowest dry density, highest void ratio but experienced the least amount of compression of all samples. The chemical weathering indices show it is the least weathered sample and as discussed previously it is a high structural *prominence*. The relict rock structure governs the material's porosity and stiffness. For completely weathered rock, if the relict rock structure decomposes, and the structural *prominence* decreases, the void ratio will decrease, and dry density will increase (Hencher 2024). This decrease in structural *prominence* will decrease the stiffness and increase the compressibility.

Figure 8-13 (c) and (d) show the plots for the coefficient of compressibility (m_v) values against the chemical weathering indices, the *CIA* and the *4Si* values, respectively. The relationships shown in these plots suggest the structural *prominence* is linked to the degree of weathering. As the state of chemical weathering increases, the structural *prominence* decreases, and the compressibility increases. Assessing the compressibility of the material to the state of weathering is a better predictor to the actual compression behaviour compared to the dry density and void ratio, as it includes the presence of the relict rock structure.

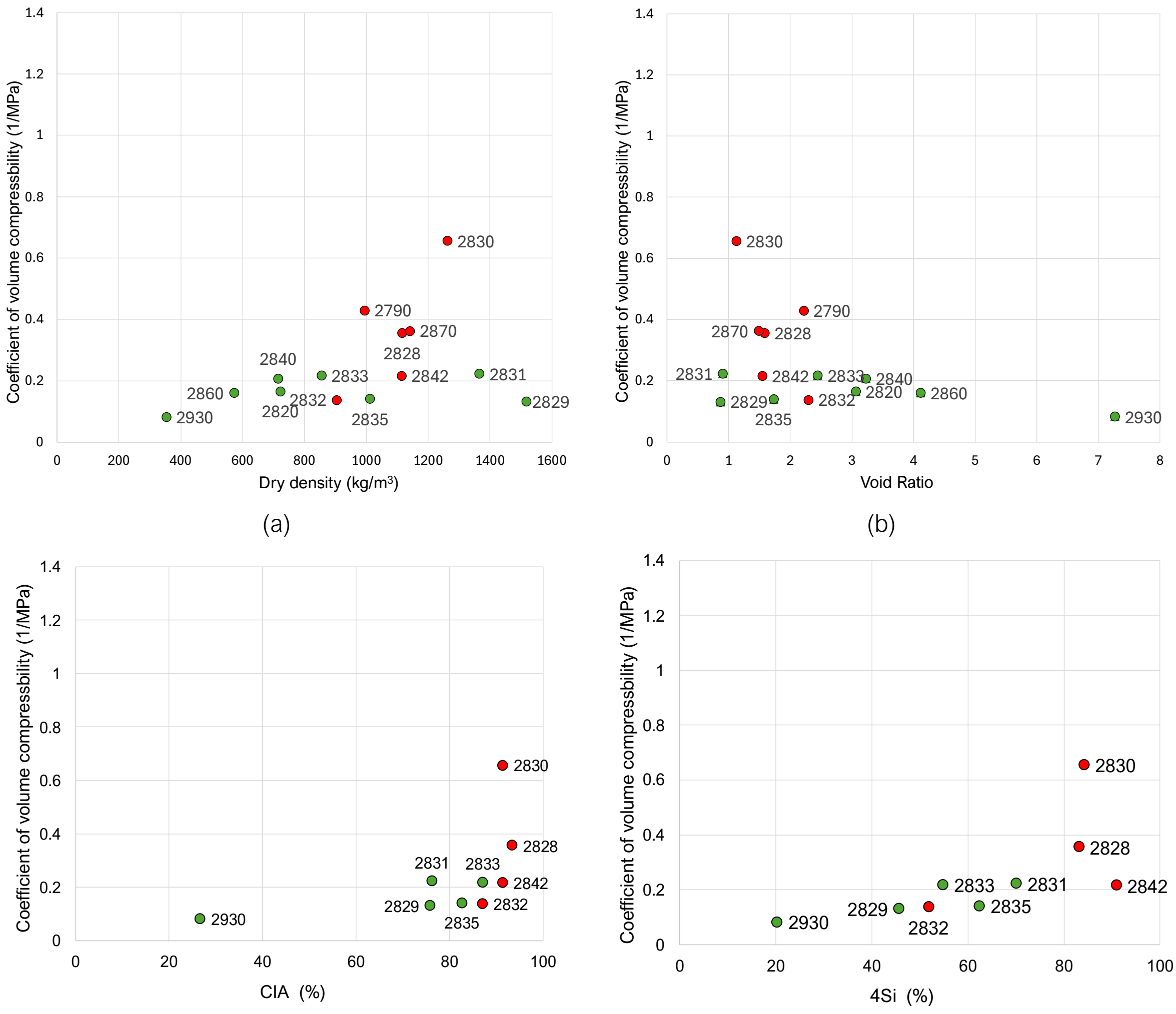

(a)

(b)

(c)

(d)

Figure 8-13 The m_v value calculated for stress increment from 50 kPa to 100 kPa plotted against (a) dry density, (b) void ratio, (c) chemical index of alteration value (*CIA*), and (d) 4Si value from the weathering intensity scale (*WIS*) for dolomite and igneous completely weathered (green plot) and residual soil (red plot)

Figure 8-14 presents photographs taken of materials with high structural *prominence.* The structural *prominence* should be treated a single parameter that can be used across different lithologies and weathering profiles. The photographs presented are of completely weathered rock originating from different parent rocks at different rates of decomposition due to the differences in climate history. All these specimens have varying void ratios and dry densities, but all have high structural *prominence.* High structural *prominence* is characterised by the presence of inter-grain relations and fractures or joints that are inherited from the parent rock. The structural *prominence* decreases when all primary rock-forming minerals have fully decomposed, microcracks form through the fabric, and pedological processes start to form and govern the pore spaces of the material. These features should be assessed on a range of scales from micrometres to centimetres. The structural *prominence* can be assessed visual by hand samples, XRCT scans, and stereo microscope, and it can be quantified using chemical weathering indices as discussed in this research.

(a)

(b)

(c)

Figure 8-14 Photographs taken of (a) completely weathered diabase sample 2829, (b) structured wad similar to sample 2930 (taken from Buttrick 1986), and (c) completely weathered andesite sample 2835 (photographs taken by D Swart)

Figure 8-15 shows the decrease of structural *prominence* with an increase in chemical weathering. The photographs are of tube samples that have been cut in half along the longitudinal axis and the two halves separated with the sampled material being allowed to break apart along pre-existing cracks or fractures, or through the soil fabric. Referring to sample 2835, the material has a structural *prominence,* and primary rock-forming minerals and texture can be seen with staining on relict fractures along which the sample broke apart. Sample 1354 exhibits relict rock structure with a significantly more quantity of pedogenic nodules and microcracks that have formed in the soil due to weathering. These features were confirmed in the XRCT scans. Sample 1357 has broken along a relict rock fracture and exhibits a weak relict rock structure. Open root channels and flow channels can be identified from the XRCT scan and on the photograph. Sample 1354 and 1357 are considered to have moderate structural *prominence*.

Sample 2842 is a sample of the residual soil and mostly comprise reddish clay with discontinuous relict rock structure zones in the lower half of the photograph. The soil structure will be controlled by pedological processes and biotic activity, and therefore this sample has lost the structural *prominence.*

It is proposed to use the concept of structural *prominence* when assessing the influence of relict rock structure on the material's mechanical performance. This study focused on compression behaviour only, and further studies would need to be conducted using more elaborate triaxial shear testing equipment. Figure 8-16 visually illustrates changes to the structural *prominence* in a weathering profile and how it influences the compression of the material. For this simplified weathering profile, the structural *prominence* is higher deeper in a profile where less weathering has occurred. Structural prominence can exist in a discontinued state in the residual soil in some cases, however, more work focusing on this would need to be done to confirm how far up into the residual soil it is present and under what conditions would this occur. Pedological features are structures formed through typical soil forming processes. This research has shown that these features, namely pedogenic nodules, biotic activity and fissures and cracks, do exist within the completely weathered rock. Pedological features are included in this schematic to show how it increases into the residual soil and mostly governs the residual soil's structure as weathering continues. The compressibility decreases with an increase in weathering and decrease in structural *prominence.* The dashed lines indicate the path the parameter will most likely follow in a weathering profile; however, the actual path will depend on numerous factors that are variable to the point where it would change from profile to profile.

Figure 8-15 Photographs taken of residual andesite sample 2842, completely weathered rock sample 1357 and 1354 retrieved near the residual soil and completely weathered rock interface and sample 2835 taken from the less weathered completely weathered rock (photographs taken by D Swart)

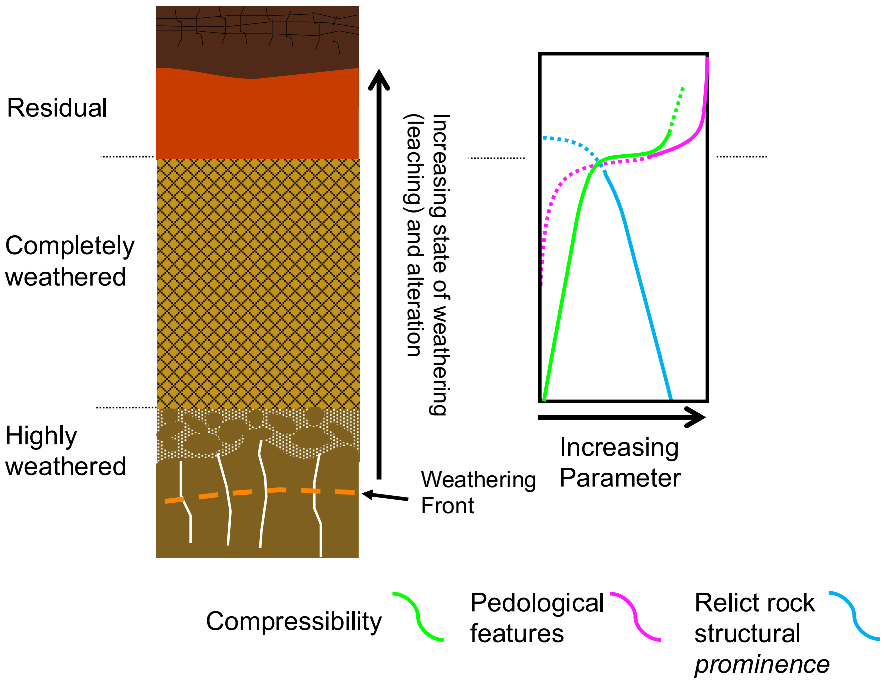

Figure 8-16 Proposed generalised structural *prominence* and compressibility profile

The simplified weathering profile on *Mn*-rich dolomite is presented in Figure 8-17. The changes in parameters and behaviour of wad are predictable due to its unique characteristics. The material is highly enriched in *Mn* oxides and under intense weathering conditions the *Mn*-oxides will be replaced by *Fe*-oxides, which will reduce the liquid limits as the high-water holding capacity of the *Mn*-oxides decreases. The replacing of Mn-oxides with Fe-oxides will weaken and break the inter-grain bonds as material transforms and changes volume and shape. A point will be reached where the highly porous structure will collapse in on itself causing the material to densify and experience a rapid decrease in the void ratio. The change in chemistry and physical state will alter the dark blue colour to a red colour, typical of a residual soil. As weathering continues further the residual dolomite will undergo pedological processes similar to any other soil.

The structural *prominence* for this weathering profile is shown and follows the same trend as the generalised profile presented in Figure 8-16. The research has shown the wad with its relict structure intact has a lower compressibility compared to the residual dolomite in the same profile. When the structure has been destroyed through remoulding, the remoulded wad has significantly higher compressibility values. The wad almost always has a lower dry density than residual dolomite but has a lower compressibility due to its high structural *prominence.* The predictability of the dry density and liquid limit in a dolomite weathering profile allows for the identification of the material based on these two parameters.

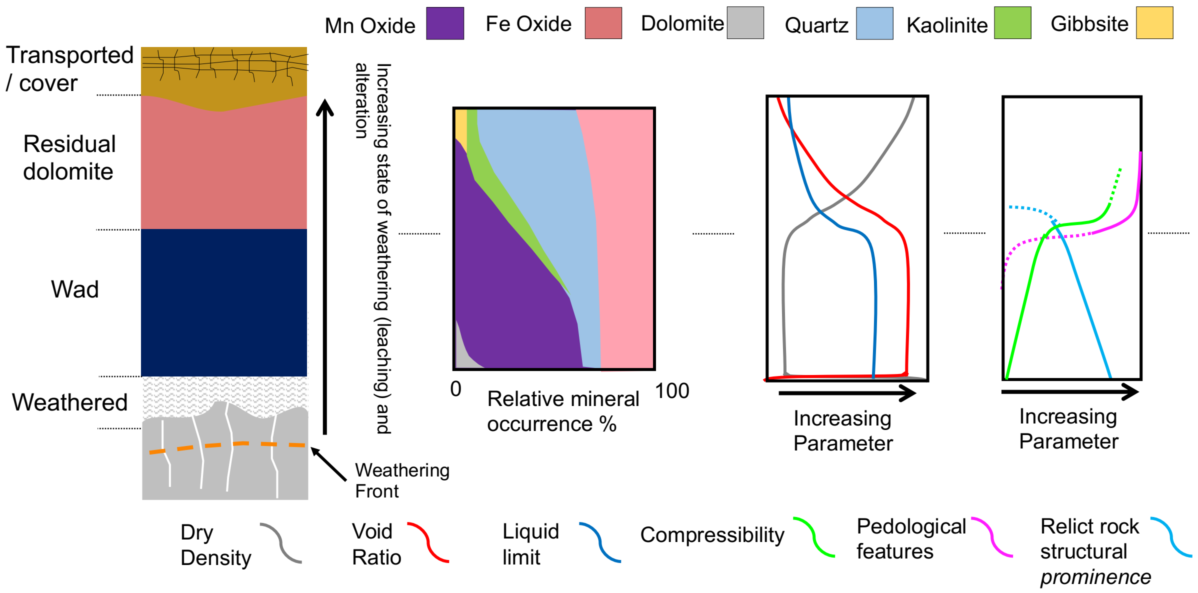

Figure 8-17 Chemical and physical profiles for dolomite weathering profiles

Swart (2019) summarised three decades of available data on dolomite residuum and found behaviour of the material is highly dependent on the relict rock structure of wad and the presence of Mn-oxides. The structure and the Mn-oxides govern the dry density and liquid limits, respectively. The data presented in Swart (2019), Bester (2021) and this study has been used to plot boundary lines within which wad and residual dolomite will plot. The purple shaded area is typical of wad, be it structured wad or non-structured wad. Wad generally exists at a dry density less than that of water, but samples have been found to exist slightly above this value and therefore the boundary line is positioned at 1050 kg/m^3. No wad sample has been found to exists at a dry density of less than 220 kg/m^3 and therefore this area has been shaded in grey to indicate no material exists here. The liquid limit of wad is generally higher than 50% but a few samples has been found to go as low as 35% and the boundary has been placed here. The parameters of residual dolomite are slightly more variable than the wad, but it mostly has a higher dry density and a lower liquid limit. The area for the residual dolomite is presented based on these trends (Figure 8-18).

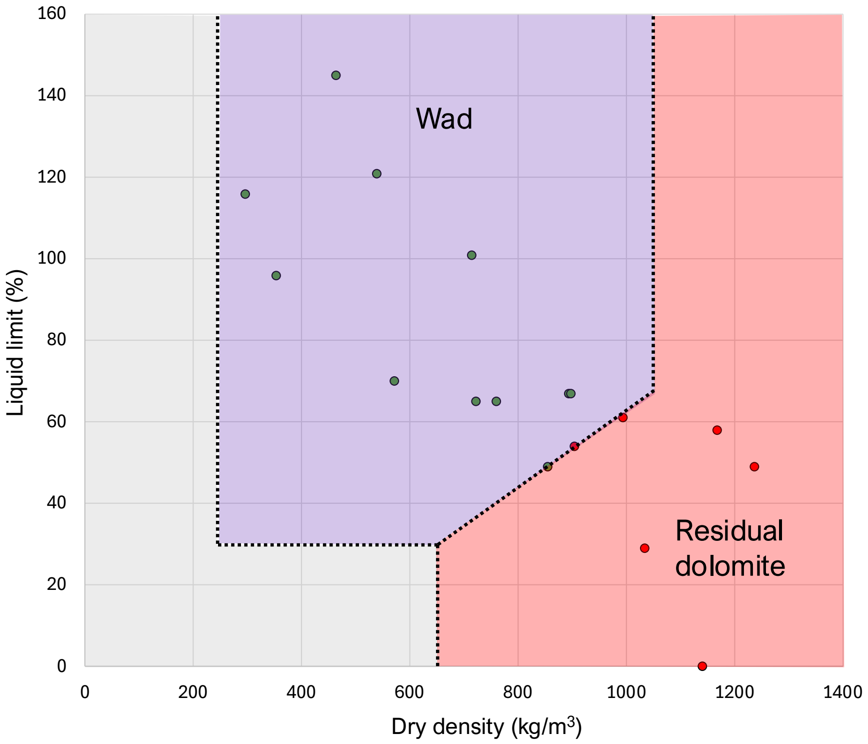

Figure 8-18 Determination of wad and residual dolomite based on the liquid limit and dry density plot

8.5 Conclusion

In this chapter, each individual profile was evaluated to understand the impact of weathering on the material sampled in the profile. A basic trend was determined and showed that compressibility increased with an increase of weathering. The profiles formed from igneous rocks showed that increased weathering tends to form clayey residual soil with very little to no remnants of relict rock structure. Consequently, this soil displayed higher compressibility compared to completely weathered rock. However, the dry density and void ratio of the igneous rock profile did not follow this trend, and no clear relationship was observed between these parameters and compressibility. The completely weathered rock was found to be in a less weathered state according to the chemical weathering indices, compared to the residual soils. Comparing the chemical weathering indices to the compressibility showed a positive relation where increased weathering results in a higher compressibility value.

The dolomite profiles were evaluated in the same way and showed a relation between the dry density and void ratio to compressibility. Generally, materials from dolomite residuum with a high void ratio and low dry density had a lower compressibility value. This seems counterintuitive but is explained by the presence of the relict rock structure. The relict rock structure provides strength and stiffness to the completely weathered rock and governs the porosity and dry density of the material. When this structure is lost in wad, the material will densify and have a higher compressibility value.

The critical importance of the presence of relict rock structure on the compressibility behaviour of the completely weathered rock has been observed in all profiles evaluated. Therefore, the novel concept of structural *prominence* is put forward to better understand the role relict rock structure has in compressibility behaviour of a material. This concept can be applied to igneous and dolomite weathering profiles and is not influenced by the dry density and void ratio of the completely weathered rock and residual soils, which are usually the key parameters in predicting soil compressibility.

9 Conclusions

The impact of chemical decomposition on weathering rock profiles formed on igneous and dolomite bedrock have been evaluated in this study. Completely weathered rock forms through moderate to intense leaching of the parent rock to the point where most of the primary rock-forming minerals have been decomposed to various secondary minerals. The parent rock fabric and macro-structure, termed together as the relict rock structure, are mostly retained through the weathering process. The relict rock structure governs the porosity and pore geometry and has been known to provide stiffness and strength to the soil during compression. Volumetric strain does occur during weathering as minerals transform and change in both volume and shape which weaken and break bonds between mineral grains. This results in the material to be *soil-like* meaning it can be broken down into individual grains by hand. The broken-down grains typically behave as a low-plasticity silt which was the targeted material in this study. The weathering process forms a relatively porous material that has varying dry density and void ratio values depending on the parent rock and weathering environment.

The chemical composition of a weathering profile is predictable and follows a certain trend once the profile has been intensely weathered. The *soil-end* of a weathering profile is typically enriched in iron and aluminium through leaching away of more mobile elements such as calcium and sodium. These immobile ions form common clay minerals such as kaolinite and gibbsite.

A residual soil forms when the relict rock structure is lost through a combination of chemical and physical changes due to continued weathering. The structure of the residual soil is governed by pedological processes and, consequently, is more compressible. The resultant grading of residual soil is generally more clayey than the completely weathered rock and typically has a higher plasticity value. As presented in this study, the soil texture of the completely weathered rock and residual soil can be determined from simple field tests that only require water and common stationery. These tests make use of use well-understood behaviour characteristic of fine-sand, silt, and clay at varying moistures to determine the plasticity of the material, and subsequently the soil texture.

The process through which completely weathered rock and residual soil forms is governed by the physical and chemical changes caused by chemical weathering. The degree of the weathering decreases with an increase in depth. The state of weathering can be quantified with the use of chemical weathering indices. The close relationship between the chemical and physical states of completely weathered rock, allows for the determination of structural *prominence* which characterises the degree to which the relict rock structure influences the compression behaviour. The structural *prominence* decreases as weathering increase and, consequently, this increases the compressibility of the material, regardless of the material's void ratio or dry density. The novel concept of structural *prominence* can be used to assist engineering geologists and geotechnical engineers to better understand the behaviour of completely weathered rock and residual soil and has been shown in this study to be a better predictor of soil compressibility than the dry density or void ratio.

9.1 Main Findings

The study was conducted with the use of traditional geotechnical laboratory methods of which the results were compared and analysed with advanced visual techniques. The laboratory testing included particle size analysis and Atterberg limits testing, chemical evaluation with the use of XRD and XRF testing methods, compression testing in oedometers, and saturated permeabilities in a triaxial cell. The advanced visual testing comprised XRCT scan that allowed for the modelling of 2D and 3D porosity and density models. These models provide invaluable insight on the structural properties that govern the compression behaviour of the completely weathered rock and residual soils. The XRCT models allowed the author to confirm the presence of relict rock structure and how it altered through weathering. These models were compared to the compression behaviour and revealed that the condition of the relict rock structure governed the strain taken under load to a greater extent than the dry density and void ratio. The state of the relict structure can only be done qualitatively through visual assessments. As discussed thoroughly in this thesis, the rock structure and state of weathering are closely linked. The degree of chemical weathering can be determined through chemical weathering indices. The chemical weathering indices and visual assessments can provide a structural *prominence* which can predict the compression of the material. The structural *prominence* can only be determined if data points exist in a profile but can be used to extrapolate the compression behaviour across the profile using much cheaper and quicker XRF testing. Samples for XRF testing can be obtained from rotary core drilling samples which makes it a powerful and novel tool to assess the compression behaviour in weathering rock profiles.

The main findings of this study are summarised as follows:

1. XRCT scans can be successfully used to assess the presence of structure in a soil material without the need to dry out the material or any other destructive sample preparation steps. It can provide information such as pores geometry in 2D and 3D, persistence of structure, and typical moisture flow paths. Depending on the sample size, the pores' structure can be confidently modelled based on the voxel data. It must be stated that final 3D porosity model is a theoretical model of the pore structure based on many factors as mentioned in this thesis.

2. The XRCT method does have limitations that were observed in this study. The method is an indirect measurement of soil structure as it is dependent on the voxel size, which is influenced by strength of XRCT, sample size, operator effectiveness.

3. Relict rock structure is a governing parameter in the compression behaviour of completely weathered rock. The structure is linked to the chemical weathering state of the soil. Therefore, chemical weathering indices are a good predictor of presence of structure in igneous and dolomite weathering profiles.

4. It seems structure does not need to be assessed on a case-by-case basis. Relict rock structure always has a positive influence on stiffness and strength and needs to be

appreciated during the evaluation of a rock weathering profile. The degree of structure present, which is dependent on the parent rock structure, should be the focus of the assessment. The degree of structure will always decrease as chemical weathering intensity increases.

5. A novel concept is put forward called the structural *prominence*. It describes the presence of the relict rock structure and how it influences the compression behaviour of completely weathered rock. As chemical weathering increases, the structural *prominence* decreases, and results in an increase in compressibility of the material

6. The structural *prominence* describes the compression behaviour well on a dolomite weathering profile. Here the wad is typically at a lower dry density and higher void ratio than the more weathered residual dolomite but has been shown to undergo less strain under the same load conditions. This is due to the high structural *prominence* expected in wad.

7. Wad has a high structural vulnerability meaning when the structure *prominence* is lost, the resultant material performs significantly poorer when placed under a load. This is an indication of the role this material has on the formation of sinkholes.

8. A new characterization method is proposed for identifying residual dolomite and wad using easily calculated parameters, namely liquid limit and dry density.

9.2 Way forward

It is recommended to evaluate the structural *prominence* across various geological weathering profiles under different climatic conditions. More rigorous testing methods such as triaxial shear testing in the laboratory and plate load testing in the field should be conducted to assess the shearing and failure characteristic against the structural *prominence* of the sample. Interdisciplinary research between the XRCT specialists and engineering geologists is recommended to improve the pore modelling of soil and completely weathered rock.

10 References

Al-Khafaji, A. W. N., and O. B. Andersland. 1992. ‘Equations for Compression Index Approximation’. *Journal of Geotechnical Engineering* 118 (1): 148–53. https://doi.org/10.1061/(ASCE)0733-9410(1992)118:1(148).

Anderson, Suzanne P. 2019. ‘Breaking It Down: Mechanical Processes in the Weathering Engine’. *Elements* 15 (4): 247–52. https://doi.org/10.2138/gselements.15.4.247.

Anhaeusser, C.R. 2006. ‘Ultramafic and Mafic Intrusions of the Kaalvaal Craton’. In *The Geology of South Africa*, edited by M.R. Johnson, C.R. Anhaeusser, and R.J. Thomas, 95–134. Pretoria: Council for Geoscience.

ASTM D2487-17e1. 2020. ‘Practice for Classification of Soils for Engineering Purposes (Unified Soil Classification System)’. ASTM International. https://doi.org/10.1520/D2487-17E01.

ASTM D2488-09a. 2009. ‘Practice for Description and Identification of Soils (Visual-Manual Procedure)’. ASTM International. https://doi.org/10.1520/D2488-09A.

Banerjee, Anupam, Ramananda Chakrabarti, and Sourav Mandal. 2016. ‘Geochemical Anatomy of a Spheroidally Weathered Diabase’. *Chemical Geology* 440 (November):124–38. https://doi.org/10.1016/j.chemgeo.2016.07.008.

Baveye, Philippe, María Balseiro-Romero, Nicolas Bottinelli, Maria Briones, Yvan Capowiez, Patricia Garnier, Alexandra Kravchenko, et al. 2022. ‘Lessons from a Landmark 1991 Article on Soil Structure: Distinct Precedence of Non-Destructive Assessment and Benefits of Fresh Perspectives in Soil Research’. *Soil Research* 60 (January). https://doi.org/10.1071/SR21268.

Berner, R. A., A. C. Lasaga, and R. M. Garrels. 1983. ‘Carbonate-Silicate Geochemical Cycle and Its Effect on Atmospheric Carbon Dioxide over the Past 100 Million Years’. *Am. J. Sci.; (United States)* 283:7 (September). https://doi.org/10.2475/ajs.283.7.641.

Berner, Robert A. 2004. ‘Processes of the Long-Term Carbon Cycle: Chemical Weathering of Silicates’. In *The Phanerozoic Carbon Cycle: CO2 and O2*, 0. Oxford University Press. https://doi.org/10.1093/oso/9780195173338.003.0004.

Bester, Deon. 2021. ‘Dolomite Hazard Assessment of Wad Rich Overburden from the Oaktree Formation, Chuniespoort Group in the Monavoni and Highveld Areas, Centurion, South Africa’. Unpublished Masters Dissertation, University of Pretoria.

Beukes, N. J., H. S. van Niekerk, and J. Gutzmer. 1999. ‘Post Gondwana African Land Surface and Pedogenetic Ferromanganese Deposits on the Witwatersrand at the West Wits Gold Mine, South Africa’. *South African Journal of Geology* 102 (1): 65–82.

Blight, G.E., and E.C. Leong. 2012. *Mechanics of Residual Soils*. Second. Taylor & Francis Group.

Blight, Geoffrey E., and Eng-Choon Leong, eds. 2012. *Mechanics of Residual Soils*. 2. ed. Boca Raton: CRC Press.

Blunt, Martin J. 2001. ‘Flow in Porous Media — Pore-Network Models and Multiphase Flow’. *Current Opinion in Colloid & Interface Science* 6 (3): 197–207. https://doi.org/10.1016/S1359-0294(01)00084-X.

Bonnet, M., L. Caner, M. Siitari-Kauppi, A. Mazurier, A.S. Mexias, N. Dani, and P. Sardini. 2022. ‘Weathering of Viamão Granodiorite, South Brazil: Part 1 – Clay Minerals Formation and Increase in Total Porosity’. *Geoderma* 424 (October):115968. https://doi.org/10.1016/j.geoderma.2022.115968.

———. 2023. ‘Weathering of Viamão Granodiorite, South Brazil: Part 2 – Initial Porosity of Un-Weathered Rock Controls Porosity Development in the Critical Zone’. *Geoderma* 429 (January):116247. https://doi.org/10.1016/j.geoderma.2022.116247.

Bouma, J. 1981. ‘Soil Morphology and Preferential Flow along Macropores’. *Agricultural Water Management* 3 (4): 235–50. https://doi.org/10.1016/0378-3774(81)90009-3.

Bourgault, Rebecca R., and Martin C. Rabenhorst. 2011. ‘Genesis and Characterization of Manganiferous Soils in the Eastern Piedmont, USA’. *Geoderma* 165 (1): 84–94. https://doi.org/10.1016/j.geoderma.2011.07.008.

Bowen, Norman L. 1929. ‘The Evolution of the Igneous Rocks’. *Nature* 124 (3126): 474–75. https://doi.org/10.1038/124474a0.

Brewer, Roy. 1965. ‘Fabric and Mineral Analysis of Soils’. *Soil Science* 100 (1): 73.

Brink, A.B.A. 1979. ‘Basement Complex: Granites’. In *Engineering Geology of South Africa*, 56–80. Building Publications.

BS 1377-5. 1990. ‘METHODS OF TEST FOR SOILS FOR CIVIL ENGINEERING PURPOSES. PART 5: COMPRESSIBILITY, PERMEABILITY AND DURABILITY TESTS’. BSI British Standards. https://doi.org/0-580-18030.

BS 1377-6. 1990. ‘Methods of Test for Soils for Civil Engineering Purposes: Consolidation and Permeability Tests in Hydraulic Cells and with Pore Pressure Measurement’. BSI British Standards. https://doi.org/10.3403/00227786.

Burmister, D.M. 1949. ‘Principles and Techniques of Soil Identification’. In *Proceedings of the 29th Annual Meeting*, 402–33. Washington, DC: Highway Research Board.

Buttrick, David Belton. 1986. ‘Wad and Ferroan Soil Developed in the Dolomitic Area South of Pretoria’. https://repository.up.ac.za/handle/2263/82505.

Cho, Tenichi, and Tohru Ohta. 2022. ‘A Robust Chemical Weathering Index for Sediments Containing Authigenic and Biogenic Materials’. *Palaeogeography, Palaeoclimatology, Palaeoecology* 608 (December):111288. https://doi.org/10.1016/j.palaeo.2022.111288.

Clothier, Brent. 2008. ‘Soil Pores’. In *Encyclopedia of Earth Sciences Series*, 693–99. Springer. https://doi.org/10.1007/978-1-4020-3995-9_548.

Cnudde, V., and M.N. Boone. 2013. ‘High-Resolution X-Ray Computed Tomography in Geosciences: A Review of the Current Technology and Applications’. *Earth-Science Reviews* 123 (August):1–17. https://doi.org/10.1016/j.earscirev.2013.04.003.

Collins, K., and A. McGown. 1974. ‘The Form and Function of Microfabric Features in a Variety of Natural Soils’. *Géotechnique* 24 (2): 223–54. https://doi.org/10.1680/geot.1974.24.2.223.

Colman, Steven M. 1982. ‘Chemical Weathering of Basalts and Andesites; Evidence from Weathering Rinds’. Report 1246. Professional Paper. USGS Publications Warehouse. https://doi.org/10.3133/pp1246.

Committee of Transport (COTO). 2020. ‘Chapter 4: Earthworks and Pavement Layers: Materials’. In *Standard Specifications for Road and Bridge Works for South Africa Road Authorities*. Pretoria: The South African National Roads Agency SOC Limited.

Daneshian, Behrooz, Ghassem Habibagahi, and Ehsan Nikooee. 2021. ‘Determination of Unsaturated Hydraulic Conductivity of Sandy Soils: A New Pore Network Approach’. *Acta Geotechnica* 16 (2): 449–66. https://doi.org/10.1007/s11440-020-01088-3.

Day, P. W. 1981. ‘Properties of Wad’. In *Seminar on Engineering Geology of Dolomite Areas*, 135–47. Pretoria: University of Pretoria.

Deng, Kai, Shouye Yang, and Yulong Guo. 2022. ‘A Global Temperature Control of Silicate Weathering Intensity’. *Nature Communications* 13 (1): 1781. https://doi.org/10.1038/s41467-022-29415-0.

Dimitrovski, K. 2019. 'Equivalent average diameter of pores - definition and determination. In *Textile Science and Economy French - Croatian Forum*; University of Zagreb, Faculty of Textile Technology: pp. 115–122. Zagreb, Croatia.

Dippenaar, M., and J. Rooy. 2014. *Review of Engineering, Hydrogeological and Vadose Zone Hydrological Aspects of the Lanseria Gneiss, Goudplaats-Hout River Gneiss and Nelspruit Suite Granite (South Africa*) University of Pretoria.

Dippenaar, M.A., B.R. Jones, J.L. Rooy, M. Maoyi, and D. Swart. 2022. *The Vadose Zone: From Theory to Practise*. Pretoria: Water Research Commission.

Dippenaar, M.A., J.L. Van Rooy, and G. Davis. 2024. ‘Engineering Geological Soil and Rock Description’. Pretoria. South Africa: South African Institute for Engineering and Environmental Geologists (SAIEG). www.saieg.co.za.

Dippenaar, Matthys. 2014. ‘Porosity Reviewed: Quantitative Multi-Disciplinary Understanding, Recent Advances and Applications in Vadose Zone Hydrology’. *Geotechnical and Geological Engineering* 32 (February). https://doi.org/10.1007/s10706-013-9704-9.

Dippenaar, Matthys A., J. Louis van Rooy, and Roger E. Diamond. 2019. ‘Engineering, Hydrogeological and Vadose Zone Hydrological Aspects of Proterozoic Dolomites (South Africa)’. *Journal of African Earth Sciences* 150 (February):511–21. https://doi.org/10.1016/j.jafrearsci.2018.07.024.

Dippenaar, Matthys A., and J. Louis Van Rooy. 2014. ‘Review of Engineering, Hydrogeological and Vadose Zone Hydrological Aspects of the Lanseria Gneiss, Goudplaats-Hout River Gneiss and Nelspruit Suite Granite (South Africa)’. *Journal of African Earth Sciences* 91 (March):12–31. https://doi.org/10.1016/j.jafrearsci.2013.11.019.

Dos Santos, Jean Cheyson Barros, Cybelle Souza De Oliveira, Emilia Le Pera, Lucas Resmini Sartor, Marcelo Metri Corrêa, Artur Henrique Nascimento Da Silva, Cândida Regina Müller, Roseclênia Alves Santos, and Antonio Carlos De Azevedo. 2022. ‘Saprolithology Applied to Pedology: Integrated Study of Soil and Saprolite Derived from Crystalline Rocks to Better Understand Properties of Whole Regoliths along a Climate Gradient (NE Brazil)’. *Geoderma* 409 (March):115602. https://doi.org/10.1016/j.geoderma.2021.115602.

Dos Santos, Jean Cheyson Barros, Cybelle Souza De Oliveira, Emilia Le Pera, Lucas Resmini Sartor, Marcelo Metri Corrêa, Artur Henrique Nascimento Da Silva, Roseclênia Alves Santos, Luis Fernando Vieira Da Silva, Cândida Regina Müller, and Antonio Carlos De Azevedo. 2022. ‘Saprolithology Applied to Pedology: Mineral Alteration in Soil-Saprolite Profiles along a Climate Gradient in Triunfo Massif (NE Brazil)’. *CATENA* 213 (June):106214. https://doi.org/10.1016/j.catena.2022.106214.

Dos Santos, Jean Cheyson Barros Dos, Emilia Le Pera, Valdomiro Severino De Souza Júnior, Cybelle Souza De Oliveira, Jérôme Juilleret, Marcelo Metri Corrêa, and Antonio Carlos De Azevedo. 2018. ‘Porosity and Genesis of Clay in Gneiss Saprolites: The Relevance of Saprolithology to Whole Regolith Pedology’. *Geoderma* 319 (June):1–13. https://doi.org/10.1016/j.geoderma.2017.12.031.

Dowding, Catherine E., Michael J. Borda, Martin V. Fey, and Donald L. Sparks. 2005. ‘A New Method for Gaining Insight into the Chemistry of Drying Mineral Surfaces Using ATR-FTIR’. *Journal of Colloid and Interface Science* 292 (1): 148–51. https://doi.org/10.1016/j.jcis.2005.05.075.

Dowding, Catherine Elaine. 2004. ‘Morphology, Mineralogy and Surface Chemistry of Manganiferous Oxisols near Graskop, Mpumalanga Province, South Africa /’. Master Thesis, Stellenbosch University. http://hdl.handle.net/10019.1/16312.

Dowding, C.E., and M.V. Fey. 2007. ‘Morphological, Chemical and Mineralogical Properties of Some Manganese-Rich Oxisols Derived from Dolomite in Mpumalanga Province, South Africa’. *Geoderma* 141 (1–2): 23–33. https://doi.org/10.1016/j.geoderma.2007.04.024.

Dowding, C.E., M.V. Fey, M.J. Borda, and D.L. Sparks. 2005. ‘A New Method for Gaining Insight into the Chemistry of Drying Mineral Surfaces Using ATR-FTIR’. *Journal of Colloid and Interface Science* 292:148–51.

Eriksson, P. G., and W. Altermann. 1998. ‘An Overview of the Geology of the Transvaal Supergroup Dolomites (South Africa)’. *Environmental Geology* 36 (1–2): 179–88. https://doi.org/10.1007/s002540050334.

Eriksson, P.G., Wladyslaw Altermann, and F.J. Hartzer. 2006. ‘The Transvaal Supergroup and Its Precursors’. *The Geology of South Africa: Johannesburg*, January, 237–60.

Fedo, Christopher M., H. Wayne Nesbitt, and Grant M. Young. 1995. ‘Unravelling the Effects of Potassium Metasomatism in Sedimentary Rocks and Paleosols, with Implications for Paleoweathering Conditions and Provenance’. *Geology* 23 (10): 921. https://doi.org/10.1130/0091-7613(1995)023<0921:UTEOPM>2.3.CO;2.

Fitts, Charles Richard. 2013. *Groundwater Science*. 2nd edition. Amsterdam: Academic Press.

Fourie, A.B., T.Y. Irfan, J.B.Queiroz Carvalho, J.V. Simmons, and L.D. Wesley. 2012. 'Microstructure, Mineralogy and Classification of Residual Soils'. In *Mechanics of Residual Soils*, edited by G.E. Blight and E.C. Leong, 41–62. CRC Press.

Fredlund, Delwyn G., and Norbert R. Morgenstern. 1977. 'Stress State Variables for Unsaturated Soils'. *Journal of the Geotechnical Engineering Division* 103 (5): 447–66. https://doi.org/10.1061/AJGEB6.0000423.

Fredlund, D.G., H. Rahardjo, and M.D. Fredlund. 2012. 'State Variables for Unsaturated Soils'. In *Unsaturated Soil Mechanics in Engineering Practice*, 80–108. John Wiley & Sons, Ltd. https://doi.org/10.1002/9781118280492.ch3.

Fredlund, D.G., and Anqing Xing. 1994. 'Equations for the Soil-Water Characteristic Curve'. *Canadian Geotechnical Journal* 31 (4): 521–32. https://doi.org/10.1139/t94-061.

Frings, Patrick J., and Heather L. Buss. 2019. 'The Central Role of Weathering in the Geosciences'. *Elements* 15 (4): 229–34. https://doi.org/10.2138/gselements.15.4.229.

Fukue, Masaharu, and Shigeyasu Okusa. 1987. 'Compression Law of Soils'. *Soils and Foundations* 27 (1): 23–34. https://doi.org/10.3208/sandf1972.27.23.

Futai, M. M., M. S. S. Almeida, and W. A. Lacerda. 2004. 'Yield, Strength, and Critical State Behavior of a Tropical Saturated Soil'. *Journal of Geotechnical and Geoenvironmental Engineering* 130 (11): 1169–79. https://doi.org/10.1061/(ASCE)1090-0241(2004)130:11(1169).

Gaspar, Tiago, Sw Jacobsz, Mario Schulz-Poblete, and David Toll. 2019. 'Measurement of the Soil Water Retention Curve: Practical Considerations'. In *Proceedings of the 17th African Regional Conference on Soil Mechanics and Geotechnical Engineering*. Cape Town, South Africa.

Gilboy, G. 1930. 'Notes on Soil Mechanics'. Massachusetts Institute of Technology (MIT).

Golden, D. C., C. C. Chen, and J. B. Dixon. 1986. 'Synthesis of Todorokite'. *Science* 231 (4739): 717–19. https://doi.org/10.1126/science.231.4739.717.

Goldich, Samuel S. 1938. 'A Study in Rock-Weathering'. *The Journal of Geology* 46 (1): 17–58. https://doi.org/10.1086/624619.

Golparvar, Amir, Matthias Kästner, and Martin Thullner. 2021. 'Pore-scale Modeling of Microbial Activity: What We Have and What We Need'. *Vadose Zone Journal* 20 (1): e20087. https://doi.org/10.1002/vzj2.20087.

Golparvar, Amir, Y. Zhou, Kejian Wu, Jingsheng Ma, and Zhixin Yu. 2018. 'A Comprehensive Review of Pore Scale Modeling Methodologies for Multiphase Flow in Porous Media'. *Advances in Geo-Energy Research* 2 (December):418–40. https://doi.org/10.26804/ager.2018.04.07.

Griffiths, Luke, Michael J. Heap, Tao Xu, Chong-feng Chen, and Patrick Baud. 2017. 'The Influence of Pore Geometry and Orientation on the Strength and Stiffness of Porous Rock'. *Journal of Structural Geology* 96 (March):149–60. https://doi.org/10.1016/j.jsg.2017.02.006.

Guggenheim, Stephen, and R. T. Martin. 1995. 'Definition of Clay and Clay Mineral: Joint Report of the Aipea Nomenclature and CMS Nomenclature Committees'. *Clays and Clay Minerals* 43 (2): 255–56. https://doi.org/10.1346/CCMN.1995.0430213.

Guidelines for Soil and Rock Logging in South Africa. 2001. 'Proceedings, Geoterminology Workshop Organised by AEG, SAICE and SAIEG'. In , 2nd Ipression.

Hall, Kevin, Colin Thorn, and Paul Sumner. 2012. 'On the Persistence of "Weathering"'. *Geomorphology* 149–150 (May):1–10. https://doi.org/10.1016/j.geomorph.2011.12.024.

Hassan, Safiya M., Callum R. Anderson, and Maarten de Wit. 2022. 'Facies Analyses and Depositional Environments of the Mio-Pliocene Alexandria Formation, Algoa Basin, South Africa'. *Journal of African Earth Sciences* 192 (August):104555. https://doi.org/10.1016/j.jafrearsci.2022.104555.

Hayes, Jorden L., Clifford S. Riebe, W. Steven Holbrook, Brady A. Flinchum, and Peter C. Hartsough. 2019. 'Porosity Production in Weathered Rock: Where Volumetric Strain

Dominates over Chemical Mass Loss’. *Science Advances* 5 (9): eaao0834. https://doi.org/10.1126/sciadv.aao0834.

Helliwell, J. 2013. ‘Applications of X-Ray Computed Tomography for Examining Biophysical Interactions and Structural Development in Soil Systems: A Review’. *European Journal of Soil Science* 64:279–97.

Hencher, Steve. 2024. *Practical Engineering Geology*. 2nd ed. London: CRC Press. https://doi.org/10.1201/9781003348894.

Hu, Wei, Rogerio Cichota, Mike Beare, Karin Müller, John Drewry, and Andre Eger. 2023. ‘Soil Structural Vulnerability: Critical Review and Conceptual Development’. *Geoderma* 430 (February):116346. https://doi.org/10.1016/j.geoderma.2023.116346.

Huat, Bujang B. K., David G. Toll, and Arun Prasad, eds. 2012. ‘Sampling and Testing of Tropical Residual Soils’. In *Handbook of Tropical Residual Soils Engineering*. CRC Press.

Huda, Walter, and R. Brad Abrahams. 2016. *Review of Radiologic Physics*. Fourth edition. Philadelphia: Lippincott Williams & Wilkins.

Hunt, Roy E. 2005. *Geotechnical Engineering Investigation Handbook*. 0 ed. CRC Press. https://doi.org/10.1201/9781420039153.

ISRM, International Society for Roc Mechanics. 1981. ‘Suggested Methods for the Rock Characterization, Testing and Monitoring’. In *ISRM Commission on Testing Methods*. Oxford: Pergamon Press.

Jacobsz, S. W. 2018. ‘Low Cost Tensiometers for Geotechnical Applications’. In *Physical Modelling in Geotechnics, Volume 1*. CRC Press.

Jacobsz, SW. 2015. ‘Trapdoor Experiments Studying Cavity Propagation’. In *Proceedings for the 1st Southern African Geotechnical Conference*. Sun City: SAICE.

Janssen, Donald J, and Barby J Dempsey. 1980. ‘Soil-Moisture Properties of Subgrade Soils’. *Transportation Research Record*.

Jenne, E. A. 1968. ‘Controls on Mn, Fe, Co, Ni, Cu, and Zn Concentrations in Soils and Water: The Significant Role of Hydrous Mn and Fe Oxides’. In *Trace Inorganics In Water*, 73:337–87. Advances in Chemistry 73. AMERICAN CHEMICAL SOCIETY. https://doi.org/10.1021/ba-1968-0073.ch021.

Kasting, James F. 2019. ‘The Goldilocks Planet? How Silicate Weathering Maintains Earth “Just Right”’. *Elements* 15 (4): 235–40. https://doi.org/10.2138/gselements.15.4.235.

Kellogg, C.E., United States Dept of Agriculture, and United States Bureau of Plant Industry. 1936. *Development and Significance of the Great Soil Groups of the United States*. Miscellaneous Publication. U.S. Government Printing Office. https://books.google.co.za/books?id=3vAjAQAAMAAJ.

Kellogg, Charles E. 1930. *Preliminary Study of the Profiles of the Principal Soil Types of Wisconsin*. Bulletin / Wisconsin Geological and Natural History Survey ; No. 77A. Madison: Published by the state. https://catalog.hathitrust.org/Record/100223373.

Kim, Tae-Hyung, and Changsoo Hwang. 2003. ‘Modeling of Tensile Strength on Moist Granular Earth Material at Low Water Content’. *Engineering Geology* 69 (3): 233–44. https://doi.org/10.1016/S0013-7952(02)00284-3.

Klausen, M.B., U. Söderlund, J.R. Olsson, R.E. Ernst, M. Armoogam, S.W. Mkhize, and G. Petzer. 2010. ‘Petrological Discrimination among Precambrian Dyke Swarms: Eastern Kaapvaal Craton (South Africa)’. *Precambrian Large Igneous Provinces (LIPs) and Their Dyke Swarms: New Insights from High-Precision Geochronology Integrated with Paleomagnetism and Geochemistry* 183 (3): 501–22. https://doi.org/10.1016/j.precamres.2010.01.013.

Knappett, Jonathan, R. F. Craig, and R. F. Craig. 2012. *Craig’s Soil Mechanics*. 8th ed. Abingdon, Oxon ; New York: Spon Press.

Koestel, J., M. Larsbo, and N. Jarvis. 2020. ‘Scale and REV Analyses for Porosity and Pore Connectivity Measures in Undisturbed Soil’. *Geoderma* 366 (May):114206. https://doi.org/10.1016/j.geoderma.2020.114206.

Lenhardt, Nils, and Patrick G. Eriksson. 2012. ‘Volcanism of the Palaeoproterozoic Bushveld Large Igneous Province: The Rooiberg Group, Kaapvaal Craton, South Africa’. *Precambrian Research* 214–215 (September):82–94. https://doi.org/10.1016/j.precamres.2011.12.003.

Letey, J. 1991. ‘The Study of Soil Structure - Science or Art’. *Soil Research* 29 (6): 699. https://doi.org/10.1071/SR9910699.

Li, Zhong-Sen, and Lian-Sheng Tang. 2019. ‘Using Synchrotron-Based X-Ray Microcomputed Tomography to Characterize Water Distribution in Compacted Soils’. *Advances in Materials Science and Engineering* 2019 (May):1–11. https://doi.org/10.1155/2019/7147283.

Liang, Yong-Hui, Wei-Hou Shui, and Shi-Feng Lu. 2022. ‘Field Practice and Ground Settlement Behaviors of a Land Creation Case in Loess Area of China’. *Bulletin of Engineering Geology and the Environment* 81 (11): 462. https://doi.org/10.1007/s10064-022-02964-w.

Liu, Xinyu, Xianwei Zhang, Lingwei Kong, Gang Wang, and Honghu Liu. 2022. ‘Chemical Weathering Indices and How They Relate to the Mechanical Parameters of Granite Regolith from Southern China’. *CATENA* 216 (September):106400. https://doi.org/10.1016/j.catena.2022.106400.

Lu, Ning. 2020. ‘Unsaturated Soil Mechanics: Fundamental Challenges, Breakthroughs, and Opportunities’. *Journal of Geotechnical and Geoenvironmental Engineering* 146 (5): 02520001. https://doi.org/10.1061/(ASCE)GT.1943-5606.0002233.

Lu, Ning, and William J. Likos. 2004. *Unsaturated Soil Mechanics*. Wiley.

Mackenzie, F., and R. Garrels. 1966. ‘Chemical Balance between Rivers and Oceans’. *American Journal of Science* v. 264 (September):507–25. https://doi.org/10.2475/ajs.264.7.507.

Makhubela, Tebogo V., Jan D. Kramers, Sibusiso M. Konyana, Herman S. Van Niekerk, and Stephan R. Winkler. 2021. ‘Erosion Rates and Weathering Timescales in the Eastern Great Escarpment, South Africa’. *Chemical Geology* 580 (October):120368. https://doi.org/10.1016/j.chemgeo.2021.120368.

McKenzie, R. M. 1972. ‘The Manganese Oxides in Soils—A Review’. *Zeitschrift Für Pflanzenernährung Und Bodenkunde* 131 (3): 221–42. https://doi.org/10.1002/jpln.19721310302.

McQueen, I. S., and R. F. Miller. 1974. ‘Approximating Soil Moisture Characteristics From Limited Data: Empirical Evidence and Tentative Model’. *Water Resources Research* 10 (June):521–27. https://doi.org/10.1029/WR010i003p00521.

Mees, F., R. Swennen, M. Van Geet, and P. Jacobs. 2003. ‘Applications of X-Ray Computed Tomography in the Geosciences’. *Geological Society, London, Special Publications* 215 (1): 1–6. https://doi.org/10.1144/GSL.SP.2003.215.01.01.

Meunier, Alain, Laurent Caner, Fabien Hubert, Abderrazak El Albani, and Dimitri Prêt. 2013. ‘The Weathering Intensity Scale (WIS): An Alternative Approach of the Chemical Index of Alteration (CIA)’. *American Journal of Science* 313 (February). https://doi.org/10.2475/02.2013.03.

Mitchell, James Kenneth, and Kenʾichi Soga. 2005. *Fundamentals of Soil Behavior*. 3rd ed. Hoboken, N.J: John Wiley & Sons.

Moreno-Maroto, José Manuel, and Jacinto Alonso-Azcárate. 2018. ‘What Is Clay? A New Definition of “Clay” Based on Plasticity and Its Impact on the Most Widespread Soil Classification Systems’. *Applied Clay Science* 161 (September):57–63. https://doi.org/10.1016/j.clay.2018.04.011.

———. 2022. ‘Evaluation of the USDA Soil Texture Triangle through Atterberg Limits and an Alternative Classification System’. *Applied Clay Science* 229 (November):106689. https://doi.org/10.1016/j.clay.2022.106689.

National Research. 2001. *Basic Research Opportunities in Earth Science*. Washington, D.C.: National Academies Press. https://doi.org/10.17226/9981.

Nelson, S.A. 2017. ‘Weathering & Clay Minerals. Lecture Notes, Department of Earth & Environmental Sciences’. Tulane University. https://www2.tulane.edu/~sanelson/eens211/weathering&clayminerals.htm.

Nesbitt, H. W., and G. M. Young. 1982. ‘Early Proterozoic Climates and Plate Motions Inferred from Major Element Chemistry of Lutites’. *Nature* 299 (5885): 715–17. https://doi.org/10.1038/299715a0.

Ng, Charles Wang Wai, and Bruce Menzies. 2014. *Advanced Unsaturated Soil Mechanics and Engineering*. London: CRC Press. https://doi.org/10.1201/9781482266122.

Norbury, David. 2020. *Soil and Rock Description in Engineering Practice 3rd Edition*. 3rd ed. Dunbeath: Whittles Publishing Ltd.

Obbes, August Murray. 1995. ‘The Structure, Stratigraphy and Sedimentology of the Black Reef-Malmani-Rooihoogte Succession of the Transvaal Supergroup South-West of Pretoria’. MSc Dissertation, University of Johannesburg.

Obermeier, S. F., and W. H. Langer. 1986. ‘Relationships between Geology and Engineering Characteristics of Soils and Weathered Rocks of Fairfax County and Vicinity, Virginia’. *Professional Paper*. https://doi.org/10.3133/pp1344.

Paniagua, P., E. Andò, M. Silva, A. Emdal, S. Nordal, and G. Viggiani. 2013. ‘Soil Deformation around a Penetrating Cone in Silt’. *Géotechnique Letters* 3 (4): 185–91. https://doi.org/10.1680/geolett.13.00067.

Partridge, T. C. 1998. ‘Of Diamonds, Dinosaurs and Diastrophism; 150 Million Years of Landscape Evolution in Southern Africa’. *South African Journal of Geology* 101 (3): 167–84.

Phillips, Debra, David Watson, Yul Roh, Tonia Mehlhorn, Ji-Won Moon, and Phil Jardine. 2006. ‘Distribution of Uranium Contamination in Weathered Fractured Saprolite/Shale and Ground Water’. *Journal of Environmental Quality* 35 (September):1715–30. https://doi.org/10.2134/jeq2005.0124.

Phillips, Jonathan D., Łukasz Pawlik, and Pavel Šamonil. 2019. ‘Weathering Fronts’. *Earth-Science Reviews* 198 (November):102925. https://doi.org/10.1016/j.earscirev.2019.102925.

Post, Jeffrey E. 1999. ‘Manganese Oxide Minerals: Crystal Structures and Economic and Environmental Significance’. *Proceedings of the National Academy of Sciences* 96 (7): 3447–54. https://doi.org/10.1073/pnas.96.7.3447.

Rabot, E., M. Wiesmeier, S. Schlüter, and H.-J. Vogel. 2018. ‘Soil Structure as an Indicator of Soil Functions: A Review’. *Geoderma* 314 (March):122–37. https://doi.org/10.1016/j.geoderma.2017.11.009.

Rahardjo, Harianto, Yongmin Kim, and Alfrendo Satyanaga. 2019. ‘Role of Unsaturated Soil Mechanics in Geotechnical Engineering’. *International Journal of Geo-Engineering* 10 (1): 8. https://doi.org/10.1186/s40703-019-0104-8.

Raymo, M. E., and W. F. Ruddiman. 1992. ‘Tectonic Forcing of Late Cenozoic Climate’. *Nature* 359 (September):117–22. https://doi.org/10.1038/359117a0.

Richardson, Justin B. 2017. ‘Critical Zone’. In *Encyclopedia of Engineering Geology*, edited by Peter Bobrowsky and Brian Marker, 1–5. Encyclopedia of Earth Sciences Series. Cham: Springer International Publishing. https://doi.org/10.1007/978-3-319-39193-9_355-1.

Riebe, Clifford, Russell Callahan, Sarah Granke, Brad Carr, Jorden Hayes, Marlie Schell, and Leonard Sklar. 2021. ‘Anisovolumetric Weathering in Granitic Saprolite Controlled by Climate and Erosion Rate’. *Geology* 49 (January). https://doi.org/10.1130/G48191.1.

Rietveld, H. M. 1969. ‘A Profile Refinement Method for Nuclear and Magnetic Structures’. *Journal of Applied Crystallography* 2 (2): 65–71. https://doi.org/10.1107/S0021889869006558.

Robb, Laurence, Guenther Brandl, Carl Anhaeusser, and Marc Poujol. 2006. ‘Archaean Granitoid Intrusions’. In *Geology of South Africa*, 57–94.

Rocchi, I., M.R. Coop, and M. Maccarini. 2017. ‘The Effects of Weathering on the Physical and Mechanical Properties of Igneous and Metamorphic Saprolites’. *Engineering Geology* 231 (December):56–67. https://doi.org/10.1016/j.enggeo.2017.10.003.

Saha, Sajib, Narain Hariharan, Hakan Sahin, Robert L. Lytton, and Dallas N. Little. 2024. 'Impact of Remolded Soil Fabric on the Volumetric Deformation Behavior of Clayey Soils'. *Transportation Geotechnics* 44 (January):101158. https://doi.org/10.1016/j.trgeo.2023.101158.

Samardzioska, Todorka, and Viktor Popov. 2005. 'Numerical Comparison of the Equivalent Continuum, Non-Homogeneous and Dual Porosity Models for Flow and Transport in Fractured Porous Media'. *Advances in Water Resources* 28 (3): 235–55. https://doi.org/10.1016/j.advwatres.2004.11.002.

SANS 3001-GR10. 2013. 'Civil Engineering Test Methods. Part GR10: Determination of the One-Point Liquid Limit, Plastic Limit, Plasticity Index and Linear Shrinkage'. Pretoria: South African Bureau of Standards (SABS).

SANS 3001-GR11. 2013. 'Civil Engineering Test Methods. Part GR11: Determination of the Liquid Limit with the Two-Point Method'. Pretoria: South African Bureau of Standards (SABS).

SANS 3001-GR12. 2013. 'Civil Engineering Test Methods. Part GR12: Determination of the Flow Curve Liquid Limit'. Pretoria: South African Bureau of Standards (SABS).

Savage, P. F. 2007. *Evaluation of Possible Swelling Potential of Soil*. SATC. https://repository.up.ac.za/handle/2263/5947.

Schaetzl, Randall J., and Michael Lawrence Thompson. 2015. *Soils: Genesis and Geomorphology*. 2nd ed. New York: Cambridge university press.

Schweitzer, J.K., Chris Hatton, and Sybrand de Waal. 1995. 'Regional Lithochemical Stratigraphy of the Rooiberg Group, Upper Transvaal Supergroup: A Proposed New Subdivision'. *South African Journal of Geology* 98 (January):245–55.

Sergeev, N. 2023. 'Quantifying Weathering Intensity Using Chemical Proxies: A Weathering Index AFB'. *Australian Journal of Earth Sciences* 70 (2): 260–84. https://doi.org/10.1080/08120099.2023.2137585.

Shaw, C.F. 1927. 'Report of Commitee on Soil Terminology'. *Am. Soil Surv. Ass. Bull* 8:66–98.

Sidebottom, Charles. 2012. *Mechanics of Residual Soils*. Edited by Geoffrey E. Blight and Eng Choon Leong. 0 ed. CRC Press. https://doi.org/10.1201/b12014.

Silva, Luis Fernando Vieira Da, Jean Cheyson Barros Dos Santos, Cybelle Souza De Oliveira, and Antonio Carlos De Azevedo. 2022. 'Saprolite: A Bibliometric Study from 1990 to 2020'. *Journal of South American Earth Sciences* 115 (April):103729. https://doi.org/10.1016/j.jsames.2022.103729.

Singh, H., and B.B.K. Huat. 2013. 'Formation and Classification of Tropical Residual Soils'. In *Handbook of Tropical Residual Soils Engineering*, edited by B.B.K. Haut, D.G. Toll, and A. Prasad, 21–64. CRC Press.

Skopp, J. 1981. 'Comment on "Micro- Meso- and Macroporosity of Soil"'. *Soil Science Society of America Journal* 45.

Sophocleous, Marios. 2010. 'Understanding and Explaining Surface Tension and Capillarity: An Introduction to Fundamental Physics for Water Professionals'. *Hydrogeology Journal* 18 (4): 811–21. https://doi.org/10.1007/s10040-009-0565-5.

Stott, P, and E Theron. 2016. 'Shortcomings in the Estimation of Clay Fraction by Hydrometer'. *Journal of the South African Institution of Civil Engineering* 58 (2): 14–24. https://doi.org/10.17159/2309-8775/2016/v58n2a2.

Strakhov, N. M. 1967. *Principles of Lithogenesis*. Edited by S. I. Tomkeieff and J. E. Hemingway. Boston, MA: Springer US. https://doi.org/10.1007/978-1-4684-8923-1.

Streckeisen, A. 1974. 'Classification and Nomenclature of Plutonic Rocks Recommendations of the IUGS Subcommission on the Systematics of Igneous Rocks'. *Geologische Rundschau* 63 (2): 773–86. https://doi.org/10.1007/BF01820841.

Sturrock, Craig J. 2022. 'Optimising the Scanning Process: Demystifying the Dark Art of Optimising Microtomography Scan Settings'. In *X-Ray Imaging of the Soil Porous Architecture*, edited by Sacha Jon Mooney, Iain M. Young, Richard J. Heck, and Stephan

Peth, 39–55. Cham: Springer International Publishing. https://doi.org/10.1007/978-3-031-12176-0_4.

Summerfield, Michael A. 2014. *Global Geomorphology*. 1st ed. Routledge. https://www.perlego.com/book/1557141/global-geomorphology-pdf?utm_source=google&utm_medium=cpc&campaignid=15853719261&adgroupid=166297292553&gad_source=1&gclid=Cj0KCQiA0MG5BhD1ARIsAEcZtwQ3cc3XeNi9ToNKB62Z4A3_k8CaGKbMdKixKu8RFnFIaWiKU7CFvUQaAu7wEALw_wcB.

Swart, D. 2019. 'Mechanical and Hydraulic Properties of Residual Dolomite and Wad Found in the Malmani Subgroup in South Africa'. MSc Dissertation, University of Pretoria.

Swart, D., M.A. Dippenaar, and J.L. Van Rooy. 2019. 'Mechanical and Hydraulic Properties of Residual Dolomite and Wad'. *South African Journal of Geology* 122 (3): 379–88. https://doi.org/10.25131/sajg.122.0024.

Swart, Duan, Matthys A. Dippenaar, and J. Louis Van Rooy. 2023. 'Field Tests for the Identification of Silts'. *Bulletin of Engineering Geology and the Environment* 82 (11): 425. https://doi.org/10.1007/s10064-023-03442-7.

Swart, Duan, Tiago Gaspar, and Matthys Dippenaar. 2021. 'Testing of Hydromechanical Properties of the Variably Saturated Residual Dolomite (Wad)'. In *Proceedings of the 20th International Conference on Soil Mechanics and Geotechnical Engineering*. Sydney.

Talib, Z. A., A. Kassim, and G. H. Yunusa. 2016. 'Influence of Relict Joints on Permeability of Residual Soil'. *IOP Conference Series: Materials Science and Engineering* 136 (1): 012015. https://doi.org/10.1088/1757-899X/136/1/012015.

Terribile, Fabio, Giuliano Langella, Florindo Antonio Mileti, Luciana Minieri, and Simona Vingiani. 2022. 'Soil Sampling and Preparation for X-Ray Imaging'. In *X-Ray Imaging of the Soil Porous Architecture*, edited by Sacha Jon Mooney, Iain M. Young, Richard J. Heck, and Stephan Peth, 19–38. Cham: Springer International Publishing. https://doi.org/10.1007/978-3-031-12176-0_3.

Terzaghi, Karl. 1943. *Theoretical Soil Mechanics*. 1st ed. Wiley. https://doi.org/10.1002/9780470172766.

Tol, Johan van. 2020. 'Hydropedology in South Africa: Advances, Applications and Research Opportunities'. *South African Journal of Plant and Soil* 37 (1): 23–33. https://doi.org/10.1080/02571862.2019.1640300.

Toll, D. G. 2012. 'The Behaviour of Unsaturated Soil'. In *A Handbook of Tropical Residual Soil Engineering*, 117–45. Taylor and Francis. https://doi.org/10.1201/b12302-9.

Totsche, Kai U., Thilo Rennert, Martin H. Gerzabek, Ingrid Kögel-Knabner, Kornelia Smalla, Michael Spiteller, and Hans-Jörg Vogel. 2010. 'Biogeochemical Interfaces in Soil: The Interdisciplinary Challenge for Soil Science'. *Journal of Plant Nutrition and Soil Science* 173 (1): 88–99. https://doi.org/10.1002/jpln.200900105.

Townsend, Frank C., Phillip G. Manke, and James V. Parcher. 1969. 'EFFECTS OF REMOLDING ON THE PROPERTIES OF A LATERITIC SOIL'. *Highway Research Record*, no. 284. https://trid.trb.org/View/121427.

U.S.D.A. 2017. 'Soil survey manual'. *Soil Survey Division Staff; Soil Conservation Service. U.S. Department of Agriculture* I (Handbook 18).

Van der Hoven, Stephen J., D. Kip Solomon, and Gerilynn R. Moline. 2003. 'Modeling Unsaturated Flow and Transport in the Saprolite of Fractured Sedimentary Rocks: Effects of Periodic Wetting and Drying'. *Water Resources Research* 39 (7). https://doi.org/10.1029/2002WR001926.

Van der Merwe, D. H. 1964. 'The Weathering of Some Basic Igneous Rocks and Their Engineering Properties'. *Civil Engineering = Siviele Ingenieurswese* 1964 (12): 213–22. https://doi.org/10.10520/AJA10212019_17003.

Van der Merwe, D. J. 1942. 'The Occurrence, Characteristics and Function of Manganese in Soil and Plant'. *Farming in South Africa* 17 (195): 360–64. https://doi.org/10.10520/AJA00148490_3865.

Vogel, Hans-Jörg, Maria Balseiro-Romero, Alexandra Kravchenko, Wilfred Otten, Valérie Pot, Steffen Schlüter, Ulrich Weller, and Philippe C. Baveye. 2022. 'A Holistic Perspective on Soil Architecture Is Needed as a Key to Soil Functions'. *European Journal of Soil Science* 73 (1): e13152. https://doi.org/10.1111/ejss.13152.

Wang, Nannan, and Tibin Zhang. 2024. 'Soil Pore Structure and Its Research Methods: A Review'. *Soil and Water Research* 19 (January). https://doi.org/10.17221/64/2023-SWR.

Wang, Yizhao, Ruiling Jia, Yadong Li, Kezheng Yang, Jie Cui, and Yi Shan. 2024. 'Study on the Mechanical Properties and Microscopic Evolution Mechanisms of Weathered Granite Soil'. *Scientific Reports* 14 (1): 24388. https://doi.org/10.1038/s41598-024-75092-y.

Wang, Yuzhu, and Sheik S. Rahman. 2023. 'Numerical Modelling of Reservoir at Pore Scale: A Comprehensive Review'. *Journal of Computational Physics* 472 (January):111680. https://doi.org/10.1016/j.jcp.2022.111680.

Warren, J. 2000. 'Dolomite: Occurrence, Evolution and Economically Important Associations'. *Earth-Science Reviews* 52 (1–3): 1–81. https://doi.org/10.1016/S0012-8252(00)00022-2.

Weinert, HH. 1980. *Natural Road Construction Materials of Southern Africa*. http://hdl.handle.net/10204/3840.

Wesley, Laurence D. 1990. 'Influence of Structure and Composition on Residual Soils'. *Journal of Geotechnical Engineering* 116 (4): 589–603. https://doi.org/10.1061/(ASCE)0733-9410(1990)116:4(589).

Wesley. 2010. *Geotechnical Engineering in Residual Soils*. 1st ed. Wiley. https://doi.org/10.1002/9780470943113.

Wesley, Laurence D. 2019. 'Genuine and False Pre-Consolidation and Yield Pressures'. Edited by A. Tarantino and E. Ibraim. *E3S Web of Conferences* 92:05001. https://doi.org/10.1051/e3sconf/20199205001.

White, Robert Edwin. 2006. *Principles and Practice of Soil Science: The Soil as a Natural Resource*. 4th ed. Malden: Blackwell publ.

Wildenschild, Dorthe, and Adrian P. Sheppard. 2013. 'X-Ray Imaging and Analysis Techniques for Quantifying Pore-Scale Structure and Processes in Subsurface Porous Medium Systems'. *Advances in Water Resources* 51 (January):217–46. https://doi.org/10.1016/j.advwatres.2012.07.018.

Wilson, M. J. 2004. 'Weathering of the Primary Rock-Forming Minerals: Processes, Products and Rates'. *Clay Minerals* 39 (3): 233–66. https://doi.org/10.1180/0009855043930133.

Wu, Hong-tao, Zi-long Zhang, and Daniel Dias. 2024. 'Prediction on Compression Indicators of Clay Soils Using XGBoost with Bayesian Optimization'. *Journal of Central South University*, June. https://doi.org/10.1007/s11771-024-5681-9.

Yong, Raymond N., Masashi Nakano, and Roland Pusch. 2012. *Environmental Soil Properties and Behaviour*. 0 ed. CRC Press. https://doi.org/10.1201/b11658.